Université Catholique de Louvain

Faculté de Pharmacie et des Sciences Biomédicales

de Duve Institute

Identification of mechanisms driving development of the bile ducts and hepatic arteries

Lila Gannoun

Mars 2022

Jury members

Supervisor

Frédéric Lemaigre, Professor
Université Catholique de Louvain

Internal jury members

Christophe Pierreux, Professor
Université Catholique de Louvain

Isabelle Leclercq, Professor
Université Catholique de Louvain

Guido Bommer, Professor
Université Catholique de Louvain

External jury members

Dirk Drasdo, Research Director
INRIA, Saclay-Ile de France

Chantal Housset, Professor
Faculté de Médecine Sorbonne Université

Remerciements

Je tiens tout d'abord à remercier mon promoteur de thèse, le professeur Frédéric Lemaigre. Frédéric, j'ai apprécié travailler dans votre laboratoire et j'ai énormément appris à vos côtés (maintenant, je peux même distinguer un aigle criard d'une bernache à cou roux !). Je vous remercie pour votre confiance durant ces 5 ans, cela m'a permis d'être plus autonome et d'avoir enfin confiance en moi. Je suis ravie de rester une année supplémentaire dans votre laboratoire, car je sais qu'il est difficile de trouver un chef aussi sympathique et à l'écoute que vous.

Je remercie également Patrick Jacquemin pour son écoute et ses conseils à toutes les réunions de labo, et même en dehors des réunions si nous en avions besoin. Merci aux membres (internes et externes) de mon jury de thèse, les professeurs Christophe Pierreux, Guido Bommer, Isabelle Leclercq, Chantal Housset et Dirk Drasdo, pour vos conseils et le temps que vous avez consacré à la lecture de ma thèse. Je tiens finalement à remercier Paul Van Liedekerke et Dirk Drasdo pour cette collaboration très intéressante qui m'a permis d'étudier un autre aspect de la science.

Un grand merci à tous mes collègues qui m'ont aidée à un moment ou l'autre de la thèse. Tout d'abord, je remercie les personnes qui m'ont formée lors de mon arrivée au laboratoire. Je remercie également mes nouveaux collègues qui m'ont soutenue jusqu'au bout de la thèse, par exemple lors de ma « petite » tendinite ! Merci également à Catalina, qui a partagé des résultats nécessaires à l'avancée de ma thèse. En plus de nos projets similaires, nous partageons cette frustration des résultats négatifs… Courage!

Alejandra, je sais que tu n'aimes pas quand je te le répète, mais MERCI ! Tu as toujours su me conseiller, tant pour les expériences au laboratoire que pour la gestion de mon stress. Tu n'hésitais pas à m'engueuler quand je stressais (parfois pour rien, je m'en rends compte) ou quand je zappais le repas du midi lors des grosses journées… Bref, j'ai bien compris qu'on ne rigolait pas avec Maman Alejandra !

Je remercie également l'équipe GEPI, toujours sympathique et de bonne compagnie lors des teambuildings ! Anna, nous sommes dans le même bateau et nous nous encourageons l'une l'autre depuis le début. Discuter et rire avec toi m'ont toujours bien aidé à avancer positivement. Merci pour tout et courage pour la fin de ta thèse !

Angeline, plus qu'une collègue… Une véritable amie ! Quel bonheur d'avoir travaillé toutes ces années à tes côtés. Toutes nos discussions de travail (tu es toujours de bon conseils), mais aussi nos petites pauses bien nécessaires pour se changer les idées … Sans oublier nos soirées zumba et body form (aïe les jambes le lendemain). L'évènement le plus important de ces 4 années est l'arrivée de ta petite princesse. J'ai tellement hâte de l'entendre dire « Tata Lila » ! Et finalement, sache que ta demande pour être ton témoin m'a beaucoup touchée… Je suis heureuse de pouvoir partager ce magnifique moment à tes côtés.

Mes derniers et grands remerciements vont aux personnes qui m'ont soutenue en dehors de mes journées de travail. Maman, papa, merci d'avoir cru en moi depuis toute petite et de m'avoir soutenue dans toutes les situations. Même si j'ai eu de drôles idées de carrière quand j'étais enfant (de volcanologue à astronaute, en passant par médecin légiste), j'espère que vous êtes fiers du domaine dans lequel je m'investis finalement. Une chose est sûre, une grande partie de ma réussite vous revient amplement. Finalement, je remercie la personne la plus impliquée (malgré lui) dans mes études, Maxime. Nous nous sommes rencontrés pendant mon mémoire, et depuis tu en as écouté des présentations ! Tes petites blagues m'ont quand même aidé à gérer mon stress : « Ça t'éNHERF de ne pas réussir à faire fonctionner NHERF-1 ! ». Pas très drôle quand on y réfléchit, mais l'amour rend aveugle…Tu m'as soutenue dans le « pire », mais tu m'as surtout appris à me déconnecter du travail, lors de nos vacances au soleil par exemple ou à Pairi Daiza (notre deuxième maison). Nous allons maintenant pouvoir commencer de nouveaux projets…

Table of contents

Summary

The liver exerts essential homeostatic functions including the production and excretion of bile. The hepatic lobules are the functional units of the liver and consist of hepatocyte cords and sinusoids that radiate from the portal area to the central vein. The portal area contains a branch of the portal vein, a hepatic artery, a bile duct and mesenchymal cells. Biliary ducts are lined by cholangiocytes and drain bile secreted in canaliculi by the hepatocytes. The hepatic mesenchyme is heterogeneous and comprises at least three cell subpopulations, namely fibroblasts, hepatic stellate cells and vascular smooth muscle cells. Development of the bile ducts, hepatic artery and mesenchyme is interdependent. However, how bile duct development is coordinated with morphogenesis of the vasculature and mesenchyme, and how bile duct lumina form and connect with the hepatocyte canaliculi remains largely unknown.

In the present thesis, we resorted to gene expression profiling in developing mouse liver and to phenotyping of transgenic mice, and found that Slit2-Robo2 signalling in the periportal mesenchyme is required for normal morphogenesis of the hepatic arteries. No impact of this signalling pathway was uncovered on bile duct morphogenesis. Further, in collaboration with computational biologists, we characterised mechanisms driving biliary lumen formation at the earliest stage of bile duct formation in embryonic liver. Our data predict that directed cell division of cholangiocytes combined with local osmotic effects and temporally-controlled differentiation of hepatoblasts to cholangiocytes are the main drivers of biliary lumen formation. Finally, we provided a preliminary description of how bile duct lumina connect with bile canaliculi in embryonic livers, and identified Claudin7 as a specific marker of the hepatoblasts/hepatocytes expressed in establishing the duct-canaliculi junctions.

In conclusion, our work identified a new signalling pathway required for hepatic artery formation. We also uncovered key mechanisms of biliary lumen formation, and an important marker expressed in junctions between bile ducts and canaliculi.

Abbreviations

Abl	Abelson tyrosine kinase
ABM	Agent-based model
ABP	Apical-Basal Polarity
AC	Apical constriction
AFP	Alpha-fetoprotein
aHSC	Activated hepatic stellate cell
ALCAM	Activated leukocyte cell adhesion molecule
AMPK	AMP-activated protein kinase
Ang1	Angiopoietin 1
aPKC	Atypical protein kinase C
αSMA	Alpha smooth muscle actin
BMP	Bone morphogenetic protein
CaHSCs	Central vein-associated Hepatic Stellate Cell
CBM	Center-based model
CC	Conserved cytoplasmic motif
CCl_4	Carbon tetrachloride
CEACAM1	Carcinoembryonic Antigen-Related Cell Adhesion Molecule 1
CNS	Central nervous system
CTCK	C-terminal cysteine knot domain
CTGF	Connective tissue growth factor
Dcc	Deleted in colorectal carcinoma
DCM	Deformable Cell Model
Dlg	Discs large
EC	Endothelial cell
ECM	Extracellular matrix
EfnB2	Ephrin B2
EGF	Epidermal growth factor
Ena	Enabled
EphB4	EPH Receptor B4

FGF	Fibroblast growth factor
FN	Fibronectin
FoxA1	Forkhead box A1
Gata4	GATA binding protein 4
GEF	Guanine nucleotide exchange factor
GFAP	Glial fibrillar associated protein
HCC	Hepatocellular carcinoma
Hes1	Hairy and enhancer of split 1
HGF	Hepatocyte growth factor
HMEC	Human microvascular endothelial cell
HNF1β	Hepatocyte nuclear factor 1 beta
HNF4α	Hepatocyte nuclear factor 4 alpha
HNF6	Hepatocyte nuclear factor 6
HSC	Hepatic stellate cell
HUVEC	Human umbilical vein endothelial cell
Jag1	Jagged1
Lam	Laminin
LEC	Luminal epithelial cells
Lg	Lethal giant larvae 5
LKB1	Liver kinase B1
LRR	N-terminal leucine rich repeat domain
Lyve1	Lymphatic vessel endothelial hyaluronic acid receptor 1
MEC	Basal myoepithelial cell
MesP1	Mesoderm posterior 1 homolog
MMP2	Matrix metalloproteinase-2
Nf2	Neurofibromatosis type 2
NGF	Nerve growth factor
NHERF1	Na+/H+ exchanger regulatory factor 1
OSM	Oncostatin M
PALS1	Protein associated with lin seven one
Par1b	Partitioning defective 1b

Par3	Partitioning defective protein 3
Par6	Partitioning defective protein 6
PaHSC	Portal vein-associated HSC
PATJ	PALS1-associated tight junction protein
PCP	Planar cell polarity
PDGF	Platelet-derived growth factor
PDPN	Podoplanin
PIP	Phosphatidylinositol phosphate
PTEN	Phosphatase and Tensin homolog
PV	Portal vein
qHSC	Quiescent hepatic sellate cell
RA	Retinoic acid
Rac1	Ras-related C3 botulinum toxin substrate 1
RBPJκ	Recombination signal binding protein for immunoglobulin kappa J
RhoA	Ras homolog gene family, member A
Robo	Roundabout
SDF1	Stromal cell-derived factor-1
SM22α	Smooth muscle protein 22α
Sos	Son of sevenless
Sox	Sex determining region Y-box
SrGAP	Slit–Robo Rho GTPase-activating protein
STM	Septum transversum mesenchyme
TβRII	TGFβ receptor II
TGFβ	Transforming growth factor beta
Thy1	Thymocyte differentiation antigen 1
TPM	Transcripts per million
TUBB3	Neuron-specific class III beta-tubulin
VEGFA	Vascular endothelial growth factor A
VEGFR1	VEGF receptor 1
VEGFR2	VEGF receptor 2
VSMC	Vascular smooth muscle cell

Wt1	Wilms tumor 1
Yap1	Yes1 associated transcriptional regulator
ZO1	Zonula occludens-1

Introduction

1. Overview of the liver

1.1. Anatomy and histology of the adult liver

The liver is the largest gland in the body, representing 2-5% of body weight in human adults and 3-5% in adult mice. It is positioned in the right upper abdomen, below the diaphragm. Lobe patterns differ between species: the four lobes of the mouse liver are right, median, left, and caudate (Fig. 1A). The human liver also has four lobes:

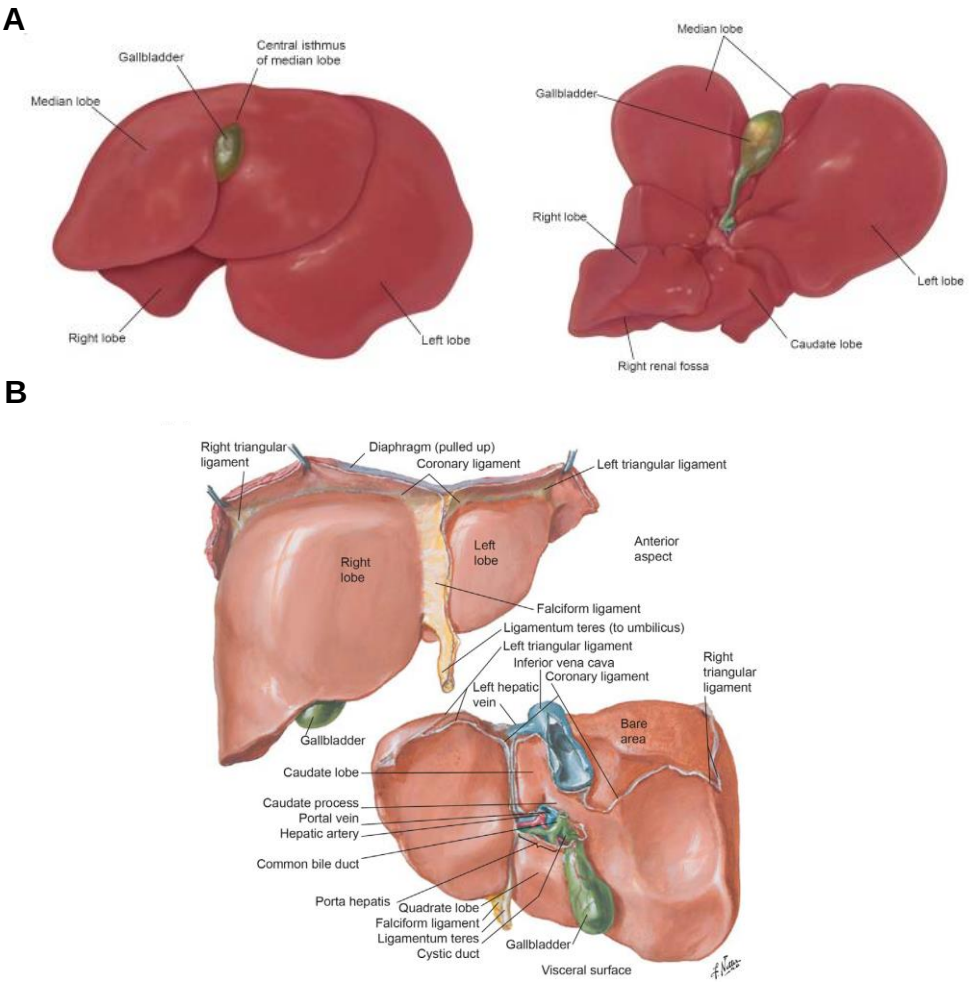

Figure 1. Anatomy of the mouse and human liver. **(A)** The mouse liver has four lobes: left, right, median, and caudate. **(B)** The human liver also has four lobes: right, left, caudate and quadrate. Several prominent surface ligaments are illustrated (Rogers and Dintzis, 2018).

right, left, caudate and quadrate, and abdominal ligaments traverse and delineate lobes (Fig. 1B). The gallbladder is located on the undersurface of the right liver lobe, except in rats and some large animals (e.g. whales) which lack a gallbladder (Rogers and Dintzis, 2018; Carotti et al., 2020).

The functional unit of the liver is the lobule (Fig. 2A). Liver lobules display a hexagonal shape and are formed by plates of hepatocytes aligned with capillaries called sinusoids. Each lobule is characterised by the presence of a central vein located in the middle of the lobule. A portal triad demarcates each corner of the hexagon and consists of a portal vein, a bile duct, and a hepatic artery embedded in mesenchymal tissue. Lymphatic vessels and nerves are also found near the portal vein. Oxygen-rich blood is supplied by the hepatic artery, mixes with blood from the portal vein in the sinusoid and flows to the central vein. In a lobule, the hepatocytes are distributed in 3 zones that exert distinct metabolic functions (Fig. 2B). These functions occur as gradients from zone 1 to zone 3, with varying gradient steepnesses. Zone 1 consists of the hepatocytes located near the portal region. It is exposed to high oxygen concentrations and plays a role in β-oxidation, gluconeogenesis, cholesterol synthesis, and amino acid catabolism. In contrast, zone 3 is located around the central vein. It is at distance of the portal region and therefore less well oxygenated. Zone 3 hepatocytes are in charge of detoxification, lipogenesis, ketogenesis, glycolysis, glycogen synthesis and glutamine formation (Krishna, 2013; Trefts et al., 2017). Finally, zone 2 is located in between zones 1 and 3, and a recent study shows that zone 2 is a source of new hepatocytes during homeostasis and regeneration (Wei et al., 2021).

In addition to the hepatocytes, which constitute ~ 78% of the liver volume, several other cell types contribute to liver function, namely sinusoidal endothelial cells, Kupffer cells, Natural Killer (NK) cells, biliary epithelial cells (or cholangiocytes), and mesenchymal cells. The latter include hepatic stellate cells (HSCs), vascular smooth muscle cells (VSMCs) and fibroblasts (Ishibashi et al., 2009; Dobie et al., 2019). The cholangiocytes, vascular cells and the three mesenchymal cell types are described in the chapters 3 to 4.

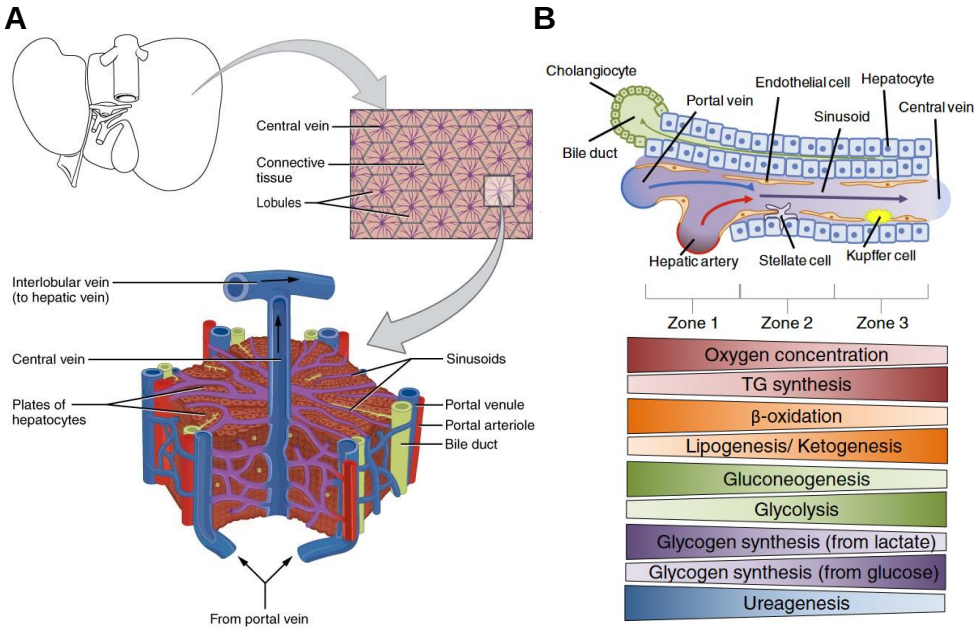

Figure 2. Organisation of the liver. (A) The liver is composed of lobules. Hepatocyte cords radiate from the peripheral portal areas towards a centrilobular vein. Each portal area contains a portal vein, a bile duct and a hepatic artery, collectively refered to as portal triad. **(B)** A schematic representation of the liver zonation and associated metabolic processes (adapted from Betts et al., 2013; Trefts et al., 2017).

1.2. Functions of the liver

The liver exerts essential exocrine, endocrine and metabolic functions which can be summarized briefly as follows:

- Exocrine functions: production and excretion of the bile.
- Endocrine functions: secretion of hormones including insulin-like growth factor 1, angiotensinogen, thrombopoietin, and hepcidin, as well as secretion of plasma proteins such as albumin, transport proteins or blood clotting factors.
- Metabolic functions: glycogen and glucose synthesis, cholesterol transport, urea metabolism, drug detoxification, clearance of bilirubin, synthesis of ketone bodies, and storage/metabolism of vitamins.

Moreover, during embryogenesis, the fetal liver is the host of hematopoiesis (Zong and Stanger, 2012; Trefts et al., 2017; Giancotti et al., 2019; Kalra et al., 2021).

2. Overview of mouse liver development

The endoderm germ layer arises from the epiblast during gastrulation and forms a primitive gut tube that is subdivided into foregut, midgut and hindgut. The foregut endoderm gives rise to the liver, extrahepatic biliary tract, pancreas, stomach, lungs and thyroid (Zaret, 2001; Zorn, 2008; Gordillo et al., 2015).

Liver development is initiated when the prehepatic endoderm acquires competence, i.e. when transcription factors, such as FoxA1 and GATA4, bind to enhancer elements of liver-specific genes such as the *Albumin* gene and enhance chromatin accessibility without stimulating the genes expression. HNF1β is also necessary for hepatic competence (Tremblay and Zaret, 2005; Lokmane et al., 2008; Zong and Stanger, 2012). The competence stage is followed shortly thereafter, i.e. around embryonic day (E) 8.5 in mice, by the specification stage during which hepatic precursor cells start to express liver specific proteins, such as albumin, transthyretin, α-fetoprotein (AFP) and Hepatocyte nuclear factor 4 alpha (HNF4α). Hepatic specification is induced by Fibroblast Growth Factors (FGFs) from the developing heart and Bone Morphogenetic Proteins (BMPs) from the Septum Transversum Mesenchyme (STM, Fig. 3). After hepatic specification, the ventral domain of the foregut adjacent to the STM thickens to form the liver diverticulum: hepatoblasts acquire a columnar shape and the diverticulum is lined by a laminin-rich basal membrane and endothelial cells. At the onset of liver bud formation, endodermal cells become hepatoblasts and transit to a pseudostratified epithelium with nuclear repositioning during cell division. Between E9.0 to E9.5, the basal membrane is degraded, allowing the hepatoblasts to expand into the STM. Formation of the liver bud requires signals from endothelial cells. After invasion of the STM, hepatoblasts proliferate allowing the liver to grow, and this proliferation is regulated by interactions with surrounding endothelial cells and hepatic mesenchyme. Wnt signalling, as well as FGF, BMP, Hepatocyte Growth Factor (HGF), Transforming Growth Factor β (TGFβ) and retinoic acid (RA), promote hepatoblast migration, proliferation, and

survival (Matsumoto et al., 2001; Zaret, 2001; Zorn, 2008; Si-Tayeb et al., 2010; Gordillo et al., 2015; Ober and Lemaigre, 2018).

The hepatoblasts are bipotent progenitors that can differentiate into hepatocytes or cholangiocytes. Hepatocyte maturation, which consists in acquisition of adult liver functions and organisation into hepatocyte cords, is stimulated by Oncostatin M (OSM), glucocorticoids, HGF and Wnt (Kamiya et al., 1999; Ito et al., 2000; Zong and Stanger, 2012).

Signalling pathways controlling cholangiocyte differentiation and bile duct morphogenesis are described in section 3.3.

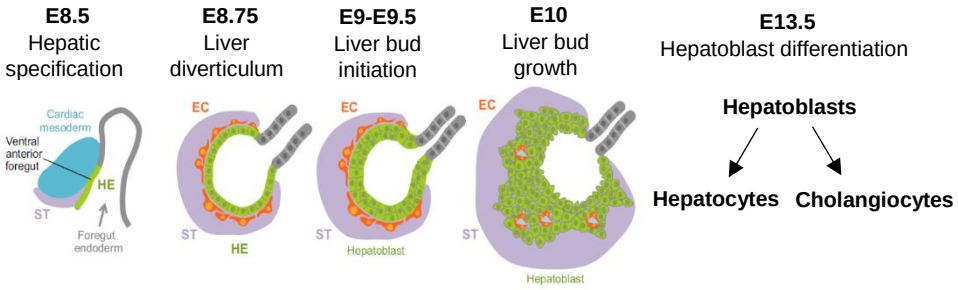

Figure 3. Mechanisms controlling early development of the liver. Signalling from the cardiac mesoderm and STM are required for hepatic specification. At E8.75, the liver diverticulum forms: hepatoblasts acquire a columnar shape and the diverticulum is lined by a basal membrane and endothelial cells. Around E9, hepatoblasts become organised as a pseudostratified epithelium. The basal membrane is subsequently degraded, allowing the hepatoblasts to expand into the STM and initiate liver bud formation. At E10, hepatoblasts proliferate and initiate differentiation into hepatocytes or cholangiocytes.
STM: septum transversum mesenchyme. HE: hepatic endoderm. EC: endothelial cell (adapted from Gordillo et al., 2015).

3. The biliary system

3.1. Organisation and function of the biliary system

The biliary system is composed of the extra- and intra-hepatic biliary systems (Fig. 4). The extrahepatic biliary system includes the common hepatic duct, common bile duct, cystic duct and gallbladder where bile is transiently stored. In the liver, the intrahepatic biliary tract is constituted by the ramification of the left and right hepatic

ducts into smaller intrahepatic bile ducts. Bile canaliculi, the smallest branches of the bile duct system, are delineated by the apical poles of adjacent hepatocytes and are connected to intrahepatic bile ducts via the canals of Hering, which are lined by cholangiocytes and hepatocytes (Saxena and Theise, 2004; Morini et al., 2020).

The biliary epithelium is known for many years to be heterogeneous at the morphological and functional level (Kanno et al., 2000). Recent single cell RNA sequencing analyses provided extensive details on this heterogeneity. Pepe-Mooney et al. (2019) showed in mice that heterogeneity reflects in part the activation of YAP signalling, a pathway required for maintaining cholangiocyte homeostasis (Verboven et al., 2021). In human liver, cholangiocyte heterogeneity was characterised by a combination of single cell and single nucleus RNA sequencing. This revealed six transcriptionally-distinct subpopulations that vary according their

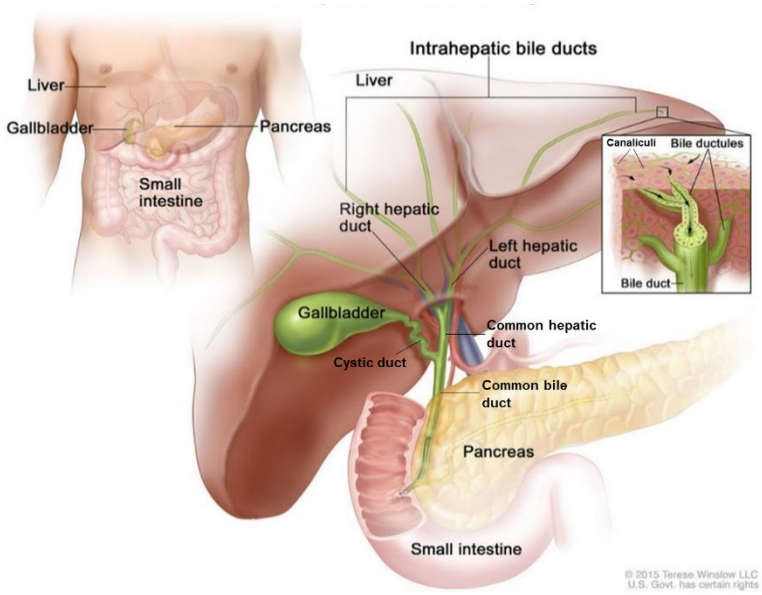

Figure 4. Schematic representation of the extra- and intra-hepatic biliary trees. The extrahepatic biliary system is composed of the common hepatic duct (hilar region) and the common bile duct (distal region). Bile is stored in the gallbladder and flows in the cystic duct to reach the small intestine via the common bile duct. The intrahepatic biliary system is composed of the right and the left hepatic ducts that ramify to form the intrahepatic bile ducts (adapted from https://www.teresewinslow.com/#/digestion/).

differentiation status, ranging from progenitor-like to hepatocyte-like and mature cholangiocytes (Andrews et al., 2021).

Bile is produced by the hepatocytes and is transported to the gut via the intra- and extra-hepatic ducts. It contains cholesterol, bile acids, bilirubin, detoxified metabolites and ions. Bile acids are synthesized from cholesterol, conjugated to glycine or taurine, and allow emulsification, digestion and absorption of fat in the small intestine (Neuman, 2020). Bilirubin is a degradation product of heme and is secreted by hepatocytes after glucuronoconjugation. Ions comprise Cl^- and $HCO3^-$, the latter being important for buffering stomach-derived acids in the gut. Importantly, during the transit through the biliary system, bile is modified by cholangiocytes and this includes secretion of Cl^-, $HCO3^-$ and water from cholangiocytes as well as reabsorption of bile acids (Tabibian et al., 2013).

3.2. Morphogenesis of the intrahepatic bile ducts

Below we describe current knowledge on intrahepatic bile duct morphogenesis. However, to put this in a wider context, we first summarize how the two intricate processes of tubulogenesis and lumenogenesis are considered in developing organs.

Models of lumenogenesis are grouped into two major categories (Fig. 5). First, lumen and tube develop from already established cellular sheets. Wrapping and budding belong this category. Second, lumen and tube formation results from de novo creation of a hollow space. Cavitation, cell hollowing and cord hollowing constitute this second category. Wrapping occurs when an epithelial sheet undergoes apical constriction to evaginate and form a tubular structure parallel to the plane of the original cell sheet. An example of wrapping includes neural tube formation in mammals. Budding is characterised by the formation of a new branch originating from a direct extension of the original tube. Examples of budding are the development of mammalian lung bronchi and kidney tubules. In cavitation, apoptosis within a cell cord creates a luminal space in the middle of the structure. Development of salivary gland illustrates cavitation. Cord hollowing uses trafficking machinery to

create a nascent apical lumen, with the formation and fusion of vesicles to the apical membrane. For lumen expansion, vesicles deliver fluids and other molecules that have osmotic properties. Cord hollowing is typically involved in development of vertebrate vasculature. Cell hollowing is similar to cord hollowing, but the lumen forms intracellularly by fusion of intracellular vesicles. Examples of cell hollowing are the excretory canal of *Caenorhabditis elegans* and *Drosophila* trachea terminal cells (Lubarsky and Krasnow, 2003; Andrew and Ewald, 2010; Wells and Patel, 2010; Sigurbjörnsdóttir et al., 2014; Teshima et al., 2015; Jewett and Prekeris, 2018).

Establishment of epithelial apico-basal polarity is at the core of tubulogenesis and depends on a series of protein complexes which regulate the formation of tight junctions and so segregate the apical and basolateral poles (Fig. 6, Datta et al., 2011). The first complex is composed of Crumbs, an apical transmembrane protein that directly binds to a PDZ domain of the Protein Associated with Lin Seven One (PALS1), whereas PALS1 is a scaffold that interacts to PALS1-associated Tight Junction protein (PATJ). The second apical complex consists of Partitioning defective protein (Par)3, Par6, and atypical protein kinase C (aPKC). The Par3/Par6/aPKC complex localizes to tight junctions and defines the apical and basolateral poles. Before cell polarization, Par3 is localized to sites of contact

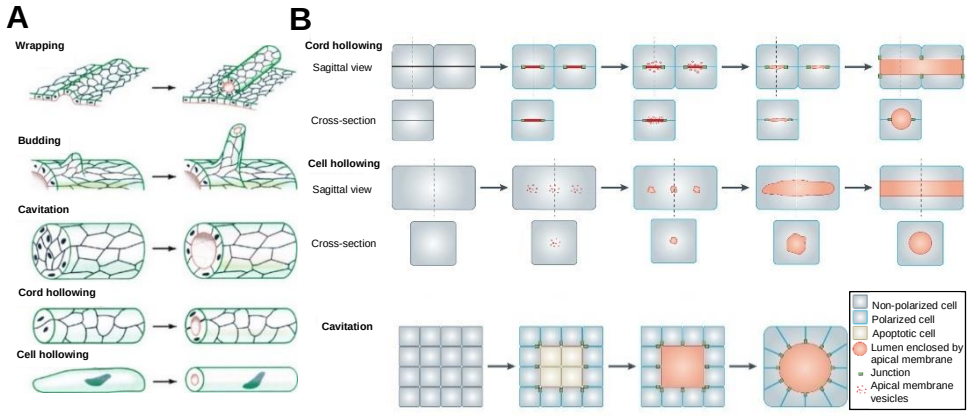

Figure 5. Models of tubulogenesis and lumenogenesis. (A) Wrapping, budding, cavitation, cord hollowing and cell hollowing are depicted. **(B)** Detailed schemes of lumen formation in cord hollowing, cell hollowing and cavitation (adapted from Lubarsky and Krasnow, 2003; Sigurbjörnsdóttir et al., 2014).

between adjacent cells, and the binding of active Cdc42 to the Par6/aPKC complex gives rise to the activation of Par3/Par6/aPKC complex at the site of the forming apical pole. The third complex consists of Scribble, Discs large (Dlg), and Lethal giant larvae 5 (Lg). The Scribble/Dlg/Lg complex is required for the establishment of the basolateral domain and is known to antagonize the Crumbs and Par complexes (Margolis and Borg, 2005; Schlüter and Margolis, 2009; Willenborg and Prekeris, 2011; Lee and Streuli, 2014; Blasky et al., 2015).

Moreover, phosphatidylinositol phosphates (PIPs) are critical in the establishment and maintenance of epithelial polarity. PI3-kinase phosphorylates PI(4,5)P2 to generate PI(3,4,5)P3 at the basolateral surface. Conversely, PTEN phosphatase, recruited by Par3 to the apical region, dephosphorylates PI(3,4,5)P3 into PI(4,5)P2, antagonizing PI3-kinase signalling. PI(4,5)P2 enhances the recruitment of

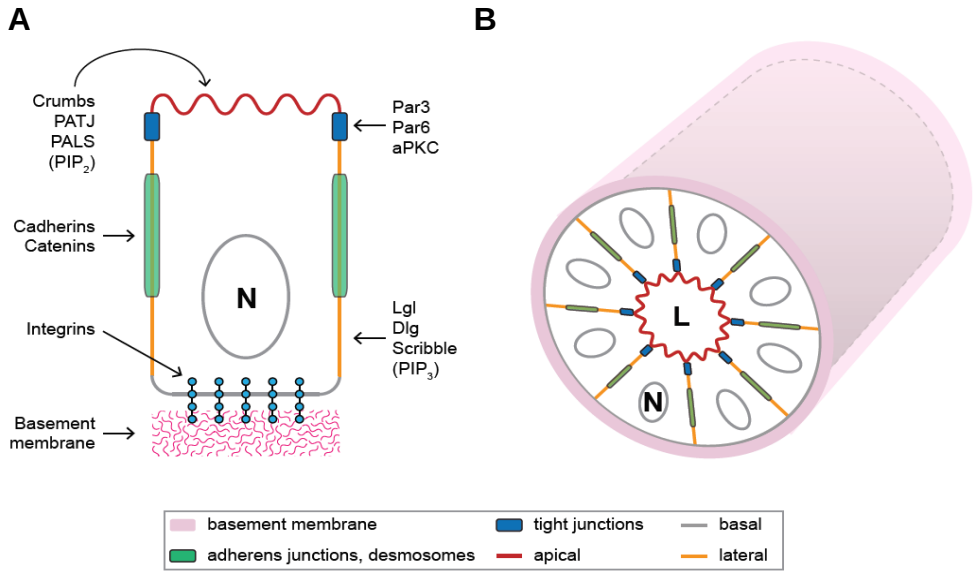

Figure 6. Epithelial cell polarity and tubular architecture. (A) Apical, lateral, and basal plasma membrane domains are composed of specific protein complexes: Crumbs/PALS1/PATJ, Par3/Par6/aPKC and Scribble/Dlg/Lg. Basal membrane is in contact with a basal lamina to provide cell attachment and integrin is involved in polarity. **(B)** Polarized epithelium surrounds a central lumen and forms a tubular structure. L: lumen. N: nucleus (Slim, 2014).

Cdc42/aPKC to the apical domain by the recruitment of Annexin-2, which assembles and activates Cdc42 and aPKC (Shewan et al., 2011).

Importantly, the extracellular matrix (ECM) is implicated in establishment of initial polarity. Indeed, *in vitro* studies demonstrated that activation of β1-integrin orients the apical pole of cysts, via Rac1 activation and laminin organisation, and establishes endothelial cell polarity (Yu et al., 2005; Zovein et al., 2010). Another study confirms the involvement of α2 β1- and α6 β4-integrins in the establishment of apico-basal cell polarity, depending on Rac1, as well as α3 β1-integrin is implicated in positioning of mitotic spindles in cysts (Myllymaki et al., 2011).

The morphogenesis of bile ducts is currently believed to occur as follows (Lemaigre, 2020). Around E14.5, a monolayer of cholangiocytes expressing the transcription factor sex determining region Y-box (SOX)9 surrounds the periportal mesenchyme: this nearly continuous structure is called the ductal plate. At E15.5, asymmetrical structures develop from the ductal plate, and small lumina become detectable (Fig. 7). These asymmetrical structures, also called primitive ductal structures, are lined by cholangiocytes (negative for HNF4α and positive for SOX9) on the portal side and by hepatoblasts (positive for HNF4α and negative for SOX9) on the parenchymal side, while becoming surrounded by mesenchyme. Progressively, hepatoblasts lining the primitive ductal structures differentiate into cholangiocytes, giving rise to mature bile ducts entirely lined by cholangiocytes and surrounded by mesenchyme (Zong et al., 2009; Antoniou et al., 2009; Poncy et al., 2015). Cholangiocytes not involved in bile duct formation redifferentiate into hepatocytes (Carpentier et al., 2011).

Three-dimensional analysis showed that duct growth is discontinuous, namely that primitive ductal structures are initially organised as small luminal spheres that progressively connect with each other to form ducts. Eventually, the bile duct network that has developed around the portal vein reorganises into a hierarchical duct network with one or two main ducts along the portal vein, interconnected with a mesh-like ductular network surrounding the vein (Takashima et al., 2015; Tanimizu et al., 2016).

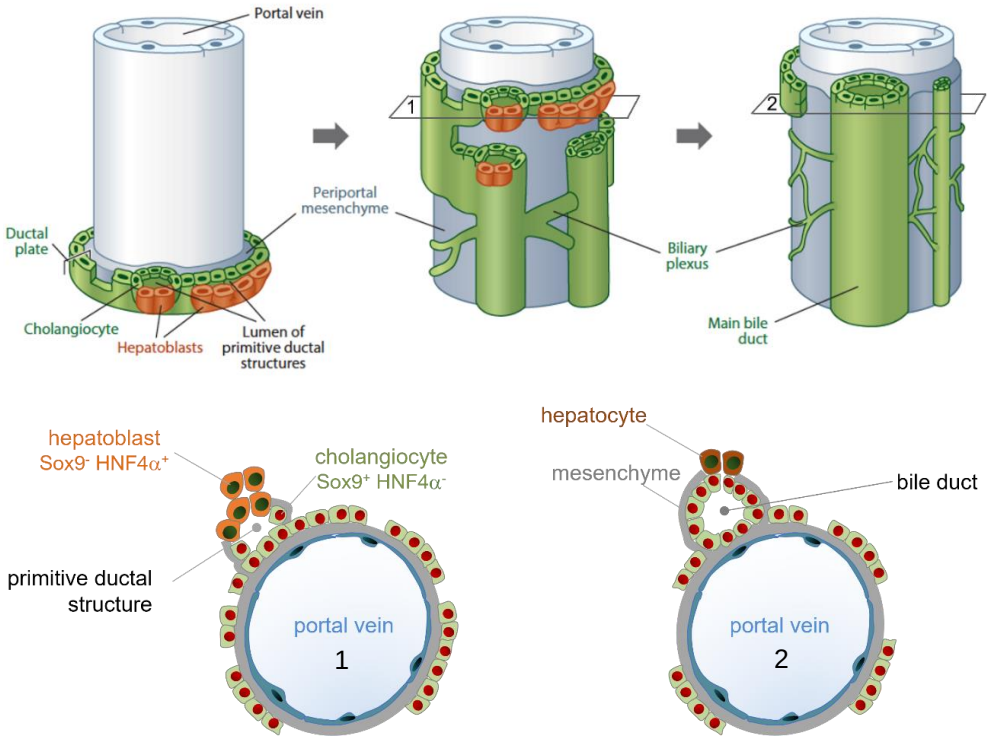

Figure 7. Morphogenesis of intrahepatic bile ducts. On section 1, the asymmetrical structure displays cholangiocytes on the side of the portal vein and hepatoblasts on the parenchymal side. On section 2, ducts have reached maturity and are entirely surrounded by mesenchyme (adapted from Lemaigre, 2020).

3.3. Differentiation of intrahepatic cholangiocytes

The extrahepatic biliary system is lined by cholangiocytes directly derived from the ventral foregut, whereas the intrahepatic biliary system is lined by cholangiocytes derived from hepatoblasts. Single cell analyses revealed that the split between the hepatocyte and intrahepatic cholangiocyte lineages occurs from E11.5 to E14.5 as evidenced by the expression of cholangiocyte-specific genes in hepatoblasts undergoing cholangiocyte differentiation (Yang et al., 2017). The latter differentiate near the portal vein and, starting around E14.5-E15.5, progressively reorganise to form bile ducts (Spence et al., 2009; Higashiyama et al., 2018).

Several signalling modules are involved in intrahepatic cholangiocyte differentiation, the best understood being the TGFβ, Notch, Hippo, and Wnt pathways. An additional, yet less well characterised, involvement of FGF- and Laminin-induced signalling has been proposed (Fig. 8, Lemaigre, 2020).

TGFβ signalling is considered to initiate biliary differentiation. A TGFβ signalling gradient is generated with the secretion of TGFβ2 and TGFβ3 from the periportal mesenchyme to the hepatoblasts. Hepatoblasts express TGFβ receptor II (TβRII), as well as some TGFβ in autocrine fashion, and subsequent activation of the TGFβ pathway induces expression of biliary-specific genes, while repressing the expression of hepatocyte/hepatoblast-specific genes via C/EBPα. The function of the TGFβ pathway is tightly controlled by a HHEX/HNF6/Onecut2/HNF1β/SOX4/SOX9/YAP transcriptional network (Clotman et al., 2005; Antoniou et al., 2009; Poncy et al., 2015).

Notch signalling is essential to cholangiocyte differentiation through interactions between the portal mesenchyme which expresses the ligand JAGGED1 (Jag1), and hepatoblasts that express the receptor NOTCH2. Stimulation of NOTCH2 directly activates expression of SOX9. Moreover, Notch signalling was also found to be critical to promote tubulogenesis. Indeed, mice with inactivation of *Hes1*, *Rbp-jk* or *Notch2* develop a ductal plate but fail to form ducts (Kodama et al., 2004; Lozier et al., 2008; Tchorz et al., 2009; Zong et al., 2009; Hofmann et al., 2010). In humans,

mutations in *JAG1* or *NOTCH2* cause Alagille syndrome, a disease characterised amongst others by bile duct paucity (Li et al., 1997; Oda et al., 1997; McDaniel et al., 2006).

Hippo signalling also regulates bile duct development. Loss of YAP1 results in the absence of bile duct formation and elevated plasma bilirubin levels (Zhang et al., 2010). Moreover, inactivation of *Neurofibromatosis type 2* (*Nf2*) increases *Notch2* expression in cholangiocytes and activation of YAP, eventually resulting in biliary overgrowth (Wu et al., 2017a). The Hippo pathway effector was shown to stimulate TGFβ secretion and so promoting biliary differentiation, while at the same time repressing expression of HNF4α, a master stimulator of hepatocyte differentiation (Lee et al., 2016). Further, deletion of *Yap1* in hepatoblasts prevents formation of the second cholangiocytes layer during bile duct development, leading to the absence of intrahepatic bile ducts (Molina et al., 2021).

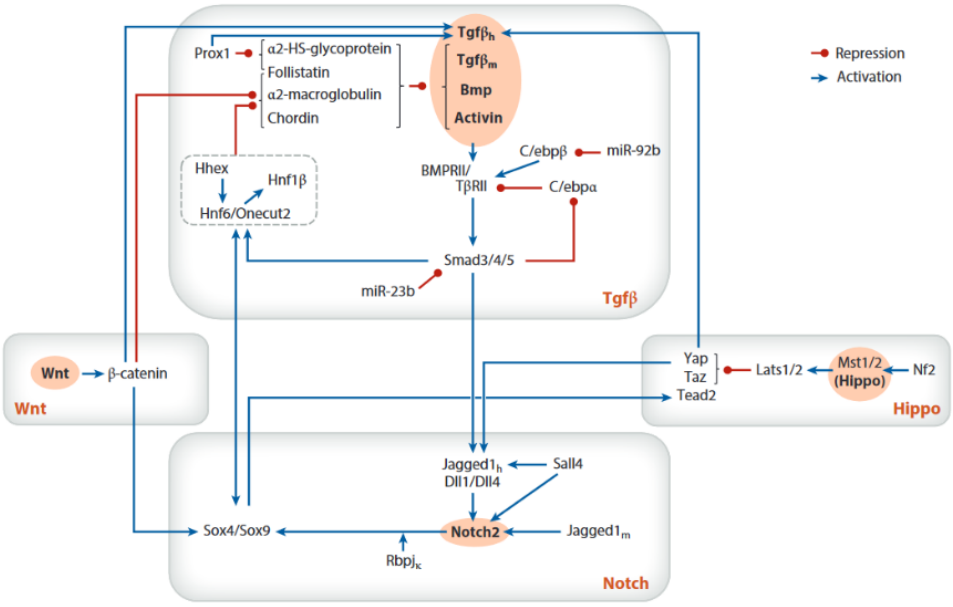

Figure 8. Four main signalling pathways control cholangiocyte differentiation. Notch, TGFβ, Wnt and Hippo are the main pathways involved in biliary differentiation (Lemaigre, 2020).

Wnt/β-catenin pathway is dispensable for differentiation of hepatoblasts into cholangiocytes, but β-catenin overexpression perturbs cholangiocyte differentiation and bile duct development (Cordi et al., 2016). It is suggested to function in part by promoting TGFβ secretion and *Sox4* expression.

FGF signalling was studied on chick livers, revealing that FGF positively regulates biliary differentiation in cooperation with BMP signalling (Yanai et al., 2008). Other studies suggest that Laminin α1 plays a role for the differentiation of hepatoblasts into cholangiocytes and for the apicobasal polarization, whereas Laminin α5 is necessary for the formation of mature bile ducts (Tanimizu et al., 2012).

How the abovementioned pathways promote differentiation of hepatoblasts to cholangiocytes is fairly well understood. However, how they might contribute to duct morphogenesis remains poorly understood. Also, information on initial lumen formation in the primitive ductal structures is limited. Cholangiocytes display apico-basal polarity as soon as they differentiate from hepatoblasts. Adjacent cholangiocytes are joined by tight junctions (zonula occludens) containing ZO1. Moreover, cholangiocytes express basolateral proteins, such as E-cadherin, β-catenin and Claudin7 (Antoniou et al., 2009; Jakab et al., 2010). Based on the analyses of 3D *in vitro* cultures and 2D sections of developing liver, biliary tubulogenesis was proposed to bear similarities with cord hollowing. Indeed, vesicular structures located at the apical pole have been detected by electron microscopy. This is similar to pancreatic lumenogenesis, during which vesicles are delivered at the apical pole of cells, leading to formation of microlumens that eventually fuse to form tubes (Kesavan et al., 2009; Hick et al., 2009; Benhamouche-Trouillet et al., 2018). However, some characteristic mechanisms of bile duct formation, such as asymmetric structures formation, make the comparison with the previously described models complicated, thereby justifying our analysis of biliary lumen formation in the present thesis.

3.4. Development of bile canaliculi

During early liver development, hepatoblasts are non-polarized and mixed with fetal hematopoietic stem cells (Fig. 9). Around E16.5-E17.5, when the number of hematopoietic stem cells in the liver decreases, hepatocytes proliferate, thereby increasing cellular adhesion between the hepatoblasts. At this stage, formation of dense hepatocyte cords is observed, as well as immature canalicular structures delineated by the apical poles of adjacent hepatocytes. The canaliculi then elongate and give rise to a canalicular network which is sealed by tight junctions and functionally connected to the intrahepatic bile ducts (Gissen and Arias, 2015; Tanimizu et al., 2016; Ober and Lemaigre, 2018). Bulkhead-like membrane structures extend from the apical pole of adjacent hepatocytes. They traverse the canaliculi and are bound by tight junctions, thereby allowing anisotropic elongation of the canaliculi (Belicova et al., 2021). The basal membrane of the hepatocytes faces sinusoidal endothelial cells (Treyer and Musch, 2013; Gissen and Arias, 2015; Morales-Navarrete et al., 2019).

In vitro, hepatocytes cultivated in collagen sandwich cultures develop bile canaliculi. Such culture systems enabled to manipulate gene expression and identify pathways regulating canaliculi formation. For instance, inhibition of AMPK or LKB1 in rat primary hepatocytes resulted in loss of canalicular network (Fu et al., 2010). In WIF-B9 cells, a hybrid hepatoma/fibroblast line, knockdown of Claudin2 prevented bile canaliculi formation and changed the hepatic polarized phenotype of the cells into a simple polarized phenotype (Son et al., 2009). Similarly, in the same cell line, downregulation of Par1b re-oriented the microtubules of hepatocytes leading to a

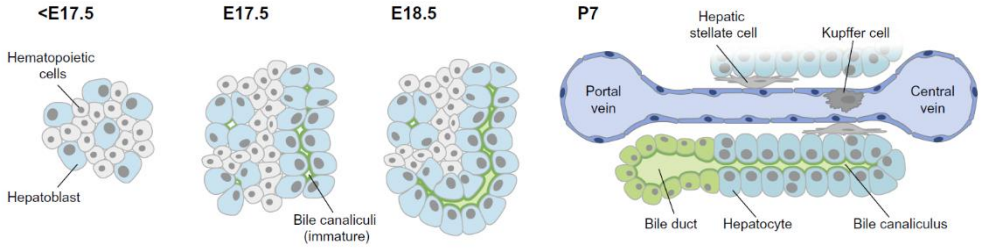

Figure 9. Development of bile canaliculi in mouse (Ober and Lemaigre, 2018).

simple apico-basal polarity (Lazaro-Dieguez et al., 2013). Moreover, OSM and Stat3 stimulate bile canaliculi formation in HepG2 hepatocarcinoma cells and primary fetal hepatic culture, respectively (Ito et al., 2000; Van der Wouden et al., 2002). Asymmetrical hepatocyte division controlled by Par1b allows the inheritance of the entire apical membrane on one of the daughter cells and is required for canaliculi elongation. The second daughter cell then generates *de novo* a new apical pole (Fig. 10, Slim et al., 2013). *In vivo*, in mouse models, bile canaliculi formation is impaired in HNF4α and LKB1 knockouts (Parviz et al., 2003; Woods et al., 2011; Homolya et al., 2014). Additional information has been collected in Zebrafish studies which demonstrated that sinusoidal cells control apico-basal polarization of the hepatocytes and canaliculi formation (Sakaguchi et al., 2008). Finally, mechanisms connecting developing canaliculi and bile ducts have not yet been characterised,

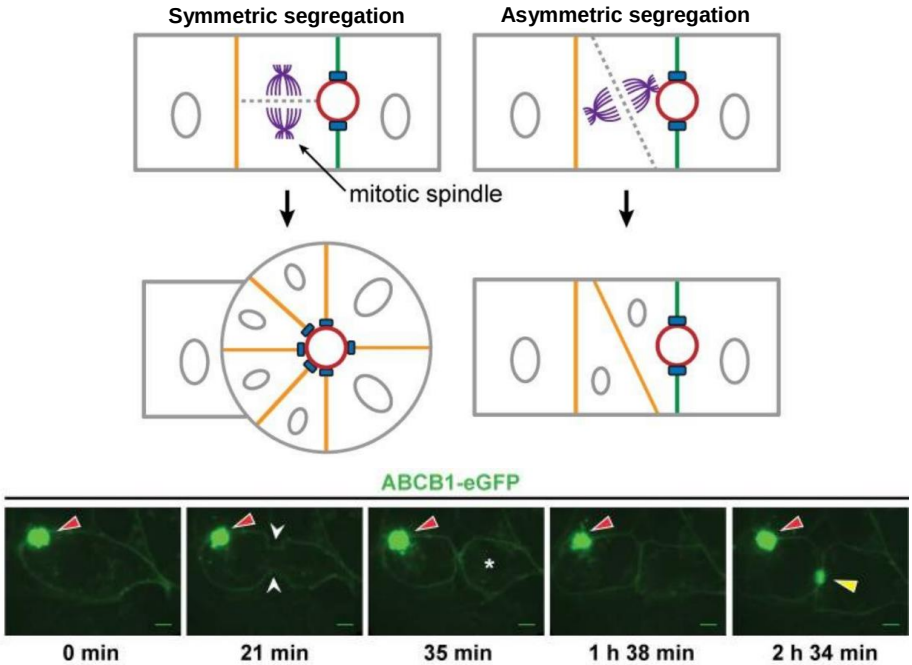

Figure 10. Schematic overview of the difference between columnar and hepatic epithelium. The upper panels show how the axis of division determines the shape of the tissue. The lower panels illustrate how the apical pole is kept in one of the two daughter cells during asymetric division (red arrow), forcing the other daughter cell to generate a new apical pole (yellow arrow). Apical pole is detected using the fusion protein ABCB1-GFP (Slim et al., 2013).

although *in vitro* protocols have now been set up to allow their study (Tanimizu et al., 2021).

4. The liver mesenchyme

4.1. Embryonic origin of liver mesenchyme

The liver mesenchyme comprises cells colonizing the portal space, the space of Disse and Glisson's capsule surrounding the liver. In the present thesis, we focus on three hepatic mesenchymal cell types, namely fibroblasts, hepatic stellate cells (HSCs; also called Ito cells) and vascular smooth muscle cells (VSMCs). They all originate from the mesoderm, and in adult liver have been characterised at the single cell level (Dobie et al., 2019).

Prior formation of the liver bud, mesoderm positive for Mesoderm posterior 1 homolog (MesP1) gives rise to the STM expressing Wilms tumor 1 (Wt1, Fig. 11). Lineage tracing experiments suggested that Wt1-positive STM subsequently gives rise to mesothelial and submesothelial cells that express podoplanin (PDPN), activated leukocyte cell adhesion molecule (ALCAM) and Wt1. Around E10.5-E13.5, Wt1-positive mesothelium migrates into the liver to generate Wt1-negative HSCs, fibroblasts and VSMCs. Precursors of HSCs and portal fibroblasts were also shown to express p75 Neurotrophin receptor (Suzuki et al., 2008). Furthermore, it was demonstrated that Wt1-positive STM can also directly give rise to intrahepatic liver mesenchymal cells during development (Fig. 11, Asahina et al., 2011; Asahina, 2012; Li et al., 2013; Lua and Asahina, 2016). The mechanisms driving development of the mesenchymal cells remain poorly understood; Wt1 has been proposed to

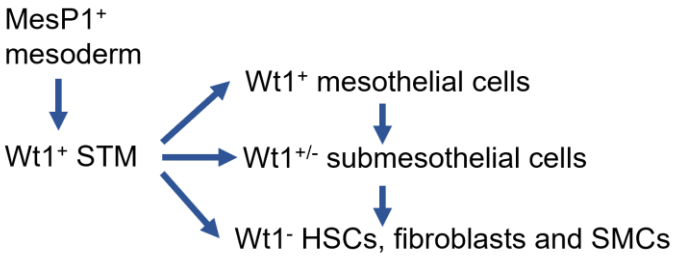

Figure 11. Summary of liver mesenchyme origin (adapted from Asahina et al., 2011).

regulate the differentiation of mesothelial cells into mesenchymal cells via a control exerted on RA signalling (Ijpenberg et al., 2007).

4.2. The hepatic fibroblasts

In fetal and adult liver, fibroblasts are located in the portal space, around central veins and in Glisson's capsule, where they are called capsular fibroblasts. In culture, fibroblasts display an elongated, flat, and spindle shape. They secrete type I collagen and other ECM components. In the liver, portal fibroblasts are the major producers of elastin. They are best identified using the markers including thymocyte differentiation antigen 1 (Thy1), fibulin 2, elastin, cofilin 1 and the ectonucleotidase 2 (Wells, 2014).

During liver development, embryonic portal fibroblasts, called myofibroblasts, express alpha smooth muscle actin (αSMA), but myofibroblasts are eventually replaced by fibroblasts expressing vimentin and loosing αSMA expression. Therefore, myofibroblasts are absent in the normal adult liver, but portal fibroblasts are a source of myofibroblasts in biliary fibrosis, during which they proliferate and differentiate into αSMA^{+} myofibroblasts (Beaussier et al., 2007; Payushina, 2012). It has also been shown that portal myofibroblasts release vascular endothelial growth factor (VEGF)A, which activates VEGF receptor (VEGFR)2 in endothelial cells and mediates proangiogenic effects (Lemoinne et al., 2015).

Portal fibroblasts interact with liver epithelial cells. As previously described in the section 3.3., interactions between embryonic portal mesenchyme and periportal hepatoblasts (via TGFβ and Notch pathways) promote cholangiocyte differentiation and bile duct morphogenesis. Moreover, in fetal liver, portal fibroblasts express laminin α1 and cholangiocytes express β1-integrin. Through this interaction, cholangiocytes and fibroblasts interact to maintain the polarity and lumen of bile ducts (Tanimizu et al., 2012).

4.3. The hepatic stellate cells

HSCs reside in the space between hepatocytes and sinusoidal endothelial cells, i.e. the space of Disse. Under physiological conditions, quiescent HSCs (qHSCs) store

retinoids in lipid droplets and function as pericytes for liver sinusoids. Markers of HSCs are desmin, reelin, glial fibrillar associated protein (GFAP), synaptophisin, synemin and p75 Neurotrophin receptor (Samama and Boehm, 2005; Xu et al., 2014; Karin et al., 2016).

In developing liver, fetal HSCs may stimulate hepatoblast proliferation by secretion of growth factors, such as HGF, pleiotrophin and FGF-10 (Asahina et al., 2002; Berg et al., 2007). In addition, HSCs regulate hematopoiesis by secretion of stromal cell-derived factor-1 (SDF1), erythropoietin and stem cell factor (Payushina, 2012).

In chronic toxic liver injury, HSCs are the major source of myofibroblasts: release of TGFβ1, PDGF, FGF or CTGF leads to activation of qHSCs into activated HSCs (aHSCs or myofibroblasts). The aHSCs produce type I collagen, extracellular matrix proteins, proinflammatory cytokines and αSMA, but lose lipid droplets and neural markers expression (Asahina, 2012; Xu et al., 2014). Unlike portal myofibroblasts, aHSCs do not express elastin and fibrillin during fibrosis (Wells, 2014).

A recent study based on the single cell RNA sequencing revealed a spatial zonation of HSCs, and designated portal vein-associated HSCs (PaHSCs) and central vein-associated HSCs (CaHSCs). They identify CaHSCs as the main cells producing collagen in the centrilobular fibrosis (Dobie et al., 2019).

4.4. The vascular smooth muscle cells

Little is known about the VSMCs located in the liver. From a general point of view, VSMCs are an important component of blood vessels. They constitute the *tunica media* of arteries and veins, and regulate blood pressure by vasoconstriction, vasodilatation and extracellular matrix production (Fig. 12). Indeed, VSMCs display a quiescent contractile state characterised by contractile proteins the expression of which evolves during maturation of the cells: early markers include αSMA and smooth muscle protein 22α (SM22α; synonym: transgelin, TAGLN), intermediate markers include h-caldesmon and calponin, and late markers include SM myosins and smoothelin (Bacakova et al., 2018; Chakraborty et al., 2021).

VSMCs possess a unique phenotypic plasticity: in vascular diseases, VSMCs switch from a contractile and non-proliferative phenotype to dedifferentiated “synthetic” and proliferative VSMCs, characterised by a loss of contractile proteins and an increase in the protein synthesis (Chakraborty et al., 2021). The Notch pathway is the main signalling pathway involved in VSMC differentiation, proliferation and cell survival. During vasculogenesis, one or more layers of VSMCs have to surround the endothelial tube in order to generate a mature vessel able to regulate blood pressure and volume. Recruitment of the VSMCs requires a PDGFB gradient secreted by endothelial cells. Then, Notch ligands expressed by endothelial cells activate Notch signalling in VSMCs, allowing integrin adhesion to the endothelial basement membrane, and maturation and differentiation of VSMCs (Baeten and Lilly, 2017). Moreover, an *in vitro* study defined the roles of Notch2 and Notch3 in VSMCs. Notch2, expressed in human aortic smooth muscle cells, inhibits PDGFB-dependent proliferation, whereas Notch3 promotes proliferation (Baeten and Lilly, 2015). Notch3 mutant mice present with a deficient maturation of cerebral VSMCs, showing that Notch3 is required for differentiation and maturation of VSMCs (Domenga et al., 2004). Another study demonstrated that Notch activity promotes contractile marker expression, such as αSMA (Noseda et al., 2006).

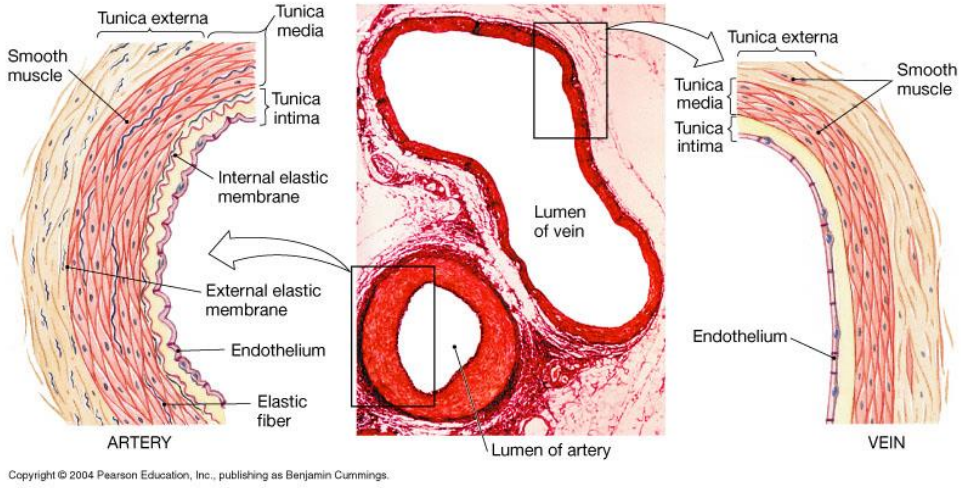

Figure 12. Comparison of artery and vein histology (© Pearson Education, Inc. 2004).

5. The hepatic vasculature

5.1. Overview of the hepatic vasculature

Blood reaches the adult liver through two blood vessels, namely the portal vein and the hepatic artery. The portal vein drains blood from the gastrointestinal tract, spleen and pancreas, contributing to ~75% of the blood flow and ~50% of the oxygen supply. The hepatic artery provides the remainder of hepatic blood flow (Cullen and Stalker, 2016).

The portal vein results from the junction of the splenic vein and the superior and inferior mesenteric veins (Fig. 13A). The portal vein penetrates the liver at the hilum and divides into a right branch and a left branch to ramify into smaller vein branches. These branches reach the sinusoids, where blood is transported to the centrilobular veins and eventually to the inferior vena cava (Carneiro et al., 2019; Morini et al., 2020).

The hepatic artery is a branch of the coeliac trunk, which divides into the gastroduodenal artery and the hepatic artery (Fig. 13B). The hepatic artery enters the hilum and bifurcates to form the right and left hepatic arteries that are parallel to the branches of the portal vein. In human liver, the right hepatic artery supplies the right lobe and the half of the caudate lobe of the liver, and extends to the gallbladder to form the cystic artery. The left hepatic artery supplies the left lobe, quadrate lobe and the other half of the caudate lobe of the liver. Moreover, the intrahepatic arterial branches supply several capillary networks, especially the periportal capillary plexus, the peribiliary capillary plexus, the *vasa vasorum* and the capillaries of the Glisson's capsule (Collardeau-Frachon and Scoazec, 2008; Bayzit Koçer et al., 2018). The hepatic artery therefore supplies oxygen and nutrients to the bile ducts, the periportal vascular plexus and the portal tract interstitium including nerves and the wall of the portal vein. The hepatic sinusoids drain blood from the portal vein and the hepatic artery, from the periphery of the hepatic lobule to the centrilobular vein (Fig. 2B). The sinusoidal endothelium is formed by endothelial cells which are fenestrated, thereby facilitating bidirectional exchanges between the hepatocytes and the blood

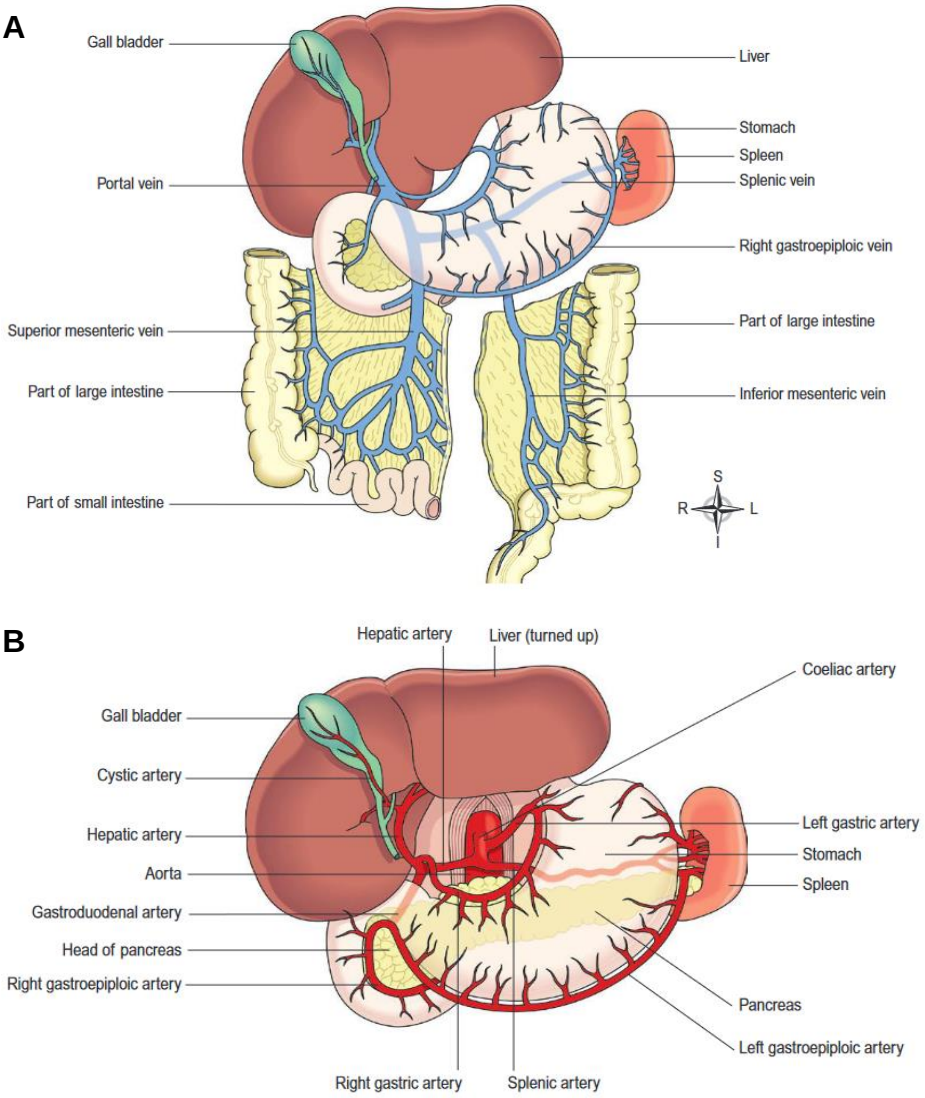

Figure 13. Scheme of the venous and arterial systems supplying blood to the liver (Waugh and Grant, 2014).

(Collardeau-Frachon and Scoazec, 2008). The sinusoidal cells are zonated and exert distinct functions along the porto-central axis. Pericentral sinusoidal cells secrete Wnt ligands that are essential regulators of hepatocyte zonation, midlobular sinusoidal cells bear similarities with lymphatics and express scavenger receptors such as Lyve1, and periportal sinusoidal cells constitute a niche for sinusoidal progenitor cells (Poisson et al., 2017; Halpern et al., 2018; Inverso et al., 2021; Koch et al., 2021). Sinusoids lack a basal membrane and are separated from the hepatocytes by the space of Disse. The fluid in the space of Disse flows to the hepatic lymphatics in the portal space and subsequently into the hepatic hilum lymphatics (Rodés et al., 2007).

5.2. Developmental origin of the liver venous system

It is usually considered that the hepatic venous system derives from the umbilical and vitelline veins. The vitelline and umbilical veins transport blood from the yolk sac and placenta to the *sinus venosus*. Vitelline and umbilical veins give rise to the hepatic venous system, although in humans the contribution of the vitelline vein is questioned. The most widely accepted view is that a intrahepatic branch of the right vitelline vein forms the portal vein.The remodelling of the intrahepatic branch of the left umbilical vein forms the *ductus venosus*, a vessel which allows oxygenated blood from the placenta to bypass the liver during the fetal period. At birth, the umbilical circulation collapses because oxygen is carried to the body via the lungs, and the portal vein remain the only afferent venous system in the liver (Lassau and Bastian, 1983; Collardeau-Frachon and Scoazec, 2008; Crawford et al., 2010). Additional sources of liver endothelial cells have been uncovered using lineage tracing approaches. Specifically in mice, hepatic endothelial cells might be contributed by a subpopulation of endodermal cells and by the endocardium of the *sinus venosus*, the cells of which being attracted to the liver by hepatoblast-secreted VEGF (Goldman et al., 2014; Zhang et al., 2016).

The liver endothelial cells undergo a significant phenotypic evolution during embryogenesis. During the prenatal period, the portal vein endothelium is arterial-like being EfnB2^{+}/EphB4^{-}, but switches at birth to a venous EfnB2^{-}/EphB4^{+} state

(Khan et al., 2016). Also, the sinusoidal endothelial cells are initially non-fenestrated and lined by a basal membrane. Subsequently, fenestrae appear and the composition of the basal membrane changes under influence of VEGF and TGFβ secreted by hepatoblasts, thereby confering to the sinusoidal cells their capacity to host hematopoietic cells. Eventually, after birth, the sinusoidal cells mature and become zonated (Poisson et al., 2017).

5.3. Hepatic artery morphogenesis

Bile ducts and hepatic artery branches are located in close proximity in the portal space, and their development is interconnected at the functional level. Indeed, mutant mice with a primary defect in the cholangiocytes (e.g. HNF6 or HNF1β knockout mice) fail to develop normal ducts and also fail to develop normal arteries (Clotman et al., 2003). In human fetuses, arterial anomalies were detected in the Meckel and Jeune syndromes: fetuses displayed an excess of hepatic arteries associated with an excess of biliary structures (Clotman et al., 2003). Still, how bile ducts and hepatic artery branches interact remains poorly characterised.

The development of the hepatic arterial system slightly differs between humans and mice. In humans, hepatic arteriogenesis starts along the ductal plate during embryogenesis, whereas in mice, hepatic artery branches form postnatally, along well-formed bile ducts. An abundant literature describes how endothelial cells and peri-endothelial cells interact during arteriogenesis in general. Endothelial cell assembly is promoted by VEGF, while PDGF-BB secreted by the endothelial cells recruits pericytes and smooth muscle cells; the artery is then stabilized by Ang1 and TGFβ signalling, likely by stimulating the interaction between endothelial and periendothelial cells. Elastin and fibrillin2 confer viscoelastic properties and strength to the arteries, and protect them from weakening and aneurysmal dilatation (Carmeliet, 2000). When addressing specifically the morphogenesis of hepatic arteries, histomorphological stainings of human fetal livers suggested that cholangiocytes and hepatoblasts promote hepatic artery morphogenesis through VEGF and Angiopoietin (Ang) signalling. Indeed, VEGFA is expressed in human fetuses by cholangiocytes of the ductal plate, likely recruiting endothelial cells,

positive for VEGFR2, into the portal mesenchyme. Then, the endothelial cells express VEGFR1. In parallel, adjacent hepatoblasts secrete Ang1, probably contributing to the recruitment of embryonic myofibroblasts expressing Tie2. Finally, myofibroblasts express Ang2 to promote arterial remodeling through an autocrine regulation (Fig. 14, Fabris et al., 2008; Ober and Lemaigre, 2018). Therefore, our understanding of the mechanisms driving hepatic arteriogenesis is to our knowledge essentially limited to gene expression data, with minimal information on the function and origin of cells involved. This justifies our study on hepatic artery development in the present thesis.

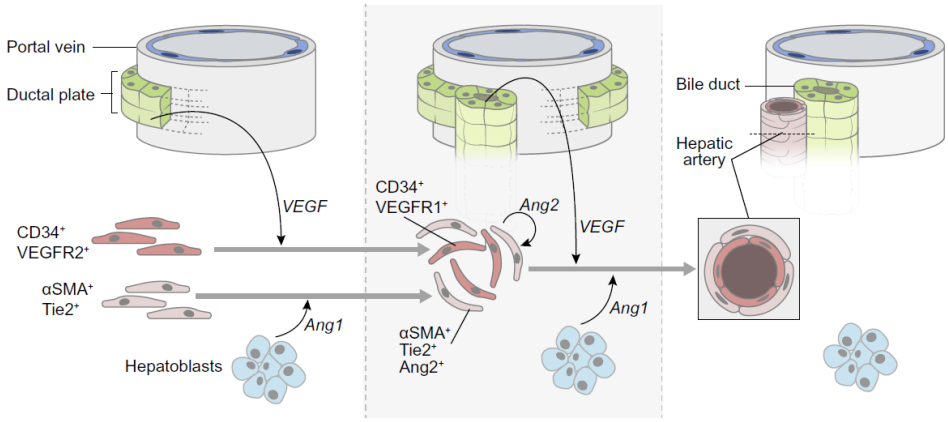

Figure 14. Scheme of hepatic artery development in human liver (Ober and Lemaigre, 2018).

6. The Slit-Robo signalling pathway

6.1. Structure of the Slit and Robo proteins

The Slit-Robo axon guidance signalling was first described in the *Drosophila* central nervous system (CNS) and determines the neuronal patterning of commissural neurons crossing the CNS midline. Four main signalling pathways belong to the « axon guidance » family: 1) Semaphorin ligands and Neuropilin/Plexin receptors, 2) Slit ligands and Roundabout (Robo) receptors, 3) Netrin ligands and deleted in colorectal carcinoma (Dcc), Frazzled (Fra, in *Drosophila*), Unc40 (in C. elegans),

Neogenin and Unc5 receptors, and 4) Ephrin ligands and Eph receptors (Long et al., 2004; Russell and Bashaw, 2018).

A single Slit has been identified in invertebrates, whereas mammals have three homologs: Slit1, Slit2 and Slit3. Moreover, three Robo proteins have been identified in *Drosophila* (Robo1, Robo2, and Robo3) and four Robo in zebrafish and mammals: Robo1/Dutt1, Robo2, Robo3/Rig1 and Robo4/Magic Roundabout. Slit ligands are secreted glycoproteins composed of four N-terminal leucine rich repeat domains (LRR1-4), six epidermal growth factor-like domains (EGF1-6), a laminin G-like (Lam) domain, three additional EGF domains (EGF7-9), and a C-terminal cysteine knot domain (CTCK, Fig. 15). Full-length Slit2 (Slit2-FL) can be cleaved between EGF5 and EGF6 by a protease to generate Slit2-N and Slit2-C fragments. Robo receptors are transmembrane proteins containing five immunoglobulin-like Ig domains, three fibronectin (FN) type III domains, a transmembrane helix, and an intracellular region with two to four conserved cytoplasmic motifs (CC). However, Robo4 receptor contains only two Ig and two FN domains (Blockus and Chédotal, 2016; Wu et al., 2017b ; Zhao and Mommersteeg, 2018 ; Bisiak and McCarthy, 2019 ; Tong et al., 2019). Slit ligands bind through their LRR2 domain to the first Ig domain (Ig1) of Robo, but interactions with other proteins have been described: Eva1C, Plexin A1, Dscam and ECM molecules including Neurexins, Type IV Collagen, Netrin 1, Dystroglycan, Glypican and Syndecan. In addition, Robo1 interacts with the Cxcr4 receptor through its CC3 domain, and heparan sulfate proteoglycans can bind to Slit and Robo proteins for axon guidance (Ypsilanti et al., 2010; Blockus and Chédotal, 2016; Bisiak and McCarthy, 2019).

6.2. Signalling downstream of Slit-Robo

Major effectors of Slit-Robo signalling are regulators of the actin cytoskeleton. These include small GTPases of the Rho family (Cdc42, RhoA and Rac1), the cytoplasmic Abelson tyrosine kinase (Abl) and the actin bundling protein Enabled (Ena) (Fig. 16, Ballard and Hinck, 2012). The Rho small GTPases are controlled by Slit–Robo Rho GTPase-activating proteins (srGAP1, srGAP2 and srGAP3) which are recruited to

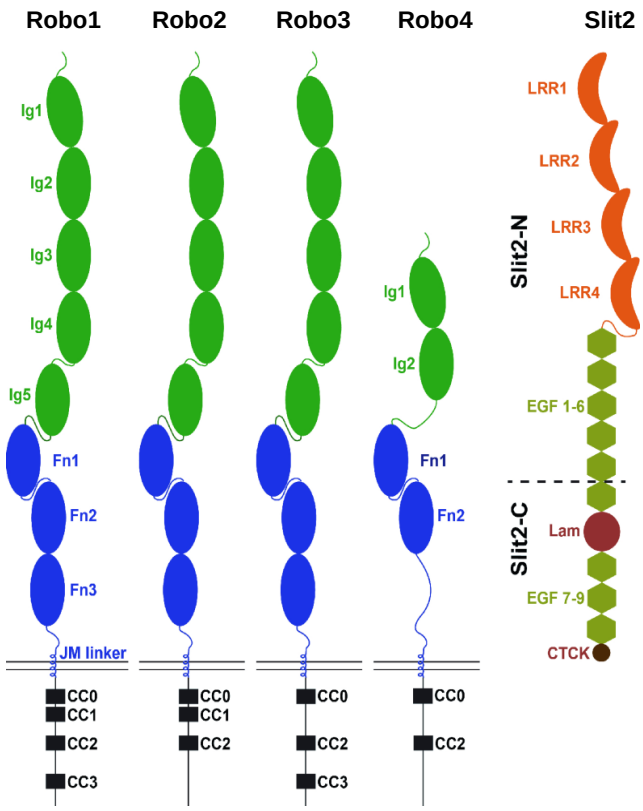

Figure 15. Structure of Slit and Robo proteins. The domain structure of Slits includes 4 leucine rich repeats (D1-D4), 6 epidermal growth factor-like (EGF) domains, a laminin G domain, 3 additional EGF domains and a C-terminal cysteine knot. Robo1, Robo2, Robo3 contain 5 immunoglobulin (Ig) and 3 fibronectin type 3 (FNIII) domains, whereas Robo4 presents only 2 Ig domains and 2 FN repeats. The intracellular domain of Robo receptors contains several conserved motifs: CC0-3 for Robo1, CC0-2 for Robo2, CC0, CC2 and CC3 for Robo3, and CC0 and CC2 for Robo4 (Bisiak and McCarthy, 2019).

the Robo receptor. Together with guanine nucleotide exchange factors (GEFs), srGAPs enable Rho small GTPases to switch between active and inactive states.

Similarly, the adaptor protein Dreadlocks (Dock, called Nck in mammals) also binds to Robo to regulate Rho small GTPase activity. SrGAPs and Dock/Nck target specific Rho small GTPases: srGAP1 inactivates RhoA and Cdc42, srGAP2 activates Rac1, srGAP3 inactivates Cdc42 and Rac1, and Dock/Nck activates Rac1 via the Sos and Pak proteins (Fig. 16A-B, Ypsilanti et al., 2010; Ballard and Hinck, 2012; Lucas and

Hardin, 2017; Gonda et al., 2020). The downstream activity of the Rho small GTPases induces changes in the cytoskeleton. In that context, Cdc42 regulates actin polymerization, thereby playing a role in filopodia formation and endosome internalization (Miki et al., 1998; Harris and Tepass, 2010). Rac signalling is essential for lamellipodia formation and cell migration, whereas RhoA regulates stress fiber formation, focal adhesion organisation, and smooth muscle contraction (Katoh et al., 2011; Steffen et al., 2013).

Slit-Robo-dependent cytoskeletal dynamics is also regulated via Ena and Abl. Ena binds to Robo and positively regulates the dynamics of filopodia, required for axonal repulsion, but can be inhibited by the Abl kinase which phosphorylates a tyrosine residue in the CC1 or CC3 domain of Robo, to antagonize Robo signalling (Fig. 16C, McConnell et al., 2016; Tong et al., 2019). Therefore, activation of Abl, Ena or Rho GTPases determines cell motility and migration.

In addition to motility, Slit-Robo signalling impacts cell adhesion. Here again, the Abl kinase is critical as it phosphorylates β-catenin, resulting in decreased affinity for N-cadherin, nuclear translocation of β-catenin, and reduced cell adhesion (Rhee et al.,

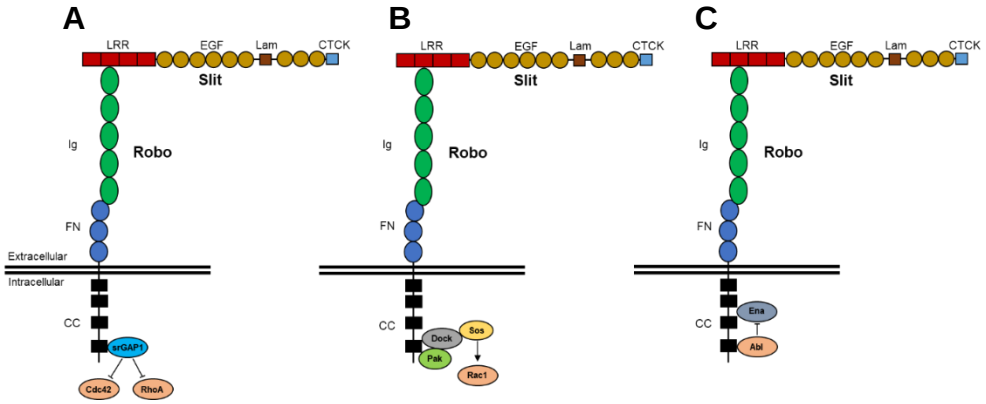

Figure 16. Slit-Robo in cytoskeleton regulation. (A) Slit-Robo regulates the Rho GTPases (Cdc42, Rac1 and RhoA) activity, leading to actin polymerization and cell migration. SrGAP1 binds to the CC3 domain of Robo to inactivate RhoA and Cdc42. **(B)** Slit-Robo regulates actin polymerization by recruiting Dock, which recruits son of sevenless (Sos) GEF and Pak p21-activated kinase. Sos activates Rac1, leading to actin polymerization. **(C)** Ena binds to Robo and inhibits cell migration by preventing actin polymerization. Abl antagonizes Slit-Robo signalling via phosphorylation of Robo and inhibition of Ena.

2007). In contrast, Slit-Robo can stimulate E-Cadherin-dependent adhesion. For instance, Slit2-Robo1 interaction inhibits Akt, a repressor of GSK3β, eventually leading to accumulation of active GSK3β. The latter impairs nuclear accumulation of β-catenin, thereby favoring adhesion. In parallel, Snail, a protein known to stimulate cell motility, is also repressed by active GSK3β, thereby further promoting E-cadherin/β-catenin complex formation (Tseng et al., 2010; Zhou et al., 2011).

6.3. Slit-Robo signalling in development

6.3.1. Nervous system

As mentioned above, Slit-Robo signalling was first discovered in the nervous system, and this stimulated pioneering research on the role of this pathway in this system. In the spinal cord, the axons of commissural neurons cross the ventral midline. The latter secretes diffusible proteins, which control growth and migration of axons across the midline. In this context, the three Slits are expressed in the ventral midline, and commissural neurons express Robo1, Robo2, and Robo3. Slit-Robo interaction acts as a repulsive axon guidance cue, as opposed to Netrin1-Dcc, which attracts commissural axons toward the midline. Slit-Robo signalling allows all commissural axons to cross the midline only once, enabling them to project to the contralateral side (Ypsilanti et al., 2010; Ballard and Hinck, 2012; Blockus and Chédotal, 2016; Tong et al., 2019).

Slit-Robo is not only involved in axon guidance, but also in the proliferation and migration of CNS progenitor cells, which express Robo1 and Robo2. Moreover, Slit-Robo controls dendrite development, especially via Slit1, Slit2 and Robo1 that inhibit neurite outgrowth in migrating interneurons (Gonda et al., 2020).

Finally, Slit-Robo is an important regulator of the morphogenesis of the olfactory tract, optic chiasm, optic tract, forebrain and hindbrain (Andrews et al., 2007).

6.3.2. Kidney

Mice lacking Slit2 or Robo2 developed supernumerary ureteric buds which were not well connected to the nephric duct (Grieshammer et al., 2004; Wainwright et al., 2015). In humans, disruption of Robo2 is associated with urinary tract anomalies and

a risk of vesicoureteral reflux (Lu et al., 2007). Moreover, srGAP1 and Robo2 are co-expressed in mouse nephrogenic mesenchyme, and mutations of srGAP1 are found in patients with congenital anomalies of the kidney and urinary tract (Hwang et al., 2015). In adult mouse kidney, Slit2 and Robo2 stabilize podocytes and thereby the function of the glomerular filtration barrier. This occurs via Slit-Robo-mediated control of actin polymerization in the podocyte foot and modulation of the foot architecture (Fan et al., 2012).

6.3.3. Mammary gland

Slit-Robo signalling restricts mammary gland branching during development. The mammary gland contains two epithelial layers: an outer layer of basal myoepithelial cells (MECs) encircling an inner layer of luminal epithelial cells (LECs). Slit2 is expressed in LECs and MECs, whereas Robo1 is expressed in MECs. An interesting crosstalk between Robo, TGFβ1, Akt, GSK3β and β-catenin controls proliferation: TGFβ1 stimulates Robo1 in MECs, and Robo1 signalling inhibits Akt, leading to activation of GSK3β and subsequent degradation of β-catenin. The latter then fails to stimulate proliferative genes (Macias et al., 2011). Along the same lines, Slit2 and Robo2 negatively regulate Wnt signalling in a subset of MECs to restrict stem cell renewal (Harburg et al., 2014).

6.3.4. Pancreas

In pancreas, Robo1 and Robo2 are required to determine pancreatic cell identity. In double knockout of Robo1 and Robo2, some pancreatic progenitor cells acquired phenotypic characteristics of hepatoblasts, and the pancreas was reduced in size. In this study, Robo receptors were reported to control the expression of Tead transcription factors and their downstream transcriptional activity (Escot et al., 2018), thereby connecting Robo signalling with Hippo-YAP signalling. Moreover, Slit-Robo signalling controls endocrine islet morphogenesis: Slit1, Slit3, Robo1 and Robo2 are expressed in α and β cells, while Slit2 is expressed in β cells. Slit2 signalling is required for β cell survival and islet formation, and Robo receptors are required in the β cells to enable maturation of mature islets (Yang et al., 2013; Adams et al., 2018; Gilbert et al., 2020).

6.3.5. Lung

In lung development, Robo1 and Robo2 are expressed by the developing pulmonary mesenchyme and airway epithelium, as well as by the dorsal mesentery connecting the foregut with the body wall. As lung development progresses, Robo1 and Robo2 become restricted to the airway epithelium (Anselmo et al., 2003). Inactivation of Robo1 and Robo2 induced a delayed separation of the foregut from the body wall, eventually leading to diaphragmatic hernia, mispositioning of the stomach in the thorax, limited lung inflation and lethality at birth (Domyan et al., 2013). Separation of the foregut from the body wall is normally promoted by Robo interacting with Slit produced by the notochord and lateral mesentery. Robo2 also regulates the balance between SOX9-expressing progenitor cells and differentiated SOX2 positive airway epithelial cells, and eventually branching morphogenesis (Goncalves et al., 2020).

Of note, Slit3 is expressed in the mesothelium of the diaphragm, and Slit3 knockout mice display diaphragmatic hernias, characterised by a defective central tendon of the diaphragm that remained fused with the liver. This leads to a herniation of the liver into the thoracic cavity similar to that observed in double Robo1/Robo2 knockout mice (Fig. 17, Yuan et al., 2003).

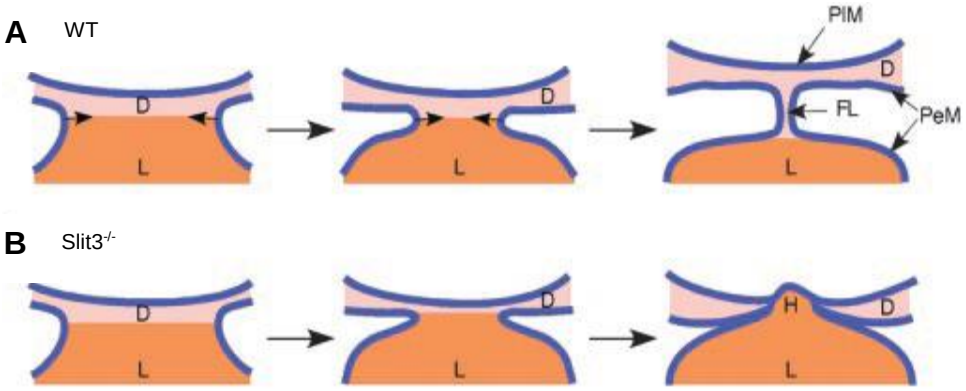

Figure 17. Role of Slit3 in development of the diaphragm and falciform ligament. (A) Scheme of normal diaphragm and falciform ligament development in wild type mice. **(B)** Scheme showing the defect of falciform ligament and herniation in Slit3 knockout mice. D: diaphragm. L: liver. H: diaphragmatic hernia. PlM: pleural mesothelium. PeM: peritoneal mesothelium. FL: falciform ligament (adapted from Yuan et al., 2003).

6.3.6. Heart

Investigation of Robo signalling uncovered a role for these genes in development of the cardiac valves, ventricular septum and pericardium, as well as in positioning of caval veins. Double Robo1 and Robo2 knockout mice displayed thickened immature semilunar and atrioventricular valves. In addition, bicuspid aortic valves were observed. Similarly, Slit3 mutants presented with thickened atrioventricular valves, whereas Slit2 mutants displayed normal atrioventricular valves but developed bicuspid aortic valves. The signalling pathway involved in these heart defects would be the Notch signalling: Robo1 mutant hearts showed a down-regulation of Notch1, HeyL, Hey1 and Hes1 (Mommersteeg et al., 2015). Mommersteeg et al. also showed that a loss of Slit3, Robo1 or both Robo1 and Robo2 induces defects in the membranous ventricular septum. However, such defect was not found in Slit2 mutants. Slit-Robo pathway is also involved in the development of the pericardium, the sinus horn myocardium, and the alignment of the caval veins. Indeed, a lack of Robo1 showed a partial absence of the pericardium, whereas Robo1 and Robo2 double mutants present reduced sinus horn myocardium, hypoplastic caval veins, and a persistent left inferior caval vein. A loss of Slit3 partially recapitulates the defects observed in Robo1 and Robo2 double mutants (Mommersteeg et al., 2013).

6.3.7. Blood vessel development

The various axon guidance pathways, namely the Slit-Robo, Netrin, Semaphorin, and Ephrin pathways, are all involved in angiogenesis. Slit-Robo signalling was found to display pro- and anti-angiogenic functions, and also behaves as a regulator of blood vessel permeability (Wu et al., 2017b).

Robo1 and Robo2 are expressed in endothelial cells and interact with Slit2 to promote angiogenesis. This was concluded from *in vivo* studies showing that Slit2, Robo1 and Robo2 promote endothelial cell migration in mouse postnatal retina and in a model of ocular neovascular disease (Rama et al., 2015), as well as from *in vitro* studies where Slit2 stimulated migration of human umbilical vein endothelial cells (HUVECs) and *in vitro* tube formation following interactions with Robo1 or Robo1-Robo4 heterodimers (Sheldon et al., 2009). Slit3 also promotes endothelial cell

migration by inducing Robo4-dependent Rac1 and RhoA activation (Zhang et al., 2009) or through activation of RhoA/Rho kinase pathway (Dou et al., 2018). Interestingly, the impact of Slit and Robo on angiogenesis depends on cell-type specificity and on the Slit-Robo pairs. Indeed, Slit2 and Robo4 interact in human microvascular endothelial cells (HMECs) to inhibit endothelial cell migration (Park et al., 2003), and Slit2-Robo4 interaction restricts VEGF-induced endothelial permeability by suppressing small GTPase Arf6 activity (Jones et al., 2009). It has also been shown that Robo4 binds UNC5B to inhibit VEGFR2 signalling, in order to stabilize blood vessels and inhibit angiogenesis (Koch et al., 2011).

Endothelial cells are surrounded by VSMCs in veins and arteries and are associated with pericytes in capillaries. Few studies have been published on Slit-Robo in VSMCs and pericytes, but it is known that Robo1, Robo4 and Slit2 are expressed by both cell types, where Slit2 prevents PDGF-mediated VSMC or pericyte migration (Liu et al., 2006; Guijarro-Muñoz et al., 2012).

6.3.8. Liver

Here again, knowledge on the function of Slit-Robo signalling is limited and the focus has been on the analysis of hepatic disease mechanisms, not on development or homeostasis. Three studies uncovered a function of Slit2 in liver fibrosis. First, increased serum Slit2 levels and hepatic expression of Slit2 and Robo1 were observed in patients with liver fibrosis. In addition, mice overexpressing Slit2 enhances liver injury and facilitates liver fibrosis induced by CCl_4 treatment. In combination with studies on an HSC cell line (LX-2) expressing Robo1, it was concluded that Slit2 and Robo1 promote aHSCs through activation of the Smad2/3 and PI3K/Akt pathways, leading to liver fibrosis (Chang et al., 2015). Similarly, Slit2-Robo2 signalling promotes the production of pro-fibrogenic mediators, including Collagen 1, TGFβ1 and CTGF, via the PI3K/Akt pathway. In this study, Slit2 bound to Robo2 in the mouse hepatic cell line JS1 and the HSCs of mouse liver (Zeng et al., 2018). The third study also described Slit2-Robo1 binding as an activator of HSCs, contributing to the survival and proliferation of HSCs via activation of ERK1/2 and p38 signalling. Their Robo1$^{-/-}$ mouse model showed that these mutant mice less

readily develop aHSC activation and liver fibrosis after bile duct ligation (Li et al., 2019).

In hepatocellular carcinoma (HCC), Robo1 and Robo2 are upregulated, whereas Slit3 is downregulated (Ito et al., 2006; Avci et al., 2008; Mano et al., 2016). Recently, the repression of Slit3 in HCC has been shown to induce tumor proliferation via the GSK3β/β-catenin pathway (Ng et al., 2018). Moreover, Robo1 promotes tumor invasion partly by the upregulation of MMP2, and promotes tumor angiogenesis in HCC through activation of Cdc42 (Ao et al., 2015; Yuan et al., 2016). Quantifications of Slit-Robo transcripts in HCC cell lines and liver tumor tissues revealed that Robo1, Robo4 and Slit2 could predict tumor stage and differentiation status (Avci et al., 2008).

7. Mathematical modelling for liver studies

Mathematical modelling is an emerging field in biomedical sciences and has become an important complementary tool to study complex biological systems. The models enable to simulate *in silico* a number of hypotheses and determine whether hypothesised mechanisms explain or not the experimental observations. The design of computational models requires an iterative process whereby experimentalists feed the model with quantitative information, and modelists contribute to refine testable hypotheses (Fig. 18).

For modelling morphogenic processes, so called "agent-based models" have been developed to mimic multicellular organisation. In such models the behaviour (division, migration,...) of each individual cell is represented. Depending on the complexity of the model, cell shape is either rigid and fixed (center-based models) or deformable (deformable cell model) (Van Liedekerke et al., 2015). The latter allows more accurate description of biological phenomenae (Van Liedekerke et al., 2020).

The use of mathematical models in the study of liver biology is illustrated by the analysis of liver regeneration after CCl_4-induced damage (Fig. 18, Drasdo et al.,

2014) . In this study, hypotheses explaining how liver architecture could be restored were tested. Morphometric data enabled the building of an agent-based model for the regenerating liver lobule, and iterative simulation/experiment rounds revealed that liver sinusoidal endothelial cells spatio-temporally orchestrate liver regeneration.

Given this background (Hoehme et al., 2010; Drasdo et al., 2014, Van Liedekerke et al., 2020), we considered that a computational approach might help in understanding mechanisms of morphogenesis operating during bile duct formation.

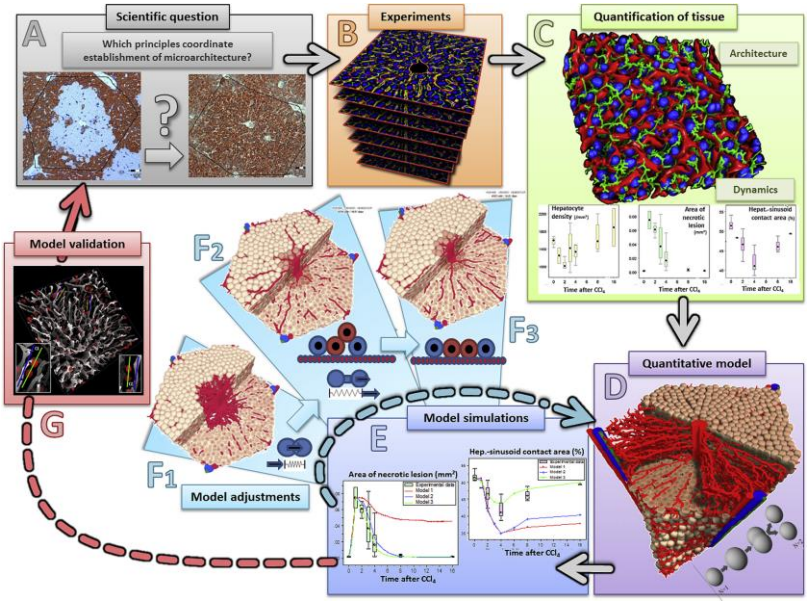

Figure 18. Application of mathematical models combined with biological analysis (Drasdo et al., 2014).

Aims of the thesis

The study of liver development uncovered several mechanisms driving differentiation of hepatoblasts to cholangiocytes. These mechanisms depend in part on interactions between embryonic portal mesenchyme and periportal hepatoblasts. However, little is known about how cholangiocytes subsequently organise in three dimensions to form bile ducts. How the bile ducts connect with the bile canaliculi at the apical pole of hepatocytes also remains unknown.

Therefore, in the present thesis we address the three following aims:

1. In the main part of our study, we hypothesized that morphogenesis of bile ducts is controlled by signalling interactions between portal mesenchymal cells and cholangiocytes. We identified the Slit-Robo pathway as a candidate and investigated its function by phenotyping livers from transgenic mice deficient in Slit2, Robo1 and Robo2. This led to the unexpected observation that the Slit-Robo pathway is involved in hepatic artery formation, but is not required for bile duct morphogenesis.

2. An essential step in duct development is the formation of a central lumen. To characterise mechanisms driving biliary lumen formation, we selected a combined experimental and computational approach, in collaboration with the group of Prof. Drasdo, expert in computational biology. Our collection of biological data in embryonic livers enabled to calibrate a new computational model that describes lumen formation and suggests the identification of the main drivers of biliary lumen formation.

3. Finally, using 2D and 3D immunostaining, we provided a preliminary description of how bile ducts connect with bile canaliculi in embryonic liver mice.

Results

1. Slit/Robo signalling controls development of the hepatic artery

Lila Gannoun[1], Catalina De Schrevel[1], Nicolas Dauguet[2], Axelle Loriot[1], Christophe Vanderaa[1], Sabine Cordi[1], Yves Heremans[3], Ilse Rooman[3], Patrick Jacquemin[1], Laurent Gatto[1], Frédéric P. Lemaigre[1,4].

[1] de Duve Institute, Université catholique de Louvain, Brussels, Belgium

[2] CYTF platform, Université catholique de Louvain, Brussels, Belgium

[3] Laboratory for Medical and Molecular Oncology, Vrije Universiteit Brussel, Brussels, Belgium

[4] Corresponding author: Frédéric P. Lemaigre, Avenue Hippocrate 75/B1-7503, 1200 Brussels, Belgium Tel: +32 2 764 75 83;
Email: frederic.lemaigre@uclouvain.be

Author contributions

LiG: gene expression profiling of developing bile ducts, analysis of Slit2 and Robo2 mutant mice, drafting and finalizing manuscript.

CDS: gene expression profiling of developing portal mesenchyme, determination of Sm22-Cre activity, drafting manuscript parts.

ND: FACS analyses.

AL, CV, LaG: bioinformatic analysis of RNA seq and single-cell RNAseq data.

YH and IR: Slit2 and Robo2 expression profiling in mutant mice.

SC: technical support to the analysis of Slit2 and Robo2 mutant mice.

FPL: design and supervision of work, drafting and finalizing manuscript.

Abstract

Hepatic lobules consist of hepatocyte cords and sinusoids that radiate from the portal area to the central vein. The portal areas contain the portal vein, a bile duct and the hepatic artery, as well as nerves, lymphatics and mesenchymal cells, the latter comprising portal fibroblasts and vascular smooth muscle cells. Normal bile duct development is required for morphogenesis of the portal mesenchyme and hepatic artery. However, how development of the bile ducts, vasculature and mesenchyme is orchestrated remains largely unknown. To address this issue, we analysed the expression of genes in developing bile ducts and mesenchyme and searched for ligand-receptor pairs expressed in cholangiocytes and mesenchymal cells. This uncovered a role for Slit2-Robo2 signalling in portal mesenchymal cells that does not impact bile duct development but which promotes development of the *tunica media* delineating the hepatic artery. Deficient formation of the artery's muscular layer is associated with perturbed artery morphogenesis.

Introduction

Analysis of the liver architecture revealed that the organ is composed of lobules consisting of hepatocyte cords and sinusoids that radiate from the portal area to the central vein. Each portal area is structurally complex as it contains a branch of the portal vein, a biliary network and a hepatic artery, as well as nerves, lymphatics and mesenchymal cells (Krishna, 2013). Biliary ducts are lined by cholangiocytes and drain bile produced by the hepatocytes. The portal vein and hepatic artery vascularise the liver, and blood from the two vessels merge into the sinusoids. The vein and artery each supply ~50% of the oxygen, but the hepatic artery contributes less than half (~25%) of the blood flow in homeostatic conditions. The hepatic mesenchyme is a heterogeneous tissue, and single cell RNA sequencing of adult Platelet-Derived Growth Factor β-positive liver mesenchyme uncovered three main subpopulations, namely fibroblasts, hepatic stellate cells (HSC) and vascular smooth muscle cells (VSMC) (Dobie et al., 2019). Fibroblasts mainly reside in the portal space. In adult homeostatic condition, portal fibroblasts are known to deposit

extracellular matrix including elastin which may confer mechanical stability to the bile ducts and vasculature (Wells, 2014). They also restrict cholangiocyte proliferation (Jhandier et al., 2005) and are precursors of myofibroblasts in fibrotic diseases (Wells, 2014). HSCs are quiescent vitamin-A storing cells and sinusoidal pericytes which, upon activation, transdifferentiate into fibrogenic myofibroblasts (Tsuchida and Friedman, 2017). VSMCs line the portal vein and also constitute the main cell type delineating the hepatic artery. The differentiation path of mesenchymal cells remains unclear since distinct mesenchymal populations with unknown fate are detected at the earliest stages of liver development (Lotto et al., 2020). However, lineage tracing experiments suggested that the three mesenchymal cell types found in adults develop from the *septum transversum*. The latter gives rise to mesothelial cells that constitute a source of HSCs and perivascular cells (Asahina et al., 2009; Asahina et al., 2011; Delgado et al., 2014).

The co-existence of biliary ducts, vessels and mesenchymal cell types within the narrow space of the portal area raises questions on potential cell-cell interactions driving tissular morphogenesis. Hepatic arteries are located adjacent to the bile ducts, and a crosstalk between hepatic artery and cholangiocytes has already been evidenced by the observation that livers with bile ducts deficient in Hepatocyte Nuclear Factor (HNF) 6 or HNF1β fail to develop normal arteries (Clotman et al., 2003). Also, in line with general knowledge on arteriogenesis (Carmeliet, 2000), analyses of human embryonic liver revealed that Vascular Endothelial Growth Factor (VEGF) A is expressed by developing cholangiocytes which likely recruit VEGF Receptor (VEGF) 2-positive endothelial cells located into the portal mesenchyme. Liver progenitor cells (hepatoblasts) produce Angiopoietin (Ang) 1 and secretion of Ang1 supposedly recruits embryonic myofibroblasts which express Ang2 to promote arterial remodeling through autocrine regulation (Fabris et al., 2008; Ober and Lemaigre, 2018). Together, these data point toward crossregulations between cholangiocytes and portal mesenchymal cells in development of the blood vessels, yet with limited knowledge on the intercellular signalling pathways controlling vessel morphogenesis.

Crosstalk between the developing bile ducts and the portal mesenchyme also controls biliary differentiation and morphogenesis. Differentiation of hepatoblasts towards the biliary lineage requires exposure to ligands of the Notch, Transforming Growth Factor β (TGFβ), integrin and Wnt signalling pathways. These ligands are expressed in the mesenchyme and their cognate receptor are found in the adjacent cholangiocytes (Antoniou et al., 2009; Couvelard et al., 1998; Gordillo et al., 2015; Hofmann et al., 2010; Kaylan et al., 2016; Lade and Monga, 2011; Lemaigre, 2020; Ober and Lemaigre, 2018; Tanimizu et al., 2012; Yanai et al., 2008; Zong et al., 2009). Later, in adult liver, a population of mesenchymal cells, likely fibroblasts, maintains cholangiocytes in a quiescent state in a Notch-dependent manner (Cordero-Espinoza et al., 2021). Reciprocally, bile duct morphogenesis impacts development of the portal mesenchyme. Indeed, inactivation of genes coding for transcription factors specifically expressed in cholangiocytes, such as SRY-related HMG box transcription factor (SOX) 4 and SOX9, leads to disruption of the bile ducts and hypotrophy of the portal mesenchyme (Poncy et al., 2015). Here again, how bile ducts and portal mesenchyme interact remains unknown.

Together, the above data highlight that development of the vasculature, mesenchyme and bile ducts in the portal area is highly interdependent. Except for the control of cholangiocyte differentiation which has been fairly well characterised, how this interdependency orchestrates duct, mesenchyme and vessel formation remains largely unexplored. To address this issue, we analysed the expression of genes in developing bile ducts and mesenchyme at critical stages of biliary morphogenesis and looked for ligand-receptor pairs expressed in cholangiocytes and mesenchymal cells. This uncovered a role for Slit-Robo signalling that unexpectedly does not impact bile duct development but which mediates interactions between mesenchymal subpopulations that promote development of the VSMC and of the hepatic artery.

Materials and Methods

Animals

Mice received humane care and the research protocol was approved by the Animal Welfare Committee of the Université Catholique de Louvain with number 2018/UCL/MD/014. All mice were housed under a 12h light/ dark cycle in individually ventilated cages supplied with RM3 chow (#801700, Tecnilab, Someren, Netherlands), acidified water, and polyvinyl chloride play tunnels. *Alfp-Cre*, *Sm22-Cre*, *Robo1*$^{-/-}$*;Robo2*$^{loxP/loxP}$, *Robo2*$^{loxP/loxP}$ and *Slit2*$^{loxP/loxP}$ mice have been described (Holtwick et al., 2002; Kellendonk et al., 2000; Long et al., 2004; Lu et al., 2007; Rama et al., 2015) and were kindly provided by F. Tronche, W. Martinet, F. Spagnoli and A. Chédotal, respectively. *Rosa26R*^{eYFP} and *Sox9-GFP* mice have been described (Gong et al., 2003; Srinivas et al., 2001).

Purification of mesenchymal cells and cholangiocytes

Pools of 15 livers at embryonic day (E) 16.5 or E18.5 were dissected and mechanically dissociated using scalpel blades as described (Van Liedekerke et al., 2021). Briefly, *Sox9-GFP* or *Sm22-Cre;Rosa26R*^{eYFP} livers were used for purification of cholangiocytes or mesenchymal cells, respectively. Subsequent chemical dissociation was performed in DMEM-F12 (#31870-025, Gibco, Life technologies, Lederberg, Belgium) containing 1 mg/ml collagenase IV (#43E14253, Worthington, New Jersey, USA), 1 mg/ml dispase (#17105-041, Gibco, Life Technologies) and 0.1 mg/ml of DNAse I (#11284932001, Roche, Mannheim, Germany) for 30 min at 37°C. An equal volume of 10% fetal bovine serum (FBS) in phosphate buffered saline (PBS) was added to stop the digestion, and cells were resuspended in 2 mM EDTA, 0.5% bovine serum albumin (BSA) in PBS and filtered on 40 µm cell strainer (#087711, Fisher Scientific Merelbeke, Belgium). Hematopoietic cells were eliminated by magnetic cell sorting using the Lineage cell depletion kit (#130090858, Miltenyi Biotech Paris, France) which contains antibodies against CD5, CD45R (B220), CD11b, Gr-1 (Ly-6G/C), 7-4, Ter-119. The cells were subjected to flow cytometry (BD FACSAria III, sample and collection tubes maintained at 4°C) and

GFP$^+$ cholangiocytes or eYFP$^+$ CD45$^-$ CD31$^-$ EpCAM$^-$ mesenchymal cells were purified. Antibodies used in flow cytometry are listed in Table 1.

Total RNA was isolated using RNAqueous® Micro kit (#AM1931, Invitrogen) according to manufacturer's protocol. RNA quality was evaluated using the Agilent RNA 6000 Pico Kit (#50671513, Agilent Technologies) and Bioanalyzer™ (Agilent Technologies) for measuring concentration and calculation of RNA integrity number (RIN).

Sequencing and bioinformatics workflow

Read quality control was performed using FastQC software v0.11.7 (Babraham Institute, Cambridge, UK). Low quality reads were trimmed and adapters were removed using Trimmomatic software v0.35 (RWTH Aachen University, Germany). Reads were aligned using HISAT2 software v2.1.0 (Johns Hopkins University School of Medicine, Center for Computational Biology, Baltimore, MD, USA) on GRCm38 mouse genome. Gene counts were generated using HTSeq-count (v0.5.4p3) software and gencode.vM15.annotation.gtf annotation file and raw counts were further converted in transcripts per million (TPM). Pathway analysis was performed using g:Profiler (Raudvere et al., 2019).

Dual RNAScope/Immunofluorescence and BaseScope

RNAScope RNA *in situ* hybridisation was performed on 6 µm sections of formalin-fixed paraffin-embedded tissues, according to the manufacturer's protocol for manual RNAscope®2.5 HD Assay—RED (#322350, Advanced Cell Diagnostics Inc.). The tissue sections were incubated at 60°C for 1h, deparaffinized 2x 5 min in xylene and dehydrated 2x 2 min in 99% ethanol. Endogenous peroxidase was blocked with hydrogen peroxide for 10 min at room temperature (RT) followed by two short washings with deionised water. Slides were heated for 10 sec at 100°C in deionised water, and antigen retrieval was performed for 15 min at 100°C using RNAscope®Target retrieval. Tissue sections were washed in deionised water and 99% ethanol. Slides were dried for 5 min at RT and tissues were delineated using an ImmEdge Hydrophobic Barrier Pen (#310018, Advanced Cell Diagnostics Inc.).

Slides were incubated for 15 min with RNAscope®Protease plus (diluted at 1/5 in deionised water) at 40°C, washed with deionised water and incubated with the probe for 2h at 40°C. The tissue sections were washed with RNAscope®Wash buffer and six amplifications were performed (using six reagents AMP1-AMP6). The signal detection followed using RNAscope®Fast A and B reagents for 10 min at RT. The slides were kept in PBS overnight and immunostaining was performed: sections were blocked for 45 min at RT in 3% milk, 10% BSA, 0.3% Tween 20 in PBS. Primary and secondary antibodies were diluted in 10% BSA, 0.3% Tween 20 in PBS and incubated respectively for 1h30 at 37°C and 1h30 at RT. Pictures were taken with Cell Observer Spinning Disk (Carl Zeiss) and Zen blue software. Primary and secondary antibodies are described in Tables 1 and 2.

BaseScope RNA *in situ* hybridisation was performed on 6 µm sections of formalin-fixed paraffin-embedded tissues, according to the manufacturer's protocol for BaseScope RED v2 kit, as described (Martens et al., 2021). The custom probes were designed to bind specifically to exon 8 of the *Slit2* gene or to exon 5 of the *Robo2* gene.

Immunofluorescence and immunohistochemistry

Immunofluorescence and immunohistochemistry (IHC) were performed on 6 µm sections of formalin-fixed paraffin-embedded (FFPE) or sucrose-embedded frozen tissues. FFPE tissue sections were deparaffinised 3x 3 min in xylene, 3 min in 99%, 95%, 70% and 30% ethanol and deionised water. Antigen retrieval was performed by micro-wave heating for 10 min or using the Lab Vision PT Module (Thermo Fisher Scientific, Waltham, MA), in 10 mM citrate pH 6 or Tris-EDTA pH 9, depending on the antibody. Sections were permeabilized for 5 min in 0.3% Triton X-100 in PBS before blocking for 45 min in 3% milk,10% BSA, 0.3% Triton X-100 in PBS. For preparation of frozen sections, livers were collected, briefly washed in PBS, and fixed overnight in 4% paraformaldehyde. Tissues were incubated in sucrose 15% in PBS for 6-12 h and overnight in sucrose 30% in PBS, before embedding in OCT and freezing in liquid nitrogen-cooled isopentane. Frozen sections were thawed at RT for 20 min and rehydrated in PBS for 10 min. Antigen retrieval was performed by 5 min

incubation in 10 mM citrate pH 6 preheated at 95°C, and sections were rinsed in deionized water and PBS, before blocking as above.

Primary antibodies were diluted in blocking solution at 4°C overnight and secondary antibodies were diluted in 10% BSA, 0.3% Triton X-100 in PBS at 37°C for 1 h. For IHC, antibody binding was visualised using 3,3'-diaminobenzidine tetrachloride (#ab64238, Abcam, Cambridge, UK), and 30% haematoxylin (#109249, Merck Millipore) was used to counterstain the tissue. Pictures were taken with Cell Observer Spinning Disk (Carl Zeiss) and Zen blue software, or with CaseViewer on scanned tissues. Primary and secondary antibodies are described in Tables 1 and 2.

Elastin-Collagen staining

Elastin-Collagen staining was performed using the Elastica Van Gieson Staining Kit (#8275.1, Carl Roth) and the manufacturer's protocol was adapted to our tissues. Staining was performed on 6 µm sections of formalin-fixed paraffin-embedded tissues. Tissue sections were deparaffinized 3x 3 min in xylene, rehydrated 3 min in 99% and 80% ethanol, and stained 30 min in the esorcinol fuchsine solution. Slides were washed with tap water until stain fades, washed with deionised water, differentiated few seconds with ethanol 80% and washed with deionized water to interrupt the differentiation. Finally, tissue sections were stained 3 min with the Van Gieson solution and shortly washed with 70%, 95% and 100% ethanol, and xylene before mounting slides with DPX (#1005790500, VWR).

Blood collection and plasma analysis

Six- to eight-week-old mice were anesthetised and blood was collected using intracardiac puncture. Plasma samples were analysed for total bilirubin, albumin, alkaline phosphatase, aspartate aminotransferase, alanine aminotransferase and lactate dehydrogenase (Fuji Dri-Chem NX500 analyzer).

Ink injection and tissue clearing

Six- to eight-week-old mice were anesthetised and transcardially perfused with PBS for 3 min (perfusion rate 5 ml/1 min). Protocols for bile duct and portal vein injections are described (Hankeova et al., 2021) and were adapted for ink injection. Briefly, black ink (Higgins Drawing Ink) was injected in the common bile duct using a PE10 tubing (#427401, BD Bioscience) attached to a 30 g needle/2ml syringe. White ink (Higgins Drawing Ink) was injected in the portal vein, using a catheter (Peripheral IV cannulae, #BDAM381312, VWR) attached to a 5 ml syringe. To visualise the hepatic arteries, we injected ink in the gastroduodenal artery according to a protocol adapted from that described for rats (Sheu et al., 2013; Shinozaki et al., 2004; Tada et al., 2006). The gastroduodenal artery was cleaned from surrounded tissue, and surgical suture (SURGICRYL 910, #15150217, SMI AG) was loosely wrapped around the artery. An incision was made in the gastroduodenal artery using a spring scissor (2mm, #15000-03, Fine Science Tools). A PE10 tubing was attached to a 30 g needle/5ml syringe, and the end of the tubing was stretched and cut at an angle to create a beveled end. The common hepatic artery was clamped, the tubing was inserted in the gastroduodenal artery, and the suture was tightened on the tubing, before injecting ink. Following ink injection, liver lobes were incubated on a rocking platform in 50% methanol for 4 h at RT, in 100% methanol overnight at RT and in benzyl alcohol (BA), benzyl benzoate (BB) solution (1BA: 2 BB) for a few hours at RT. Pictures were taken with a Stereo Microscope Stemi SV6 (Zeiss) and a Moticam X3 camera.

Statistical analysis

Single comparisons between two experimental groups measuring plasma levels were done using a paired Student's t test. For morphometric analyses of hepatic arteries, significance was assessed by a Student's t-test with Welch's correction. For calculation of adjusted p-value in gene expression analyses, a Benjamini-Hochberg correction was applied. P-value <0.05 was considered significant. Statistical analyses were performed using Graphpad Prism 9.

Results

Axon guidance signals are expressed in developing bile ducts and portal mesenchyme

To search for mesenchyme-bile duct interactions, we separately purified the portal mesenchyme and cholangiocytes from mouse livers at E16.5 and E18.5, namely two stages that are critical for morphogenesis of the bile ducts. Cholangiocytes were purified from *Sox9-GFP* livers which express GFP specifically in cholangiocytes (Demarez et al., 2018), and mesenchymal cells were isolated from *Sm22-Cre;Rosa26R*^{eYFP} livers. The latter express eYFP from the *Rosa26* locus when recombined by *Sm22-Cre* which is reportedly active in the developing portal mesenchyme (Hofmann et al., 2010). We confirmed this activity of *Sm22-Cre* and showed that it is detectable pre- and postnatally in the portal mesenchymal cells (Fig. 1A). At these stages, undifferentiated mesenchymal cells widely express α smooth muscle actin (αSMA), a marker which upon differentiation will become restricted to VSMCs (Dobie et al., 2019; Villeneuve et al., 2009). CD90 (Thy1) is also expressed in the mesenchymal precursor cells and remains detectable in portal fibroblasts (Dobie et al., 2019). Sections of *Sm22-Cre;Rosa26R*^{eYFP} livers showed activity of *Sm22-Cre* in progenitors of VSMCs and portal fibroblasts as evidenced by αSMA/eYFP and CD90/eYFP co-stainings (Supplementary Information; Fig. S1A). Very rare parenchymal cells co-expressed eYFP and the HSC marker reelin (RELN), and *Sm22-Cre* activity in this cell type was not considered significant (Fig. S1A). In addition, a small subset of parenchymal hematopoietic cells was eYFP-positive, including a small subset of Ter119-positive erythroblasts, but not the CD45-positive leucocytes located around the portal vein (Fig. S1B). We did not detect eYFP in bile ducts, hepatocytes or endothelial cells. We concluded that *Sm22-Cre* is appropriate to investigate gene function in developing portal mesenchymal cells that are precursors of VSMCs and portal fibroblasts.

Purified cholangiocytes and mesenchymal cells were subjected to RNA sequencing (Fig. 1A-B). We reasoned that genes involved in morphogenesis should display differential expression in cholangiocytes or mesenchymal cells between E16.5 and

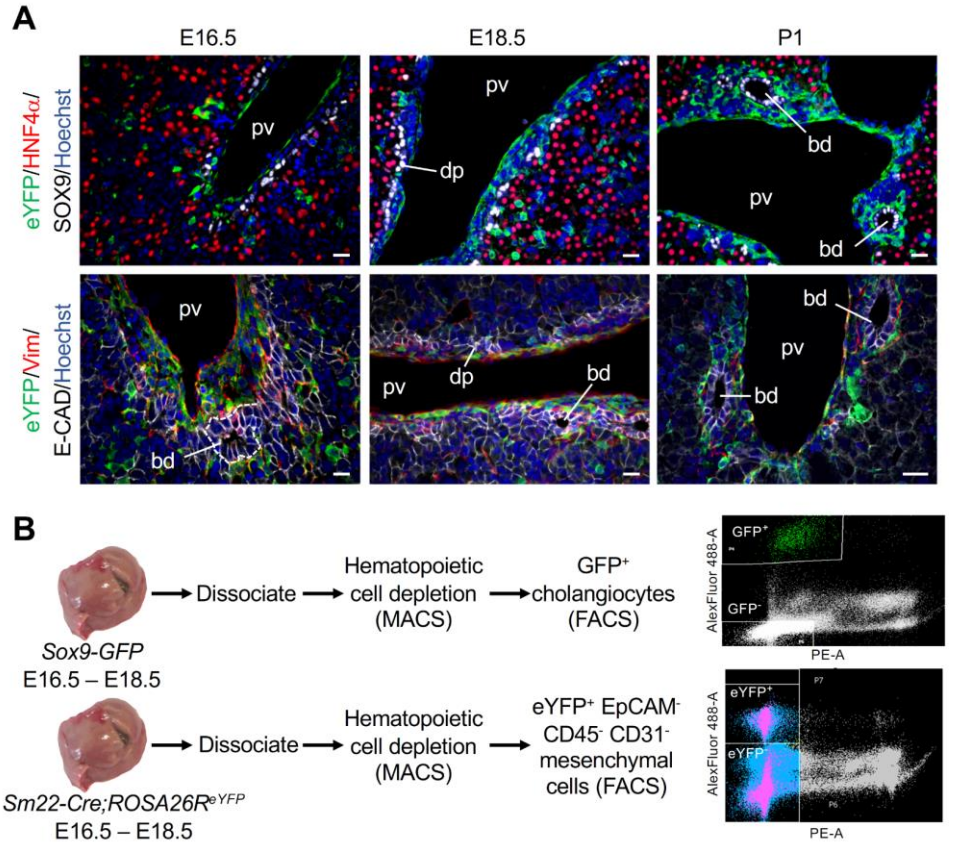

C

Mesenchymal cells

KEGG pathway	Term ID	p_{adj}	$-\log_{10}(p_{adj})$
ECM receptor interaction	04512	1.535×10^{-21}	
Focal adhesion	04510	2.976×10^{-21}	
Axon guidance	**04360**	1.741×10^{-16}	
PI3K-Akt signaling	04151	1.659×10^{-13}	
Pathways in cancer	05200	2.642×10^{-10}	
HPV infection	05165	2.884×10^{-10}	
Relaxin signaling	04926	3.123×10^{-9}	
Protein digestion	04974	5.425×10^{-9}	
AGE-RAGE signaling	04933	1.926×10^{-8}	
Hippo signaling	04390	2.615×10^{-8}	
Dilated cardiomyopathy	05414	6.579×10^{-8}	
cGMP-PKG signaling	04022	6.973×10^{-7}	
Hypertrophic cardiomyopathy	05410	7.502×10^{-7}	
Amoebiasis	05146	1.594×10^{-6}	
ARV cardiomyopathy	05412	1.907×10^{-6}	

Cholangiocytes

KEGG pathway	Term ID	p_{adj}	$-\log_{10}(p_{adj})$
Focal adhesion	04510	3.713×10^{-11}	
ECM receptor interaction	04512	1.833×10^{-10}	
PI3K-Akt signaling	04151	8.518×10^{-10}	
HPV infection	05165	4.270×10^{-7}	
Protein digestion	04974	1.573×10^{-6}	
Signaling regulating pluripotency	04550	5.755×10^{-5}	
Wnt signaling	04310	7.816×10^{-5}	
Proteoglycans in cancer	05205	8.062×10^{-5}	
Pathways in cancer	05200	7.588×10^{-4}	
Hippo signaling	04390	9.741×10^{-4}	
Axon guidance	**04360**	1.976×10^{-3}	
Amoebiasis	05146	5.128×10^{-3}	
Breast cancer	05224	5.824×10^{-3}	
Gastric cancer	05226	6.326×10^{-3}	
Basal cell carcinoma	05217	6.342×10^{-3}	

Figure 1. Purification and gene expression in developing cholangiocytes and portal mesenchymal cells. (A) Analysis of *Sm22-Cre;Rosa26R*^{eYFP} livers shows eYFP expression in VIMENTIN-expressing mesenchymal cells, not in epithelial HNF4α- or Sox9-positive cells. bd, bile duct; dp, ductal plate; m, mesenchyme; pv, portal vein. Size bars: 20 µm. **(B)** eYFP$^+$ CD45$^-$ CD31$^-$ EpCAM$^-$ mesenchymal cells and GFP$^+$ cholangiocytes were FACS-purified from *Sm22-Cre;Rosa26R*^{eYFP} and *Sox9-GFP* livers, respectively, after hematopoietic cell depletion. **(C)** Pathway enrichment analysis of genes upregulated at E18.5 as compared to E16.5 ($\log_2$

fold change ≥ 1, p_{adj} <0.05) identifies the axon guidance pathway both in mesenchymal cells and cholangiocytes.

E18.5. Further, we focused on genes coding for ligands produced by cholangiocytes and for their cognate receptors in mesenchymal cells; or *vice-versa*. Fig. 1C provides a pathway enrichment analysis of genes showing a $\log_2$ fold increase ≥ 1 (p_{adj} <0.05) from E16.5 to E18.5. Our attention was caught by the axon guidance pathway which was enriched during development of both the portal mesenchyme and cholangiocytes. We next decided to focus on the Slit/Roundabout (Robo) pathway because the RNA sequencing detected SLIT ligand and ROBO receptor expression in cholangiocytes and mesenchyme.

Expression of *Slit*/*Robo* genes

To characterise the expression of *Slit* and *Robo* genes, we turned to RNAScope *in situ* hybridisation and to immunostaining, depending on the availability of antibodies. *Slit2* expression in liver was strongest in the portal area, where it was detected in cholangiocytes lining developing ducts, mesenchymal cells and portal endothelium (Fig. 2A). This expression was transient in biliary cells (E16.5 to postnatal day (P) 1) and portal endothelium (E16.5-E18.5) but was detected at all pre- and postnatal stages tested in the mesenchyme. At P10, *Slit2* was detected in CD90-expressing portal fibroblasts and in very rare αSMA-positive VSMCs lining the portal vein or hepatic artery, but not in parenchymal DESMIN-expressing HSCs (Fig. 2A). This fitted with the data of Dobie et al. (2019) who, in adult liver mesenchymal cells, only detected *Slit2* in fibroblasts (Fig. S2A).

Hepatic expression of *Robo2* was mainly detected in the embryonic portal mesenchyme, predominantly in cells adjacent to developing ducts; this observation was confirmed at the protein level by immunostaining (Fig. 2B). At P10, *Robo2* was co-expressed with DESMIN in parenchymal HSCs, and was detected at low levels in a limited number of periportal CD90-expressing fibroblasts (white arrowheads in Fig. 2B). It was not found in αSMA-expressing VSMCs lining the portal vein or hepatic artery (Fig. 2B).

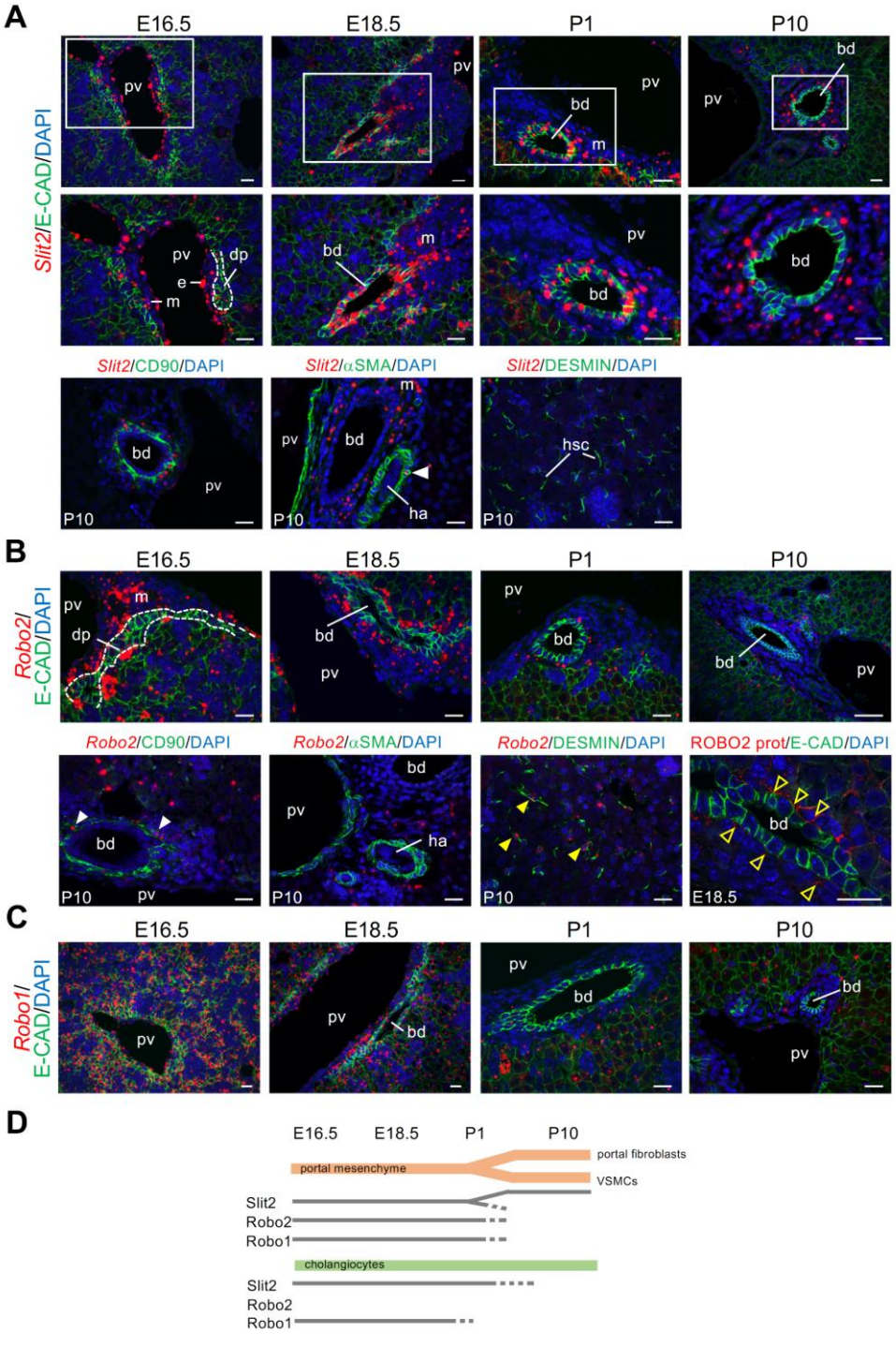
A
E16.5
E18.5
P1
P10
Slit2/E-CAD/DAPI
pv
bd
m
dp
e
Slit2/CD90/DAPI
Slit2/αSMA/DAPI
Slit2/DESMIN/DAPI
hsc
ha
P10
B
Robo2/
E-CAD/DAPI
Robo2/CD90/DAPI
Robo2/αSMA/DAPI
Robo2/DESMIN/DAPI
ROBO2 prot/E-CAD/DAPI
E18.5
C
Robo1/
E-CAD/DAPI
D
portal mesenchyme
portal fibroblasts
VSMCs
Slit2
Robo2
Robo1
cholangiocytes

Figure 2. Expression of *Slit* and *Robo* genes in developing liver. (A) *In situ* hybridisation of *Slit2* reveals transient expression in cholangiocytes (E16.5 to P1), and expression in portal mesenchyme at pre- and postnatal stages, essentially in CD90-expressing postnatal portal fibroblasts. The white arrowhead points to a VSMC expressing *Slit2*. **(B)** *Robo2* RNA and protein (open yellow arrowheads) are expressed in the embryonic and neonatal mesenchyme (portal mesenchyme and HSCs). At P10, *Robo2* is only detected in HSCs (yellow arrowheads). **(C)** *Robo1* RNA is widely detected in the embryonic liver, namely in hepatoblasts, cholangiocytes, mesenchyme and endothelial cells. After birth, *Robo1* expression progressively decreases in the portal area. **(D)** Summary of *Slit2*, *Robo1* and *Robo2* expression in the portal area. bd, bile duct; dp, ductal plate; ha, hepatic artery; m, mesenchyme; pv, portal vein. Size bars: 20 µm.

Robo1 displayed wide expression in developing liver. It was detected in the parenchymal hepatoblasts, as well as in the portal area during development, namely in biliary, mesenchymal and portal endothelial cells (Fig. 2C) Hepatic *Robo1* expression was progressively reduced after birth: it was nearly not detected in the portal area but is known to persist in HSCs (Fig. 2C and Fig. S2A) (Chang et al., 2015; Dobie et al., 2019).

The other members of the *Slit* and *Robo* gene families were also considered. *Slit1* was barely detectable in the developing portal area, whereas *Slit3* was expressed only in a very small subset of cholangiocytes, as well as in portal endothelial cells at a distance from the developing bile ducts (Fig. S2B). *Robo3* and *Robo4* are considered specific to the nervous system and endothelial cells, respectively, and were not considered relevant for our study. Analysis of single-cell RNA sequencing published by Wang and coworkers (Wang et al., 2020) supports the absence of *Robo3* and *Robo4* in the epithelial cells and mesenchyme (Fig. S2C). The expression of *Slit2*, *Robo1* and *Robo2* in developing cholangiocytes and/or periportal mesenchymal cells is summarized in Fig. 2D.

Slit2 expression in developing cholangiocytes is dispensable for bile duct and hepatic artery morphogenesis

To investigate if production of SLIT2 by cholangiocytes might impact bile duct morphogenesis or hepatic artery formation, we conditionally inactivated its expression by mating *Slit2*$^{loxP/loxP}$ mice with *Alfp-Cre* mice. The *Alfp-Cre* transgene induces recombination of loxP-flanked genes in hepatoblasts, meaning that the

progeny of these cells, namely cholangiocytes and hepatocytes, have their loxP-flanked alleles inactivated. At birth, the *Alfp-Cre;Slit2*$^{loxP/loxP}$ mice showed normal biliary ducts (Fig. 3A). The ducts were delineated by well-differentiated and well-polarised cholangiocytes, as evidenced by their transcription factor profile (SOX9^{+}, HNF4α^{-}, C/EBPα^{-}), and by the location of β-CATENIN and E-CADHERIN at the basolateral sides, and MUCIN1 at the apical poles. Hepatic arteries in mice normally develop a few days after birth and displayed a normal phenotype in P10 *Alfp-Cre;Slit2*$^{loxP/loxP}$ knockout livers, as shown by immunostaining of their *tunica media*

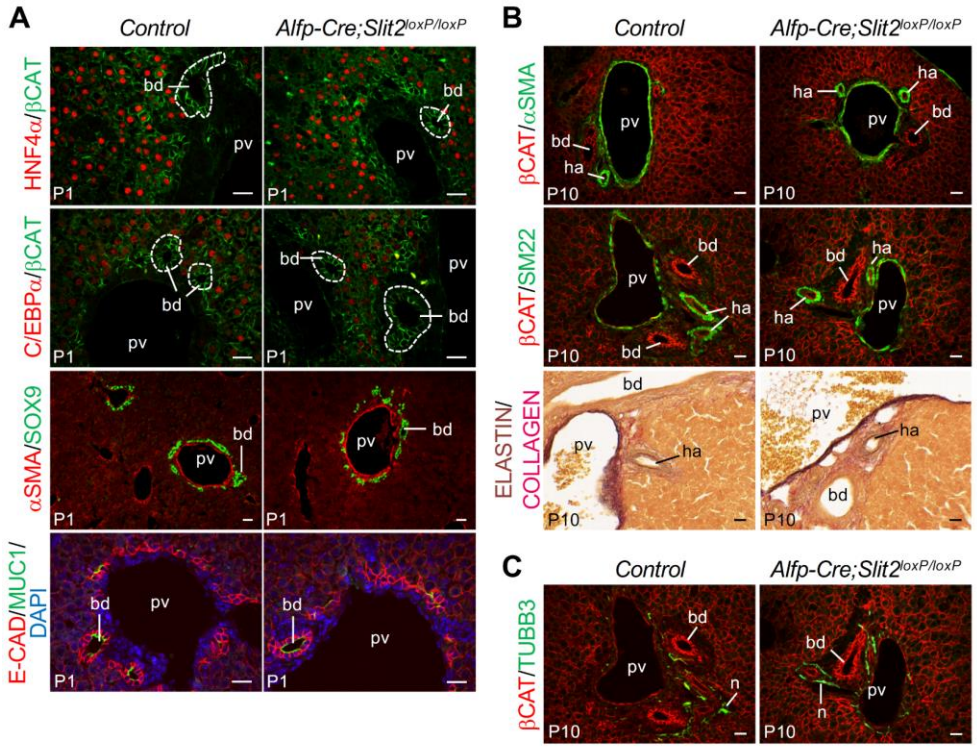

Figure 3. Biliary and hepatic artery morphogenesis does not require *Slit2* expression in cholangiocytes. (A) Bile ducts are normal and delineated by well-differentiated and well-polarised cholangiocytes in the absence of SLIT2 in hepatic epithelial cells of *Alfp-Cre;Slit2*$^{loxP/loxP}$ mice (n=7). **(B)** The absence of SLIT2 in cholangiocytes is associated with normal development of hepatic arteries, as shown by αSMA, SM22, ELASTIN and COLLAGEN staining in *Alfp-Cre;Slit2*$^{loxP/loxP}$ mice (n=7). **(C)** TUBB3 staining shows periportal nerves (n=7). bd, bile duct; ha, hepatic artery; n, nerve; pv, portal vein. Size bars: 20 µm.

using antibodies against SM22 (synonym: transgelin) and αSMA, or by detection of ELASTIN (Fig. 3B). The muscular layer surrounding the portal vein appeared normal as well and neural class III tubulin (TUBB3)-expressing nerves were also detected in the portal space of the mutant livers (Fig. 3B-C). We concluded that expression of *Slit2* is dispensable for normal development of the bile ducts and portal vasculature.

Slit2 expression in mesenchymal cells is dispensable for bile duct development but is required for normal morphogenesis of hepatic arteries

We next addressed the role of *Slit2* expression in the portal mesenchyme by mating the above described *Sm22-Cre* mice with *Slit2*$^{loxP/loxP}$ mice. Here again we found no biliary anomaly: at P10, *Sm22-Cre;Slit2*$^{loxP/loxP}$ mice developed bile ducts with normal morphology and surrounded by well-polarised and well-differentiated cholangiocytes (Fig. 4A). There was no evidence of cholestasis as shown by normal levels of plasma bilirubin (Fig. 4B). Moreover, retrograde injection of ink in the common bile duct followed by tissue clearing did not reveal anomalies of the intrahepatic biliary tree (Fig. 4C). TUBB3-expressing nerves were detected in the portal space of the control and mutant livers, as well as lymphatics (Fig. 4A and Fig. 5A).

However, when immunostaining to detect αSMA, SM22, SMOOTHELIN and ELASTIN, we observed arterial anomalies in the *Sm22-Cre;Slit2*$^{loxP/loxP}$ mice at P10. The arterial phenotype was variable, with approximately 50% of animals (6 out of 11) displaying no detectable phenotype, the others (5 out of 11) presenting with a reduction in the thickness of the *tunica media* ranging from nearly no VSMCs surrounding the arterial endothelium to a limited decrease in the arterial wall's thickness. Fig. 5A illustrates three phenotypes observed in *Sm22-Cre;Slit2*$^{loxP/loxP}$ mice, namely the presence of normal arteries, the lack of detectable VSMCs around the arteries, and an intermediate phenotype with reduced thickness of the artery's muscular layer. This phenotype was confirmed quantitatively (Fig. 5B). We measured the ratio of the surface of the muscle layer to the total artery area; this was significantly reduced in the knockouts. Accordingly, the ratio of the arterial luminal area to the surface of the muscle layer was increased in the mutant livers.

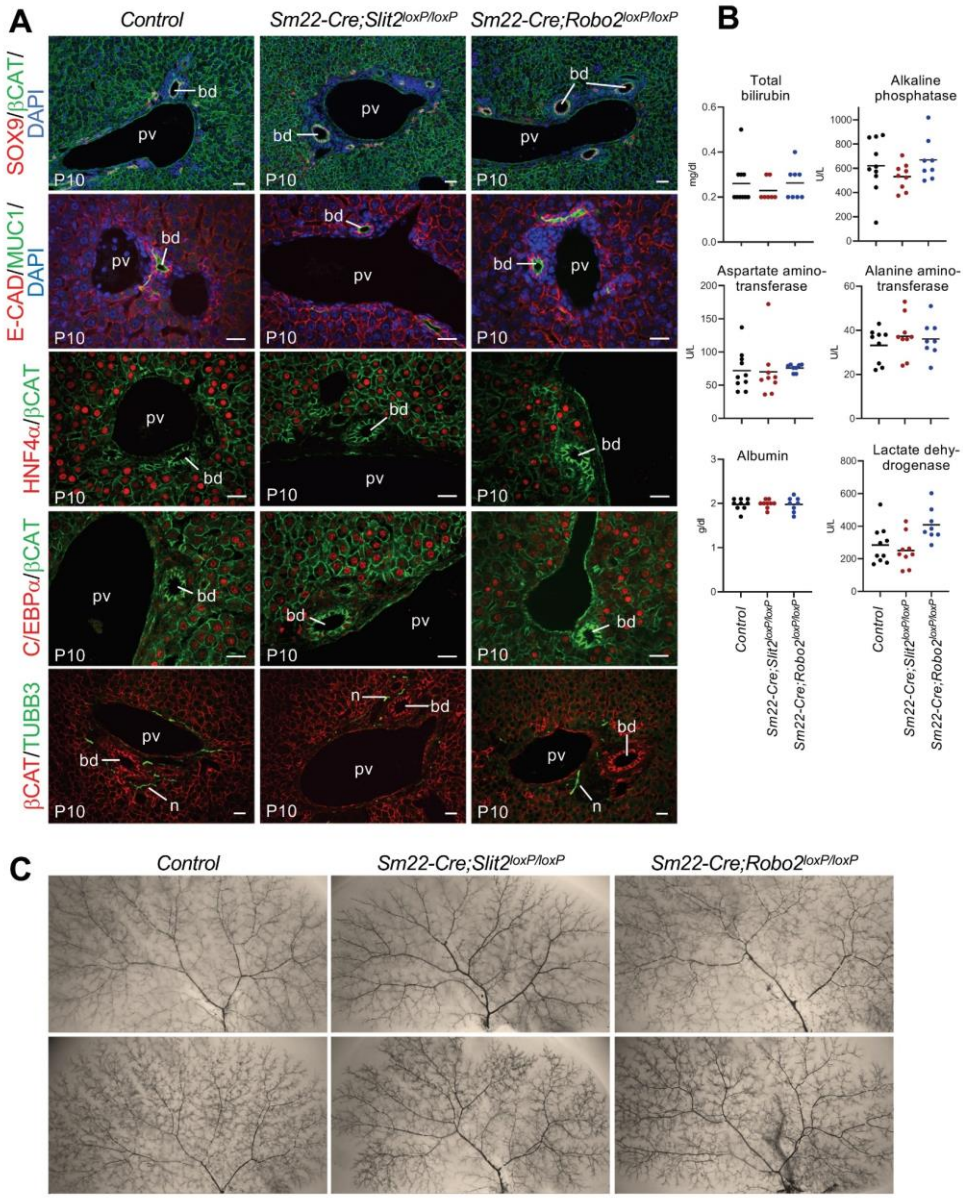

Figure 4. Biliary morphogenesis does not require *Slit2* or *Robo2* expression in portal mesenchymal cells. (A) Bile ducts are well-formed and delineated by well-differentiated and well-polarised cholangiocytes in the absence of SLIT2 or ROBO2 in the mesenchyme of *Sm22-Cre;Slit2*$^{loxP/loxP}$ (n=11) and *Sm22-Cre;Robo2*$^{loxP/loxP}$ (n=7) mice. **(B)** At 2 months, plasma levels of total bilirubin, albumin, alkaline phosphatase, aspartate aminotransferase, alanine aminotransferase and lactate dehydrogenase do not show significant difference

between *Sm22-Cre;Slit2*$^{loxP/loxP}$ (n=9), *Sm22-Cre;Robo2*$^{loxP/loxP}$ (n=8) and control (n=10) mice. Dots represent individual measurements. **(C)** Retrograde injection of ink in the common bile duct followed by tissue clearing reveals normal biliary tree in 2 months-old control (n=6), *Sm22-Cre;Slit2*$^{loxP/loxP}$ (n=7) and *Sm22-Cre;Robo2*$^{loxP/loxP}$ (n=4) mice. bd, bile duct; ha, hepatic artery; n, nerve; pv, portal vein. Size bars: 20 µm.

To avoid a potential bias related to arterial size, these measurements were performed on hepatic arteries that have a cross-sectional area inferior or superior to 2000 μm^2. The number of animals and hepatic arteries measured in these experiments is shown in Table 3. The phenotypic heterogeneity did not reflect variable efficiency of *Sm22-Cre*-mediated inactivation of the *Slit2* gene. *Sm22-Cre* is indeed widely active in the portal mesenchyme of all animals as determined by eYFP induction in *Sm22-Cre;Rosa26R*^{eYFP} livers (Fig. S1). Moreover, *in situ* RNA hybridisation using a BaseScope probe targeting the floxed exon 8 of *Slit2* showed efficient inactivation of the gene, in all portal areas (Fig. S3). Therefore, the heterogeneous phenotype resulted from biological but not from technical variability.

Animals displaying reduced thickness of the hepatic artery wall also showed deficient ELASTIN production around the arterial epithelium (Fig. 6A). We hypothesized that this, combined with reduced *tunica media*, may impact the overall morphology of the hepatic artery and therefore visualised the artery using ink injection. The results showed that control livers displayed straight artery branches, whereas localised distortions were observed in a subset of artery branches of *Sm22-Cre;Slit2*$^{loxP/loxP}$ livers (red arrows in Fig. 6B). The latter were interpreted as resulting from pressure-induced distortions of arteries that have a less resistant wall. Consistent with the phenotypic variability of the mice, only a subset of mice displayed the morphological anomalies.

We concluded that the expression of *Slit2* in the portal mesenchyme is not required for bile duct formation, but is necessary for normal development of the VSMCs that constitute the *tunica media* of the hepatic artery.

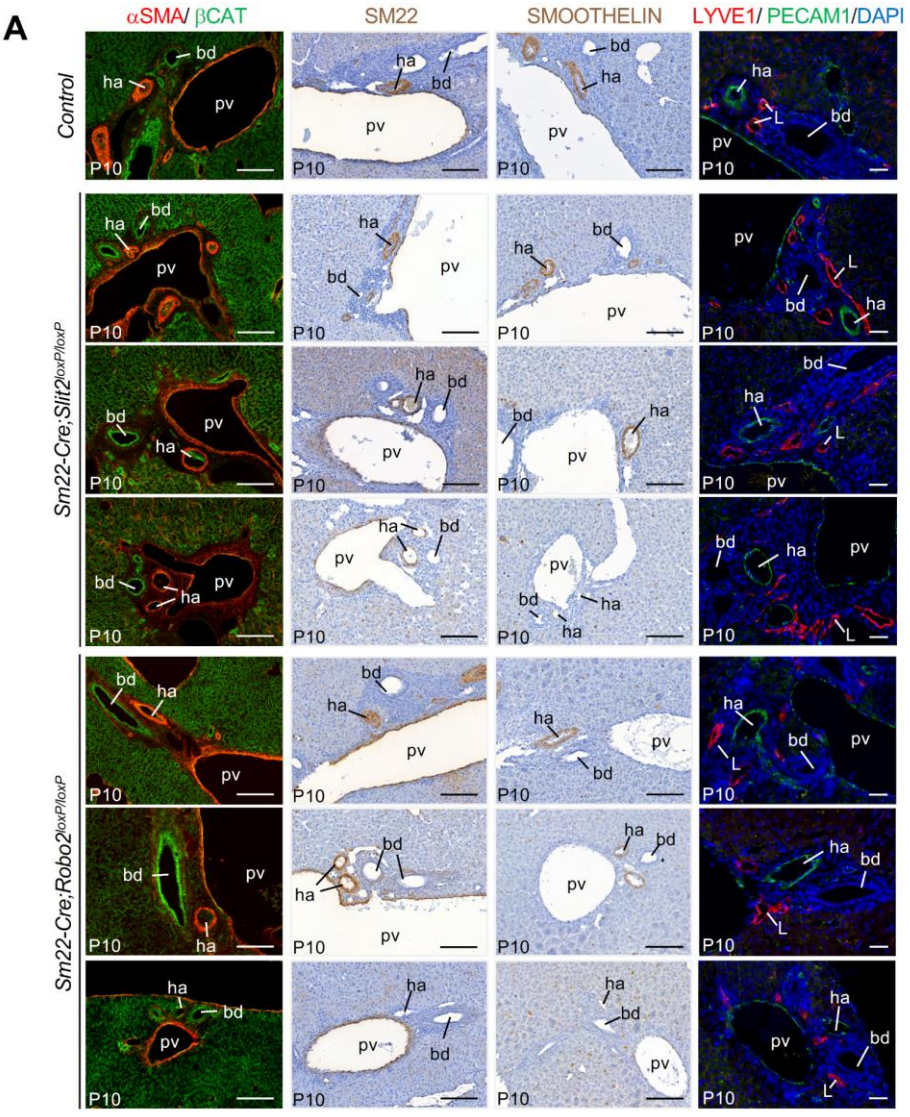
A
αSMA/ βCAT
SM22
SMOOTHELIN
LYVE1/ PECAM1/DAPI
Control
Sm22-Cre;Slit2loxP/loxP
Sm22-Cre;Robo2loxP/loxP
ha
bd
pv
L
P10

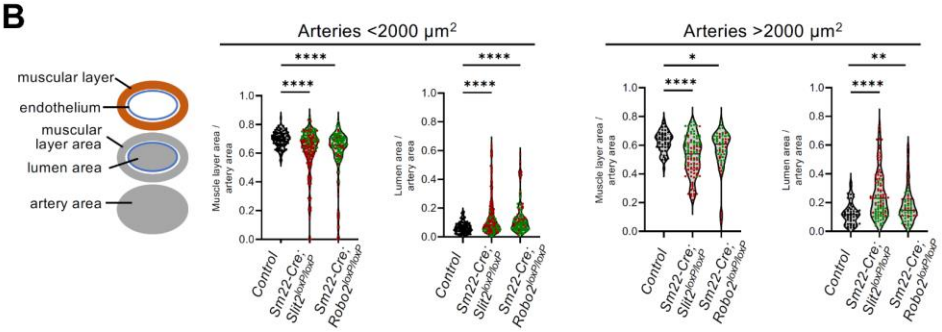
B
muscular layer
endothelium
muscular layer area
lumen area
artery area
Arteries <2000 µm²
Arteries >2000 µm²
Muscle layer area / artery area
Lumen area / artery area
****
*
**
Control
Sm22-Cre; Slit2loxP/loxP
Sm22-Cre; Robo2loxP/loxP

Figure 5. *Slit2* or *Robo2* inactivation in portal mesenchymal cells perturbs muscle layer formation around hepatic arteries. (A) Immunostaining of αSMA, SM22 and SMOOTHELIN reveals: normal muscle layer (6 out of 11n *Sm22-Cre;Slit2$^{loxP/loxP}$* and 5 out of 7n *Sm22-Cre;Robo2$^{loxP/loxP}$*), a decrease in muscle layer thickness (4 out of 11n *Sm22-Cre;Slit2$^{loxP/loxP}$* and 1 out of 7n *Sm22-Cre;Robo2$^{loxP/loxP}$*) or a lack of muscle layer (1 out of 11n *Sm22-Cre;Slit2$^{loxP/loxP}$* and 1 out of 7n *Sm22-Cre;Robo2$^{loxP/loxP}$*) around the hepatic arteries. Immunostaining of CD31 and LYVE1 shows normal endothelial cells and presence of lymphatic vessels in control and mutant mice. bd, bile duct; ha, hepatic artery; L, lymphatic vessel; pv, portal vein. Size bars: 20 µm. **(B)** The muscle layer and lumen area of hepatic arteries were measured, showing a significantly reduced thickness of the muscle layer and increased lumen area, both in small (<2000 µm^2) and large (>2000 µm^2) arteries. * p<0.5; ** p<0.1; ***p<0.01; **** p<0.001). Dots represent individual measurements (see Table 3). Black dots, hepatic arteries in control mice; green dots, hepatic arteries in mutant mice showing a normal muscle layer; red dots, hepatic arteries in mutant mice with decreased muscle layer thickness. Black line is median.

Robo2 expression in mesenchymal cells is dispensable for bile duct development but is required for normal morphogenesis of hepatic arteries

SLIT2 is a secreted ligand of ROBO receptors, of which ROBO2 is abundantly expressed in embryonic portal mesenchyme in close vicinity of the bile ducts (Fig. 2B). To determine if ROBO2 is involved in hepatic artery development, we characterised the phenotype of *Sm22-Cre;Robo2$^{loxP/loxP}$* mice in which *Robo2* is inactivated in the mesenchyme. Similar to *Slit2* inactivation in the mesenchyme, no evidence was found for abnormal differentiation and polarity of cholangiocytes, or for abnormal morphogenesis of bile ducts in *Sm22-Cre;Robo2$^{loxP/loxP}$* mice (Fig. 4). Portal nerves and lymphatics were also detected normally, and liver function assessed by plasma levels of hepatic enzymes, albumin and bilirubin was unaffected (Fig. 4A-B and Fig. 5A). The efficiency of *Sm22-Cre*-mediated inactivation of *Robo2* was demonstrated using ROBO2 protein immunostaining and BaseScope *in situ* hybridisation targeting the floxed exon 5 (Fig. S3).

However, again similar to *Sm22-Cre;Slit2$^{loxP/loxP}$* mice, a subset of *Sm22-Cre;Robo2$^{loxP/loxP}$* mice displayed hepatic artery anomalies. Two mice out of 7 showed reduced or lack of detectable muscular layer, as evidenced by αSMA, SM22, SMOOTHELIN and ELASTIN stainings (Fig. 5A and Fig. 6A). This phenotype was confirmed quantitatively using the same measurements as those performed in *Sm22-Cre; Slit2$^{loxP/loxP}$* livers (Fig. 5B). Ink injection into the hepatic artery further

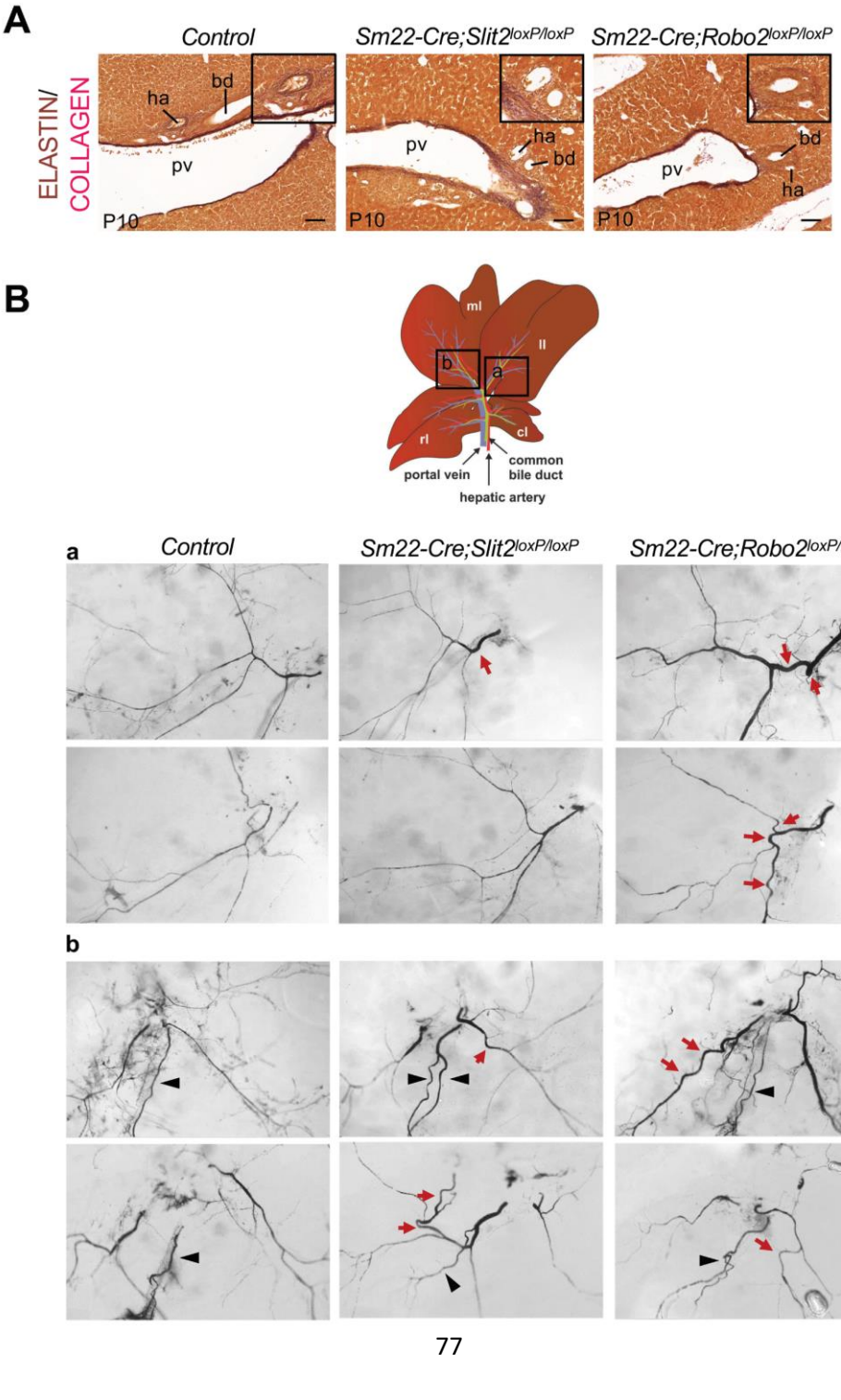
A
Control
Sm22-Cre;Slit2loxP/loxP
Sm22-Cre;Robo2loxP/loxP
ELASTIN/
COLLAGEN
ha
bd
pv
P10
B
ml
ll
b
a
rl
cl
portal vein
common
bile duct
hepatic artery
a
Control
Sm22-Cre;Slit2loxP/loxP
Sm22-Cre;Robo2loxP/loxP
b

Figure 6. *Slit2* or *Robo2* inactivation in portal mesenchymal cells reduces the hepatic artery stiffness. (A) Reduced ELASTIN staining around hepatic arteries in *Sm22-Cre;Slit2$^{loxP/loxP}$* and *Sm22-Cre;Robo2$^{loxP/loxP}$* mice. bd, bile duct; ha, hepatic artery; pv, portal vein. Size bars: 50 µm. **(B)** Ink injection in the gastroduodenal artery followed by clearing of median lobe (a) and left lobe (b) shows a irregularly-shaped morphology (red arrowheads) of the arteries in 2 month-old *Sm22-Cre;Slit2$^{loxP/loxP}$* (2 out of 4n) and *Sm22-Cre;Robo2$^{loxP/loxP}$* (2 out of 4n) mice, compared to control mice (n=5). Black arrowhead, gallbladder artery.

revealed perturbed morphology, with artery branches showing localised distortions, again like in SLIT2-deficient livers (Fig. 6B).

ROBO1 is another receptor of SLIT2, also expressed in the developing portal mesenchyme (Fig. 2C). The role of *Robo1* was assessed in *Robo1$^{-/-}$* and *Sm22-Cre;Robo1$^{-/-}$;Robo2$^{loxP/loxP}$* mice. The inactivation of *Robo1* was associated with neonatal death of most animals, with few animals surviving beyond birth, as described earlier (Li et al., 2015). At birth, the ducts were normal in *Robo1$^{-/-}$* mice, as evidenced by normal expression of the differentiation and polarity markers SOX9, MUCIN1 and E-CADHERIN. At birth, combined inactivation of *Robo1* and *Robo2* in *Sm22-Cre;Robo1$^{-/-}$;Robo2$^{loxP/loxP}$* mice also revealed normal bile ducts (Fig. S4). No animals survived beyond birth, precluding analysis of arterial development in the combined absence of ROBO1 and ROBO2.

Together, our data indicate that mesenchymal expression of *Robo1* and *Robo2* is not required for normal bile duct development. In contrast, Robo2 is required for normal hepatic artery development, and the phenotype resulting from *Robo2* inactivation, which is similar to that of *Slit2* inactivation, suggests that ROBO2 is the receptor of SLIT2 during development of the hepatic artery's *tunica media*.

Discussion and Perspectives

SLIT/ROBO signalling and bile duct development

In the present chapter, we searched for mechanisms orchestrating the morphogenesis of the bile ducts, portal mesenchyme and vasculature in the developing liver. Our gene profiling experiments suggested that SLIT-ROBO signalling may play a role in this process, since *Slit* expression was detected in cholangiocytes and mesenchyme, and *Robo* in the mesenchyme. Moreover, gene inactivation studies enabled us to demonstrate that mesenchymally-produced SLIT2 ligand and ROBO2 receptor are required for optimal development of the hepatic artery branches. No evidence was found for a role of SLIT2/ROBO2 in morphogenesis of the bile ducts.

Earlier work has demonstrated that morphogenesis of the portal mesenchyme depends on bile duct development (Poncy et al., 2015). It was therefore tempting to speculate that SLIT2 secretion by developing cholangiocytes would impact development of the mesenchyme or vasculature via ROBO receptors. Our present data did not reveal such function for SLIT2, thereby raising questions on the role of SLIT2 in cholangiocytes. *Slit2* expression in cholangiocytes was detected during bile duct development and was not maintained at a later stage, suggesting that it is required only in development. The lack of detectable mesenchymal defect in early postnatal livers whose cholangiocytes were deficient in *Slit2* argues in favor of mechanisms compensating for the lack of SLIT2. Compensation by *Slit3* is an option, because it has been detected in developing cholangiocytes. However, unless the absence of SLIT2 would induce overexpression of *Slit3*, a compensatory role of *Slit3* in mesenchyme morphogenesis seems unlikely given the small subset of cholangiocytes expressing this gene in normal condition.

SLIT2 being expressed both by cholangiocytes and mesenchymal cells, we also hypothesised that SLIT2 could impact bile duct morphogenesis, via an autocrine or a paracrine mechanism. In this case, ROBO1 appeared as a candidate receptor for SLIT2, as it is expressed transiently in developing cholangiocytes. However, neither

inactivation of *Slit2* in the mesenchyme or cholangiocytes, nor inactivation of *Robo1* by means of a constitutive *Robo1*$^{-/-}$ knockout led to defective biliary morphogenesis. Here again, compensation by *Slit3* can be envisaged. In contrast, we did not detect ROBO receptors other than ROBO1 in the cholangiocytes, leaving open the question of the potential role of SLIT2/ROBO1 interactions in cholangiocytes.

SLIT/ROBO signalling and hepatic artery development

SLIT/ROBO signalling is active in mesenchymal precursor cells. Inactivation of *Slit2* or *Robo2* in mesenchymal cells is associated with hepatic artery defects, namely reduced morphogenesis of the *tunica media*. How could SLIT/ROBO impact VSMC development? The phenotypes of *Sm22-Cre;Slit2*$^{loxP/loxP}$ and *Sm22-Cre;Robo2*$^{loxP/loxP}$ mice significantly overlap, strongly suggesting that SLIT2 controls artery development via ROBO2. In normal mice, the hepatic artery develops postnatally starting around P10 (Clotman et al., 2003), i.e. at a period at which the expression of *Slit2* and *Robo2* is decreasing and is negligible in VSMCs surrounding the forming hepatic artery. This suggests that aberrant SLIT/ROBO signalling in precursor cells causes a defect which manifests itself at a later stage.

Studying adult mouse liver, Henderson and coworkers subjected PDGFRβ^{+} mesenchymal cells to single cell RNA sequencing and identified 3 separate populations, namely fibroblasts located in the portal space and around the central vein, HSCs distributed in the parenchyma, and VSMCs lining the portal vein and hepatic artery (Chang et al., 2015; Dobie et al., 2019). These cells originate from the *septum transversum*, and possibly from hepatomesenchymal cells derived from early hepatoblasts (Asahina et al., 2009; Asahina et al., 2011; Delgado et al., 2014; Lotto et al., 2020). How those cells differentiate *in vivo* remains unknown. Focusing on the periportal mesenchymal cells at E18.5 and P1, our data show that αSMA, a marker specific for the adult VSMCs, is expressed widely in the developing portal mesenchyme, *i.e.* not restricted to the muscular layer surrounding the portal vein (Fig. S1A). This strongly suggests that at the early stages which precede formation of the hepatic artery, the αSMA^{+} cells comprise precursors of the VSMCs. Therefore, we propose that *Slit2* and *Robo2* control VSMC development at the precursor stage.

SLIT/ROBO signalling and mesenchymal cell migration. How could SLIT2/ROBO2 control development of the precursors of hepatic artery VSMCs? The three mesenchymal cell types found in adults develop from the *septum transversum* which gives rise to mesothelial cells. A subset of the latter migrate into the liver and give rise to HSCs and perivascular cells (Asahina et al., 2009; Asahina et al., 2011; Delgado et al., 2014). SLIT-ROBO signalling is well known to control cell migration (Steffen et al., 2013). Moreover, according to the single cell RNA sequencing analysis performed by Wang and coworkers, the hepatic mesenchyme already expresses *Robo2* (Wang et al., 2020) (Fig. S2C). Therefore, we can speculate that *Robo2* controls migration of hepatic mesenchymal cells during development. The same reasoning could apply to *Slit2*, since it is also detected at E14.5 in the mesenchyme, yet at lower levels than ROBO2 (Fig. S2C). Importantly, our data do not show absence of all portal mesenchymal cell types in the absence of SLIT2 or ROBO2, only reduction or absence of VSMCs. This means that migration of only a subset of mesenchymal cells would be controlled by SLIT2 and ROBO2 at early stages of liver development, and that VSMC precursors would already be specified and distinct from other mesenchymal cell precursors. At present, we lack information on the differentiation path and migration of the mesenchymal cells to support this hypothesis. Co-staining of *Slit2* or *Robo2* with HSC markers (e.g. RELN), VSMC markers (e.g. SMOOTHELIN, SM22) or fibroblast markers (e.g. CD90/Thy1, NTPDase2 (synonym: ENTPD2)) might help to characterise the differentiation status and the location of the mesenchymal cells during liver development. At the molecular and cellular level, migration of portal mesenchymal cells can be investigated *in vitro* (Pijuan et al., 2019): FACS-purified PDGFRβ^{+} mesenchymal cells can be cultured according to Cordero-Espinoza et al. (Cordero-Espinoza et al., 2021) and treated with a soluble ROBO2-Fc chimeric receptor that acts as SLIT ligands trap (Escot et al., 2018; Zhang et al., 2010).

SLIT/ROBO signalling and mesenchymal cell differentiation. Differentiation of VSMC precursors might occur early during liver development as suggested above. Alternatively, a pool of precursors common to HSCs, fibroblasts and VSMCs might form and migrate to the periportal space during liver development, and only

differentiate towards either of the three lineages at the end of gestation or early postnatal period. In that case, SLIT2 and ROBO2 would control VSMC development in the perinatal period (Fig. 7A). Here again, information is lacking on the perinatal differentiation path of the mesenchymal cells. Single cell RNA sequencing might help solving this issue, as well as co-stainings on sections as proposed in the previous paragraph. Similarly, *in vitro* cultures of mesenchymal cells should enable investigation of the mechanisms of SLIT/ROBO-controlled differentiation. In parallel with the analysis of differentiation, we cannot exclude that VSMC precursors fail to proliferate or enter in apoptosis in the absence of SLIT2 or ROBO2; this can be investigated in our mouse models by immunostainings of Ki67 and cleaved caspase-3.

At the present stage of our work, the identity of the VSMC precursors in which *Slit2* and *Robo2* are expressed remains unclear. We showed that both genes are expressed in CD90-expressing fibroblasts. The latter actually constitute only a fraction of the portal fibroblasts, and co-detection of *Slit2* and *Robo2* with ENTPD2, which is widely expressed in portal fibroblasts (Dobie et al., 2019) (Fig. S5) would provide a more complete picture of *Slit2* and *Robo2* expression. Two models can be envisaged. In a first model, *Slit2* and *Robo2* exert autocrine or paracrine effects on mesenchymal precursors, and these effects are required to allow SLIT/ROBO-controlled fibroblasts to differentiate into VSMCs. In a second model, *Slit2* and *Robo2* exert autocrine or paracrine effects on fibroblast precursors, and these effects are required to allow the SLIT/ROBO-controlled fibroblasts to send signals to VSMC precursors which then differentiate toward mature VSMCs lining the artery (Fig. 7B). The second model is inspired by the observation that fibroblasts interact with bone marrow-derived mesenchymal stem cells (MSCs) to promote MSCs differentiation into VSMCs (Li et al., 2018). In the work of Li et al., the two cell types do not need to directly contact each other contact but likely interact by secreted intercellular signals. If a similar mechanism operates in the portal area, we can speculate that SLIT/ROBO-controlled fibroblasts secrete insulin-like growth factor 1 (IGF1): IGF1 is strongly expressed in the portal fibroblasts, the IGF1 receptor (IGF1R) is expressed in VSMCs (Dobie et al., 2019) (Fig. S5), and IGF1 is known to stimulate VSMC

proliferation and migration while inhibiting apoptosis (Bornfeldt et al., 1994; Chen et al., 1998; Fang et al., 2019; Kavurma et al., 2007). This hypothesis can be tested *in vitro* using cultured portal mesenchymal cells.

Endothelial cells are known to signal to VSMCs via PDGF, Ang1/Tie2, Sphingosine-1-phosphate and TGFβ, or via direct contact between the two cell types through Notch, Ephrin and Connexin pathways (Lilly, 2014). Our data do not exclude such interactions between the hepatic artery endothelium and the surrounding VSMCs. However, we have not detected *Sm22-Cre* activity in endothelial cells, eliminating the possibility that our observed phenotypes result from *Slit2* or *Robo2* inactivation in endothelial cells. We can however not eliminate the possibility that *Slit/Robo*-controlled fibroblasts modulate development of the arterial endothelium, and that in turn the endothelium would fail to recruit VSMCs as a result of perturbed endothelium

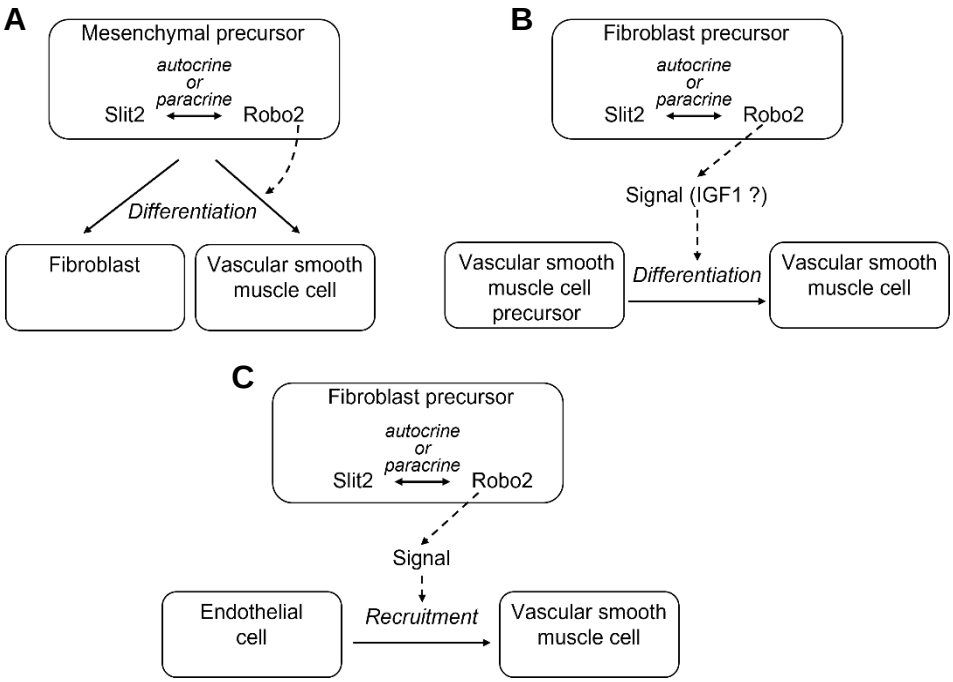

Figure 7. Models for VSMC perturbation. (A) Defect in mesenchymal cell differentiation, **(B)** Defect in VSMC differentiation, resulting from perturbed fibroblast-VSMC interactions, and **(C)** Defect in VSMCs recruitment, resulting from perturbed fibroblast-endothelial cell interactions.

maturation (Fig. 7C). In line with the latter hypothesis, Chang and coworkers found differential expression of *Slit* genes among distinct fibroblast populations and proposed that fibroblasts may post "road signs" that guide the vasculature (Chang et al., 2002).

Pathophysiological consequences of hepatic artery deficiency

Our data reveal a role for *Slit2* and *Robo2* in VSMC precursors that impacts the organisation of mature VSMCs around the hepatic artery. Our work so far focused on the earliest stage of artery development, and we still need to verify if the arterial defect persists in adults, or if the observed phenotype reflects retarded maturation. Still, the early defect impacts adult arteries as evidenced by the latter's distorted morphology. Whether this impacts tissue oxygenation remains to be determined using hypoxyprobe, but we already noticed that liver function - assessed by plasma levels of bilirubin and hepatic proteins - is not affected in the mutant mice. Importantly, the arterial defect and the role of *Slit2* and *Robo2* need to be investigated in pathological conditions. In this context, if and how blood flow is affected during liver regeneration following partial hepatectomy needs to be determined. Indeed, portal flow is not regulated, in contrast to the artery flow which increases as a result of arterial dilatation to compensate blood supply in case of reduced portal flow (Cullen and Stalker, 2016; Lautt, 2007).

Vascular smooth muscle cells lining the portal vein and the hepatic artery

No anomaly was found in the VSMCs surrounding the branches of the portal vein. Also, anterograde injection of ink into the portal vein followed by tissue clearing revealed no portal vein dysmophogenesis (Fig. S6). Our data indicate that when the portal mesenchyme expands during growth, the inactivation of *Slit2* or *Robo2* only impacts the artery and not the portal vein, suggesting that development of vein-associated VSMCs and artery-associated VSMCs remains independent and occurs via distinct mechanisms.

Gene inactivation strategy

Our gene inactivation strategy resorted to the use of *Sm22-Cre*-driven gene recombination to target the embryonic portal mesenchyme. This strategy was sucessfully used by Hofmann and coworkers when studying Jagged-Notch signalling in bile duct development (Hofmann et al., 2010). *Sm22-Cre* mice harbour a randomly inserted transgene that drives Cre expression under control of 2.8 kb of the *Sm22α* gene (Holtwick et al., 2002). The alternative line with Cre inserted in frame in exon 1 of the *Sm22α* gene was not considered because *Sm22-CreKI* is reportedly not functional in the embryo (Zhang et al., 2006) (https://www.jax.org/strain/006878). Greenhalgh and coworkers listed mouse lines with Cre activity in non-parenchymal cells of the liver (Greenhalgh et al., 2015). Among the listed lines which were potential candidates for our study, *Pdgfrb-Cre* and *Lrat-Cre* are active in adult portal mesenchyme (Henderson et al., 2013; Mederacke et al., 2013) but to our knowledge, no information is available on prenatal activity. *Vimentin-CreER* was used to investigate HSCs but this line did not show activity in the portal mesenchyme of homeostatic liver (Troeger et al., 2012). *Nkx3.2-Cre* is active in the pancreatic mesenchyme but not in liver (Landsman et al., 2011; Verzi et al., 2009). *Gata4-G2-Cre* marks the *septum tranversum* cells, but also a subset of $CD45^+$ leucocytes, which may interfere with our objective to investigate portal mesenchymal cells since $CD45^+$ cells are present in the periportal space (Delgado et al., 2014).

Our current analysis extends the data of Hofmann and coworkers (Hofmann et al., 2010), since we show here that *Sm22-Cre* is active in $CD90^+$ and in αSMA^+ periportal cells, which we consider precursors of the VSMCs. These data support that the *Sm22-Cre* line fits the goals of our study well, yet a more optimal line would drive expression of Cre^{ER} instead of Cre. This would enable time-controlled activity of Cre and allow to determine the timing at which *Slit2* and *Robo2* are critical for VSMC development.

Supplementary Tables

Table 1. Primary antibodies.

Primary antibodies	Species	Dilution	Application	Antigen retrieval	Reference
E-Cadherin	Mouse IgG2a	1/200	IF, paraffin section	MW, citrate	BD Biosciences (610181)
Sox9	Rabbit	1/1000	IF, paraffin section	MW, citrate	Homemade
Robo2	Mouse IgG1	1/200	IF, paraffin section	MW, citrate	Santa Cruz (sc-376177)
Thy-1	Rabbit	1/200	IF, paraffin section	MW, citrate	Cell Signaling (13801S)
Desmin	Mouse IgG1	1/100	IF, paraffin section	MW, citrate	Sigma-Aldrich (D1033)
Reelin	Goat	1/50	IF, paraffin or frozen section	PT-module, EDTA or water bath, citrate	R&D Systems (AF3820)
αSMA	Mouse IgG2a	1/75	IF, paraffin section	MW, citrate or EDTA	Agilent Dako (M085101-2)
GFP	Goat	1/100	IF, paraffin section	PT-module, EDTA	Abcam (#AB6673)
Sm22	Rabbit	1/100	IF, paraffin section	MW, citrate	Proteintech (10493-1-AP)
Muc-1	Armenian Hamster	1/300	IF, paraffin section	MW, citrate	Invitrogen (MA5-11202)
HNF4α	Mouse IgG2a	1/350	IF, paraffin section	MW, citrate	R&D Systems (PP-H1415-00)
β-Catenin	Mouse IgG1	1/1000	IF, paraffin section	MW, citrate	BD Biosciences (610153)
C/EBPα	Rabbit	1/300	IF, paraffin section	MW, citrate	Santa Cruz (sc-61)
TUBB3	Mouse IgG2a	1/800	IF, paraffin section	MW, citrate	Biolegend (801213)
Smoothelin	Rabbit	1/1000	IF, paraffin section	MW, EDTA	Abcam (ab219652)
Lyve1	Rabbit	1/500	IF, paraffin section	MW, citrate	Abcam (ab14917)
PECAM1 (CD31)	Rat	1/75	IF, paraffin section	MW, citrate	Dianova (DIA-310)
Vimentin	Rabbit	1/100	IF, paraffin section	MW, citrate	Cell signaling (57415)
CD45	Rat	1/50	IF, frozen or paraffin section	Water bath, citrate	BD Biosciences (550539)
Ter119	Rabbit	1/500	IF, paraffin section	MW, citrate	Biolegend (116233)

Thy1	Rat	1/100	IF, frozen section	Water bath, citrate	Abcam (ab3105)
GFP	Chicken	1/1000	IF, frozen or paraffin section	Water bath, citrate	Abcam (ab13970)
EpCAM (APC)	Rat	0.125µg/ 10^6 cells	FACS sorting	-	Invitrogen (17-5791-82)
CD45 (Brilliant Violet 421)	Rat	0.25µg/ 10^6 cells	FACS sorting	-	Biolegend (103134)
CD31 (PE/Cyanine7)	Rat	0.25µg/ 10^6 cells	FACS sorting	-	Biolegend (102418)

Table 2. Secondary antibodies.

Secondary antibodies	Species	Dilution	Reference
Anti-Rabbit HRP	Goat	1/1000	Invitrogen (31460)
Anti-Rat Alexa Fluor 488	Donkey	1/1000	Invitrogen (A21208)
Anti-Rat Alexa Fluor 594	Donkey	1/1000	Invitrogen (A21209)
Anti-Mouse IgG2a Alexa Fluor 488	Goat	1/1000	Invitrogen (A21131)
Anti-Mouse IgG2a Alexa Fluor 594	Goat	1/1000	Invitrogen (A21135)
Anti-Mouse IgG2a Alexa Fluor 647	Goat	1/1000	Invitrogen (A21241)
Anti-Armenian Hamster Alexa Fluor 594	Donkey	1/500	Jackson ImmunoResearch (127-585-099)
Anti-Rabbit Alexa Fluor 594	Donkey	1/1000	Invitrogen (A21207)
Anti-Rabbit Alexa Fluor 488	Donkey	1/1000	Invitrogen (A21206)
Anti-Rabbit Alexa Fluor 647	Donkey	1/1000	Invitrogen (A31573)
Anti-Mouse IgG1 Alexa Fluor 594	Goat	1/1000	Invitrogen (A21125)
Anti-Mouse IgG1 Alexa Fluor 488	Goat	1/1000	Invitrogen (A21121)
Anti-Mouse IgG1 Alexa Fluor 647	Goat	1/1000	Invitrogen (A21240)
Anti-Goat Alexa Fluor 488	Donkey	1/1000	Invitrogen (A11055)
Anti-Goat Alexa Fluor 594	Donkey	1/1000	Invitrogen (A11058)
Anti-Chicken Alexa Fluor 488	Goat	1/1000	Invitrogen (A11039)
Anti-Mouse total Alexa fluor 594	Donkey	1/1000	Invitrogen (A21203)

Table 3. Number of mice and associated hepatic arteries analysed in Fig. 5B.

P10 Control (n=4)	< 2000 µm^2	> 2000 µm^2
#1	20	16
#2	40	15
#3	35	11
#4	15	9
P10 Sm22-Cre Slit2$^{lox/lox}$ (n=9)	**< 2000 µm^2**	**> 2000 µm^2**
#1	39	15
#2	23	17
#3	20	16
#4 (most severe phenotype)	16	2
#5	22	10
#6	26	18
#7	20	13
#8	16	4
#9	18	11
P10 Sm22-Cre Robo2$^{lox/lox}$ (n=7)	**< 2000 µm^2**	**> 2000 µm^2**
#1	22	17
#2	27	9
#3	29	14
#4	23	16
#5 (most severe phenotype)	12	3
#6	22	5
#7	15	11

Supplementary Figures

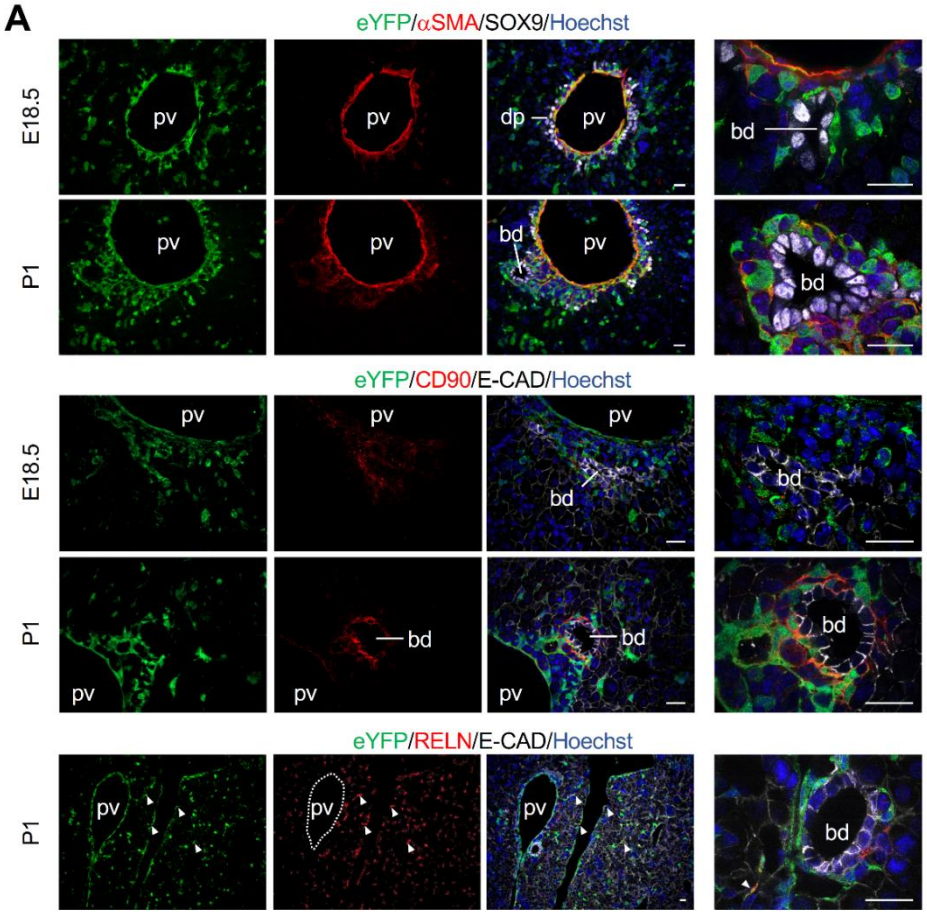

Supplementary Figure 1. eYFP expression in *Sm22-Cre;Rosa26R^{eYFP}* livers. (A) Staining of αSMA, CD90 and eYFP at E18.5 and P1 reveals activity of *Sm22-Cre* in portal mesenchyme, namely progenitors of VSMCs and portal fibroblasts. Few RELN-expressing cells express eYFP (white arrowheads). **(B)** CD45, Ter119 and eYFP co-staining did not show expression of eYFP in periportal leukocytes and only in rare parenchymal erythroblast. bd, bile duct; dp, ductal plate; pv, portal vein. Size bars: 20 µm.

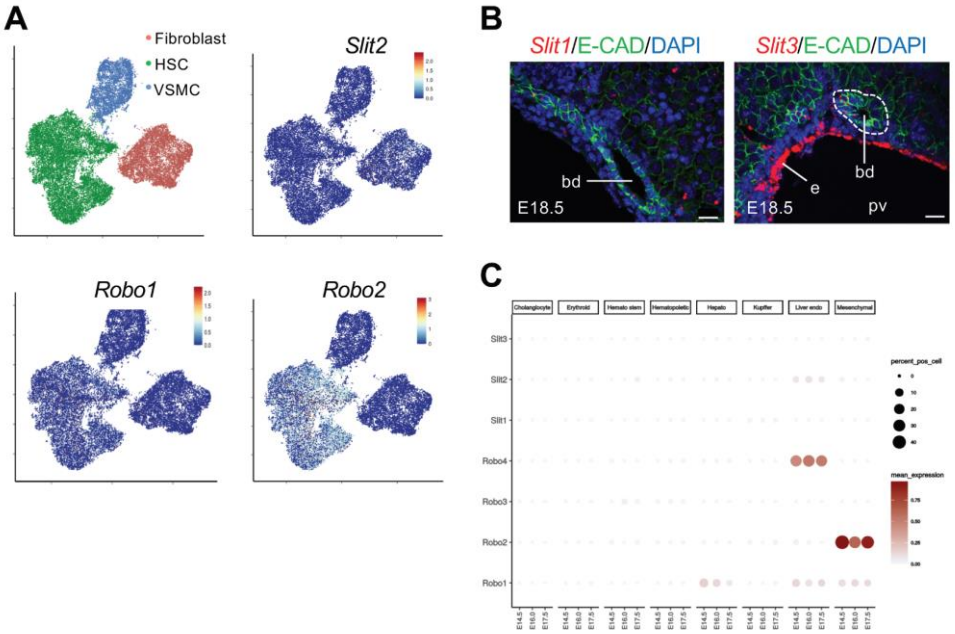

Supplementary Figure 2. Expression of *Slit* and *Robo* genes in developing and adult liver. (A) Single cell RNA sequencing performed on adult mesenchyme (Dobie et al., 2019) detects *Slit2* in fibroblasts, and *Robo1* and *Robo2* in HSCs. **(B)** *In situ* hybridisation of *Slit1* does not reveal expression in embryonic liver (E18.5), while *Slit3* RNA is detected in portal vein endothelium and weakly expressed in cholangiocytes. bd, bile duct; e, endothelium; pv, portal vein. Size bars: 20 µm. **(C)** Single cell RNA sequencing performed on embryonic liver cell types detected a subset of Slit and Robo in epithelial and mesenchymal cells (Wang et al., 2020).

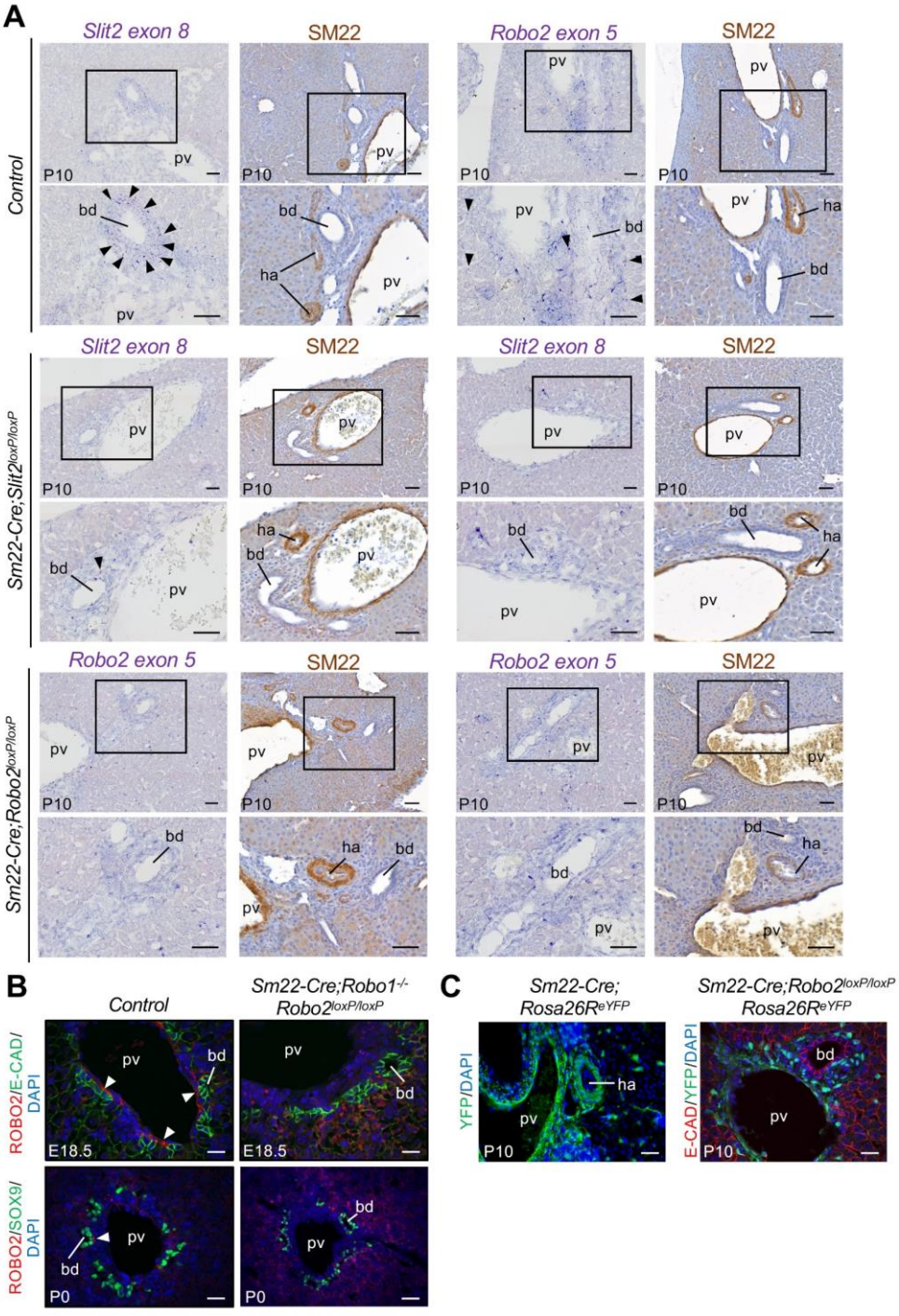
A
Slit2 exon 8
SM22
Robo2 exon 5
SM22
Control
Sm22-Cre;Slit2loxP/loxP
Sm22-Cre;Robo2loxP/loxP
P10
pv
bd
ha
B
Control
Sm22-Cre;Robo1-/-
Robo2loxP/loxP
ROBO2/E-CAD/
DAPI
ROBO2/SOX9/
DAPI
E18.5
P0
C
Sm22-Cre;
Rosa26ReYFP
Sm22-Cre;Robo2loxP/loxP
Rosa26ReYFP
YFP/DAPI
E-CAD/YFP/DAPI
P10

Supplementary Figure 3. Efficiency of Sm22-Cre in the studied transgenic mouse models. (A) *In situ* RNA hybridisation (BaseScope) detecting exon 8 of *Slit2* or exon 5 of *Robo2* shows efficient inactivation of *Slit2* and *Robo2* genes in *Sm22-Cre;Slit2*$^{loxP/loxP}$ and *Sm22-Cre;Robo2*$^{loxP/loxP}$ mice, respectively. In parallel, staining of SM22 shows the biological heterogeneity of the arterial phenotype. The black arrowheads point to cells in which *Slit2* or *Robo2* RNA is detected. **(B)** Immunostaining of ROBO2 confirms the absence of ROBO2 protein in *Sm22-Cre;Robo1*$^{-/-}$*;Robo2*$^{loxP/loxP}$ mice. **(C)** Activity of *Sm22-Cre* is confirmed by immunostaining of eYFP on *Sm22-Cre;Robo2*$^{loxP/loxP}$*;Rosa26R*^{eYFP} livers, like in *Sm22-Cre; Rosa26R*^{eYFP} livers. bd, bile duct; ha, hepatic artery; pv, portal vein. Size bars: 20 µm (white) or 50 µm (black).

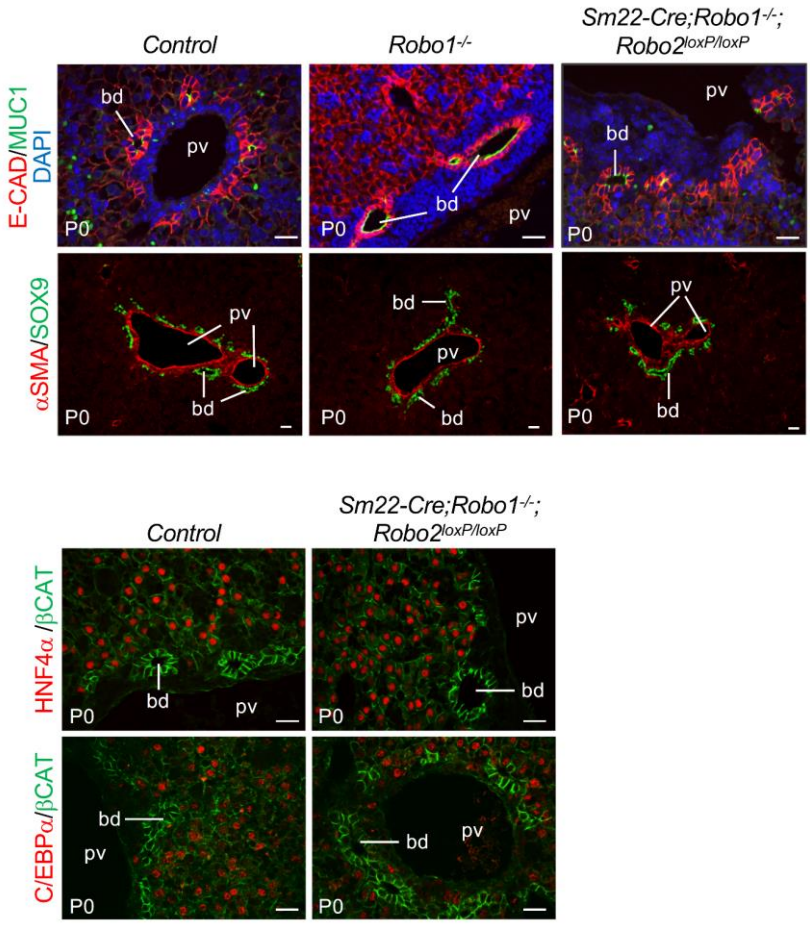

Supplementary Figure 4. *Robo1* and *Robo2* are dispensable for biliary morphogenesis. At birth, bile ducts are normal and delineated by well-differentiated and well-polarised cholangiocytes in the absence of *Robo1* and *Robo2* in *Robo1*$^{-/-}$ (n=4) and *Sm22-Cre;Robo1*$^{-/-}$*;Robo2*$^{loxP/loxP}$ (n=6) mice.

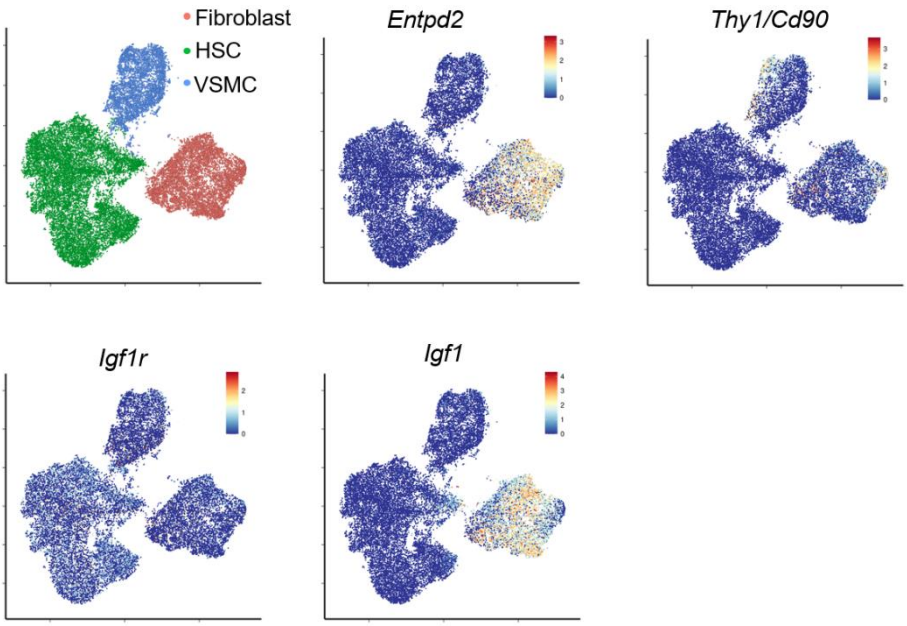

Supplementary Figure 5. Expression of *Entpd2*, *Thy1*, *Igf1* and *Igf1r* in hepatic mesenchyme. Single cell RNA sequencing performed on adult mesenchyme identifies *Thy1/Cd90* and *Entpd2* as markers of fibroblasts, with *Thy1/Cd90* à being expressed only in a subset of fibroblasts. *Igf1* is detected in fibroblasts and its receptor in VSMCs. Data are from Dobie et al. (2019).

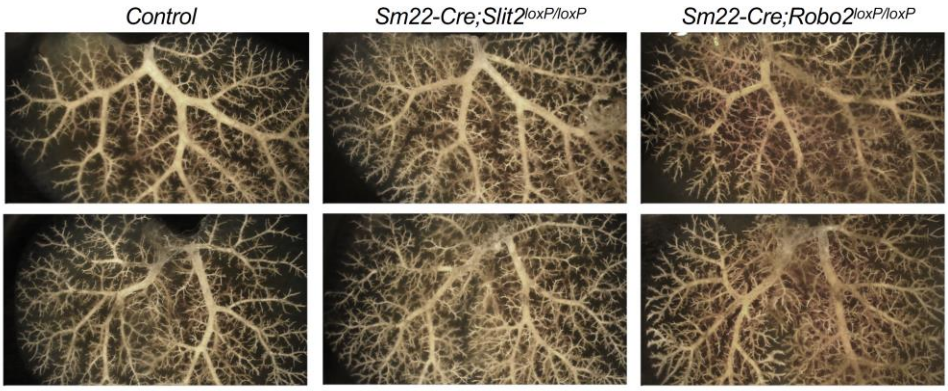

Supplementary Figure 6. Portal vein morphogenesis does not require *Slit2* or *Robo2* expression in portal mesenchymal cells. Ink injection in the portal vein followed by clearing of left lobe (upper pictures) and median lobe (bottom pictures) reveals normal portal vein branches in 2 months-old control (n=3), *Sm22-Cre;Slit2*$^{loxP/loxP}$ (n=3) and *Sm22-Cre;Robo2*$^{loxP/loxP}$ (n=3) mice.

References

Antoniou, A., Raynaud, P., Cordi, S., Zong, Y., Tronche, F., Stanger, B.Z., Jacquemin, P., Pierreux, C.E., Clotman, F., Lemaigre, F.P., 2009. Intrahepatic bile ducts develop according to a new mode of tubulogenesis regulated by the transcription factor SOX9. Gastroenterology 136, 2325-2333.

Asahina, K., Tsai, S.Y., Li, P., Ishii, M., Maxson, R.E., Jr., Sucov, H.M., Tsukamoto, H., 2009. Mesenchymal origin of hepatic stellate cells, submesothelial cells, and perivascular mesenchymal cells during mouse liver development. Hepatology 49, 998-1011.

Asahina, K., Zhou, B., Pu, W.T., Tsukamoto, H., 2011. Septum transversum-derived mesothelium gives rise to hepatic stellate cells and perivascular mesenchymal cells in developing mouse liver. Hepatology 53, 983-995.

Bornfeldt, K.E., Raines, E.W., Nakano, T., Graves, L.M., Krebs, E.G., Ross, R., 1994. Insulin-like growth factor-I and platelet-derived growth factor-BB induce directed migration of human arterial smooth muscle cells via signaling pathways that are distinct from those of proliferation. J Clin Invest 93, 1266-1274.

Carmeliet, P., 2000. Mechanisms of angiogenesis and arteriogenesis. Nat Med 6, 389-395.

Chang, H.Y., Chi, J.T., Dudoit, S., Bondre, C., van de Rijn, M., Botstein, D., Brown, P.O., 2002. Diversity, topographic differentiation, and positional memory in human fibroblasts. Proc Natl Acad Sci U S A 99, 12877-12882.

Chang, J., Lan, T., Li, C., Ji, X., Zheng, L., Gou, H., Ou, Y., Wu, T., Qi, C., Zhang, Q., Li, J., Gu, Q., Wen, D., Cao, L., Qiao, L., Ding, Y., Wang, L., 2015. Activation of Slit2-Robo1 signaling promotes liver fibrosis. J Hepatol 63, 1413-1420.

Chen, Y., Capron, L., Magnusson, J.O., Wallby, L.A., Arnqvist, H.J., 1998. Insulin-like growth factor-1 stimulates vascular smooth muscle cell proliferation in rat aorta in vivo. Growth Horm IGF Res 8, 299-303.

Clotman, F., Libbrecht, L., Gresh, L., Yaniv, M., Roskams, T., Rousseau, G.G., Lemaigre, F.P., 2003. Hepatic artery malformations associated with a primary defect in intrahepatic bile duct development. J Hepatol 39, 686-692.

Cordero-Espinoza, L., Dowbaj, A.M., Kohler, T.N., Strauss, B., Sarlidou, O., Belenguer, G., Pacini, C., Martins, N.P., Dobie, R., Wilson-Kanamori, J.R., Butler, R., Prior, N., Serup, P., Jug, F., Henderson, N.C., Hollfelder, F., Huch, M., 2021. Dynamic cell contacts between periportal mesenchyme and ductal epithelium act as a rheostat for liver cell proliferation. Cell Stem Cell 28, 1907-1921.

Couvelard, A., Bringuier, A.F., Dauge, M.C., Nejjari, M., Darai, E., Benifla, J.L., Feldmann, G., Henin, D., Scoazec, J.Y., 1998. Expression of integrins during liver organogenesis in humans. Hepatology 27, 839-847.

Cullen, J.M., Stalker, M.J., 2016. Chapter 2 - Liver and Biliary System, in: Maxie, M.G. (Ed.), Kennedy & Palmer's Pathology of Domestic Animals: Volume 2 (Sixth Edition), pp. 258-352.e251.

Delgado, I., Carrasco, M., Cano, E., Carmona, R., Garcia-Carbonero, R., Marin-Gomez, L.M., Soria, B., Martin, F., Cano, D.A., Munoz-Chapuli, R., Rojas, A., 2014. GATA4 loss in the septum transversum mesenchyme promotes liver fibrosis in mice. Hepatology 59, 2358-2370.

Demarez, C., Gerard, C., Cordi, S., Poncy, A., Achouri, Y., Dauguet, N., Rosa, D.A., Gunning, P.T., Manfroid, I., Lemaigre, F.P., 2018. MicroRNA-337-3p controls hepatobiliary gene expression and transcriptional dynamics during hepatic cell differentiation. Hepatology 67, 313-327.

Dobie, R., Wilson-Kanamori, J.R., Henderson, B.E.P., Smith, J.R., Matchett, K.P., Portman, J.R., Wallenborg, K., Picelli, S., Zagorska, A., Pendem, S.V., Hudson, T.E., Wu, M.M., Budas, G.R., Breckenridge, D.G., Harrison, E.M., Mole, D.J., Wigmore, S.J., Ramachandran, P., Ponting, C.P., Teichmann, S.A., Marioni, J.C., Henderson, N.C., 2019. Single-Cell Transcriptomics Uncovers Zonation of Function in the Mesenchyme during Liver Fibrosis. Cell Rep 29, 1832-1847.

Escot, S., Willnow, D., Naumann, H., Di Francescantonio, S., Spagnoli, F.M., 2018. Robo signalling controls pancreatic progenitor identity by regulating Tead transcription factors. Nat Commun 9, 5082.

Fabris, L., Cadamuro, M., Libbrecht, L., Raynaud, P., Spirli, C., Fiorotto, R., Okolicsanyi, L., Lemaigre, F., Strazzabosco, M., Roskams, T., 2008. Epithelial expression of angiogenic growth factors modulate arterial vasculogenesis in human liver development. Hepatology 47, 719-728.

Fang, X.-S., Zhang, M.-H., Zhang, X.-Z., Guo, J.-Y., Jin, Z., 2019. Insulin-like growth factor-1 inhibits the apoptosis of rat gastric smooth muscle cells cultured under high glucose condition through PI3K-Akt-PKC-Ca2+ pathway. Biotechnology & Biotechnological Equipment 33, 456-464.

Gong, S., Zheng, C., Doughty, M.L., Losos, K., Didkovsky, N., Schambra, U.B., Nowak, N.J., Joyner, A., Leblanc, G., Hatten, M.E., Heintz, N., 2003. A gene expression atlas of the central nervous system based on bacterial artificial chromosomes. Nature 425, 917-925.

Gordillo, M., Evans, T., Gouon-Evans, V., 2015. Orchestrating liver development. Development 142, 2094-2108.

Greenhalgh, S.N., Conroy, K.P., Henderson, N.C., 2015. Cre-ativity in the liver: transgenic approaches to targeting hepatic nonparenchymal cells. Hepatology 61, 2091-2099.

Henderson, N.C., Arnold, T.D., Katamura, Y., Giacomini, M.M., Rodriguez, J.D., McCarty, J.H., Pellicoro, A., Raschperger, E., Betsholtz, C., Ruminski, P.G., Griggs, D.W., Prinsen, M.J., Maher, J.J., Iredale, J.P., Lacy-Hulbert, A., Adams, R.H., Sheppard, D., 2013. Targeting of alphav integrin identifies a core molecular pathway that regulates fibrosis in several organs. Nat Med 19, 1617-1624.

Hofmann, J.J., Zovein, A.C., Koh, H., Radtke, F., Weinmaster, G., Iruela-Arispe, M.L., 2010. Jagged1 in the portal vein mesenchyme regulates intrahepatic bile duct development: insights into Alagille syndrome. Development 137, 4061-4072.

Holtwick, R., Gotthardt, M., Skryabin, B., Steinmetz, M., Potthast, R., Zetsche, B., Hammer, R.E., Herz, J., Kuhn, M., 2002. Smooth muscle-selective deletion of guanylyl cyclase-A prevents the acute but not chronic effects of ANP on blood pressure. Proc Natl Acad Sci U S A 99, 7142-7147.

Jhandier, M.N., Kruglov, E.A., Lavoie, E.G., Sevigny, J., Dranoff, J.A., 2005. Portal fibroblasts regulate the proliferation of bile duct epithelia via expression of NTPDase2. J Biol Chem 280, 22986-22992.

Kavurma, M.M., Figg, N., Bennett, M.R., Mercer, J., Khachigian, L.M., Littlewood, T.D., 2007. Oxidative stress regulates IGF1R expression in vascular smooth-muscle cells via p53 and HDAC recruitment. Biochem J 407, 79-87.

Kaylan, K.B., Ermilova, V., Yada, R.C., Underhill, G.H., 2016. Combinatorial microenvironmental regulation of liver progenitor differentiation by Notch ligands, TGFbeta, and extracellular matrix. Sci Rep 6, 23490.

Kellendonk, C., Opherk, C., Anlag, K., Schutz, G., Tronche, F., 2000. Hepatocyte-specific expression of Cre recombinase. Genesis 26, 151-153.

Krishna, M., 2013. Microscopic anatomy of the liver. Clin Liver Dis (Hoboken) 2, S4-S7.

Lade, A.G., Monga, S.P., 2011. Beta-catenin signaling in hepatic development and progenitors: which way does the WNT blow? Dev Dyn 240, 486-500.

Landsman, L., Nijagal, A., Whitchurch, T.J., Vanderlaan, R.L., Zimmer, W.E., Mackenzie, T.C., Hebrok, M., 2011. Pancreatic mesenchyme regulates epithelial organogenesis throughout development. PLoS Biol 9, e1001143.

Lautt, W.W., 2007. Regulatory processes interacting to maintain hepatic blood flow constancy: Vascular compliance, hepatic arterial buffer response, hepatorenal reflex, liver regeneration, escape from vasoconstriction. Hepatol Res 37, 891-903.

Lemaigre, F.P., 2020. Development of the Intrahepatic and Extrahepatic Biliary Tract: A Framework for Understanding Congenital Diseases. Annu Rev Pathol 15, 1-22.

Li, J., Ye, Y., Zhang, R., Zhang, L., Hu, X., Han, D., Chen, J., He, X., Wang, G., Yang, X., Wang, L., 2015. Robo1/2 regulate follicle atresia through manipulating granulosa cell apoptosis in mice. Sci Rep 5, 9720.

Li, N., Sanyour, H., Remund, T., Kelly, P., Hong, Z., 2018. Vascular extracellular matrix and fibroblasts-coculture directed differentiation of human mesenchymal stem cells toward smooth muscle-like cells for vascular tissue engineering. Mater Sci Eng C Mater Biol Appl 93, 61-69.

Lilly, B., 2014. We have contact: endothelial cell-smooth muscle cell interactions. Physiology (Bethesda) 29, 234-241.

Long, H., Sabatier, C., Ma, L., Plump, A., Yuan, W., Ornitz, D.M., Tamada, A., Murakami, F., Goodman, C.S., Tessier-Lavigne, M., 2004. Conserved roles for Slit and Robo proteins in midline commissural axon guidance. Neuron 42, 213-223.

Lotto, J., Drissler, S., Cullum, R., Wei, W., Setty, M., Bell, E.M., Boutet, S.C., Nowotschin, S., Kuo, Y.Y., Garg, V., Pe'er, D., Church, D.M., Hadjantonakis, A.K., Hoodless, P.A., 2020. Single-Cell Transcriptomics Reveals Early Emergence of Liver Parenchymal and Non-parenchymal Cell Lineages. Cell 183, 702-716 e714.

Lu, W., van Eerde, A.M., Fan, X., Quintero-Rivera, F., Kulkarni, S., Ferguson, H., Kim, H.G., Fan, Y., Xi, Q., Li, Q.G., Sanlaville, D., Andrews, W., Sundaresan, V., Bi, W., Yan, J., Giltay, J.C., Wijmenga, C., de Jong, T.P., Feather, S.A., Woolf, A.S., Rao, Y., Lupski, J.R., Eccles, M.R., Quade, B.J., Gusella, J.F., Morton, C.C., Maas, R.L., 2007. Disruption of ROBO2 is associated with urinary tract anomalies and confers risk of vesicoureteral reflux. Am J Hum Genet 80, 616-632.

Martens, S., Coolens, K., Van Bulck, M., Arsenijevic, T., Casamitjana, J., Fernandez Ruiz, A., El Kaoutari, A., Martinez de Villareal, J., Madhloum, H., Esni, F., Heremans, Y., Leuckx, G., Heimberg, H., Bouwens, L., Jacquemin, P., De Paep, D.L., In't Veld, P., D'Haene, N., Bouchart, C., Dusetti, N., Van Laethem, J.L., Waelput, W., Lefesvre, P., Real, F.X., Rovira, M., Rooman, I., 2021. Discovery and 3D imaging of a novel DeltaNp63-expressing basal cell type in human pancreatic ducts with implications in disease. Gut 0, 1-13.

Mederacke, I., Hsu, C.C., Troeger, J.S., Huebener, P., Mu, X., Dapito, D.H., Pradere, J.P., Schwabe, R.F., 2013. Fate tracing reveals hepatic stellate cells as dominant contributors to liver fibrosis independent of its aetiology. Nat Commun 4, 2823.

Ober, E.A., Lemaigre, F.P., 2018. Development of the liver: Insights into organ and tissue morphogenesis. J Hepatol 68, 1049-1062.

Pijuan, J., Barcelo, C., Moreno, D.F., Maiques, O., Siso, P., Marti, R.M., Macia, A., Panosa, A., 2019. In vitro Cell Migration, Invasion, and Adhesion Assays: From Cell Imaging to Data Analysis. Front Cell Dev Biol 7, 107.

Poncy, A., Antoniou, A., Cordi, S., Pierreux, C.E., Jacquemin, P., Lemaigre, F.P., 2015. Transcription factors SOX4 and SOX9 cooperatively control development of bile ducts. Dev Biol 404, 136-148.

Rama, N., Dubrac, A., Mathivet, T., Ni Charthaigh, R.A., Genet, G., Cristofaro, B., Pibouin-Fragner, L., Ma, L., Eichmann, A., Chedotal, A., 2015. Slit2 signaling through Robo1 and Robo2 is required for retinal neovascularization. Nat Med 21, 483-491.

Raudvere, U., Kolberg, L., Kuzmin, I., Arak, T., Adler, P., Peterson, H., Vilo, J., 2019. g:Profiler: a web server for functional enrichment analysis and conversions of gene lists (2019 update). Nucleic Acids Res 47, W191-W198.

Sheu, A.Y., Zhang, Z., Omary, R.A., Larson, A.C., 2013. Invasive catheterization of the hepatic artery for preclinical investigation of liver-directed therapies in rodent models of liver cancer. Am J Transl Res 5, 269-278.

Shinozaki, K., Ebert, O., Kournioti, C., Tai, Y.S., Woo, S.L., 2004. Oncolysis of multifocal hepatocellular carcinoma in the rat liver by hepatic artery infusion of vesicular stomatitis virus. Mol Ther 9, 368-376.

Srinivas, S., Watanabe, T., Lin, C.S., William, C.M., Tanabe, Y., Jessell, T.M., Costantini, F., 2001. Cre reporter strains produced by targeted insertion of EYFP and ECFP into the ROSA26 locus. BMC Dev Biol 1, 4.

Steffen, A., Ladwein, M., Dimchev, G.A., Hein, A., Schwenkmezger, L., Arens, S., Ladwein, K.I., Margit Holleboom, J., Schur, F., Victor Small, J., Schwarz, J., Gerhard, R., Faix, J., Stradal, T.E., Brakebusch, C., Rottner, K., 2013. Rac function is crucial for cell migration but is not required for spreading and focal adhesion formation. J Cell Sci 126, 4572-4588.

Tada, M., Hatano, E., Taura, K., Nitta, T., Koizumi, N., Ikai, I., Shimahara, Y., 2006. High volume hydrodynamic injection of plasmid DNA via the hepatic artery results in a high level of gene expression in rat hepatocellular carcinoma induced by diethylnitrosamine. J Gene Med 8, 1018-1026.

Tanimizu, N., Kikkawa, Y., Mitaka, T., Miyajima, A., 2012. alpha1- and alpha5-containing laminins regulate the development of bile ducts via beta1 integrin signals. J Biol Chem 287, 28586-28597.

Troeger, J.S., Mederacke, I., Gwak, G.Y., Dapito, D.H., Mu, X., Hsu, C.C., Pradere, J.P., Friedman, R.A., Schwabe, R.F., 2012. Deactivation of hepatic stellate cells during liver fibrosis resolution in mice. Gastroenterology 143, 1073-1083 e1022.

Tsuchida, T., Friedman, S.L., 2017. Mechanisms of hepatic stellate cell activation. Nat Rev Gastroenterol Hepatol 14, 397-411.

Van Liedekerke, P., Gannoun L., Loriot, A., Lemaigre, F.P., Drasdo, D., 2021. Quantitative modeling identifies critical cell mechanics driving bile duct lumen formation. PLoS Comp Biol in press.

Verzi, M.P., Stanfel, M.N., Moses, K.A., Kim, B.M., Zhang, Y., Schwartz, R.J., Shivdasani, R.A., Zimmer, W.E., 2009. Role of the homeodomain transcription factor Bapx1 in mouse distal stomach development. Gastroenterology 136, 1701-1710.

Villeneuve, J., Pelluard-Nehme, F., Combe, C., Carles, D., Chaponnier, C., Ripoche, J., Balabaud, C., Bioulac-Sage, P., Lepreux, S., 2009. Immunohistochemical study of the phenotypic change of the mesenchymal cells during portal tract maturation in normal and fibrous (ductal plate malformation) fetal liver. Comp Hepatol 8, 5.

Wang, X., Yang, L., Wang, Y.C., Xu, Z.R., Feng, Y., Zhang, J., Wang, Y., Xu, C.R., 2020. Comparative analysis of cell lineage differentiation during hepatogenesis in humans and mice at the single-cell transcriptome level. Cell Res 30, 1109-1126.

Wells, R.G., 2014. The portal fibroblast: not just a poor man's stellate cell. Gastroenterology 147, 41-47.

Yanai, M., Tatsumi, N., Hasunuma, N., Katsu, K., Endo, F., Yokouchi, Y., 2008. FGF signaling segregates biliary cell-lineage from chick hepatoblasts cooperatively with BMP4 and ECM components in vitro. Dev Dyn 237, 1268-1283.

Zhang, H.Y., Zheng, L.F., Yi, X.N., Chen, Z.B., He, Z.P., Zhao, D., Zhang, X.F., Ma, Z.J., 2010. Slit1 promotes regenerative neurite outgrowth of adult dorsal root ganglion neurons in vitro via binding to the Robo receptor. J Chem Neuroanat 39, 256-261.

Zhang, J., Zhong, W., Cui, T., Yang, M., Hu, X., Xu, K., Xie, C., Xue, C., Gibbons, G.H., Liu, C., Li, L., Chen, Y.E., 2006. Generation of an adult smooth muscle cell-targeted Cre recombinase mouse model. Arterioscler Thromb Vasc Biol 26, e23-24.

Zong, Y., Panikkar, A., Xu, J., Antoniou, A., Raynaud, P., Lemaigre, F., Stanger, B.Z., 2009. Notch signaling controls liver development by regulating biliary differentiation. Development 136, 1727-1739.

2. Quantitative modeling identifies critical cell mechanics driving bile duct lumen formation

Paul Van Liedekerke, Lila Gannoun, Axelle Loriot, Frédéric P. Lemaigre, Dirk Drasdo.

In this publication, I collected all the biological data in Figs 1-3-4-6-8-9, and contributed to draft the manuscript.

PLOS COMPUTATIONAL BIOLOGY

RESEARCH ARTICLE

Quantitative modeling identifies critical cell mechanics driving bile duct lumen formation

Paul Van Liedekerke[1,2,4☯‡*], **Lila Gannoun**[2☯], **Axelle Loriot**[2], **Tim Johann**[3], **Frédéric P. Lemaigre**[2‡], **Dirk Drasdo**[1,3,4‡*]

1 Inria Saclay Île-De-France, Palaiseau, France, **2** de Duve Institute, Université Catholique de Louvain, Brussels, Belgium, **3** Leibniz Research Centre for Working Environment and Human Factors at the Technical University Dortmund, Dortmund, Germany, **4** Inria de Paris & Sorbonne Université LJLL, Paris, France

☯ These authors contributed equally to this work.
‡ These authors are joint co-senior authorship on this work.
* Paul.Van_Liedekerke@inria.fr (PVL); Dirk.Drasdo@inria.fr (DD)

Citation: Van Liedekerke P, Gannoun L, Loriot A, Johann T, Lemaigre FP, Drasdo D (2022) Quantitative modeling identifies critical cell mechanics driving bile duct lumen formation. PLoS Comput Biol 18(2): e1009653. https://doi.org/10.1371/journal.pcbi.1009653

Editor: David M. Umulis, Purdue University, UNITED STATES

Received: March 26, 2021

Accepted: November 16, 2021

Published: February 18, 2022

Peer Review History: PLOS recognizes the benefits of transparency in the peer review process; therefore, we enable the publication of all of the content of peer review and author responses alongside final, published articles. The editorial history of this article is available here: https://doi.org/10.1371/journal.pcbi.1009653

Data Availability Statement: Immunostainings: this data is entirely contained within the manuscript. The RNA-seq data have been deposited in the Gene Expression Omnibus (GEO)

Abstract

Biliary ducts collect bile from liver lobules, the smallest functional and anatomical units of liver, and carry it to the gallbladder. Disruptions in this process caused by defective embryonic development, or through ductal reaction in liver disease have a major impact on life quality and survival of patients. A deep understanding of the processes underlying bile duct lumen formation is crucial to identify intervention points to avoid or treat the appearance of defective bile ducts. Several hypotheses have been proposed to characterize the biophysical mechanisms driving initial bile duct lumen formation during embryogenesis. Here, guided by the quantification of morphological features and expression of genes in bile ducts from embryonic mouse liver, we sharpened these hypotheses and collected data to develop a high resolution individual cell-based computational model that enables to test alternative hypotheses in silico. This model permits realistic simulations of tissue and cell mechanics at sub-cellular scale. Our simulations suggest that successful bile duct lumen formation requires a simultaneous contribution of directed cell division of cholangiocytes, local osmotic effects generated by salt excretion in the lumen, and temporally-controlled differentiation of hepatoblasts to cholangiocytes, with apical constriction of cholangiocytes only moderately affecting luminal size.

Author summary

The initial step in bile duct development is the formation of a biliary lumen, a process which involves several cellular mechanisms, such as cell division and polarization, and secretion of fluid. However, how these mechanisms are orchestrated in time and space is difficult to understand. Here, we built a computational model of biliary lumen formation which represents every cell and its function in detail. With the model we can simulate the effect of biophysical aspects that affect duct formation. We have tested the individual and combined effects of directed cell division, apical constriction, and osmotic effects on lumen expansion by varying the parameters that control their relative strength. Our

database and assigned the identifier GSE163062. In Fig 3C, all relevant data are in the graph. All the simulation data created in Figs 7, 8, 9 and 10 are simulation data can be plotted using the accompaying python script (delivered as supplementary information). This paper entered editorial review prior to the code availability policy of 30/03/2021.

Funding: The work of PVL and DD were supported by LiSyM (nr 031L0045) by BMBF (http://www.bmbf.de). PVL, DD and FPL acknowledge iLITE (nr ANR-16-RHUS-0005-16) by ANR (http://www.anr.fr). The work of FPL was supported by D.G. Higher Education and Scientific Research of the French Community of Belgium (grant ARC 15/20-065, http://www.recherchescientifique.be/). FPL and AL acknowledge the Fonds de la Recherche Scientifique FRS-FNRS (Belgium; grants T.0158.20 and J.0115.20, https://www.frs-fnrs.be/). L.G. holds a PhD fellowship from the Fonds pour la Formation à la Recherche dans l'Industrie et dans l'Agronomie (Belgium; grant 1.E071.18, https://www.frs-fnrs.be/). The funders had no role in study design, data collection and analysis, decision to publish, or preparation of the manuscript.

Competing interests: The authors have declared that no competing interests exist.

simulations suggest that successful bile duct lumen formation requires the simultaneous contribution of directed cell division of cholangiocytes, local osmotic effects generated by salt excretion in the lumen, and temporally-controlled differentiation of hepatoblasts to cholangiocytes, with apical constriction of cholangiocytes only moderately affecting luminal size.

Introduction

The liver is composed of multiple repetitive anatomical and physiological units, the liver lobules. A liver lobule is approximately hexagonal in shape and is fed by oxygen rich blood from the hepatic artery, and oxygen-poor blood from the portal vein. Inside the lobule the blood flows through complex network of capillaries with a design that promotes a maximal exchange of molecules between blood and hepatocytes until it drains into the central vein. Bile is eliminated via the bile canaliculi, and collected by biliary ducts that carry the bile to the gallbladder and eventually to the intestine. Defects in the biliary duct system resulting from defective development or from disease, e.g. by ductal reaction [1] can significantly impact life quality and survival of a patient. A deep understanding of the processes underlying lumen formation during bile duct development is crucial to intervene in such defective cases, and can furthermore be used to engineer functional liver tissue in vitro.

In embryonic liver, cholangiocytes and hepatocytes differentiate from bipotent hepatoblasts. Differentiation of cholangiocytes is spatially restricted around the mesenchyme associated with the branches of the portal vein [2, 3]. The conversion of hepatoblasts to cholangiocytes is induced by cell-cell contacts between the mesenchymal cells and adjacent hepatoblasts, as well as by factors secreted by the mesenchyme which target receptors at the membrane of the hepatoblasts [4].

Hepatoblasts that have differentiated to cholangiocytes initially constitute a "ductal plate", which is a discontinuous and single-layered sheet of cholangiocytes located near the portal mesenchyme (Fig 1A and 1C). Duct morphogenesis is then initiated by the appearance of several lumina delineated on the portal side by ductal plate cholangiocytes, and on the parenchymal side by hepatoblasts. Therefore, the initial ductal structures are lined by two distinct cell types. When duct formation proceeds, the hepatoblasts which delineate the parenchymal side of the lumina progressively differentiate to cholangiocytes [3–8].

Bile duct lumen formation proceeds according to a cord hollowing process which, consists in the appearance of a lumen between adhering cells [5, 8, 9]. Lumenogenesis implies that the cells which delineate an apical lumen coordinately undergo apico-basal polarization and develop adhesive junctions [10, 11]. A space can form between the apical surfaces of cells that face each other, as a result of repulsive forces, exocytosis of vesicles containing luminal components, or accumulation of fluid. Fluid leakage should then be prevented by junctional complexes between the cells that delineate the apical luminal space. Putting these notions in the context of biliary lumen formation, earlier work has shown that cholangiocytes develop apical poles when they start forming the ductal plate (Fig 1C). Polarization is initiated in single cholangiocytes and extends to adjacent cholangiocytes, likely via Notch and Neurofibromin 2 signaling. The cholangiocytes then coordinately and collectively contribute to delineate a lumen together with hepatoblasts [5, 8, 12]. Still, the driving forces allowing lumen formation remain unclear.

Computational models offer means to simulate a set of hypothesized mechanisms free from unknown influences and identify whether this set is either able or fails to explain experimental

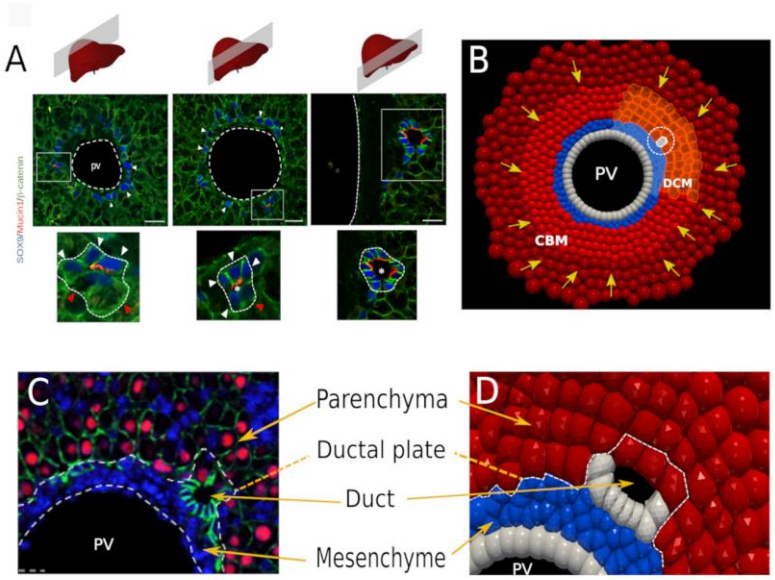

Fig 1. Experimental images and computational approach of bile duct lumen formation. (A) The bile ducts mature from the hilum (right panel) to the periphery of the liver lobes (left panel), as illustrated with sections made at several distances from the hilum in mouse embryonic day (E) 18.5 liver. Nascent lumina are identified with Mucin-1 staining. White arrowheads point to SOX9-expressing cholangiocytes; red arrowheads point to hepatoblasts delineating nascent lumina. Size bar is 20 μm. (B) Snapshot of the equivalent in silico model showing the CBM and DCM regions. The initial cholangiocyte is marked by a dashed circle. The yellow arrows indicate the background pressure forces. (C) Tissular organization of the developing liver. The portal vein (PV) is delineated by an endothelium and is surrounded by mesenchyme. Cholangiocytes form a discontinuous layer of cells called ductal plate. When lumina start to form they are delineated by cholangiocytes and Hepatocyte Nuclear Factor 4 (HNF4)-expressing hepatoblasts (red). Epithelial cells are identified by beta-catenin staining (green); DAPI stains nuclei (blue). The left panel illustrates a section through a mouse liver at E18.5; the right panel (D) shows the tissular architecture in a close-up of the in silico model.

https://doi.org/10.1371/journal.pcbi.1009653.g001

observations, which in the latter case indicates missing or false hypotheses. Over the past years, a class of computational models, called agent-based models (ABM), have been increasingly deployed to better understand the role of mechanics in tissue growth, regeneration and development. In ABMs of tissues, each cell is represented individually and is characterized by its behavior as well as by state changes. For example, a cell may be able to grow, divide, migrate, and undergo state changes, whereby the state might represent a cell type, activation state, etc. Cell dynamics and state are formalized by mathematical rules or equations. Parameters at the cell-level may be functions of intracellular molecular processes such as e.g. signaling events. ABMs have been explored in discrete and continuum space. In continuum space, a first large class of ABM are called center-based models (CBM), in which a cell shape is rigid and geometrically approximated by an object that represents a coarse-grained description of cell shape

only in a statistical sense by occupying a region in space where most of the cell volume is located [13–23]. A second class can be largely categorized as "deformable" models, e.g [24–38], in which cell shape is resolved explicitly, hence permitting a much more accurate representation of the interplay of cell shape and forces on the cell. The use of deformable models may be considered as mandatory in cases where cell shape is assumed to be a critical determinant, for example, driving or controlling local cell arrangements.

At the onset of biliary morphogenesis, very small lumina and a high variability in cell shapes are observed close to the formed lumina, meeting precisely the conditions to use a deformable model. For these reasons, we employed a high resolution model for the local arrangement of cells forming the lumen, and a CBM far from the lumen-forming region (Fig 1B). We called this model the "Deformable Cell Model" (DCM). The cell surface is flexible and its shape adapts naturally to the environmental constraints.

The DCM allows coupling to CBMs, because in both models spatial displacements are based on the calculation of physical forces or mechanisms that can be represented by a physical force, as e.g. compression forces emerging from cell proliferation in a tissue. The coupling permits simulation of tissue organization processes in a hybrid mode, where the CBM can represent cells for which a lower resolution is sufficient, while the DCM accounts for the regions where high resolution is required [37] (see S1 Text for more details).

We extended the recently established model [37], that can simulate growth and proliferation in monolayers, spheroids, and regeneration after drug-induced damage in a liver lobule, with the ability of a cell to acquire a polarity defining the polar direction, and distinguish an apical and basal side. Each cell may be subject to active cortical tension and apical constriction, and can form Tight junctions (TJ) with other cells. Finally, we allowed the inclusion of local osmotic effects that potentially arise in the lumen area (see Computational models).

In this work, we have included three different mechanisms that are hypothesized to contribute to lumen formation. We first investigated the individual effects of each of these mechanisms, namely: coordinated cell division, apical constriction and osmotic effects.

Our simulations showed that each of these mechanisms can create a lumen in an idealized system without boundary conditions. In a second stage, guided by the quantification of morphological features and expression of genes in developing bile ducts of embryonic mouse liver, we constructed an in silico system representing a portion of the lobule containing the portal vein and surrounding tissue (see Fig 1B and 1D).

Using this architecture we have simulated the effects of the aforementioned mechanisms both individually and combined. We found that contrary to the idealized system, a coordination of these mechanisms is necessary to initiate lumen formation and allow further lumen growth.

Materials and methods

Ethics statement

Mice received humane care and the research protocol was approved by the Animal Welfare Committee of the Universite Catholique de Louvain with number 2018/UCL/MD/014.

Animals

All mice (CD1 strain) were housed under a 12h light/12h dark cycle in individually ventilated cages supplied with RM3 chow (#801700, Tecnilab, Someren, Netherlands), acidified water and polyvinyl chloride play tunnels. Sox9-GFP mice have been described [39].

Cell isolation and RNA extraction

Pools of 15 livers from Sox9-GFP mice at E16.5 or E18.5 were dissected, minced and dissociated in DMEM-F12 (#31870–025, Gibco, Life technologies, Lederberg, Belgium) containing 1 mg/ml collagenase IV (#43E14253, Worthington, New Jersey, USA), 1 mg/ml dispase (#17105–041, Gibco, Life technologies) and 0.1 mg/ml of DNAse I (#11284932001, Roche, Mannheim, Germany) for 30 min at 37˚C. Digestion was stopped by adding an equal volume of 10% foetal bovine serum in phosphate buffered saline (PBS) and cells were resuspended in 2 mM EDTA, 0.5% bovine serum albumin in PBS and filtered on 40 μm cell strainer (#087711, Fisher Scientific, Merelbeke, Belgium). CD5+/CD45R+/CD11b+/7/4+/Ly-6G/C+/Ter119+ hematopoietic cells were eliminated by MACS separation using the "Lineage Cell depletion Kit" (#130090858, Miltenyi Biotech, Paris, France). Sox9-GFP+ cells were isolated by fluorescence-activated cell sorting (BD FACSAria III, sample and collection tubes maintained at 4˚C). Total RNA was isolated using RNAqueous Micro kit (#AM1931, Invitrogen, Carlsbad, CA, USA) according to manufacturer's protocol. RNA quality was evaluated using the Agilent RNA 6000 Pico Kit (Agilent Technologies, Santa Claa, CA, USA) and Bioanalyzer (Agilent Technologies) for measuring concentration and calculation of RNA integrity number (RIN).

RNA sequencing and bioinformatics workflow

Read quality control was performed using FastQC software v0.11.7 (Babraham Institute, Cambridge, UK). Low quality reads were trimmed and adapters were removed using Trimmomatic software v0.35 (RWTH Aachen University, Aachen, Germany). Reads were aligned using HISAT2 software v2.1.0 (Johns Hopkins University School of Medicine, Center for Computational Biology, Baltimore, MD, USA) on GRCm38 mouse genome. Gene counts were generated using HTSeq-count (v0.5.4p3) software and gencode.vM15.annotation.gtf annotation file and raw counts were further converted in transcripts per million (TPM).

Immunofluorescence and imaging

Immunofluorescence stainings were performed on 6 μm sections of formalin-fixed paraffin-embedded tissues. Tissue sections were deparaffinized 3x 3 min in xylene, 3 min in 99%, 95%, 70% and 30% ethanol and deionized H_2O. Antigen unmasking was performed by micro-wave heating for 10 min in 10 mM sodium citrate pH 6. Sections were permeabilized for 5 min in 0.3% Triton X-100 PBS solution before blocking for 45 min in 0.3% milk, 10% bovine serum albumin, 0.3% Triton X-100 in PBS. Primary and secondary antibodies were diluted in blocking solution and incubated respectively at 4˚C overnight and 37˚C for 1 h. Pictures for immunofluorescence were taken with Cell Observer Spinning Disk (Carl Zeiss, Oberkochen, Germany) and Zen blue software (Carl Zeiss). Primary and secondary antibodies are described in Table 1.

Computational models

Deformable cell model (DCM). In the DCM used throughout this work the 3D cell surface was discretized by a set of nodes which are connected by viscoelastic elements [27, 35, 37]. The nodes and their connecting elements generate a triangulation of the cell surface. The total force on each node sums up all forces on that node including mechanical forces within the cortex, external cell-cell contact interaction forces, nodal forces originating from volume conservation, as well as cell migration and osmotic effects. We note here that, although the model components are essentially 3D, all simulations are performed in a 2D slice of the bile ducts by constraining movement to the (x, y)-plane, which may be referred to as "2.5D".

Table 1. Antibodies used for immunostaining.

PRIMARY ANTIBODY	SPECIES	SOURCE	REFERENCE NUMBER	DILUTION
ZO-1	Rabbit	Invitrogen	61–7300	1/100
SOX9	Rabbit	Merck Millipore	AB5535	1/250
HNF4a	Mouse (IgG2a)	R&D Systems	PP-H1415–00	1/350
Ki67	Mouse (IgG1)	BD Biosciences	556003	1/250
Mucin-1	Armenian Hamster	Invitrogen	MA5–11202	1/350
β-catenin	Mouse (IgG1)	BD Biosciences	610153	1/1000
E-Cadherin	Mouse (IgG2a)	BD Biosciences	610181	1/200
SECONDARY ANTIBODY	**SPECIES**	**SOURCE**	**REFERENCE NUMBER**	**DILUTION**
Alexa Fluor 488 anti-rabbit	Donkey	Invitrogen	A21206	1/1000
Alexa Fluor 594 anti-rabbit	Donkey	Invitrogen	A21207	1/1000
Alexa Fluor 647 anti-mouse IgG2a	Goat	Invitrogen	A21241	1/1000
Alexa Fluor 488 anti-mouse IgG1	Goat	Invitrogen	A21121	1/1000
Alexa Fluor 594 anti-armenian hamster	Goat	Jackson ImmunoResearch	127–585–160	1/1000

https://doi.org/10.1371/journal.pcbi.1009653.t001

The dynamics of the cell is determined by an equation for each node according to Newton's second law, whereby inertia effects are negligible compared to friction forces. For any node i of a cell (the cell index has been dropped here for clarity) in which $\vec{v}_i$ denotes the velocity of node i (see Fig 2A), the equation reads:

$$\underbrace{\Gamma_{ns,i}\vec{v}_i}_{\text{substrate friction}} + \underbrace{\sum_j \Gamma_{nn,ij}(\vec{v}_i - \vec{v}_j)}_{\text{node-node friction}} = \underbrace{\sum_j \vec{F}_{e,ij}}_{\text{in-plane}} + \underbrace{\sum_m \vec{F}_{m,i}}_{\text{bending}} + \underbrace{\vec{F}_{vol,i}}_{\text{volume change}} + \underbrace{\vec{F}_{rep,i} + \vec{F}_{adh,i}}_{\text{contact}} + \underbrace{\vec{F}_{mig,i}}_{\text{migration}} + \underbrace{\vec{F}_{osm,i}}_{\text{osmosis}}. \quad (1)$$

The matrix Γ_{ns} is the cell-substrate viscous friction matrix and Γ_{nn} the node-node friction matrix originating from viscous effects inside the cell or between two cells. The first and the 2nd term on the rhs. represent the in-plane elastic forces and bending forces in the cortex, respectively, determined by the elastic parameters of the cortex. The third term on the rhs. is a volume force controlled by the cell cytoplasm compressibility and water in/outflow. The fourth term ($\vec{F}_{adh,i}$, $\vec{F}_{rep,i}$) describes the adhesion and repulsion forces on the local surface element in presence of nearby objects such as another cell. The adhesive forces are controlled by the specific adhesion energy parameter W which is determined by the cadherin density on the cell surface. The repulsive forces prevent that the surfaces of two different cells can interpenetrate. Both terms are calculated from the Maugis-Dugdale theory of adhesive bodies. We assume that cell migration can be present if cells are locally surrounded by ECM. A resulting force $\vec{F}_{mig}$, un-directed and mimicked by a Brownian motion term with zero mean and uncorrelated in time, is distributed equally on all nodes. The final term describes external pressure forces due to osmotic effects if these are present (for more details on the force terms, see S1 Text).

Cell division is mimicked by a process in which the mother cell is replaced by a pair of daughter cells which initially are both contained by the mother cell envelope (see Fig 2G), as described in S1 Text. The direction in which the cell divides can be chosen randomly (as is the

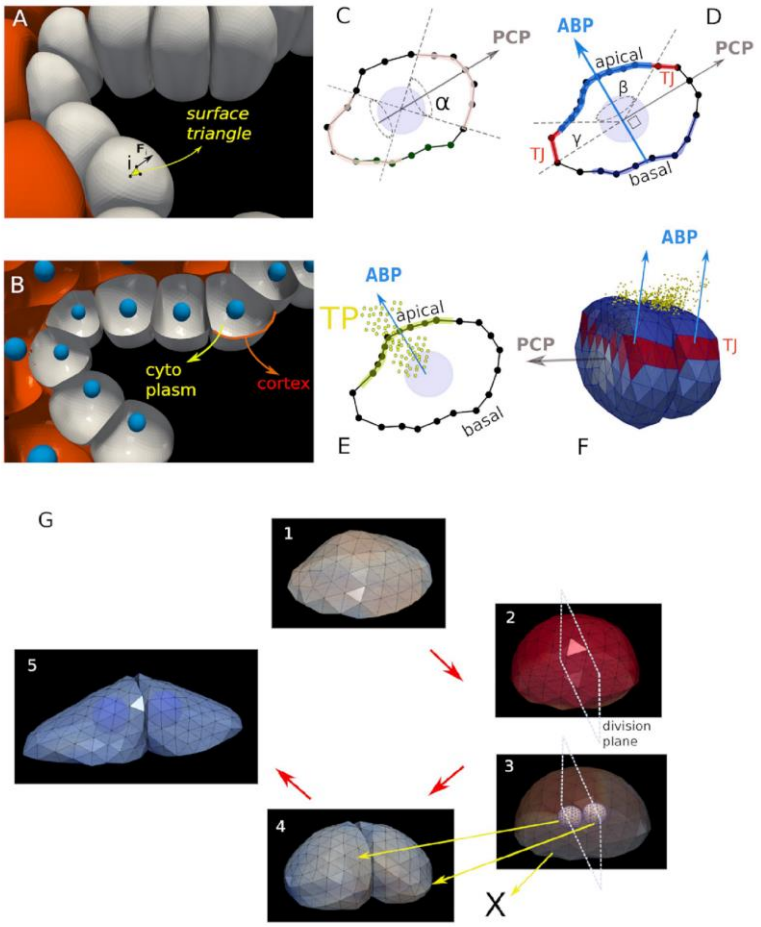

Fig 2. The DCM functional elements. (A) Cell surface element (triangle) with nodal force. (B) Horizontal cut section through the DCM model plane, indicating cytoplasm and cortex of the cells. C-E are cross sections through individual cells. C) 2D sketch defining the polarity vector (PCP) formed by the two cones with opening angle α. Note that the zone of polarity is assumed to be symmetric. (D) Definition of the Apical-Basal vector (ABP). (E) Tracer Particles (TP) moving across the apical surface of the cell. (F) Tight junctions between two cells in contact represented by red colored triangles. (G) Overview of the different stages for the DCM cell division algorithm, extended from [37] 1: A cell with arbitrary shape. 2: just

before cell division, the cell rounds up. A division plane is chosen. 3: Two new smaller spherical cells are created on both sides of the plane inside the mother envelope. Both daughter cells first grow artificially fast ("sub-simulation") within the boundaries of the mother envelope, to reach their target initial volume. 4: Shortly after, the mother envelope is removed. The cells adapt to their new environment. 5: Two new growing and adhering cells have been created (nuclei are shown).

https://doi.org/10.1371/journal.pcbi.1009653.g002

case for non polarized hepatocytes) or with a preferred direction. In the present case division perpendicular to the apico-basal axis is required to generate two daughter cells that maintain the epithelium single-layered and the division direction is along the polarization vector. As the DCM are parameterized by physical quantities, the range of its parameter values can mostly be readily estimated (see Table 2).

New extensions to the DCM. Three major new extensions were made to permit model simulations for virtual tests of the key hypotheses of early bile duct formation. Firstly, a polarity vector for each cell was introduced, indicating the Planar Cell Polarity (PCP), and an apical-basal vector, indicating the Apical-Basal Polarity (ABP), see e.g. [40]. The polarity vector can determine in which direction a cell divides (as opposed to random division directions). The ABP vector determines the area of cell apical constriction (AC) as the apicial region of the cell is defined relative to the ABP vector. Secondly, the model has been extended with the capability to form apical Tight Junctions (TJ) between cells. These are limited surface zones where

Table 2. Nominal physical parameter values for the model. An (*) denotes parameter variability meaning that the individual cell parameters are picked from a Gaussian distribution with ±10% on their mean value. CR: Calibration Runs. Unless indicated, the cell parameters for the CBM and DCM are identical. PC: Personal communication.

Parameter	symbol	unit	value	ref
Deformable Cell Model				
Radius Hepatoblasts	R_c	μm	8.8 – 12	observation, [45]
Radius Cholangiocytes	R_c	μm	8.8 – 12	observation, [45]
Radius Mesenchyme	R_c	μm	8.8 – 12	observation, [45]
Cycle time*	τ	h	24	[45]
Cortex Young's modulus	E_{cor}	Pa	1000	[46]
Cortex thickness	h_{cor}	nm	500	observation
Cortex Poisson ratio	ν_{cor}	-	0.5	[47]
Cell bulk modulus	K_V	Pa	750 – 2500	[45, 47]
Global cell-cell adhesion energy	W	J/m^2	$9 \cdot 10^{-4}$	[45],CR
Apical adhesion energy	W_{ap}	J/m^2	10^{-6}	CR
Nodal friction	γ_{int}	Ns/m^3	$1 \cdot 10^{-4}$	CR
Cell-cell friction	γ_{ext}	Ns/m^3	$5 \cdot 10^{10}$	[48, 49],CR
Cell-ECM friction	γ_{ECM}	Ns/m^3	10^8	[48],CR
Cell-liquid friction	γ_{liq}	Ns/m^3	500	CR
Motility	D	m^2/s	10^{-16}	[45, 50]
Center Based Model				
Young's modulus*	E	Pa	450	[45]
Poisson's modulus	ν	–	0.47	[45]
Motility	D	m^2/s	10^{-16}	[45, 50]
Lobule				
Radius portal vein	R_{pv}	μm	50	[45]
Pressure lumen ducts	P_L	Pa	0 – 100	CR
Pressure tissue	P_b	Pa	50	PC

https://doi.org/10.1371/journal.pcbi.1009653.t002

cells strongly attach to each other (see Fig 2F). Finally, to simulate osmotic effects in the extracellular space, the concept of "Tracer Particles" (TP) has been introduced to mimic osmotic effects caused by local differences in salt concentration. For the technical aspects of the implementation we refer to S1 Text.

The polarity vector bound to each cell can define zones of the cell surface, which are more adhesive or less adhesive (e.g. by zones with different cadherin density). Here these zones are assumed to be formed by cones centralized in the cell and aligned by the polar vector (Fig 2C). The polar surface zone on the cell is assumed to be symmetrical along both cone sides, and the angle of the cone determines the surface area (as in [13, 41]).

The ABP vector can mark a bi-conical region where later apical constriction can occur. To mimic the constriction effect which is driven by actin-myosin contractions and whereby the apical side of the cell surface contracts, the equilibrium distance between nodes are reduced to a shorter distance. As a consequence the nodes will move towards each other until a new mechanical equilibrium is reached. A distinction can be made in the model for "circumferential" constriction (ring-like zone where the cytoskeleton contracts) and "medioapical" constriction where the contraction is situated in the apical domain [42] (see S1 Text). On the opposite basal side, the cell surface remains as before, see cartoon Fig 2D. An internal structure was not needed to capture the key physics of the constriction process but could be added to the model, at the expense of more parameters (the explicit representation of the internal cytoskeleton would require the remodeling of the cytoskeleton rorganisation during apical constriction). and computational time. As the cortex is contracted on the apical side, the nodes smoothly move from the basal side to the apical side.

Tight junctions (TJ) are the areas at cell-cell contacts that have a much higher adhesion energy than the regular adhesive zones. The TJ regions were defined relative to the APB vector and by the width of the region. The TJ is represented in the model as a conical region (belt) with a certain width controlled by an angle γ (see Fig 2D). The "belt" is part of the cell's lateral surface and separates the apical region and the basal region.

Tracer Particles (TP) are discrete particles representing clouds of molecules that can be secreted by a cell (Fig 2E). The TP can diffuse into the extracellular space without interacting with each other. They can mark a part of the surface of a cell if they come in contact with free surface area of that cell. Once a part the DCM has been marked, it can become unmarked if it comes again in contact with a part from another cell (e.g. through adhesion). If the TP represent salt ions, we use these marks to define the regions in the extracellular space where a net osmotic pressure on the cell surface is generated due to water attraction. Conceptually similar, TP could also represent signaling molecules that are sensed by nearby cells. However, since bile starts to flow around E16.5-E17.5, i.e. slightly later than the initiation of bile duct lumen formation (E15.5) [7], TP's cannot correspond to bile at the onset of lumen formation. We assume in our model that tracer particles are excreted on the apical side of the cell.

Center based model (CBM). The high spatial accuracy of the DCM causes longer computation times, which can limit the use of that model for large cell populations. In CBMs the individual cell shape is not represented explicitly, simplifying and approximating the results, but significantly reducing the computational time. As for the DCM, the CBM is able to mimic active migration, growth and division, and interaction with other cells or a medium. The CBM is here used to model the parts of the system that do not require knowledge of the precise cell shape. Nevertheless the CBM needs to fulfill its role as a component with a realistic behavior and, if replaced by a DCM, should not lead to different simulation results. We here use the CBM to model the boundary of the portal vein (PV), which we assume to not move during the time course of the simulation, and the hepatoblasts that do not participate in bile duct formation, but exert a certain mechanical force to the inner cells closer to the PV (Fig 1C).

As for the DCM, the movement of cells in the CBM is described by Newton's law of motion. Different from the DCM, where all forces on a large set of nodes characterizing cell shape has been considered, in the CBM only forces on the center of mass of the cell is taken into account. The center of mass position of each cell i is obtained from a Langevin equation of motion, which summarizes all forces on that cell including a force term mimicking its micro-motility:

$$\Gamma_{ECM}\vec{v}_i + \sum_j \Gamma_{cc}(\vec{v}_i - \vec{v}_j) = \sum_j \vec{F}_{cc,ij} + \vec{F}_{mig,i} \quad (2)$$

The lhs. describes cell-matrix friction, cell-capsule friction and cell-cell friction, respectively. Accordingly, Γ_{ECM} and Γ_{cc} denote the friction tensors for cell-ECM and cell-cell friction. The first term on the rhs. of the equation of motion represents the cell-cell repulsive and adhesive forces $\vec{F}_{cc}$, which can be approximated by the Johnson-Kendall-Robert (JKR) model, approximating cells by isotropic homogeneous sticky elastic bodies that are moderately deformed if pressed against each other [43]. It is well-known that the original JKR contact model becomes inaccurate in systems with large cell densities, where it underestimates the contact forces and becomes inconsistent with the forces in the DCM [44]. Here, a modification of the JKR contact force model was calibrated with DCM using the calibration procedure. As a consequence, as long as cell shape does not largely deviate from a sphere, CBM and DCM generate statistically equivalent simulation results and can be used in a hybrid model by switching between them if necessary (see ref. [37] and S1 Text for details). The 2nd term is an active force term $\vec{F}_{mig}$, mimicking the cell micro-motility. Similar to the DCM the $\vec{F}_{mig}$ is mimicked by a Brownian motion term with zero mean value and uncorrelated in time.

Results

Morphological features of cells during biliary lumenogenesis

First, we present the experimental observations that support alternative hypotheses on the mechanisms controlling early lumen formation during duct development. In a second step, the three different hypotheses are tested.

At the onset of biliary lumen formation, cholangiocytes are located adjacent to the peripportal mesenchyme, which separates the cholangiocytes from the endothelial cells lining the portal vein. The parenchyma is predominantly composed of beta-catenin-positive hepatoblasts, hematopoietic cells and vascular spaces (Fig 1A) [51]. Beta-catenin is here used as an epithelial marker.

Lumen formation was shown to be initiated at single cholangiocytes expressing Na+/H+ exchanger regulatory factor 1 (NHERF1) and Moesin at their apical pole [8]. Fig 1A extends this information by illustrating the expression of Mucin1 (MUC1), a cell surface glycoprotein, at the apical pole of cholangiocytes. Initially, a single cholangiocyte, identified by expression of the biliary marker SRY-related HMG box transcription factor 9 (SOX9) expresses Mucin-1 (MUC1). The expression of MUC1 then spreads to adjacent cholangiocytes, in parallel with expansion of the lumen and differentiation of hepatoblasts into cholangiocytes. The various steps of lumen formation are shown in Fig 1A at embryonic day (E) 18.5 within the same liver. This is made possible because duct formation progresses from the liver hilum to the periphery of the lobes, with more mature structures being located near the hilum and less mature structures more peripheral in the liver.

Lumen formation is associated with apico-basal polarization of the cholangiocytes. This is well illustrated by expression of NHERF1, Moesin, MUC1 and osteopontin, all at the apical pole of the cholangiocytes (refs. [5, 8] and Fig 1A). Further, when determining the presence of

tight junctions between cells delineating a developing lumen, the tight junction marker Zonula Occludens 1 (ZO1) was detectable at the junction between adjacent cholangiocytes and between a cholangiocyte and a hepatoblast in asymmetrical ductal structures (Fig 3A). In contrast, adjacent hepatoblasts delineating a developing duct lumen do not yet express detectable ZO1 near the biliary lumen, indicating that tight junction formation parallels maturation of the hepatoblasts to cholangiocytes.

Hypothesis I: Differential proliferation rates. Since the portal vein is surrounded by a double layer consisting of an inner cholangiocyte and an outer hepatoblast cell layer, differential proliferation rates within the two distinct layers may create buckling forces large enough to rupture the contacts between the two layers leading to generation of a lumen. Therefore, we measured the percentage of proliferating cholangiocytes and hepatoblasts. Using SOX9/Ki67 and HNF4/Ki67 co-stainings we found that 26.0% of SOX9-positive cholangiocytes and 10.7% of HNF4-positive hepatoblasts were proliferating at E16.5 (Fig 3B) (n = 3 livers; 630 cholangiocytes and 549 hepatoblasts were analyzed). The first hypothesis studied below by the computational model is that this difference may be responsible for lumen formation.

Hypothesis II: Apical constriction. Formation of a lumen in a cylindrical duct implies that the apical pole of the cells aligning the lumen is (geometrically) shorter than the opposite basal pole. We verified that this was the case. We measured the length of the apical and basal poles of cells involved in the formation of asymmetrical ductal structures (Fig 3C). Apical shortening was obvious in cholangiocytes, despite significant cell-to-cell variability. The heterogeneous morphology and circumferential expression of E-cadherin in hepatoblasts did not allow us to delineate the apical and basal sides or measure the length of the poles. However, plotting the length of the apical sides as a function of the length of the basal sides in cholangiocytes showed that all cells display apical constriction, the ratio of basal/apical length being > 1. Therefore, apical constriction whereby the apical shortening is driven by an active constriction of the apical side of the cholangiocytes, would be a candidate mechanism for the lumen formation.

Hypothesis III: Osmosis-driven lumen formation. The accumulation of fluid may be a potential driving force for lumenogenesis. Such accumulation of fluid is expected to result from osmotic changes and water transport, which depend on ion transporters and water channels. To verify if ion transporters and aquaporins were expressed at the onset of lumenogenesis, we purified the cholangiocytes at E16.5 and E18.5. Embryonic livers from SOX9-GFP embryos were dissociated; hematopoietic cells were removed by magnetic cell sorting, and GFP+ cells were FACS-purified. Total RNA was extracted and subjected to RNA sequencing. Expression of apical Aquaporins 1 and 8, Multidrug resistance 1 P-glycoprotein (Abcb1/Mdr1), Na+-independent Cl−/HCO3− exchanger (Slc4a2/Ae2), Cystic fibrosis transmembrane regulator (Cftr) and Na+/HCO3− cotransporter (Slc4a4/Nbc1) was measured. Their expression by cholangiocytes is required for fluid secretion [52, 53] and was detected at E16.5 and E18.5. This indicates that regulators of ion and water transport were present when bile starts to flow (E17.5-E18.5) [7] and even earlier (E16.5) at the onset of lumenogenesis (Fig 4). Hence osmosis is another candidate for lumen formation. In intrahepatic bile ducts, regulated and inducible water influx creates unidirectional advection.

In summary, we identified three candidate mechanisms possibly driving bile duct formation, each of them being compatible with experimental observations: (1) Differential proliferation rates within the cholangiocyte and hepatoblast cell layer within the double layer aligning the portal vein. (2) Apical constriction in at least one of the two cell layers. (3) Secretion of water by osmosis if the salt concentration at the two-layer interface is locally elevated, and fluid leakage is restricted by tight junctions. However, the double layer is constrained on the side of the cholangiocyte layer by mesenchyme enclosing the lumen of the portal vein and on

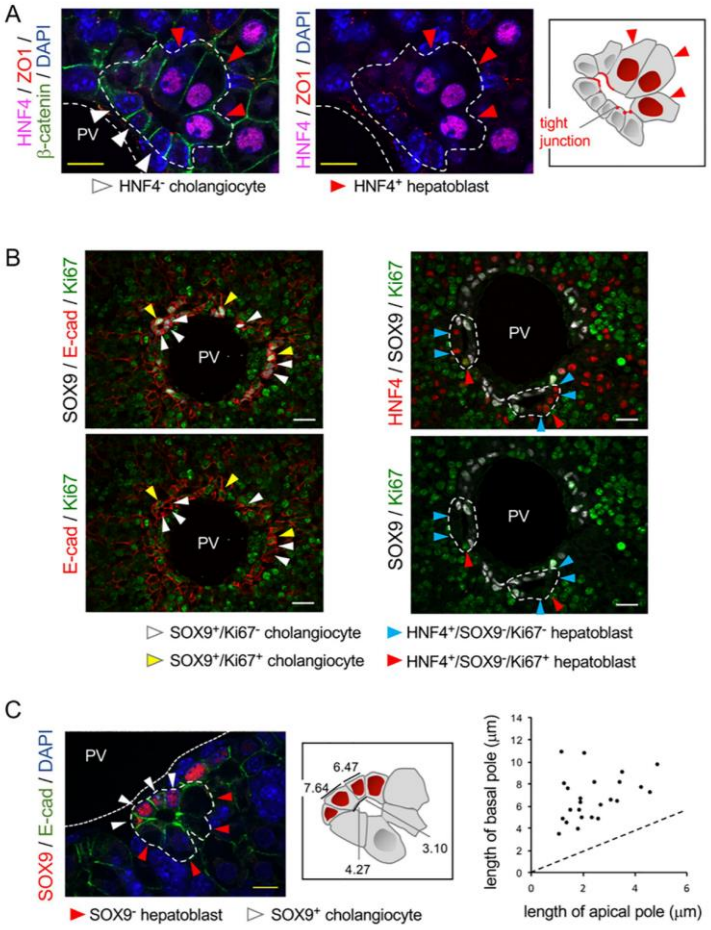

Fig 3. Morphological features of cells delineating developing biliary lumen. (A) Tight junctions are detected between HNF4- cholangiocytes and between cholangiocytes and HNF4+ hepatoblasts; but not between adjacent hepatoblasts. (B) Proliferating SOX9+ cholangiocytes and HNF4+ hepatoblasts are detected by Ki67-staining in E16.5 embryonic livers. E-cad: E-cadherin. (C) Apical constriction in cholangiocytes. Developing ducts are delineated by white dotted lines. White size bar, 20 micrometer; yellow size bar 10 micrometer. PV: portal vein.

https://doi.org/10.1371/journal.pcbi.1009653.g003

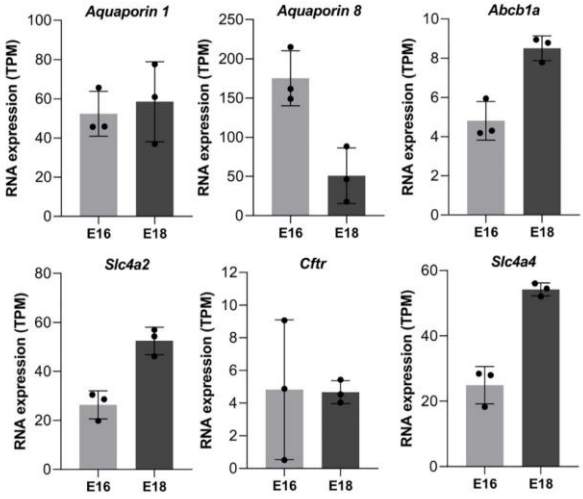

Fig 4. Expression of ion transporters and water channels during biliary lumenogenesis. Expression of ion transporters and aquaporins was measured by RNA sequencing of total RNA extracted from purified developing cholangiocytes. Bars are standard deviation (SD).

https://doi.org/10.1371/journal.pcbi.1009653.g004

the side of the hepatoblast layer by a largely unstructured mass of proliferating hepatoblasts, blood vessels and hematopoietic cells that may exert mechanical compressive stress on the double layer and hence counteract lumen formation. The balance of arising forces, proliferating forces, bending forces, deformation and contraction forces, is impossible to estimate by reasoning alone. Hence we implemented a representative tissue section within a computational ABM and simulated each of the three hypothesized mechanisms to explore whether any of the three hypotheses would have to be excluded based on physical interactions. This is possible as the computational model is parameterized by measurable parameters, for which the ranges are largely known.

In a next step we tested whether each of the three candidate mechanisms is able to generate a lumen in an idealized layer before embedding the bi-layer into its natural environment during bile duct formation.

Computational model: Each mechanism is able to generate a lumen in an isolated double layer

To illustrate the effect of differential proliferation, apical constriction and osmotic forces, we first considered a minimal, idealized subsystem of two layers of each 10 cells which adhere to each other (Fig 5). The model assumes translational symmetry in the direction perpendicular to the represented cut section, as this is the case over several cell diameters in the experiments

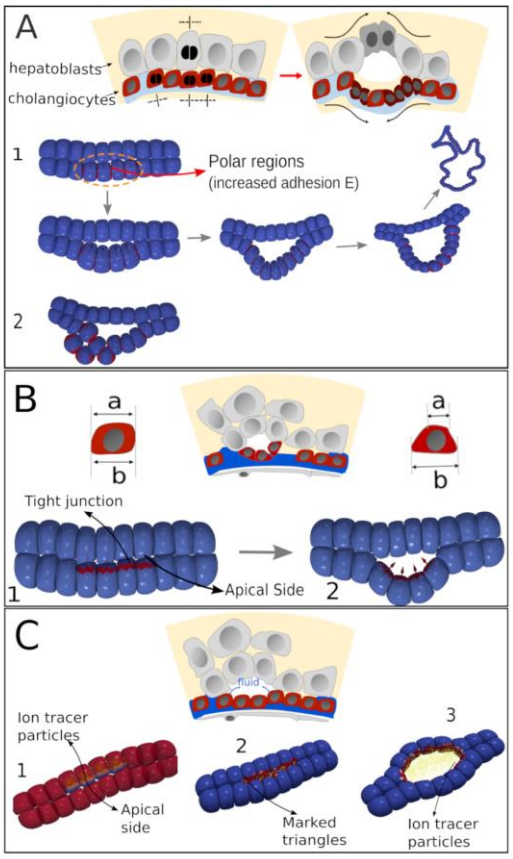

Fig 5. Possible mechanisms of lumen formation in a cell bi-layer. (A) Cell division. 1: double layer of cells with 4 dividing cells (indicated by orange dashed line). Cell division goes along PCP. 2: random directed cell division. (B) Apical constriction on the same 4 cells. Note the wedge-like shape of the four center cells with apical membrane marked in red in configuration 2 compared to configuration 1. (C) Osmosis initiated by 4 cells inducing hydrostatic pressure in extracellular space.

https://doi.org/10.1371/journal.pcbi.1009653.g005

in Fig 1A. The system is assumed to be embedded in a fluid medium without external resistance from other cells or ECM. Simulations with this system can help us to understand the effects of these mechanisms in the absence of effects from surrounding cells.

Mechanism I: Creation of a lumen by pure cell division. Cell proliferation can introduce a buckling instability in epithelial sheets and formation of cavities (see e.g. [41, 54]). We illustrate this with a simulation of our reduced system. Four cells in the upper layer are selected as proliferating. All other cells remain quiescent. Furthermore, only these 4 cells are assumed to be polarized. The polarization direction is here uniquely determined by the mutual adhesive contact regions between the cells (identified by triangles of the cell surface) between a cell-cell contact of the same type (red marks in Fig 5A) [55]. Thus, for each of these cells the polarization vector is initially parallel to the layer, but can change and is updated along with the relative positions of the cells. In addition, an apical side and basal side are introduced (determined by an apical vector, which is perpendicular to the polar vector). The apical side is oriented towards the other cell layer, while the basal side is oriented outwards. Two cases are now distinguished: (i) When cell division occurs, the division direction is always along the polar vector (Fig 5A). Moreover, the polar contact area is assumed to be populated with a higher intercellular density of molecular complexes forming tight junctions and thus higher in adhesion energy, compared to the average cell adhesion energy. In contrast, the apical side area has almost no cadherins. (ii) The cells are still assumed to be polarized, having still an inhomogenous distribution of adhesion contacts, but this polarization has no effect on the orientation of proliferation, which is here chosen from a random uniform distribution (Fig 5A).

For both cases we assume that only the lower cells can proliferate without any restriction (division time 24h). For case (i) the formation of a convexly shaped lumen after a few cell divisions occurs (Fig 5A and S1 Video). The convex shape of the lumen is conserved even after several cell divisions but eventually, new buckling effects will arise. In contrast, case (ii) does not result in a clear single lumen formation, as cells basically move in random directions due to the proliferation, thereby filling up any previously formed cavity (see Fig 5A and S2 Video). This shows the importance of both cell polarity and polar division in lumen creation, consistent with the findings in ref. [56].

Mechanism II: Creation of a lumen by apical constriction. During apical constriction, the surface area of the apical side shrinks due to a local contractile effect of the cortical cytoskeleton. When this effect takes place on several adhering cells simultaneously, a new mechanical equilibrium emerges, driving the layer to bend outwards. Apical constriction has been modeled using vertex models showing that it can significantly contribute to tissue distortion [57–59], and by center-based models to explain gastrulation in sea urchin [41]. Here, we further assume that along with apical constriction, Tight Junctions (TJ) are also present. TJ involve adherent junctions which are usually localized at the apico-lateral borders of epithelial cells [60].

In the minimal system, first the apical vectors of the four upper cells are defined. These point towards the underlying cell layer (red arrows in Fig 5B). The apical vectors define the cone of the apical region in those cells (Fig 5B, dark blue regions). These regions have by default a much smaller adhesion energy (W_{ap}) than the rest of the cell surface. On the contrary, the tight junction regions (red triangles in Fig 5B) have a higher adhesion energy. From the moment at which a strong constriction is applied in the apical region a small cavity is forming. No cell division is involved. We note here that when packed in a sheet, such as occurs with the four central cells, the DCM simulations show slightly wedge-like cell shapes (see Fig 5B and S3 Video) as often depicted in textbooks. Altogether, these simulations show that apical constriction of cells can indeed create a small initial cavity.

Mechanism III: Creation of a lumen by osmotic effects induced by ions. As previously explained, regulators of ion and water transport could be identified on the apical side of cholangiocytes at the onset of lumenogenesis. This machinery enables to generate differences in the mole fraction of solutes between a cell and extracellular cavities, which could for example have been formed by vesicle exocytosis. This could result in osmotic pressure-driven water flow, until the hydrostatic and osmotic pressures in the cavity and outside are balanced [61, 62]. The excretion of ions and their diffusion is mimicked in the computational model by tracer particles (TP). In the simulation we assume that the four cells are now able to secrete ions (TPs) through a specific region of the cell area (Fig 5C). In agreement with the experiments the "permeable" region is the apical side of the cells, which in turn is determined by the cell's APB vector. As in the previous case, this vector points towards the other cell layer. Right after the simulation has started the tracer particles are created in the cell center and diffuse inside the cell. They gradually move towards the cell boundary and can, mediated by ion channels and transporters, cross the cell membrane on the apical side where there is free extracellular space, contributing to an increased osmotic pressure. (Fig 5C, right). Generally, the osmotic pressure difference -for simplicity assumed here to be constant- triggers water inflow into the initially present small extracellular cavities. The inflowing water exerts a hydrostatic pressure on the cell walls delineating the cavity (marked by red triangles in Fig 5C, middle) and pushes them away, hence increasing the cavity volume. Whether cells from the one layer will be separated from those of the other layer, will depend on the competition between the pressure forces and the surface adhesion forces between the cells. In Fig 5C, right the simulation case is shown where the cell-cell adhesion energy between the two cell layers at the apical side is relatively small compared to the osmotic energy. As a consequence, the cell layer separates from the other layer and a cavity is formed that keeps on growing (see also S4 Video). When the osmotic pressure is finally equilibrated with the tensile adhesive stress between the cells, the lumen stops growing. However, if the osmotic forces were too large, the lumen would eventually burst. Here the presence of tight junctions between the cells helps prevent bursting as they reinforce the cell-cell adhesion and provide a larger mechanical resistance to osmotic forces. Moreover, the tight junctions prevent ions from moving through the cell-cell boundary regions thereby hindering leakage out of the formed cavity. The latter phenomenon can only be modeled approximately at the chosen DCM resolution but by adopting a higher resolution, this would become possible, see section Discussion and conclusions.

Model: Simulation of lumen formation in bile duct system

In the previous section it has been shown by computational modeling that initial lumen formation can independently be induced by each of the three different hypothesized mechanisms in an idealized system, with no external constraints, to a "minimal" configuration of cells. In the next step we examined whether these mechanisms are able to cause lumen formation if surrounded by tissue, which is the situation during bile duct development in the developing embryo. In addition, since hepatoblasts lining the emerging lumen are gradually replaced by cholangiocytes, the combined effects of "non-mechanical" cues, such as the experimentally observed cell cycle progression and cell signalling, have to be taken into account. Our modeling strategy is to identify the minimal set of mechanisms that are able to cause lumen formation, starting from the time point where no lumen is present (few or no cholangiocytes) until a full lumen completely surrounded by cholangiocytes has been established (see Fig 1).

Configuration of the in-silico embryonic liver system. Bile duct formation is guided by a complex interplay of cell signaling and cell mechanics, resulting in initial lumen formation, the formation of tubular branches, and possibly merging of those branches [3]. Simulating this

entire development would require a full 3D simulation demanding large computational power and additional three-dimensional experimental data. Here the focus is on the initial stage of formation of a single bile duct. Because of the translational symmetry along the portal vein, this can be mimicked by simulation of the tissue organisation dynamics in a 2D section of the portal vein area chosen such that the forming lumen lies in the simulated section. In the simulations this is obtained by constraining the cell motion within a plane created by a transversal cut of the portal vein, noticing that the bile ducts develop parallel to the portal vein. This chosen model configuration is representative of the configuration in the experimental images.

To cope with the higher computation time of the DCM, a hybrid model of DCM and CBM has been constructed in which the DCM and CBM cells interact in a mechanically consistent way [37]. The cells initially are labeled as either being endothelial cells, hepatoblasts (and hematopoietic cells), or mesenchymal cells. The mesenchyme and the hepatoblasts in the active segment localized closest to the mesenchyme are represented by a DCM, the hepatoblasts further away from the portal vein are represented by a CBM. The latter cells are assumed to not directly participate in bile duct formation. This turned out to be a self-consistent assumption in that during the simulations no re-arrangements of cells occurred that resulted in direct interactions of CBM cells and DCM cells lining the emerging lumina. The portal vein endothelial cells are represented by CBM cells fixed in space. This is justified as blood flow through the portal vein, which is evidenced on histological sections by the presence of red blood cells [51], would have a similar stabilizing effect. The limited amount of ECM present in intercellular space was not explicitly modeled. However, as in ref. [37], ECM-cell friction has been considered at those surface regions of each cell that are not in direct contact with other cells.

In the experimental images the cholangiocytes appear to be significantly smaller than the surrounding hepatoblasts. Their cell surface ratios (extrapolated from the circumference) varied by up to a factor of 2 to 4 (see Fig 6). The size difference of hepatoblasts to cholangiocytes may be attributed to three main causes: (i) cholangiocytes are likely responsible for excreting salts into the luminal space through the apical side, thereby attracting water. This water

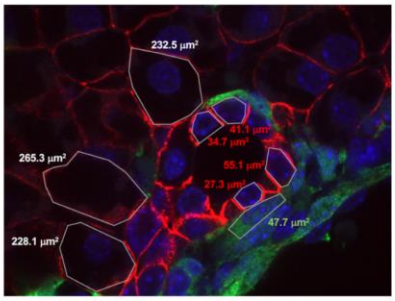

Fig 6. Detail image of the lumen with indicated cell surface areas. White numbering: hepatoblasts, red numbering: cholangiocytes, green numbering: mesenchyme. The picture is from an E18.5 mouse liver expressing eYFP in the mesenchyme. Red membrane staining of hepatoblasts and cholangiocytes: E-cadherin; green staining of mesenchyme: eYFP.

https://doi.org/10.1371/journal.pcbi.1009653.g006

content may be partially withdrawn from the cholangiocytes themselves (i-a). On the other hand, aquaporins are also present on the basal side (i-b). The cholangiocytes seem thus to act as a "pump", withdrawing water from regions further away from the bile duct. (ii) Cholangiocytes being neighbors to hepatoblasts may instantly look smaller because they are likely the differentiated daughter cells of a former hepatoblast. Indeed, it was observed that some hepatoblasts adjacent to a cholangiocyte still have a large size but start expressing some cholangiocyte-specific proteins (SOX9+). Upon cell division, they may become cholangiocytes expressing high levels of SOX9+. Hence, we may also assume that cholangiocytes induce active hepatoblast-to- cholangiocyte transformation. (iii) The volume of a mature cholangiocyte is inherently smaller than that of a hepatoblast. This also means that after a hepatoblast divides, the two daughter cholangiocytes have a volume that is relatively large compared to a mature cholangiocyte. As a consequence, the criterion for cell division, i.e. doubling of the initial volume, will be reached relatively quickly and a new cell division will take place shortly after the first cell division. This results in cholangiocytes which are significantly smaller than the original hepatoblasts.

The hypotheses i-b), ii) and iii) have been adopted in our model. However, it is not excluded that hypothesis i-a) is also valid, solely or in combination with i-b). The former could be tested in more depth by adding an extra equation for the change in cell reference volume that describes how much water a cholangiocyte loses during and after its differentiation. However, in the scope of this paper this option has not been considered. Because of hypothesis iii), an initially fast appearance of several new cholangiocytes may occur (Fig 1A). This seems to be in agreement with the experimentally observed configuration (Fig 3A), where four adjacent cholangiocytes in a row are observed, while the other (bigger) cells are still merely hepatoblast.

The cells are initially configured as shown in Fig 1C. The initial size of all the cells is randomly sampled from a Gaussian distribution with average size $d_{mes} = 10\ \mu m \pm 10\%$ for the mesenchymal cells, $d_{hep} = 15\ \mu m \pm 10\%$ for the hepatoblasts. In order to mimic the movement constraints in the tissue model, we have applied a Boundary Conditions (BC) on the outer circumferential side. The tissue is allowed to expand due to cell growth, yet a constant "background" pressure P_b is exerted on to the outer hepatoblasts in radial directions towards the portal vein, mimicking the mechanical resistance of the surrounding tissue (see Fig 1B). The reference value was set to $P_b = 50$ Pa (personal communication with Adrian Ranga, KULeuven, Belgium), which is of the same order of magnitude as the elastic modulus of liver matrix [63]. On the inner boundary, the fixed endothelial cells (CBM) prevent cells from moving toward the portal vein. More details and technical aspects about the BC are given in the Appendix. An animation of the system can be viewed in S5 Video

The simulations start with the assumption that a lumen originates from a single hepatoblast located in the middle of a segment (Fig 1). At a certain point in time, a differentiation of this hepatoblast into a cholangiocyte is induced, likely mediated by contacts between portal vein-associated mesenchymal cells and adjacent hepatoblasts. The new cholangiocyte undergoes cell cycle progression. The initial size of the cholangiocyte is set to 0.75 times the size of a hepatoblast. The cholangiocyte is assumed to have acquired an apical direction pointing away from the portal vein centre and hence a polar direction perpendicular to the apical direction [40]. After some time, the cholangiocyte divides, creating two daughter cells. These two adherent daughter cholangiocytes are initially proliferating and also become immediately polarized with the same polarity as the mother cell.

We recall that about 20% of the cholangiocytes nearest to the portal vein are proliferating (Ki67+ staining) between E16.5 and E18.5. This is in contrast with the hepatoblasts of which only 11% proliferate. Similar behavior was observed in ref. [64]. As information about the

exact mechanisms maintaining these proliferation rates was lacking, an algorithm was implemented enforcing the experimentally observed rates.

The algorithm keeps track of the number of proliferating cells for each cell type, and randomly picks cells that become quiescent if the observed number of proliferation in the simulation exceeds the experimentally observed number (see S1 Text).

Simulation of hypotheses. In this section we present the results of simulations applied to the hypotheses introduced above in the context of a developing embryonic liver (section Computational model: Each mechanism is able to generate a lumen in an isolated double layer). The complexity of the model is increased stepwise, and the simulated lumen shapes and sizes are compared to the experimentally observed ones. All simulations ran for 24 hours after the time point at which the first cholangiocyte appeared. This initial cholangiocyte gets polarized. The basal membrane of the cholangiocyte is oriented towards the mesenchyme (Fig 1A), while the apical vector points away from the PV centre, and the polar vector is aligned with the PV tangent. This can be induced by laminins present in the ECM surrounding the portal vein [65]. The division orientation is thus tangential to the PV, as depicted in (Fig 7A). Notch-like signaling from cholangiocytes to adjacent hepatoblasts is possible, meaning that a hepatoblast can differentiate into a cholangiocyte provided that hepatoblasts are in contact with each other, and that the hepatoblast contacts a free extracellular space (here the duct lumen). The cholangiocyte will try to orient its apical vector to the free extracellular space. The signaling is controlled by a single time parameter T_N. We assume that $T_N > 0$ as otherwise the hepatoblasts transform immediately to cholangiocytes, which would be in contrast with the gradual expression of SOX9 observed in Fig 3C (left panel). Here, we postulate that $T_N = 2h$. However, the effect of T_N will be further studied below. For each model and parameter set, 5 simulations were run, each representing a different realization of a stochastic process. The average of these runs were used as comparison.

The models discussed hereafter add one or several components to the reference scenario defined as "Model 0" (see Table 3), where the initial daughter cholangiocytes proliferate further in random directions. In model 0, apical constriction and osmotic effects are absent. The results of the simulation with model 0 show a growth in which few hepatoblasts develop to cholangiocytes, without any cavity formation and lumen growth (snapshot in Fig 7B).

Model 1. In model 1 the cholangiocytes become polarized and the division is oriented along the PCP vector (Fig 2E). Both cholangiocyte daughter cells inherit the polarization direction of the mother cell right after cell division. The results with model 1 show the creation of a small cavity, but without clear and stable lumen growth over time (Fig 7C and 7D) as the cavity surface remains smaller than the cross sectional surface of one cell. This is in contrast to the findings of mechanism I (section Model: Testing of three basic mechanisms). The difference can be attributed to the fact that in model 1 the surrounding cells are exerting a pressure preventing further growth of the cavity.

Model 2. We extend model 1 with the capacity of the cholangiocytes to perform constriction of the apical side. This involves a ring-like zone of strong constriction with the tight junctions, and a weaker constriction of the apical domain (see S1 Text for details). All other mechanisms are the same as in model 1. Compared to the runs of Model 1, we find an initial stronger signal for cavity area, due to the retraction of the apical domain caused by the mechanical forces of apical constriction. However, this signal is not maintained as it weakens after $t = 12h$ and becomes similar to Model 1 after 24h, see Fig 7C. The reason is that despite the shape formation, the increasing compression due to cell division in combination with the pressure exerted by the surrounding tissue does not allow formation of a stable cavity.

Model 3. Model 3 adopts all the characteristics of model 2 and extends the capacity of the cholangiocytes to excrete molecules in the extracellular space inducing an osmotic activity (Fig

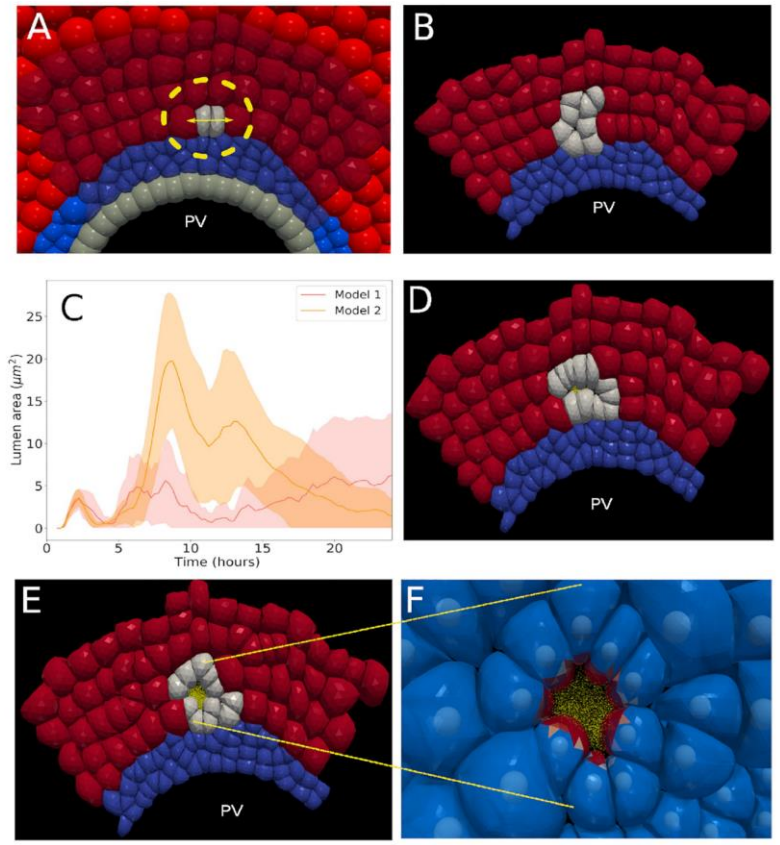

Fig 7. Simulation results for Models 1 and 2. (A) Immediately after the initial state, where a cholangiocyte divides in two daughter cells. The division direction is indicated by the arrow. (B) Snapshot of a simulation for Model 0 ($t = 12$). (C) Lumen area versus time for models 1 and 2, for different runs (no osmotic effects present). The solid lines are the average of 5 stochastic realizations of the same parameter set, while the shadowed regions indicate the two times standard deviation interval of these realizations. (D) Snapshot of a simulation for Model 1 ($t = 12$). (E) Snapshot of a simulation for Model 2 ($t = 12$). The red, grey and blue cells indicate hepatocytes, cholangiocytes and the mesenchyme respectively. (F) simulation snapshots for model 2 showing TP's (yellow) and apical sites of the cholangiocytes (red).

https://doi.org/10.1371/journal.pcbi.1009653.g007

Table 3. Models and the feature they represent.

Model	Cell division dir.	apical constriction	Osmotic effects
Model 0	random	no	no
Model 1	oriented	no	no
Model 2	oriented	yes	no
Model 3	oriented	yes	yes

https://doi.org/10.1371/journal.pcbi.1009653.t003

8). Expression of ion and water transporters was measured to study possible evidence in favor of the hypothesis that osmotic pressure could be generated at this stage. However, as we have no exact information about the osmotic pressure nor about the osmotic activity over time, we simulate different scenarios with varying pressure, assuming that this pressure remains approximately constant over the considered time period. As shown in Fig 8A and 8C, this hypothesis has a significant impact on the results. For a osmotic pressure $P_L = 25Pa$, lower than the tissue background pressure $P_b = 50Pa$, the lumen size does not become significantly

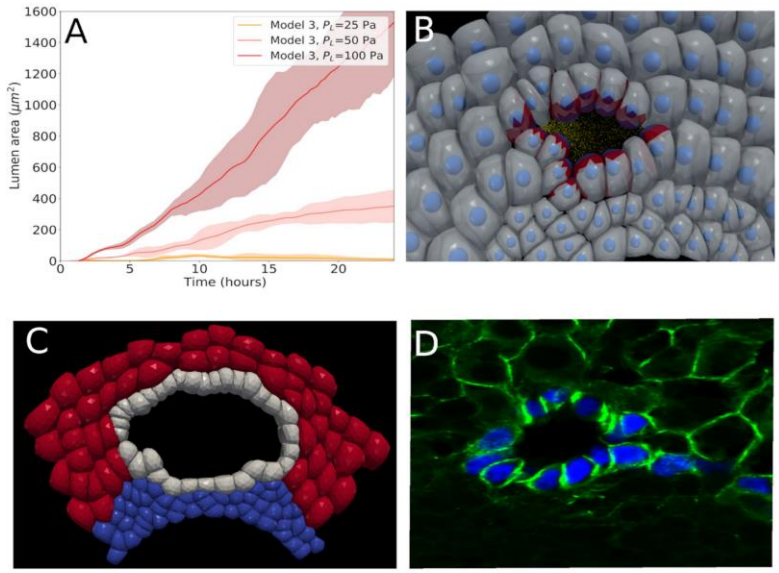

Fig 8. Simulation results for Model 3. (A) lumen area versus time for different osmotic pressures. The solid lines are the average of 5 stochastic realizations of the same parameter set, while the shadowed regions indicate the minimum and maximum values of these realizations. (B-C) Snapshot of a simulation for Model 3 ($P_L = 50Pa$ and $P_L = 100Pa$ respectively). In B, the red zones indicate increased cell-cell adhesion due to presence of TJ. (D) Picture of typical bile duct lumen for an embryo at E18.5 (SOX9, blue; beta-catenin, green).

https://doi.org/10.1371/journal.pcbi.1009653.g008

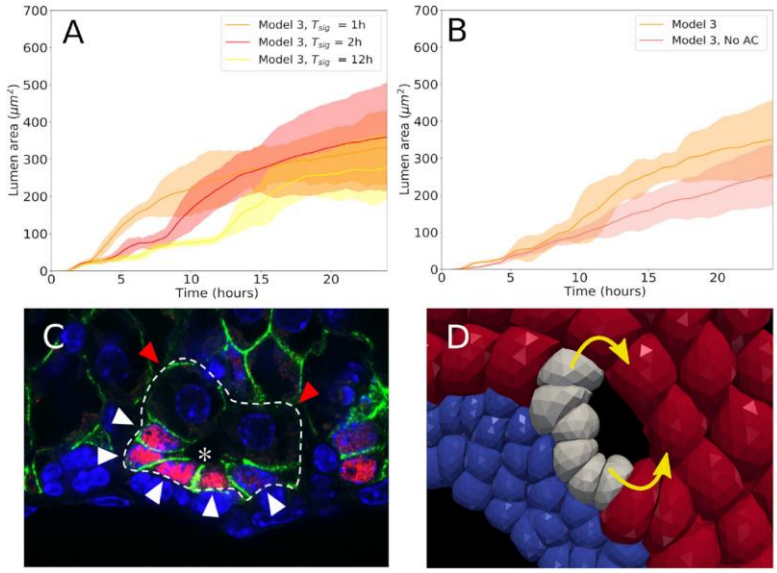

Fig 9. Simulation results for Model 3, assuming $P_l = 50Pa$: Lumen area versus time. (A) influence of cell-to-cell signalling times T_{sig}. (B) influence of absence or presence of Apical constriction (AC). The solid lines are the average of 5 stochastic realizations of the same parameter set, while the shadowed regions indicate the two times standard deviation interval of these realizations. An increase in lumen area from zero to $\sim 350\mu m^2$ in 24 hours is realistic since the area of lumina near the hilum ranged from 7 to 36 μm^2 at E16.5 and from 116 to 674 μm^2 at E18.5 (n = 10 at each stage) (C) Microscopic picture of small lumen with cholangiocytes (white arrowheads) and hepatoblasts (red arrowheads). Tissue section is stained to detect SOX9 (red), beta-catenin (green) and nuclei (DAPI, blue). (D) Snapshot of simulation showing a configuration comparable to that in panel C. The yellow arrows indicate the direction of cell-cell signalling during the formation.

https://doi.org/10.1371/journal.pcbi.1009653.g009

larger than the lumina obtained with Model 1 and Model 2, while similar as in those cases it tends to collapse at the end of the period. However assuming $P_L = 50Pa$ a drastic increase in lumen size can be observed. Interestingly, the lumen size becomes almost stable for $P_L = 50Pa$ while it continues to increase sharply for $P_L = 100Pa$. This shows that a control of osmosis could be an important factor in the lumen stability. In this regard it is also interesting to see how much of the lumen formation can be attributed to apical constriction. To study this question, simulations of Model 3 ($P_L = 50Pa$) have been performed for which AC has been omitted. The results, shown in Fig 9B, indicate that the presence of AC (as compared to no AC) speeds up the lumen formation, although it does not seem to play a major role to finally establish a stable lumen. In conclusion, oriented cell division in combination of osmotic control is able to generate a stable lumen. (An example animation of a simulation can be viewed in S6 Video).

Using Model 3 we also studied how lumen formation is influenced by the cell-to-cell signalling time, i.e the average time it takes for a cholangiocyte to induce differentiation of a

neighboring hepatoblast (Fig 9C and 9D). We recall that only hepatoblasts delimiting an initial (possibly initially very small) lumen can differentiate. The signalling time T_{sig} was varied between $1h$ and $12h$. Here, the model runs show (Fig 9A) that the influence is limited to the initial stage of lumen formation, where a short T_{sig} (= 1h) favors a quicker onset of lumen formation as compared to the case $T_{sig} = 12h$. This can be mainly attributed the earlier cell division of the cells bordering on the lumen, cfr. point ii) in section Configuration of the in-silico embryonic liver system. Hence, the cell-to-cell signaling time seems to determine the onset of cell division and thereby the time at which the lumen becomes visible. For larger simulation times the difference between the model runs becomes much smaller, as at this point all the cells delimiting the lumen have become cholangiocytes and there is no further differentiation.

There are also cell specific mechanical parameters which will potentially deviate the force balance in this bile-duct system, and thus potentially the lumen dynamics. The most obvious one here is cell to cell adhesion energy. Secondly, cell stiffness may influence the mechanical balance as well. We have performed additional simulations here to illustrate the effect of those parameters. First, we have performed a simulation set in which we assume a higher global adhesion energy between the cells, but whereby the cadherin density on the apical poles of the cells remains low. An overall higher adhesion energy between the cells modifies the forces needed to separate cells and thus the origin of the lumen and evolution its size. The effect of a two times higher global adhesion, on the lumen size is shown below in (Fig 10A). As could be expected here, a higher adhesion energy decreases the lumen size compared to the nominal adhesion energy value, a consequence of the higher forces between the cells that need to be overcome by the osmotic pressure. We here also verified the case where local adhesion would be higher than expected, i.e. at the apical sides of the cells. In particular, we asked ourselves whether the observed low density of cadherins on the apical side compared to the cell to cell junctions are key to a lumen initiation. To this end, we ran simulations in which the apical specific adhesion energy was increased from $W_{ap} = 10^{-6}\ J/m^2$) to the global nominal adhesion energy ($W_{ap} = 9.10^{-4}\ J/m^2$) between the cells. This mimics the scenario in which one would observe a homogeneous cadherin distribution. The result shown in (Fig 10B–10C) now shows an overall significant drop of the lumen size. However, the results are lumen pressure dependent. If the nominal value of the lumen pressure are assumed, no lumen develops. If a higher lumen pressure is assumed $P_l = 70Pa$, several realizations suggest that a small lumen may develop (Fig 10C). This suggests a critical importance of the balance between apical adhesion energy ans osmotic pressure: if the adhesion forces between the apical sides of the cells would be too high, lumen initiation may be impeded, hence preventing normal bile duct development.

Lastly, we performed simulations in which the cells have different mechanical properties. We looked here at the case in which the cells are of a stiffer type. For this we set double values of the cortical stiffness and the volume control stiffness, compared to the nominal values. The results did not show a significant effect on lumen size. Absence of such effect could be expected, as the internal forces inside the cell are changed here, but not the ones between the cells.

Discussion and conclusions

In the presented work, a high resolution model was established to better understand which mechanisms are capable of forming a lumen during bile duct development, using a combined data-based and computational model-based strategy. The selection of hypotheses in the computational model was informed by investigations at the molecular level that suggest several mechanisms controlling lumen formation, namely apico-basal polarization, apical

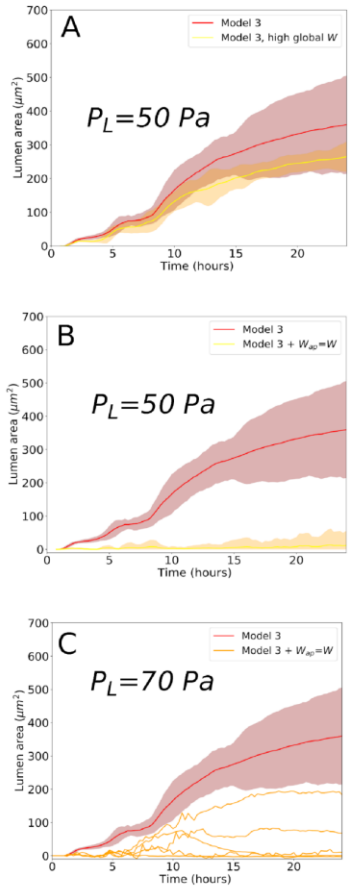

Fig 10. Simulation results compared to Model 3 with nominal parameters. (A) Effect of a higher global cell-cell adhesion energy value. (B-C) Effect of an apical adhesion energy value equal to the global cell-cell adhesion energy ($W_{ap} = W$), for $P_l = 50Pa$ and $P_l = 70Pa$ respectively. In the last figure, only the individual realizations are shown for clarity reasons.

https://doi.org/10.1371/journal.pcbi.1009653.g010

constriction, cell-cell repulsion, creation of apical surfaces, secretion of ions or vesicle exocytosis [10]. In a first step, morphometric data for the building of the computational model of biliary lumenogenesis were collected with a focus on quantifying cell proliferation and apical constriction. Expression of ion and water transporters was measured to identify possible evidence for the hypothesis that an osmotic pressure could be generated at the earliest stage of biliary lumenogenesis. Further, bile duct lumen formation occurs as a variant of cord hollowing. Standard cord hollowing is characterized by the creation of a lumen within a cylindrical cord of cells [9]. In bile ducts, the lumen forms between cells that have distinct phenotypes, namely between cholangiocytes and hepatoblasts [5]. Since hepatoblasts differentiate to cholangiocytes during biliary lumenogenesis, the dynamic phenotypic changes of cells lining the developing lumen was equally considered.

In the second step the computational model was established to unravel and quantify mechanisms that support lumenogenesis. This consists in a single-cell (agent)-based approach, in which every cell is represented in spatial detail, taking into account the physical forces that determine the cell's shape and motion. The forces that play an essential role in lumen formation during embryonic development allegedly are those that originate from (1) pure cell division, (2) apical constriction, or (3) osmotic effects. The goal was to quantify the extent to which each of the mechanisms may influence the lumen formation.

To verify the effects of individual physical forces originating from cell division, apical constriction or osmosis, we have first built an isolated, minimal system of adhering cells freely floating in a liquid medium. Our simulations in such an idealized system have shown that each of the three mechanisms can indeed induce lumen formation, provided that the cells are polarized and each of the mechanisms is properly oriented, which in the model was implemented as a polarization vector providing a direction. However, in a real embryonic tissue, cells feel continuous "background forces" from the other growing cells. To take these forces into account an in-silico model mimicking the tissue micro-architecture around the portal vein has been built, in which the various cell types, namely mesenchyme, cholangiocytes and hepatoblasts, have been included. The underlying assumption was that the bile duct originates from a single hepatoblast that differentiates into a cholangiocyte, thereby acquiring the capacity to signal to neighboring hepatoblasts. Our model parameters were informed by the experimentally observed proliferation rates of the hepatoblasts and cholangiocytes. Similar to the minimal system, three submodels have been proposed that implement the individual effects of the three mechanisms. From the sampling of 24h simulation runs the conclusions were: (i) directed cell division alone can initiate a cavity but cannot maintain it during 24h; (ii) including apical constriction in the cholangiocytes improves initial cavity formation but did not give a stable lumen growth. In both cases the background pressure forces are too high and induce a collapse of the cavity; (iii) directed cell division combined with apical constriction and induced osmotic effects of the cholangiocytes creates a stable lumen provided that the osmotic pressure has approximately the same magnitude as the background pressure of tissue. A too low osmotic pressure resulted in a collapse of the cavity whereas a too high one resulted in an unrealistically large growth of the lumen. We hypothesize here that the cholangiocytes excrete ions that serve as signaling molecules; (iv) the cell-to-cell signaling period (the time between sending the signaling and responding to it) controls the time needed for a cholangiocyte to induce differentiation of an adherent hepatoblast. This may play a role in the rate of lumen formation, but does not affect the lumen's final size. In a former ordinary differential equation-based model, Gin and co-workers found a control of cyst lumen size in vitro when elastic tensile stress balanced osmotic pressure whereby cell proliferation occurs in response to lumen expansion [61]. This mechanism is largely in line with our findings. Lumen formation in our work is studied within

the framework of a single-cell model which permits to include cell-cell adhesion forces and cell-to-cell signalling.

Cell signaling time, which impacts temporal control of differentiation of hepatoblasts to cholangiocytes, also emerged from the modeling as a key regulator of lumen formation. This is not surprising since differentiation consists in acquisition of cell-type specific form and function, and these include the above-mentioned polarization and secretory capacity of the cholangiocytes. The overarching role of differentiation highlighted in our modeling is supported by the analyses of congenital malformations of the bile ducts in humans. Congenital ductopenia, or paucity of the bile ducts, is indeed observed in rare human diseases, Alagille syndrome being the best studied among them. It is characterized by the absence of bile duct formation and results from aberrant Notch signaling consecutive to mutations affecting the *JAGGED1* or *NOTCH2* gene [66]. Mouse models knockout for Notch signalling effectors enabled to identify a critical lumenogenic role of hepatoblast to cholangiocyte differentiation [12]. Such mouse models also underline the importance of Notch-mediated control of cholangiocyte polarity in shaping the architecture of the epithelium lining the ducts and determining lumen size and maintenance [67]. Since Notch signaling stimulates expression of genes normally located at the apical pole of the cholangiocytes, including the chloride transporter CFTR, it is likely that deficient lumen formation associated with perturbed Notch signaling results in part from perturbed osmosis. Moreover, Notch signaling functions also by stimulating expression of the transcription factor *HNF1b*, a transcription factor known to control polarity genes [12, 68], thereby establishing a molecular cascade between Notch, differentiation and polarity. Mice knockout for *Hnf1b* display aberrantly-shaped cholangiocytes and enlarged and irregular lumen at the onset of bile duct formation, but these lumina eventually collapse leading to absence of well-defined bile ducts, as in patients with deficient *HNF1b* gene [69, 70]. Whether this relates to abnormal osmosis was not determined, but again is very likely. Together, these observations support the importance of our modeling to test hypotheses explaining how bile ducts may fail to form in human disease.

Our DCM is built in a modular fashion such that cellular detail can be added or removed easily. One could, for example, add components representing an internal cytoskeleton, or add more degrees of freedom to the structure, to obtain a more accurate representation of cell shape. Although these will inevitably bring more complexity to the model, they may become necessary when studying problems such as bile canaliculi formation which demand a finer scale.

Supporting information

S1 Text. This text contains more detailed information about the model algorithms and parameters.
(PDF)

S1 Video. Animation of simulation. Cell division provoking cavity formation: Hypothesis I, case polar directed division.
(MP4)

S2 Video. Animation of simulation. Cell division provoking cavity formation: Hypothesis I, random directed division.
(MP4)

S3 Video. Animation of simulation. Apical constriction provoking cavity formation: Hypothesis II.
(MP4)

S4 Video. Animation of simulation. Osmotic effects provoking cavity formation: Hypothesis III.
(MP4)

S5 Video. Animation of simulation. Whole system simulation with bile duct formation (Model 3).
(MP4)

S6 Video. Animation of simulation. Close-up of simulation with bile duct formation (Model 3).
(MP4)

S1 Data. Data points generated by simulations. All figures with simulation data can be generated using the python script delivered for each figure.
(ZIP)

Acknowledgments

We would like to thank Adrian Ranga for the useful discussion about liver tissue elasticity, and Nicolas Dauguet for help with cell sorting. The software TiSim generated by the group of D. Drasdo was extended to perform the simulations in this paper.

Author Contributions

Conceptualization: Paul Van Liedekerke, Frédéric P. Lemaigre, Dirk Drasdo.

Formal analysis: Paul Van Liedekerke, Lila Gannoun, Axelle Loriot, Frédéric P. Lemaigre, Dirk Drasdo.

Funding acquisition: Frédéric P. Lemaigre, Dirk Drasdo.

Investigation: Paul Van Liedekerke, Lila Gannoun, Dirk Drasdo.

Methodology: Paul Van Liedekerke, Lila Gannoun, Axelle Loriot, Dirk Drasdo.

Project administration: Frédéric P. Lemaigre, Dirk Drasdo.

Software: Paul Van Liedekerke, Tim Johann.

Supervision: Frédéric P. Lemaigre, Dirk Drasdo.

Validation: Paul Van Liedekerke, Dirk Drasdo.

Visualization: Paul Van Liedekerke, Lila Gannoun.

Writing – original draft: Paul Van Liedekerke, Lila Gannoun, Axelle Loriot, Frédéric P. Lemaigre, Dirk Drasdo.

Writing – review & editing: Paul Van Liedekerke, Frédéric P. Lemaigre, Dirk Drasdo.

References

1. Sato K, Marzioni M, Meng F, Francis H, Glaser S, Alpini G. Ductular Reaction in Liver Diseases: Pathological Mechanisms and Translational Significances. Hepatology. 2019; 69(1):420–430. https://doi.org/10.1002/hep.30150 PMID: 30070383
2. Gordillo M, Evans T, Gouon-Evans V. Orchestrating liver development Development 2015 142: 2094–2108; https://doi.org/10.1242/dev.114215 PMID: 26081571

3. Ober EA, Lemaigre FP. Development of the liver: Insights into organ and tissue morphogenesis; Journal of Hepatology. 2018; https://doi.org/10.1016/j.jhep.2018.01.005 PMID: 29339113
4. Lemaigre FP. Development of the Intrahepatic and Extrahepatic Biliary Tract: A Framework for Understanding Congenital Diseases. Annual Review of Pathology: Mechanisms of Disease. 2020; https://doi.org/10.1146/annurev-pathmechdis-012418-013013 PMID: 31299162
5. Antoniou A, Raynaud P, Cordi S, Zong Y, Tronche F, Stanger BZ, et al. Intrahepatic Bile Ducts Develop According to a New Mode of Tubulogenesis Regulated by the Transcription Factor SOX9. Gastroenterology. 2009; https://doi.org/10.1053/j.gastro.2009.02.051 PMID: 19403103
6. Takashima Y, Terada M, Kawabata M, Suzuki A. Dynamic three-dimensional morphogenesis of intrahepatic bile ducts in mouse liver development. Hepatology. 2015; https://doi.org/10.1002/hep.27436 PMID: 25212491
7. Tanimizu N, Kaneko K, Itoh T, Ichinohe N, Ishii M, Mizuguchi T, et al. Intrahepatic bile ducts are developed through formation of homogeneous continuous luminal network and its dynamic rearrangement in mice. Hepatology. 2016; https://doi.org/10.1002/hep.28521 PMID: 26926046
8. Benhamouche-Trouillet S, O'Loughlin E, Liu CH, Polacheck W, Fitamant J, McKee M, et al. Proliferation-independent role of NF2 (Merlin) in limiting biliary morphogenesis. Development (Cambridge). 2018; https://doi.org/10.1242/dev.162123 PMID: 29712669
9. Lubarsky B, Krasnow MA. Tube morphogenesis: Making and shaping biological tubes Cell 2003 Jan 10; 112(1):19–28. https://doi.org/10.1016/S0092-8674(02)01283-7 PMID: 12526790
10. Datta A, Bryant DM, Mostov KE. Molecular regulation of lumen morphogenesis; Curr Biol 2011 Feb 8; 21(3):R126–36. https://doi.org/10.1016/j.cub.2010.12.003 PMID: 21300279
11. Blasky AJ, Mangan A, Prekeris R. Polarized Protein Transport and Lumen Formation During Epithelial Tissue Morphogenesis. Annual Review of Cell and Developmental Biology. 2015; https://doi.org/10.1146/annurev-cellbio-100814-125323 PMID: 26359775
12. Zong Y, Panikkar A, Xu J, Antoniou A, Raynaud P, Lemaigre F, et al. Notch signaling controls liver development by regulating biliary differentiation. Development. 2009; https://doi.org/10.1242/dev.029140 PMID: 19369401
13. Drasdo D, Hoehme S, Block M. On the Role of Physics in the Growth and Pattern Formation of Multi-Cellular Systems: What can we Learn from Individual-Cell Based Models. Journal of Statistical Physics. 2007; 128:287–345. https://doi.org/10.1007/s10955-007-9289-x
14. Schaller G, Meyer-Hermann M. Multicellular tumor spheroid in an off-lattice Voronoi-Delaunay cell model. Phys Rev E. 2005; 71(5):51910. https://doi.org/10.1103/PhysRevE.71.051910
15. Geris L, Van Liedekerke P, Smeets B, Tijskens E, Ramon H. A cell based modelling framework for skeletal tissue engineering applications Journal of biomechanics. 2010; 43(7). PMID: 19962147
16. Vermolen F J, Gefen A. A semi-stochastic cell-based formalism to model the dynamics of migration of cells in colonies Biomechanics and Modeling in Mechanobiology. 2012; 11(1).
17. Schlueter D.K., Ramis-Conde I, Chaplain M.A.J. Multi-scale modelling of the dynamics of cell colonies: insights into cell adhesion forces and cancer invasion from in silico simulations J. R. Soc. Interface 12: 20141080. https://doi.org/10.1098/rsif.2014.1080
18. Basan M, Prost J, Joanny JF, Elgeti J. Dissipative particle dynamics simulations for biological tissues: rheology and competition. Physical biology. 2011; 8(2):26014. https://doi.org/10.1088/1478-3975/8/2/026014 PMID: 21460431
19. Van Liedekerke P, Neitsch J, Johann T, Alessandri K, Nassoy P, Drasdo D. Quantitative agent-based modeling reveals mechanical stress response of growing tumor spheroids is predictable over various growth conditions and cell lines. PLoS Computational Biology. 2019, https://doi.org/10.1371/journal.pcbi.1006273
20. Ghaffarizadeh A., Heiland R., Friedman S.H., Mumenthaler S.M., and Macklin P., PhysiCell: an open source physics-based cell simulator for 3-D multicellular systems PLoS Comput. Biol. 14(2): e1005991, 2018. https://doi.org/10.1371/journal.pcbi.1005991 PMID: 29474446
21. Delile J., Herrmann M., Peyriéras N, Doursat R. A cell-based computational model of early embryogenesis coupling mechanical behaviour and gene regulation. newblock Nat Commun 8, 13929 (2017). https://doi.org/10.1038/ncomms13929 PMID: 28112150
22. González-Valverde I., García-Aznar J.M. An agent-based and FE approach to simulate cell jamming and collective motion in epithelial layers. Comp. Part. Mech. 6, 85–96 (2019). https://doi.org/10.1007/s40571-018-0199-2
23. Colombi A, Scianna M, Preziosi L. A hybrid integro-differential model for the early development of the zebrafish posterior lateral line. J Theor Biol. 2021, https://doi.org/10.1016/j.jtbi.2020.110578 PMID: 33417902

24. Rejniak K A An immersed boundary framework for modelling the growth of individual cells: An application to the early tumour development Journal of Theoretical Biology. 2007, doi: https://doi.org/10.1016/j.jtbi.2007.02.019
25. Fedosov DA, Caswell B, Karniadakis GE. Systematic coarse-graining of spectrin-level red blood cell models. Computer Methods in Applied Mechanics and Engineering. 2010; 199(29–32):1937–1948. https://doi.org/10.1016/j.cma.2010.02.001 PMID: 24353352
26. Jamali Y, Azimi M, Mofrad M RK, A sub-cellular viscoelastic model for cell population mechanics PLoS One. 2010; https://doi.org/10.1371/journal.pone.0012097 PMID: 20856895
27. Odenthal T, Smeets B, Van Liedekerke P, Tijskens E, Van Oosterwyck H, Ramon H. Analysis of Initial Cell Spreading Using Mechanistic Contact Formulations for a Deformable Cell Model. PLoS Computational Biology. 2013; 9(10):e1003267. https://doi.org/10.1371/journal.pcbi.1003267 PMID: 24146605
28. Tozluoğlu M., Tournier A., Jenkins R. et al. Matrix geometry determines optimal cancer cell migration strategy and modulates response to interventions. Nat Cell Biol, 2013. PMID: 23792690
29. Sandersius SA, Weijer CJ, Newman TJ. Emergent cell and tissue dynamics from subcellular modeling of active biomechanical processes. Physical Biology. 2011; 8:45007. https://doi.org/10.1088/1478-3975/8/4/045007 PMID: 21750367
30. Tanaka S, Sichau D, Iber D. LBIBCell: a cell-based simulation environment for morphogenetic problems. Bioinformatics. 2015; https://doi.org/10.1093/bioinformatics/btv147 PMID: 25770313
31. Belmonte JM, Clendenon SG, Oliveira GM, et al. Virtual-tissue computer simulations define the roles of cell adhesion and proliferation in the onset of kidney cystic disease. Mol Biol Cell. 2016; 27(22):3673–3685. https://doi.org/10.1091/mbc.E16-01-0059 PMID: 27193300
32. Hirashima T, Rens E.G., Merks R.M.H. Cellular Potts Modeling of Complex Multicellular Behaviors in Tissue Morphogenesis Dev Growth Differ. 2017 https://doi.org/10.1111/dgd.12358 PMID: 28593653
33. Bessonov N., Volpert V. Deformable Cell Model of Tissue Growth Computation 2017,
34. Chen J, Weihs D, Van Dijk M, Vermolen Fred J. A phenomenological model for cell and nucleus deformation during cancer metastasis, Biomechanics and Modeling in Mechanobiology. 2018. https://doi.org/10.1007/s10237-018-1036-5 PMID: 29845458
35. Smeets B, Cuvelier M, Pešek J, Ramon H. The Effect of Cortical Elasticity and Active Tension on Cell Adhesion Mechanics. Biophys J. 2019. https://doi.org/10.1016/j.bpj.2019.01.015 PMID: 30773295
36. Ioannou F., Dawi Malik A., Tetley Robert J., Mao Yanlan, Muñoz José J Development of a New 3D Hybrid Model for Epithelia Morphogenesis Frontiers in Bioengineering and Biotechnology 2020,. https://doi.org/10.3389/fbioe.2020.00405 PMID: 32432102
37. Van Liedekerke P, Neitsch J, Johann T, Warmt E, Gonzàlez-Valverde I, Hoehme S, et al. A quantitative high-resolution computational mechanics cell model for growing and regenerating tissues. Biomechanics and Modeling in Mechanobiology. 2020, https://doi.org/10.1007/s10237-019-01204-7
38. Heck T, Vargas DA, Smeets B, Ramon H, Van Liedekerke P, Van Oosterwijck H. The role of actin protrusion dynamics in cell migration through a degradable viscoelastic extracellular matrix: Insights from a computational model. PLOS Computational Biology 16(1): e1007250. https://doi.org/10.1371/journal.pcbi.1007250 PMID: 31929522
39. Gong S, Zheng C, Doughty ML, Losos K, Didkovsky N, Schambra UB, Nowak NJ, et al. A gene expression atlas of the central nervous system based on bacterial artificial chromosomes. Nature 2003, https://doi.org/10.1038/nature02033 PMID: 14586460
40. Nissen SB, Rønhild S, Trusina A, Sneppen K. Theoretical tool bridging cell polarities with development of robust morphologies. eLife. 2018; https://doi.org/10.7554/eLife.38407 PMID: 30477635
41. Buckling instabilities of one-layered growing tissues. Phys Rev Lett 84:4244–4247 (2000). https://doi.org/10.1103/PhysRevLett.84.4244 PMID: 10990656
42. Martin A. C., Goldstein B. Apical constriction: themes and variations on a cellular mechanism driving morphogenesis. Development, 141(10), 1987–1998.
43. Chu YS, Dufour S, Thiery JP, Perez E, Pincet F. Johnson-Kendall-Roberts Theory Applied to Living Cells. Physical Review Letters. 2005; 94(2):28102. https://doi.org/10.1103/PhysRevLett.94.028102 PMID: 15698233
44. Van Liedekerke P, Palm MM, Jagiella N, Drasdo D. Simulating tissue mechanics with agent-based models: concepts, perspectives and some novel results. Computational Particle Mechanics. 2015; 2 (4):401–444. https://doi.org/10.1007/s40571-015-0082-3
45. Hoehme S, Brulport M, Bauer A, Bedawy E, Schormann W, Hermes M, et al. Prediction and validation of cell alignment along microvessels as order principle to restore tissue architecture in liver regeneration. Proceedings of the National Academy of Sciences. 2010; 107(23):10371–10376. https://doi.org/10.1073/pnas.0909374107 PMID: 20484673

46. Brugues J, Maugis B, Casademunt J, Nassoy P, Amblard F, Sens P Dynamical organization of the cytoskeletal cortex probed by micropipette aspiration. PNAS. 2010, https://doi.org/10.1073/pnas.0913669107 PMID: 20713731

47. Tinevez JY, Schulze U, Salbreux G, Roensch J, Joanny JF, Paluch E. Role of cortical tension in bleb growth. Proceedings of the National Academy of Sciences of the United States of America. 2009; 106 (44):18581–6. https://doi.org/10.1073/pnas.0903353106 PMID: 19846787

48. Galle J, Loeffler M, Drasdo D. Modeling the effect of deregulated proliferation and apoptosis on the growth dynamics of epithelial cell populations in vitro. Biophysical journal. 2005; 88(1):62–75. https://doi.org/10.1529/biophysj.104.041459 PMID: 15475585

49. Buske P, Galle J, Barker N, Aust G, Clevers H, Loeffler M. A Comprehensive Model of the Spatio-Temporal Stem Cell and Tissue Organisation in the Intestinal Crypt. PLoS Comput Biol. 2011; 7(1): e1001045. https://doi.org/10.1371/journal.pcbi.1001045 PMID: 21253562

50. Drasdo D, Hoehme S. Modeling the impact of granular embedding media, and pulling versus pushing cells on growing cell clones. New Journal of Physics. 2012; 14(5):55025. https://doi.org/10.1088/1367-2630/14/5/055025

51. Wilding Crawford L, Foley JF, Elmore SA. Histology atlas of the developing mouse hepatobiliary system with emphasis on embryonic days 9.5–18.5. Toxicologic Pathology. 2010; https://doi.org/10.1177/0192623310374329 PMID: 20805319

52. Boyer JL. Bile formation and secretion. Comprehensive Physiology. 2013; https://doi.org/10.1002/cphy.c120027 PMID: 23897680

53. Tabibian JH, Masyuk AI, Masyuk TV, O'Hara SP, LaRusso NF. Physiology of cholangiocytes. Comprehensive Physiology. 2013; https://doi.org/10.1002/cphy.c120019 PMID: 23720296

54. Inoue Y., Tateo I., Adachi T. Epithelial tissue folding pattern in confined geometry. Biomech Model Mechanobiol 19, 815–822 (2020). https://doi.org/10.1007/s10237-019-01249-8 PMID: 31728791

55. Gloerich M, Bianchini JM, Siemers KA, Cohen DJ, Nelson WJ. Cell division orientation is coupled to cell-cell adhesion by the E-cadherin/LGN complex. Nature Communications. 2017; https://doi.org/10.1038/ncomms13996 PMID: 28045117

56. Overeem AW, Bryant DM, van IJzendoorn SC. Mechanisms of apical-basal axis orientation and epithelial lumen positioning.* Trends Cell Biol. 2015. https://doi.org/10.1016/j.tcb.2015.04.002 PMID: 25941134

57. Fletcher AG, Osterfield M, Baker RE, Shvartsman SY. Vertex models of epithelial morphogenesis. Biophys J. 2014. https://doi.org/10.1016/j.bpj.2013.11.4498

58. Inoue Y, Suzuki M, Watanabe T, Yasue N, Tateo I, Adachi T, et al. Mechanical roles of apical constriction, cell elongation, and cell migration during neural tube formation in Xenopus. Biomechanics and Modeling in Mechanobiology. 2016; https://doi.org/10.1007/s10237-016-0794-1 PMID: 27193152

59. Okuda S, Takata N, Hasegawa Y, Kawada M, Inoue Y, Adachi T, et al. Strain-triggered mechanical feedback in self-organizing optic-cup morphogenesis. Science Advances. 2018; https://doi.org/10.1126/sciadv.aau1354 PMID: 30474058

60. Citi S. The mechanobiology of tight junctions; 2019. Biophys Rev 11, 783–793 (2019). https://doi.org/10.1007/s12551-019-00582-7 PMID: 31586306

61. Gin E, Tanaka EM, Brusch L. A model for cyst lumen expansion and size regulation via fluid secretion. J Theor Biol. 2010; 264(3):1077–88. https://doi.org/10.1016/j.jtbi.2010.03.021 PMID: 20303986

62. Dasgupta S, Gupta K, Zhang Y, Viasnoff V, Prost J Physics of lumen growth Proceedings of the National Academy of Sciences 2018, 115 (21) E4751–E4757; https://doi.org/10.1073/pnas.1722154115

63. Desai SS, Tung JC, Zhou VX, Grenert JP, Malato Y, Rezvani M, et al. Physiological ranges of matrix rigidity modulate primary mouse hepatocyte function in part through hepatocyte nuclear factor 4 alpha. Hepatology. 2016; https://doi.org/10.1002/hep.28450 PMID: 26755329

64. Yang L, Wang WH, Qiu WL, Guo Z, Bi E, Xu CR. A single-cell transcriptomic analysis reveals precise pathways and regulatory mechanisms underlying hepatoblast differentiation. Hepatology. 2017; https://doi.org/10.1002/hep.29353 PMID: 28681484

65. Tanimizu N, Kikkawa Y, Mitaka T, Miyajima A. α1- and α5-containing laminins regulate the development of bile ducts via β1 integrin signals. J Biol Chem. 2012 Aug 17; 287(34):28586–97. https://doi.org/10.1074/jbc.M112.350488 PMID: 22761447

66. Mitchell E, Gilbert M, Loomes KM. Alagille Syndrome. Clin Liver Dis. 2018; 22(4):625–641. https://doi.org/10.1016/j.cld.2018.06.001 PMID: 30266153

67. Andersson ER, Chivukula IV, Hankeova S, Sjöqvist M, Tsoi YL, et al. Mouse Model of Alagille Syndrome and Mechanisms of Jagged1 Missense Mutations. Gastroenterology. 2018; 154(4):1080–1095. https://doi.org/10.1053/j.gastro.2017.11.002 PMID: 29162437

68. Poncy A, Antoniou A, Cordi S, Pierreux CE, Jacquemin P, et al. Transcription factors SOX4 and SOX9 cooperatively control development of bile ducts. Dev Biol. 2015; 404(2):136–48. https://doi.org/10.1016/j.ydbio.2015.05.012 PMID: 26033091

69. Coffinier C, Gresh L, Fiette L, Tronche F, Schütz G, et al. Bile system morphogenesis defects and liver dysfunction upon targeted deletion of HNF1beta. Development. 2002; 129(8):1829–38. https://doi.org/10.1242/dev.129.8.1829 PMID: 11934849

70. Roelandt P, Antoniou A, Libbrecht L, Van Steenbergen W, Laleman W, et al. HNF1B deficiency causes ciliary defects in human cholangiocytes. Hepatology. 2012; 56(3):1178–81. https://doi.org/10.1002/hep.25876 PMID: 22706971

Supplementary information 1: Model description

Basic DCM forces

In this section the force contributions acting on a cell within the deformable cell model (DCM) are summarized.

Elastic forces cortex

The cell surface in the DCM is triangulated with visco-elastic elements along the edges linking neighbouring nodes. The forces between the nodes mimic the cortical tensions. The membrane envelope is assumed to not significantly contribute to these forces as the presence of caveolae can significantly reduce its mechanical resistance [1]. We assume that cell deformation dynamics can be reasonably approximated by Kelvin-Voigt elements. The internal force $\mathbf{F}_{int}$ originating from a Kelvin-Voigt viscoelastic element between node nodes i and j reads:

$$\begin{aligned}\mathbf{F}_{int,ij} &= \mathbf{F}_{e,ij} - \gamma \mathbf{v}_{ij} \\ &= -k_s(l_{ij} - l_{ij}^0)\mathbf{e}_{ij} - \gamma \mathbf{v}_{ij},\end{aligned} \tag{1}$$

where γ denotes the friction coefficient, $l_{ij}^0 = ||\mathbf{r}^0_{ij}|| = ||\mathbf{r}^0_j - \mathbf{r}_i^0||$ and $l_{ij} = ||\mathbf{r}_{ij}||$ are the initial (cell at rest) and actual lengths between the nodes, and $\mathbf{v}_{ij} = \mathbf{v}_j - \mathbf{v}_i$ is the relative velocity of nodes *i,j*. The force balance equation with external forces $\mathbf{F}_{ext}$ demands that $\mathbf{F}_{ext} + \mathbf{F}_{int} = \mathbf{0}$, hence:

$$\mathbf{F}_{ext,ij} - k_s(l_{ij} - l_{ij}^0)\mathbf{e}_{ij} - \gamma \mathbf{v}_{ij} = \mathbf{0}. \tag{2}$$

The linear spring constant for a sixfold symmetric triangulated lattice can be related approximately to the cortex Young modulus E_{cor} with thickness h_{cor} by [2]

$$k_s \approx \frac{2}{\sqrt{3}} E_{cor} h_{cor}. \tag{3}$$

Besides tension, the cortex resists to bending. The bending resistance in the cortex is incorporated by the angular resistance of the hinges determined by two adjacent triangles $T_1 = \{ijk\}$ and $T_2 = \{ijl\}$. This can be accounted for by the bending moment M:

$$M = k_b sin(\theta - \theta_0) \tag{4}$$

where k_b is the bending constant, and θ is is the angle between the normal vectors to the triangles $\mathbf{n}_\alpha, \mathbf{n}_\beta$ by their scalar product $(\mathbf{n}_\alpha \mathbf{n}_\beta) = cos(\theta)$. θ_0 is the angle of spontaneous curvature. A spontaneous curvature denotes the curvature for which the bending energy is zero.

The moment M can be transformed to an equivalent force system $\mathbf{F}_{m,z}$ ($z \in \{ijl\}$) for the triangles T_1 and T_2 where here for T_1 we can compute $\mathbf{F}_{m,i} = M/l_1 \mathbf{n}_1$ using l_1 as the distance between the hinge of the triangle pair and the point i, and similar expression for $\mathbf{F}_{m,l}$. The forces working on nodes j,k must at least fulfill $\mathbf{F}_{m,i} + \mathbf{F}_{m,j} + \mathbf{F}_{m,k} + \mathbf{F}_{m,l} = 0$ to conserve total momentum, see e.g. [3,4]. The bending stiffness of the cortex is approximated by

$$k_b \approx \frac{E_{cor} h_{cor}^3}{12(1-\nu^2)} \quad (5)$$

where v ≈ 0.5 is the Poisson's ratio of the cortex. Note that the elastic modulus of the cortex, E_{cor} enters both, the bending force and the tension force.

Volume forces

The volume change of the cell depends on the applied pressure and the cell bulk modulus K_V. The total compressibility of the cell depends on volume fraction of water in the cytosol, the cytoskeleton (CSK) volume fraction and structure, and the compressibility of the individual organelles. In addition, it may be influenced by the permeability of the plasma membrane for water, the presence of caveolae, and active responses inside and of the cell. We calculate the internal pressure in a cell by the logarithmic strain for volume change:

$$p = -K_V log(\frac{V}{V_0}) \quad (6)$$

whereby V is the actual volume and V_0 is the reference volume i.e., the volume of the cell not subject to compression forces. For small deviations of V from V_0, $p \approx K_V (V - V_0)/V_0$. Within our model the volume V of the cell is computed summing up the

volumes of the individual tetrahedra that build up the cell. The nodal force is obtained by multiplying the pressure with the nodal Voronoi area S_i (see [5]), i.e. $\mathbf{F}_{vol,i} = pS_i\mathbf{R}_i$ where the local curvature vector $\mathbf{R}_i$ is computed for that node using a discrete Laplace-Beltrami operator [7].

Contact model and adhesive forces

Whereas in a CBM, cells interact through central forces described by (modified) Hertz or JKR theory for adhesive spheres, in DCM the interaction forces need to be defined for each node individually, thereby requiring a representation of local surface heterogeneities. The approach followed in this work adopts a discretised Maugis-Dugdale theory. The Maugis-Dugdale theory for adhering bodies is a generalization of the JKR theory for spheres [6]. This theory captures the full range between the Derjaguin-Muller-Toporov (DMT) zone of long reaching adhesive forces of a hard homogeneous isotropic elastic sphere and small adhesive deformations in the Johnson-Kendall-Roberts (JKR)-limit of a soft homogeneous isotropic elastic sphere of short interaction ranges. Here, we associate to each triangle of the cell surface a circumscribing sphere reflecting the local curvature. Two triangles belonging to different cells can locally interact by collision of their associated spheres. To compute the magnitude of these interactions with respect to the nodes of the triangles, we use the general Maugis-Dugdale stress, which is integrated over the common contact area between the triangles, resulting in the net forces on the nodes of the two interacting triangles (see [3,7] for more details). The adhesion force is fully determined by the specific adhesion energy W and the typical effective adhesive range h_0 that reflects the attractive cutoff distance between the bodies. We set $h_0 = 2 \cdot 10^{-8}m$ in all the simulations [8].

In our model, Maugis-Dugdale theory is applied to every set of triangles which constitute the cell surface. A varying number of cadherin bonds is mimicked by varying the adhesion energy along the cell surface triangles.

Migration forces

In models in which cell movement and deformation is mimicked by force-balance equations following Newton's law of motion as this is the case for the DCM and CBM, migration is usually modelled by an active migration force F^{mig} representing the random micro-motility of a cell. For the sake of simplicity, the cell shape, filopodia etc. movements during migration are not detailed in the model but instead the different mechanisms in cell migration are lumped into one net force which is uniformly distributed to the nodes the cell if not mentioned otherwise. For specific applications, the forces might be non-uniformly distributed. In absence of influences that impose a certain direction or persistence, it is commonly assumed that the migration force is stochastic, formally resulting in $\mathbf{F}^{mig} = \mathbf{F}^{ran}$, with $(\mathbf{F}^{ran}) = 0$, and $(\mathbf{F}^{ran}(t) \otimes \mathbf{F}^{ran}(t')) = \mathbf{M}\delta(t - t')$, where **M** is an amplitude 3 × 3 matrix and relates to the diffusion tensor **D** of the cell. As cell migration is active, depending on the local matrix density and orientation of matrix fibers, the autocorrelation amplitude matrix **M** cannot a priori be assumed to follow a fluctuation-dissipation (FD) theorem. However, "measuring" the position of a cell in the simulations the position autocorrelation function might be experimentally used to determine the diffusion tensor using $(((\mathbf{r}(t + \tau) - \mathbf{r}(t)) \otimes (r(t + \tau) - r(t))) = 6\mathbf{D}_\tau$, and **M** be calibrated such that the numerical solution of the equation of motion for the cell position reproduces the experimental result for the position-autocorrelation function. For example, in a homogeneous environment **M** can be casted into a form formally equivalent to the FD-theorem, leading to an k_BT-equivalent for cellular systems, that is controlled by the cell itself [9,10].

Note, we assume here a momentum transfer to the ECM by applying the ECM friction and active micro-motility term, but we do not model the ECM explicitly.

Cell cycle and cell division

During cytokinesis, the continuous shrinking of the contractile ring, together with the separation of the mitotic spindle, gradually divides the mother cell into two daughter cells. After mitosis the cell has split up in two adhering cells. Such a process of cell

division in 2D deformable cells has been previously described (e.g. [11]) but it can be costly and tedious to perform in 3D.

As we are merely interested in long term effects (i.e. hundreds of cell divisions), and as the cytokinesis is a short process compared to the duration of the entire cell cycle, we avoid these particular tedious intermediate steps in our model, and directly create two new adhering cells that are within the shape of the mother cells just before its division using the basic algorithm established in ref. [12].

In our algorithm, the two created daughter cells are initially round and separated from each other by the division plane. They grow artificially fast until they reach the boundary of the mother envelope. The division plane is removed from the system after the daughter cells have found a mechanical equilibrium in this envelope. We have here slightly extended our algorithm to mimic the very short rounding-up period just before division (see Fig 2G in main text). This is achieved by setting the equilibrium edge lengths (see below) of the triangulation temporarily to a smaller value This can cause a slight increased pressure in the cell during division.

In the simulations, cells grow by increasing their volume and surface and they can divide when their actual volume reaches a target volume. This target volume is predefined and is for a newborn cell by default set to twice the volume of that newborn cell. The orientation of cell division can be chosen randomly (as would be the case for non polarized hepatocytes) or with a preferred direction. The latter is the case when a polarized cell divides. In this case the division direction is the polarization vector. As observed experimentally, we also implement a temporary and short rounding up period just before cells division. This has a consequence that the cell volume slightly drops and hence the pressure inside the cell increases, causing a rounding of the surface. The shortening of the vertex edges is chosen such that this pressure increase is not more than 100 to 200 *Pa*, achieved by modifying the lengths from l_0 to $0.95 * l_0$. The rounding up period in our model does not take more than 5% of the total cell cycle time.

The cells in our system can either be proliferating or quiescent. Immediately after cell division, all cells are assumed to proliferate. A change to quiescence is here assumed to be induced by chemical signals of other cells. To ensure in the simulations that only the fraction of the cells is growing conform with the experimental observations, an algorithm is invoked that sweeps every time step over a certain cell type and ensures that the prescribed fraction of proliferating cells is maintained. The picking of cells that need to go to quiescence is done randomly. This algorithm was chosen as the mechanistic control of how many cells divide was not subject of the present simulation study.

DCM extension: Polarity vector

A normalized polarity vector $\vec{P}$ (PCP) is assigned to each of the cells. This vector defines for every cell two opposite conical polar regions (see Fig 2A in main text). The triangular regions on the cell surface that are marked as polar are defined by the scalar product condition:

$$\|\vec{P} \cdot \vec{N}_i\| < a, \quad (7)$$

where N_i is a normalized vector with origin the center of mass of the cell, and pointing to the middle of triangle i. The area of the polar region a can be chosen according to $0 < a < 1$. We chose in the simulations of this work $a = 0.7$. This corresponds to a bi-conical area with angle α of approximately 60 degrees. The polar regions (triangles) may have different physical properties than the rest of the cell surface, such as a different specific adhesion energy. The PCP vector is assumed to be perpendicular to the apico-basal vector, which is enforced in the model with every timestep (we note here that in our planar simulations neither the PCP nor ABP have a Z component).

DCM extensions : apical vector, apical constriction and tight junctions

Every cell also has an apical vector $\vec{A}$ (ABP), which defines the apical and basal side of the cell. Similar to the polar regions, the apical and basal triangular regions on the cell surface are defined by the conditions:

$$\vec{A} \cdot \vec{N}_i > b \text{ (apical region)} \qquad (8)$$

and

$$\vec{A} \cdot \vec{N}_i < -b \text{ (basal region)} \qquad (9)$$

Like for the polar vector, this corresponds to a conical area with angle β and the scalar value of b ∈ [0,1] determines the area of the regions, however the difference is that the apical side of the cell may have different physical properties than the basal side. In this work the cortical cytoskeleton on the apical side can contract, causing apical constriction.

In the model, the apical vector is assumed every time step to point towards the principal region where the cell surface has the freest area, in line with the assumption made that the apical side forms the cell's interface with the lumen. Because for every triangle of a cell the free area and contact area is known after applying the contact model, the principal vector $\vec{A}$ can obtained by

$$\vec{A} = \sum_i \vec{N}_i / \| \sum_i \vec{N}_i \|. \qquad (10)$$

Here the summation only counts triangles that have a very small contact area with a triangle from another cell. These conditions can for example be fulfilled when gaps between cells are created due to osmotic effects (e.g. onset of a small cavity). $\vec{A}$ is updated every timestep, except during cell division and a short relaxation phase right after cell division.

Adherent cells can also develop tight junctions (TJ) between them. In the model, we define for every cell that has an apical vector, a region with TJ triangles i that fulfill the condition:

$$\vec{A} \cdot \vec{N}_i > c_1 \text{ and } \vec{A} \cdot \vec{N}_i < c_2 \qquad (11)$$

Here c_1 and c_2 are the limit values that define a conical ribbon along the cell where TJ can be present (see Fig 2D in main text). The parameter values for c_1 and c_2 are chosen such that the ribbon is about 1 or maximum at 2 triangles thick. As TJs denote areas on the cell surface with a reinforced connection, a larger specific adhesion energy is assigned to these areas than to the other surface areas. As such, when two triangles of different cells with a TJ come into contact, the force necessary to separate them will be much higher than for normal cell-cell contacts.

The apical constriction on the apical side is modeled as a shortening of the equilibrium element lengths between connected nodes that are located within the apical region (see below). This results in a movement of the two nodes towards each other. The shortening operation is executed only once. After a certain relaxation time a new force equilibrium is reached between the nodes. The modification of the equilibrium element lengths of the nodal springs during apical constriction are computed assuming two different zones:

$$l_0 := l_0 * d_2 \text{ for: } \vec{A} \cdot \vec{N}_i > c_2 \text{ and } \vec{A} \cdot \vec{N}_i < c_1, \qquad (12)$$

which is the zone of the tight junctions, and

$$l_0 := l_0 * d_1 \text{ for: } \vec{A} \cdot \vec{N}_i > c_1. \qquad (13)$$

in the apical domain.

To simulate the presence of an apical circumferential ring, the strongest constriction is applied in the zone of the TJ ribbon, whereas a lower constriction is applied in the apical domain ($0 < d_2 < d_1 < 1$). We have adopted the values $d_2 = 0.5$ and $d_1 = 0.7$. This warrants a strong contraction. Moreover, the adhesive energy on the apical

side is assumed to be lower than elsewhere on the cell because generally one observes that cadherin staining is less strong there (see Fig A1B).

DCM extensions : Osmotic effects and signalling

We assume that osmotic forces in the system result from differences of solutes e.g by molecules such as salts that are released from the cell into the extracellular space. These molecules further diffuse locally and cause a concentration gradient with more distant locations. For example, if one cell starts to excrete ions, a salt concentration gradient is generated attracting water molecules towards the cell potentially causing a hydrostatic pressure increase strong enough to push away cells in the direct neighborhood of the central cell. As a consequence, an extracellular space can arise, depending in shape and size on the dynamics and mechanics of the surrounding cells. One way to simulate the diffusion process of salts and flow of water could be to solve a system of partial differential equations (PDEs) for diffusive transport of salt and the advection of water. As the surrounding cells reorganise during the lumen formation process and hence the shape of the extracellular space changes, the boundary conditions for the PDEs change constantly. The constant change requires high resolution meshing and constant re-meshing of the complex cavity, which is numerically complicated and

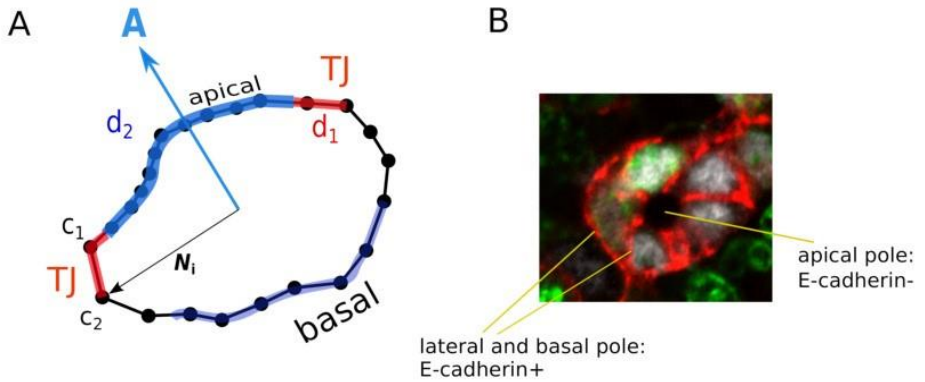

Figure A1. Cartoon indicating the parameters needed to determine the apical domain and apical circumferential ring.

computationally time consuming. To alleviate this, inspired by smoothed particle hydrodynamics methods [13], we introduce the concept of “tracer particles (TP)”, which are small ”inert” particles. They can diffuse freely inside the cell or in the extracellular space without mutual interaction (see Fig 2F in main text). All the tracer particles (we used about 500 in numbers per cell) are initially inside the cell and start diffusing from there. The advantage of using particles to mimic the fluid is that their motion can be simulated by a Newton’s equation of motion as for the cells, hence the coupling of fluid movement and cell deformation is straightforward.

The force on each particle originates principally from Brownian motion as and its magnitude is controlled by the TP diffusion coefficient. Additionally, a small force component is exerted to them in the apical direction to facilitate their movement towards the apical side which can be justified by directional vesicle transport towards lumen in polarized cells [14].

To ensure that the TP can leave the cell only through a certain region, we define a “transparent” region for each cell surface through which these particles can move into the extracellular space. The transparent region is equal to the apical side of the cells. In other parts of the cell, the particles cannot move across the cell surface. The particles can thus locally cross the cell boundary when moving from inside to outside, but are always repelled when trying to move back from the outside to the inside of the cell. These particles do not represent individual ions but rather each population of ions approximately obtained by integrating the spatial density of ions over local space regions. Nevertheless, to ensure diffusion constant is similar to that of the ions, the particles are assigned with the diffusion coefficient of the ion species.

In the extracellular space a tracer particles marks a triangle if it is in close proximity of that triangle representing a free cell surface piece, not in full contact with another cell. As there are many TP present, all free surface areas of a cell will progressively become marked. To simulate the resulting hydrostatic pressure on that cell, each marked triangle receives an external force $\vec{F}_{osm} = PA_i\vec{n}_i$, where *P* is the assumed hydrostatic pressure that corresponds to the osmotic pressure generated by the difference in ion concentration $\vec{n}_i$. (assumed constant here), and

A_i is the surface of the marked triangle with local normal Triangles belonging to two different cells that are in contact with each other have a negligible probability to be marked as the particles cannot access the space between them.

CBM forces

The CBM does not resolve cell shape explicitly. Forces are in the CBM are assumed to be exerted on the center of mass of the cell.

Adhesive and repulsive forces

In the CBM, cells are approximated by homogeneous, isotropic, elastic and adhesive spheres which split into two adherent cells during mitosis. Under conditions met in this work [16,17], the total cell to cell interaction force can be approximated by the JKR force. The interaction force is computed by

$$Fcc,ij = \frac{4\hat{E}}{3\hat{R}}\left[a(\delta_{ij})\right]^3 - \sqrt{8\pi\sigma\hat{E}\left[a(\delta ij)\right]^3} \quad (14)$$

The contact radius a in Eq. 14 if a function of the overlap $\delta_{ij} = ||\vec{r}_j - \vec{r}_i|| - R_i - R_j$ between the cell, allows to compute the cell-cell contact area, and can be obtained from:

$$\delta_{ij} = \frac{a^2}{\hat{R}} - \sqrt{\frac{2\pi\sigma}{\hat{E}}}a. \quad (15)$$

In the latter equations, $\hat{E}$ and $\hat{R}$ are defined as

$$\hat{E} = \left(\frac{1-\nu_i^2}{E_i} + \frac{1-\nu_j^2}{E_j}\right)^{-1} \text{ and } \hat{R} = \left(\frac{1}{R_i} + \frac{1}{R_j}\right)^{-1},$$

with E_i and E_j being the cell Young's moduli, v_i and v_j the Poisson numbers and R_i and R_j the radii of the cells i and j, respectively.

To enforce consistency with the by construction more accurate DCM that explicitly accounts for multi-body interactions, the Young modulus for every cell E_i in the JKR

model was replaced by an ”apparent” Young’s modulus $\tilde{E}_i$ that increases as function of the local cell density [12]:

$$\tilde{E}_i = E_i + a_0\tilde{d}_i + a_1\tilde{d}_i^2 + a_3\tilde{d}_i^3 + a_4\tilde{d}_i^4$$

Here, $\tilde{d}_i =< 1 - ||\vec{r}_j - \vec{r}_i||/(R_{ref,i} + R_{ref,j}) >$ is the dimensionless average cell-cell distance. The parameters ai can be determined in a calibration experiment, where one compresses a spheroid and measures the force between the cells [1,12].

Because the CBM and the DCM are used in hybrid mode, they can make contact with each other. Using the Maugis-Dugdale formulation this can be solved in a natural way. The contact between a CBM and a triangle of the DCM is resolved using the triangle-triangle contact formulation for two DCMs, yet one of the triangles circumscribing sphere is here replaced by the sphere of the CBM cell itself. When the contact force is calculated, it is for the CBM directly passed to its center of mass.

CBM: Migration forces

The same principles for modeling the migration force in the DCM are applied to the CBM, whereby the migration force in the CBM is directly applied to the cell center.

CBM: Cell division

As in the DCM, if the cell passed a critical volume $V_{crit} = 2V_{0,i}$, the cell undergoes mitosis and two new cells with volume $V_{0,i}/2$ are created. A simplified version of the division algorithm consists of placing directly two smaller daughter cells in the space originally filled by the mother cell at the end of the interphase [15,16]. When the two daughter cells are created, their reorganise in space driven by their cell-cell interaction force as well as the interaction forces of the two daughter cells with their other surrounding cells until mechanical equilibrium is reached. If the space filled by the mother cell is small, which is often the case for cells in the interior of a cell population, the local interaction forces occurring after replacing the mother cell by two spherical daughters, can adopt large (un-physiological) values leading to unrealistic large cell displacements. This can be circumvented by truncating the

contact force to a maximal value, or temporarily reducing the contact stiffness between the daughter cells during division.

Cell-to-cell signalling

In our model, we assume that Notch-jagged signalling between cholangiocytes and hepatocytes is governed by several of conditions. First, we assume that their common contact area must be sufficiently high. Thus, a minimal number of triangles (or surface area) of both cells must be in mutual contact: $A_T > A_{min}$, where A_T is the total contact area between two cells, and the parameter Amin is set arbitrarily to 20% of the cell surface. We found that this parameter does not influence the results significantly provided that A_{min} is larger than zero. However, this condition alone is not enough for a hepatocyte to transform into a cholangiocytes, as then any hepatocyte in the tissue adjacent to a cholangiocytes would be able to transform at some point, causing a homogeneous spread of cholangiocytes, which is not observed experimentally. Hence, the second condition for the transformation is that the hepatocyte must delimit an existing (possibly small) lumen. Third, we also need to introduce a transition contact time T_{sig} which specifies the minimum time the signalling needs in order for a hepatocyte to change to a cholangiocyte. A value T_{sig} = 0 would mean here that the transformation is immediate, which is not observed as some hepatocytes may express weak $SOX9^+$ signals but have a much larger size than a mature cholangiocyte. The signalling time is likely limited by the cell cycle time. When a hepatocyte gets the signal to transform, we assume that it will be fully differentiated upon the next cell division. We set here T_{sig} = 2h as default value.

Initialization of model and boundary conditions of bile-duct system

The cells are initially positioned side by side on concentric circles with curvature determined by the radius of the portal vein. The most inner layer represents the portal vein endothelial for which we assume the positions are fixed during the simulations. The second layer are the mesenchyme, followed by the hepatoblasts, partially represented by the DCM and the outer layers fully represented by the CBM.

A background pressure P_b of the CBM hepatoblasts needs to be exerted at the outer border of the segment as a result of radial tissue growth and resistance from nearby cells. This is achieved in the model by exerting an inward body force to the outermost border cells such that the inner hepatoblasts represented by the DCM have an average internal pressure of P_b. For the DCM, the pressure is calculated by Eq.6. For the CBM the pressure p_i on a cell *i* is derived from the virial stress and given by:

$$p_i = \frac{1}{3} tr(\sigma_i \qquad \sigma_i = \frac{1}{\mathcal{V}_i} \sum_j \left(\vec{F}_{ij} \otimes \vec{r}_{ij} \right) \quad \text{(16)}$$

, with

being the stress tensor quantifying the stresses cell *i* experiences subject to contact forces with $\vec{F}_{ij}$ other cells *j* [9]. Here, ~r_{ij} is the vector pointing from the center of cell *i* to the cell *j* with $||\vec{r}_{ij}|| = d_{ij}/2$ and V_i is the *sampling* volume which can be taken as the cell volume.

To ensure the cells remain in a planar configuration, we apply a small penalty force on the center-of-mass of all the cells each time the center of mass moves away from the XY plane. A simulation then starts in which only the cells positions are updated and a mechanical equilibrium is reached. This configuration is then used for all further simulations.

Calculation of the bile duct lumen area

We obtain the lumen area by considering the triangles of the cells that are marked by tracer particles. The procedure to compute the lumen volume is conceptually similar to how the volume of a cell is computed given its triangulated structure (see ref. [12]). First, the geometric center of all these triangles is computed, resulting in a vector pointing to the geometric center of the bile duct. From this point, we compute the signed volume of each tetrahedron with as base a marked triangle and as top the geometric center. The sign here is determined by the normal vector of the triangle. This is done for all marked triangles, and subsequently these volumes are then summed up. This gives a reasonable estimation of the volume confined by the marked cells.

Computational scheme executed during simulation

The simulations have been performed in TiSim, a computational platform for tissue simulations based on agent-based models. This software will be released in the near future. In every timestep, the new positions of the nodes of the DCM and the centers of the CBM are sought, given the forces that act on them. To compute these forces, one must execute a contact detection algorithm over the arrays of interacting objects to know which objects (triangles, spheres) can interact. This is a computationally expensive task which requires an effective method. We have here used a bounding box algorithm associated which each triangle and sphere. To compute the cell positions, the system of equations (1) and (2) in the main text are solved simultaneously. This is a linear system which can be solved efficiently by a conjugate gradient (CG) method. As the CG iterations are taking a large part of the computational time, especially as the system becomes larger, we have parallelized some loops in the CG algorithm using OpenMP. The optimal number of threads is here typically 2 to 3. After the velocities are calculated, we use an Euler scheme to obtain the positions. We have used in all simulations a stable timestep of 1s. The full bile duct system of cells after 24h of simulation time contains about 20000 nodes from the DCM, 500 nodes from the CBM, and 7500 tracer particles. The time so solve this system takes about 48h on a modern machine (Intel(R) Xeon(R) Gold 6136).

Based on the cell positions and forces, actions are undertaken in the algorithm. In Fig A2, a model flow chart is given with the principal algorithms that are executed every timestep. The algorithms that are cell -type dependent, are colored according to the cell type.

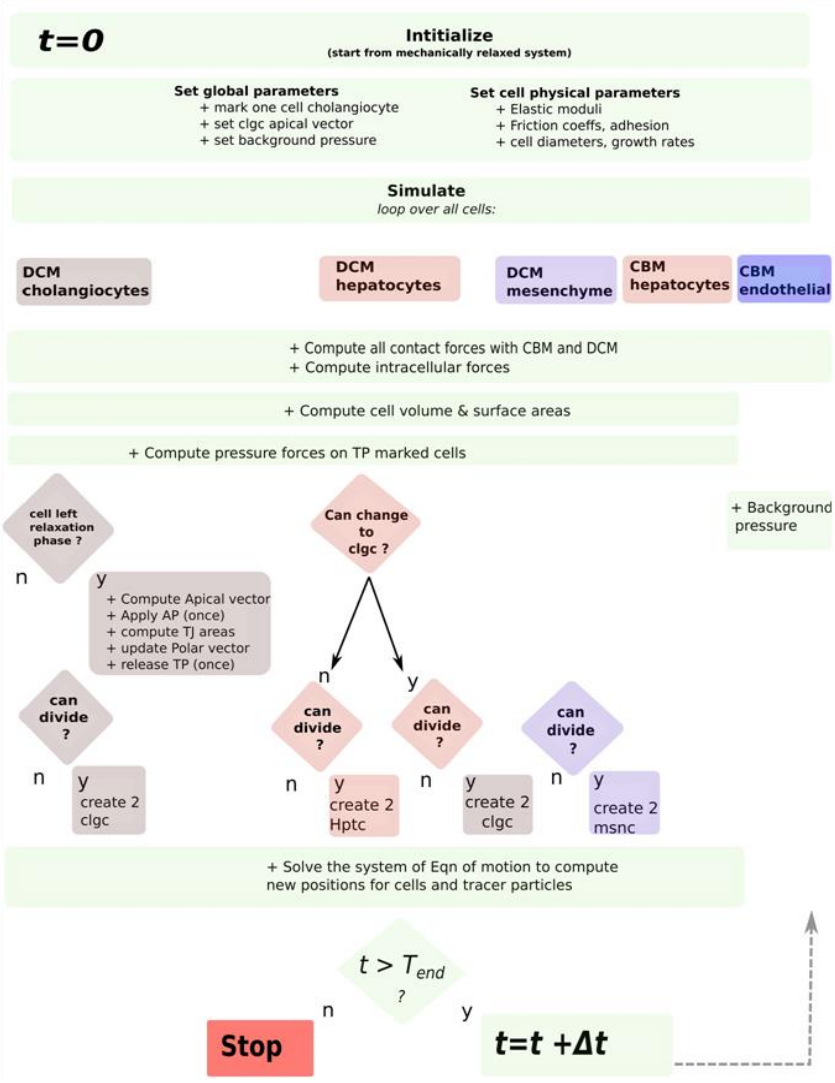

Figure A2. Computational scheme executed during simulation.

References

1. Van Liedekerke P, Neitsch J, Johann T, Alessandri K, Nassoy P, Drasdo D. Quantitative agent-based modeling reveals mechanical stress response of growing tumor spheroids is predictable over various growth conditions and cell lines. PLoS Computational Biology. 2019;doi:10.1371/journal.pcbi.1006273.

2. Boal D. Mechanics of the Cell. 2nd ed. Cambridge University Press; 2012.

3. Smeets B, Odenthal T, Keresztes J, Vanmaercke S, Van Liedekerke P, Tijskens E, Saeys W, Van Oosterwyck H, Ramon H. Modeling contact interactions between triangulated rounded bodies for the discrete element method Computer Methods in Applied Mechanics and Engineering; 2014, 227.

4. Smeets B, Cuvelier M, Peˇsek J, Ramon H. The Effect of Cortical Elasticity and Active Tension on Cell Adhesion Mechanics. Biophys J. 2019. doi:10.1016/j.bpj.2019.01.015.

5. P. Van Liedekerke, A. Buttenschoen, and D. Drasdo, “Off-lattice agent-based models for cell and tumor growth: Numerical methods, implementation, and applications,” in *Numerical Methods and Advanced Simulation in Biomechanics and Biological Processes*, Miguel Cerrolaza Sandra Shefelbine Diego Garz´on-Alvarado, 2017.

6. Maugis D Adhesion of spheres: the JKR-DMT transition using a Dugdale model. J Colloid Interface Sci 150(1):243–269.

7. Odenthal T, Smeets B, Van Liedekerke P, Tijskens E, Van Oosterwyck H, Ramon H. Analysis of Initial Cell Spreading Using Mechanistic Contact Formulations for a Deformable Cell Model. PLoS Computational Biology. 2013;9(10):e1003267. doi:10.1371/journal.pcbi.1003267.

8. Leckband D., Israelachvili J. Intermolecular forces in biology. Q Rev Biophys 34(2):105–267 2001.

9. Van Liedekerke P, Palm MM, Jagiella N, Drasdo D. Simulating tissue mechanics with agent-based models: concepts, perspectives and some novel results. Computational Particle Mechanics. 2015;2(4):401–444. doi:10.1007/s40571-015-0082-3.

10. Drasdo D, Hoehme S. Modeling the impact of granular embedding media, and pulling versus pushing cells on growing cell clones. New Journal of Physics. 2012;14(5):55025.

11. Jamali Y, Azimi M, Mofrad M RK, A sub-cellular viscoelastic model for cell population mechanics. PLoS One. 2010; doi:10.1371/journal.pone.0012097.

12. Van Liedekerke P, Neitsch J, Johann T, Warmt E, Gonza`lez-Valverde I, Hoehme S, et al. A quantitative high-resolution computational mechanics cell model for growing and regenerating tissues. Biomechanics and Modeling in Mechanobiology. 2020;doi:10.1007/s10237-019-01204-7.

13. Heck T, Vargas DA, Smeets B, Ramon H, Van Liedekerke P, Van Oosterwijck H. The role of actin protrusion dynamics in cell migration through a degradable viscoelastic extracellular matrix: Insights from a computational model. PLOS Computational Biology 16(1): e1007250. https://doi.org/10.1371/journal.pcbi.1007250.

14. Benhamouche-Trouillet S, O'Loughlin E, Liu CH, Polacheck W, Fitamant J, McKee M, et al. Proliferation-independent role of NF2 (Merlin) in limiting biliary morphogenesis. Development (Cambridge). 2018;doi:10.1242/dev.162123.

15. Schaller G, Meyer-Hermann M. Multicellular tumor spheroid in an off-lattice Voronoi-Delaunay cell model. Phys Rev E. 2005;71(5):51910. doi:10.1103/PhysRevE.71.051910.

16. Galle J, Loeffler M, Drasdo D. Modeling the effect of deregulated proliferation and apoptosis on the growth dynamics of epithelial cell populations in vitro. Biophysical journal. 2005;88(1):62–75.

17. Drasdo D, Hoehme S, Block M. On the Role of Physics in the Growth and Pattern Formation of Multi-Cellular Systems: What can we Learn from Individual-Cell Based Models. Journal of Statistical Physics. 2007;128:287–345.

18. Hoehme S, Brulport M, Bauer A, Bedawy E, Schormann W, Hermes M, et al. Prediction and validation of cell alignment along microvessels as order principle to restore tissue architecture in liver regeneration. Proceedings of the National Academy of Sciences. 2010;107(23):10371–10376.

3. Morphogenesis of hepatocyte canaliculi-bile duct junctions

In this section, I collected all the data.

This chapter constitutes the first description of the morphogenesis of junctions between developing bile ducts and hepatocyte canaliculi. Functional data will be collected by my host laboratory.

Introduction

Whereas the mechanisms of the hepatocyte and cholangiocyte differentiation have been investigated in detail, we do not currently understand how these two cell types connect to each other to form a functional intrahepatic biliary system. In the adult liver, bile canaliculi are delineated by the apical poles of adjacent hepatocytes. The canaliculi drain the bile towards the bile ducts and the junctions are constituted by so-called canals of Hering which are delineated both by hepatocytes and cholangiocytes (Fig. 1). In mouse livers, the canals of Hering are identified on tissue sections by co-immunostaining for CEACAM1 which labels the canaliculus, and for laminin which marks the basal pole of the cholangiocyte (Fig. 2).

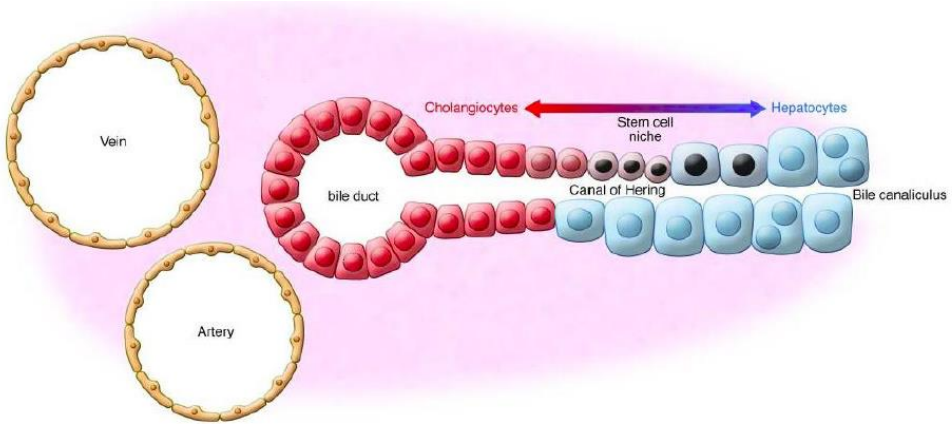

Figure 1. Organisation of a canal of Hering (From Kordes and Haussinger, 2013 and modified by de Roissart, 2018).

The aim of this chapter is to describe how the junctions between the canaliculi and bile ducts form at different stages of the liver development, and to identify at what stage these junctions become functional in embryonic livers.

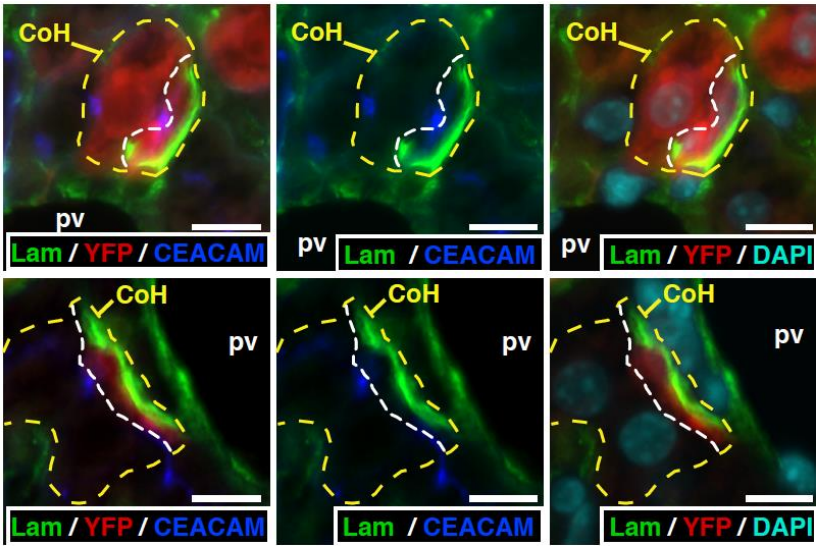

Figure 2. Canal of Hering in mouse liver. Laminin marks the basal pole of the cholangiocyte, CEACAM1 labels the lumen of the canaliculus, and DAPI stains nuclei. YFP labeling (red) in these experiments resulted from SOX9-CreER^{T2}; ROSA26R^{eYFP} mice. The white dotted line separates the cholangiocyte from the hepatocyte. CoH, canal of Hering (yellow dotted line); pv, portal vein (Carpentier et al., 2011).

Methods

2D immunostaining

Immunofluorescence stainings were performed on 6 µm sections of formalin-fixed paraffin-embedded tissues. Tissue sections were deparaffinized 3x 3 min in xylene, 3 min in 99%, 95%, 70% and 30% ethanol and deionized water. Antigen retrieval was performed by micro-wave heating for 10 min or at 95°C for 20 min, in 10 mM citrate pH 6. Sections were permeabilized for 5 min in 0.3% Triton X-100 in PBS before blocking for 45 min in 3% milk, 10% BSA, 0.3% Triton X-100 in PBS. The sections were incubated in blocking solution at 4°C overnight with the followings primary antibodies: anti-NHERF1 rabbit polyclonal antibody (#ab3452, Abcam, 1/500), anti-CEACAM1 mouse monoclonal antibody (#LS-C106710, LifeSpan,

1/1000) and anti-E-Cadherin mouse antibody (#610181, BD Biosciences, 1/200). Secondary antibodies were diluted in 10% BSA, 0.3% Triton X-100 in PBS and sections were incubated at 37°C for 1 h. Pictures for immunofluorescence were taken with Cell Observer Spinning Disk (Carl Zeiss) and Zen blue software.

3D immunostaining on free-floating sections

Immunofluorescence stainings were performed on 100 µm sections of formalin-fixed agarose-embedded tissues. Antigen retrieval was performed with a water bath for 30 min at 80°C in 10 mM sodium citrate pH 8.5. Sections were washed in PBS and permeabilized for 1 h in 0.3% Triton X-100 in PBS before blocking in 10% FBS, 2% BSA, 0.1% Triton X-100 in PBS for 2 h at RT. The sections were incubated in 10% FBS, 0.1% Triton X-100 in PBS for 24 h at 4°C, with the followings primary antibodies: anti-CEACAM1 mouse antibody (#LS-C106710, LifeSpan, 1/1000) and anti-Claudin7 rabbit (#ab27487, Abcam, 1/200). Secondary antibodies were diluted in 10% FBS, 0.1% Triton X-100 in PBS and sections were incubated at 4°C overnight. Pictures for immunofluorescence were taken with Cell Observer Spinning Disk (Carl Zeiss) and Zen blue software.

Bile flow visualisation

Pregnant mice were injected into the tail vein with 200 µl of fluorescent bile acid cholyl-lysyl-fluorescein (#451041, Corning) at the concentration of 18.5 µg/ml. Mice were sacrified 10 min later, and embryonic livers were collected and frozen with isopentane vapours immersed in liquid nitrogen (tissues must not be in contact with any liquid). Sections were prepared using cryostat and were directly imaged with the fluorescence microscope.

Results

Since the canaliculi are delineated by the apical poles of adjacent hepatocytes, we first co-stained embryonic liver sections with antibodies to simultaneously detect the apical pole of hepatocytes (CEACAM1) and cholangiocytes (NHERF1) (Benhamouche et al., 2018). This was performed at two developmental stages, namely E18.5 and P1. Fig. 3 illustrates a developing bile duct at E18.5, lined on the

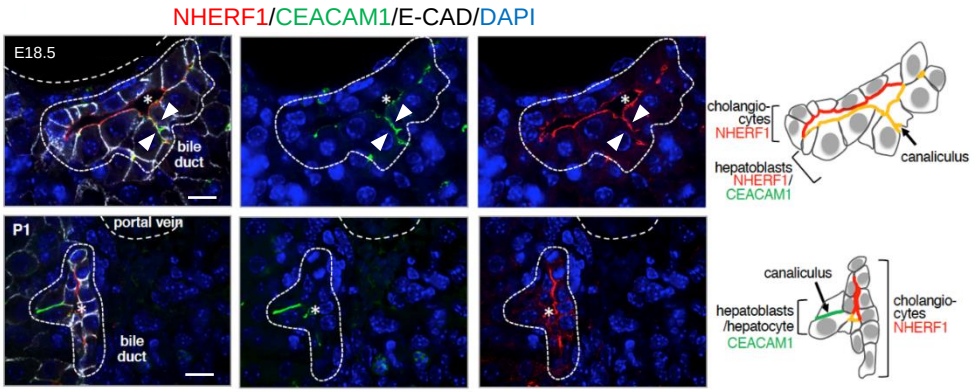

Figure 3. Development of duct canaliculi junctions. The apical pole of hepatocytes and cholangiocytes were labeled to detect NHERF1 and CEACAM1 expression at E18.5 (top panels) and P1 (bottom panels). DAPI stains nuclei, E-Cadherin delineates the basolateral poles of hepatocytes and cholangiocytes. *: bile duct lumen

portal side by NHERF1^{+} CEACAM1^{-} cholangiocytes, and on the parenchymal side by NHERF1^{+} CEACAM1^{+} hepatoblasts. While developing ducts are known to be asymmetrical at the onset of their formation, the particularity of the asymmetrical structure illustrated here were the two hepatoblasts (arrowheads) which establish a canalicular connection with the other hepatoblasts of the parenchyma. These two hepatoblasts were NHERF1^{+} CEACAM1^{+}. Later, at P1, hepatoblasts have matured to hepatocytes and their canaliculi connect with the lumen of NHERF1^{+} cholangiocytes; these canaliculi no longer express NHERF1 expression but maintain CEACAM1. Together these data show, first, that duct-canaliculi junctions form at a stage where developing bile ducts are still in asymmetrical configuration, and, second, that the gene expression profile of canaliculi evolves with time.

We next wished to visualise the junctions in three dimensions and immunostained 100 µm sections. The latter were analyzed by confocal microscopy and 3D images were reconstructed by confocal stacking (Fig. 4). These experiments were performed using anti-CEACAM1 antibodies to detect the canaliculi, and anti-Claudin7 antibodies which specifically mark the cholangiocytes (Seth et al., 2014). Surprisingly, we observed that hepatoblasts forming junctions with bile ducts express both CEACAM1 and Claudin7 at their canalicular membrane, whereas all other

hepatoblasts expressed only CEACAM1 indicating that Claudin7 specifically marks those hepatoblasts which form the duct-canaliculi junction.

Next, we wanted to demonstrate the functionality of these developing junctions, by visualising the bile flow in embryonic livers. We injected pregnant mice, at E16.5 and E18.5, with cholyl-lysyl-fluorescein (CLF), a fluorescein-labeled bile acid analog, and collected the livers 10 min after injection. At E16.5, accumulation of CLF was detected in developing ducts near some portal veins, as well as in canaliculi (Fig. 5). At E18.5, a higher number of ducts near the portal veins contained CLF. These data demonstrate that bile acids can flow from hepatoblasts to bile ducts starting at E16.5.

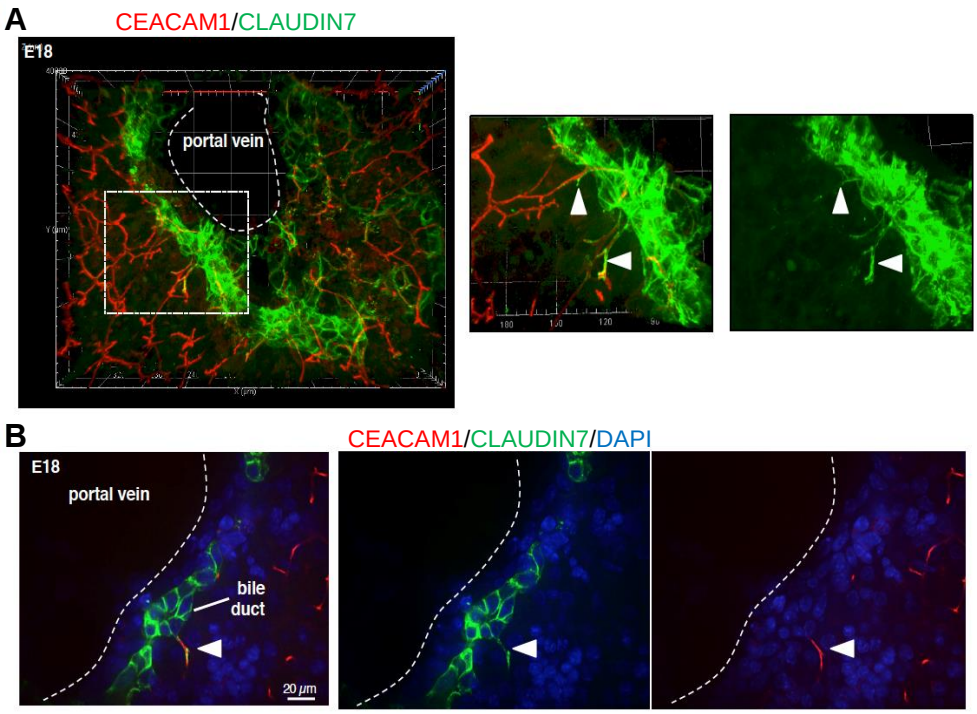

Figure 4. Expression of Claudin7 in bile duct-canaliculi junctions. (A) 3D reconstruction from confocal stackings of a branch of the portal vein surrounded by Claudin7^{+} bile ducts and CEACAM1^{+} hepatoblasts at E18.5. In addition, canaliculi of hepatocytes forming a junction with ducts express Claudin7. **(B)** Visualisation of duct-canaliculi junction on 2D sections from E18.5 mouse livers. Arrowheads point to expression of Claudin7 in canaliculi.

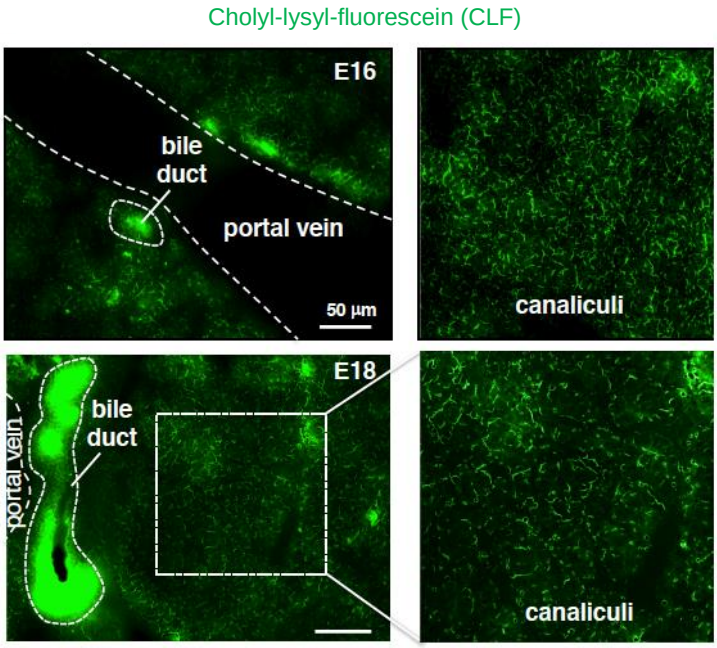

Figure 5. Bile flow visualisation. Pregnant females were injected with the CLF and embryonic livers were collected to visualise the flow of CLF in the liver.

Discussion

Despite that many studies have been devoted to liver development, the mechanisms controlling formation of bile duct-canaliculi junctions remain unknown. This results in part from the limited number of *in vitro* models available to investigate such morphogenic events. Recently, Tanimizu and coworkers (2021) identified 2D hepatobiliary culture conditions, in which the bile canalicular network in hepatocyte clusters is functionally connected to the biliary network, as evidenced by fluorescent bile acids flowing from caniliculi to duct-like structures delineated by cholangiocytes. Similarly, Ramli et al. (2020) developed 3D hepatic organoids in culture from induced pluripotent stem cells, and these organoids contained hepatocyte-like cells whose canaliculi functionally connected with biliary cysts. However, to our knowledge, no publication describes the mechanisms establishing canaliculi-duct connections.

Our observation that Claudin7 specifically marks those hepatoblasts that connect with the bile ducts opens some perspectives. Analyses of single cell RNA sequencing data (Su et al., 2017; Yang et al., 2017) did unfortunately not identify a subpopulation of Claudin7-expressing hepatoblasts, since the expression of the gene was not detected in these experiments. Identifying such subpopulations might have uncovered other specificities of these hepatoblasts.

Claudins are a family of 24 members with molecular weights between 20 kDa to 33 kDa. They are constituted of four transmembrane domains and two extracellular loops which are involved in homophilic and/or heterophilic interactions required for tight junction formation. Claudin7 is more widely expressed at the membrane of developing cholangiocytes. How this impacts its function in this cell type is not clear. We note that Claudin7 interacts with β1-integrin in colon cancer and lung cancer cells and inhibits proliferation and migration of the cells (Lu et al., 2015; Li et al., 2019) by promoting cell-matrix interactions. In case such interaction occurs in cholangiocytes, we suggest that Claudin7 may modulate the function of β1-integrin which is required for morphogenesis of a biliary luminal structures *in vitro*, most likely through binding to laminins: Tanimizu et al. (2012) showed that a line of liver progenitor cells is unable to form luminal cysts in 3D cultures when β1-integrin was inhibited by blocking antibodies; these authors also showed that laminins α1 and α5 are required for cholangiocyte differentiation and subsequent tube formation. In parallel, Claudin7 may form complexes with EpCAM and promote cell-cell adhesion (Le Naour and Zoller, 2008).

In hepatoblasts at E18.5, Claudin7 is restricted to the canaliculi, suggesting that it is here located at tight junctions. The wide expression in cholangiocytes and canalicular location in hepatocytes persists in adults, when the two cell types have matured (Holczbauer et al., 2014). However, at the onset of duct-canaliculi junction formation, Claudin7 is restricted to those hepatoblasts involved in establishing the junction, not in parenchymal hepatoblasts. At later stages, all hepatocytes express Claudin7 at the canalicular pole, yet a much lower level than in cholangiocytes (Holczbauer et al., 2014). In hepatocytes, it is likely that claudin7's functions relates

to tight junction organisation. However, how it is restricted to a subset of hepatoblasts in development and later expressed in all mature hepatocytes is unknown. Also, whether Claudin7 in hepatoblasts is required for the formation of duct-canaliculi junctions remains unknown as well, but could be investigated by loss-of-function experiments *in vivo* or *in vitro*.

References

Benhamouche-Trouillet, S., O'Loughlin, E., Liu, C.H., Polacheck, W., Fitamant, J., McKee, M., El-Bardeesy, N., Chen, C.S., McClatchey, A.I., 2018. Proliferation-independent role of NF2 (merlin) in limiting biliary morphogenesis. Development 145.

Carpentier, R., Suner, R.E., van Hul, N., Kopp, J.L., Beaudry, J.B., Cordi, S., Antoniou, A., Raynaud, P., Lepreux, S., Jacquemin, P., Leclercq, I.A., Sander, M., Lemaigre, F.P., 2011. Embryonic ductal plate cells give rise to cholangiocytes, periportal hepatocytes, and adult liver progenitor cells. Gastroenterology 141, 1432-1438, 1438 e1431-1434.

De Roissart, J., 2018. Functional role of the ductular reaction in the maintenance of the hepatobiliary bile flow, Faculté de médecine et médecine dentaire. Université Catholique de Louvain.

Holczbauer, A., Gyongyosi, B., Lotz, G., Torzsok, P., Kaposi-Novak, P., Szijarto, A., Tatrai, P., Kupcsulik, P., Schaff, Z., Kiss, A., 2014. Increased expression of claudin-1 and claudin-7 in liver cirrhosis and hepatocellular carcinoma. Pathol Oncol Res 20, 493-502.

Kordes, C., Haussinger, D., 2013. Hepatic stem cell niches. J Clin Invest 123, 1874-1880.

Le Naour, F., Zoller, M., 2008. The tumor antigen EpCAM: tetraspanins and the tight junction protein claudin-7, new partners, new functions. Front Biosci 13, 5847-5865.

Li, W., Xu, C., Wang, K., Ding, Y., Ding, L., 2019. Non-tight junction-related function of claudin-7 in interacting with integrinbeta1 to suppress colorectal cancer cell proliferation and migration. Cancer Manag Res 11, 1443-1451.

Lu, Z., Kim, D.H., Fan, J., Lu, Q., Verbanac, K., Ding, L., Renegar, R., Chen, Y.H., 2015. A non-tight junction function of claudin-7-Interaction with integrin signaling in suppressing lung cancer cell proliferation and detachment. Mol Cancer 14, 120.

Ramli, M.N.B., Lim, Y.S., Koe, C.T., Demircioglu, D., Tng, W., Gonzales, K.A.U., Tan, C.P., Szczerbinska, I., Liang, H., Soe, E.L., Lu, Z., Ariyachet, C., Yu, K.M., Koh, S.H., Yaw, L.P., Jumat, N.H.B., Lim, J.S.Y., Wright, G., Shabbir, A., Dan, Y.Y., Ng, H.H., Chan, Y.S., 2020. Human Pluripotent Stem Cell-Derived Organoids as Models of Liver Disease. Gastroenterology 159, 1471-1486 e1412.

Seth, A., Ye, J., Yu, N., Guez, F., Bedford, D.C., Neale, G.A., Cordi, S., Brindle, P.K., Lemaigre, F.P., Kaestner, K.H., Sosa-Pineda, B., 2014. Prox1 ablation in hepatic progenitors causes defective hepatocyte specification and increases biliary cell commitment. Development 141, 538-547.

Su, X., Shi, Y., Zou, X., Lu, Z.N., Xie, G., Yang, J.Y.H., Wu, C.C., Cui, X.F., He, K.Y., Luo, Q., Qu, Y.L., Wang, N., Wang, L., Han, Z.G., 2017. Single-cell RNA-Seq analysis reveals dynamic trajectories during mouse liver development. BMC Genomics 18, 946.

Tanimizu, N., Kikkawa, Y., Mitaka, T., Miyajima, A., 2012. alpha1- and alpha5-containing laminins regulate the development of bile ducts via beta1 integrin signals. J Biol Chem 287, 28586-28597.

Yang, L., Wang, W.H., Qiu, W.L., Guo, Z., Bi, E., Xu, C.R., 2017. A single-cell transcriptomic analysis reveals precise pathways and regulatory mechanisms underlying hepatoblast differentiation. Hepatology 66, 1387-1401.

General discussion and perspectives

In the present thesis, we investigated mechanisms driving morphogenesis of the bile ducts and hepatic arteries. First, when studying signalling interactions between mesenchymal cells and cholangiocytes in the portal space, we identified axon guidance genes of the Slit-Robo pathway as regulators of hepatic artery formation. Second, in collaboration with computational experts, we generated a quantitative computational model that was calibrated with morphometric data and which allows to predict the impact of the main drivers of biliary lumen formation. Third, following-up on our work on biliary lumen formation, we collected preliminary data describing how bile ducts connect with hepatocyte canaliculi in embryonic livers.

1. Axon guidance genes in liver development

We have discussed in detail the role of Slit-Robo signalling in the results chapter devoted to this pathway and proposed a number of perspectives to address how Slit-Robo might control the formation of the hepatic artery's *tunica media*. However, we suggest that investigation of other axon guidance pathways deserves attention, namely Eph/Ephrin, Semaphorin/Plexin-Neuropilin, and Netrin/DCC-Unc5-Unc40 which were identified in our gene expression profiling of embryonic cholangiocytes and mesenchymal cells. Moreover, single cell RNA sequencing by Wang et al. (2020) confirms the expression of members of these pathways in several liver cell types, including cholangiocytes and mesenchyme (Fig. 1). This raises the possibility of autocrine or paracrine regulation during biliary morphogenesis or mesenchyme growth.

1.1. Axon guidance pathways in liver

Similar to the Slit-Robo pathway, the role of the Ephrin, Semaphorin, and Netrin pathways have essentially been studied in hepatic diseases. The Semaphorin pathway was studied in liver fibrosis. HSCs increase their production of Semaphorin 7A upon TGFβ stimulation, and this is associated with a rise in fibrogenic and inflammation markers (De Minicis et al., 2013). Also, in a mouse model of liver injury,

Semaphorin 3E is produced by degenerating hepatocytes, thereby contributing to HSC activation and inhibition of sinusoidal angiogenesis (Yagai et al., 2014). After CCl_4-induced liver injury, the EphrinB2/EphB4 signalling pathway is activated in HSCs, promoting chemotaxis of sinusoidal endothelial cells for sinusoidal remodeling (Das et al., 2010). Another study established a role for EphrinB2 as a downstream mediator of PDGF in the process of HSC-driven angiogenesis (Semela et al., 2008). Netrin-1 is expressed in the liver and is known to control leukocyte trafficking during inflammation. This prompted researchers to evaluate the impact of administering Netrin-1 to a mouse model of APAP-induced hepatotoxicity and to demonstrate that exogenous Netrin-1 enhances tissue regeneration (Duan et al., 2020).

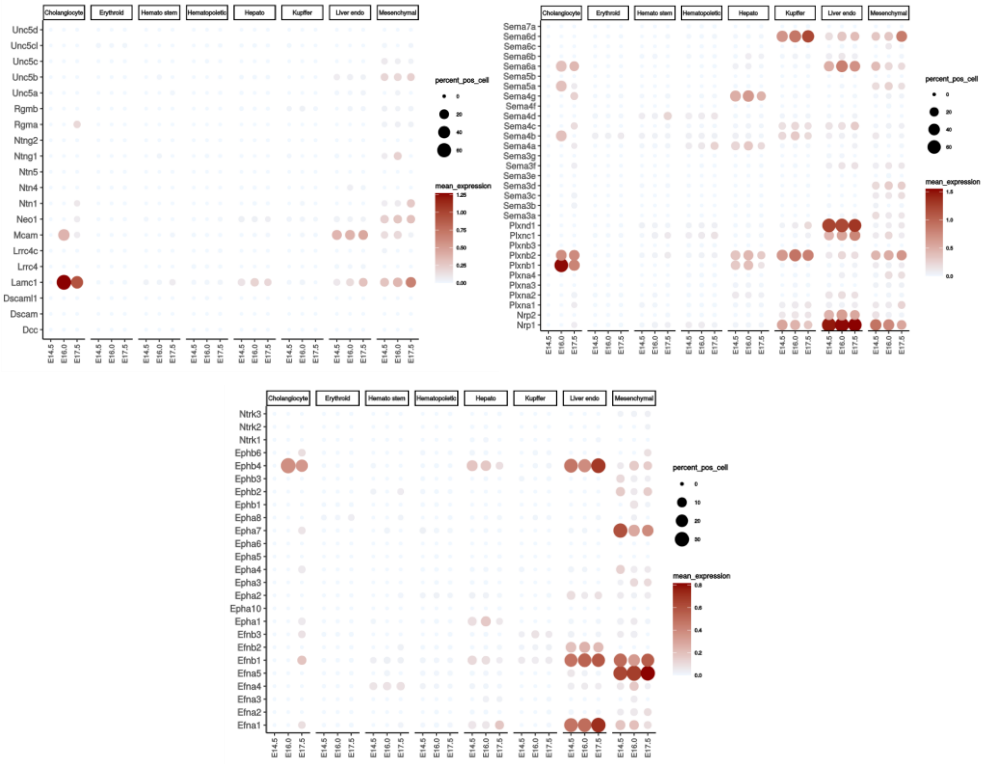

Figure 1. Expression of genes of the Netrin, Semaphorin and Ephrin pathways in developing liver. Single cell RNA sequencing performed on different embryonic liver cell types (Wang et al., 2020) shows, in the epithelial cells and mesenchyme, the gene expression of the three signalling pathways.

Taken together, these publications reveal a role for axon guidance genes in liver diseases, but the lack of information on these pathways during liver development would further justify research in embryonic liver.

1.2. Axon guidance pathways in VSMCs

Our work on Slit-Robo signalling underscores the importance of axon guidance genes in VSMC development. Beyond the topic of hepatic artery, it is known that a VSMC-specific GEF for Rho (Vsm-RhoGEF) is expressed in VSMCs of several organs including the liver. Its activity is regulated by EphrinA1-mediated activation of EphA4 receptor, thereby contributing to vascular contraction (Ogita et al., 2003). More closely related to our findings on hepatic arteries, mice lacking EphrinB2 in vascular smooth muscle develop vessel wall defects and aortic aneurysms. These phenotypes were associated with impaired Tiam1 expression and excessive activation of MAP kinase and JNK (Nakayama et al., 2013). The Netrin pathway is also involved in VSMC biology. Indeed, Netrin4 has been studied in VSMC adhesion and migration, and its overexpression increases their coverage of endothelial cells tubes. In this context, Netrin4 is required for blood vessel integrity, through regulation of both endothelial cells and VSMCs (Lejmi et al., 2014). Finally, the involvement of Semaphorins in VSMC development is illustrated by the observation that Semaphorin 3A favors formation of NRP1-Plexin A1 complexes at the expense of NRP1-PDGFRβ complex, thus inhibiting phosphorylation of PDGFRβ and reducing VSMC proliferation and migration (Lu et al., 2019). Together, these data underline the importance of axon guidance pathways in VSMC structure and function, and suggest that they may control hepatic artery morphogenesis.

1.3. Perspectives

The above data support a hitherto undescribed role of axon guidance genes in liver development. We propose to address this issue using the same approach as for Slit-Robo signalling, namely expression profiling starting with the genes expressed at a high level, followed by functional *in vivo* and *in vitro* studies. We are aware of the difficulty that loss of function experiments may meet with difficulties related to redundant functions of members of the axon guidance pathways.

2. Biliary lumen formation

Biological processes such as lumen formation rely on multiple intracellular and intercellular mechanisms whose complexity are hard to grasp. Structure and function evolve with time, adding additional complexity to the biological system. In this context, computational modelling enables the integration of distinct mechanisms and allows quantitative simulations that test hypotheses, eventually guiding the design of the most appropriate experiments (Drasdo et al., 2014).

In the present thesis, we collected morphometric data to calibrate a computational model with which we tested the potential involvement of several processes that were candidate regulators of biliary lumen formation. We found that the simultaneous contribution of directed cell division of cholangiocytes, local osmotic effects generated by salt excretion in the lumen, and temporally controlled differentiation of hepatoblasts to cholangiocytes are likely essential for appropriate biliary lumen formation in embryonic livers. In contrast, apical constriction of cholangiocytes was predicted to moderately affect luminal size.

2.1. Advantages and limitations of our combined computional/ experimental approach

In vivo and *in vitro* experimental studies are labor-intensive, time-consuming and often expensive. Their combination with *in silico* studies can reduce the number of hypothesis to be tested, and consequently the costs and time devoted to solve questions. Importantly, *in silico* modelling can raise questions that cannot emerge from experimental observations only. Also, the number of animals used in research is expected to be reduced. Finally, computational simulations can predict what cannot easily be illustrated with biological data.

The limitations of modelling are on one hand related to the computing power required by the specific software and high-performance computing hardware. On the other hand, the modelling is restricted by the known information introduced into the model, whereas experimental observations *in vivo* still integrate the unknowns of biology. An example of such limitations is that our *in silico* approach of biliary lumen formation

was disconnected from hepatocyte canaliculi formation, despite that *in vivo* there is evidence that canaliculi formation contributes to biliary morphogenesis. For instance, in results chapter (3nd part), we show that at E16.5 bile acids can transit through canaliculi and become detectable in developing ducts near the portal vein. This allows us to hypothesise that the entry of bile components from canaliculi into the ducts may contribute to determine the ducts' luminal size. Recent work indicates that bile acids secreted by the hepatocytes in the canaliculi reach the bile ducts by diffusion (reviewed in Vartak et al., 2021). Bile acids can trigger intracellular production of cAMP by cholangiocytes following interactions with the TGR5 receptor, and subsequently induce osmotic flow in the ducts. Together, we can suggest that the establishment of canaliculi-duct junctions influences biliary lumen size. However, our data also show that the smallest biliary luminal structures are delineated by only a few cholangiocytes and hepatoblasts which are not connected with canaliculi (Fig. 1A in results chapter, 2nd part). Therefore, the onset of biliary lumen formation is likely independent from canaliculi formation and from the presence of bile.

2.2. Perspectives

As briefly discussed in the results chapter, this model could support studies on hepatic diseases, in particular when lumina need to be created, *e.g.* during ductular reactions establishing new connections between the biliary system and the hepatocyte canaliculi (Clerbaux et al., 2019). The implementation of the model, possibly recalibrated with new morphometric data, could help identifying (de)regulated processes occuring in disease. For instance, it is noteworthy that our model underlines the impact of tight junctions while others have shown that Grhl2 positively regulates the lumen size of bile ducts by establishing functional tight junctions (Senga et al., 2012). Similarly, the importance of hepatoblast-to-cholangiocyte differentiation is highlighted in the model, and it is this process which is perturbed in Alagille syndrome, a disease characterised by biliary paucity.

The project of modelling biliary lumen formation was initiated with the aim to contribute quantitative information to facilitate *in vitro* production of liver tissue. Regenerative therapy of the liver indeed requires the production of functional hepatic

tissue that is able to recapitulate liver functions, including secretion and elimination of bile. We therefore hope that our model will help experimentalists to diagnose the processes that might need to be improved to appropriately control *in vitro* development of bile ducts, for instance by identifying genes that are misexpressed and whose corrected expression is expected to restore essential processes predicted by the modelling.

3. Claudin7 function in development of bile duct-canaliculi junctions

Mechanisms controlling the formation of duct-canaliculi junctions are still unknown. During my thesis, I collected images in developing liver illustrating the morphogenesis of these junctions. The more surprising result is the detection of Claudin7 in hepatoblasts connected with the developing bile ducts. This finding raises several new questions.

3.1. General roles of Claudins

Our data reveal that Claudin7 is expressed at the apical pole of hepatoblasts connected with bile ducts, while cholangiocytes lining bile ducts express Claudin7 at the basolateral side. We thus need to investigate in which conditions Claudin7 is expressed in the apical or basolateral sides. Some Claudins, such as Claudin-1, -3, -5, -11, -14 and -19, have a sealing function in tight junctions (TJ) while Claudins-2, -10, -15 and -17 have paracellular channel functions (Castro Dias et al., 2019; Gunzel and Fromm, 2012). For instance, in the liver, Claudin2 was proposed to allow water to move across hepatic TJ from the sinusoidal to the canalicular side (Matsumoto et al., 2014). We note however that this specific role of Claudin2 is recently debated (Vartak et al., 2021).

In skin, small intestine, colon, kidney and lung, Claudin7 is associated with basolateral membranes (Li et al., 2004; Coyne et al., 2003; Fujita et al., 2006; Brandner et al., 2015), and some of its functions are to regulate paracellular permeability and cell attachment through β1-integrin (Lu et al., 2015; Tanaka et al., 2015). However, the apical expression of Claudin7 is barely described in the

literature. Only one study established that EpCAM depletion in MDCK culture leads to small amount of Claudin7 localized to TJ, and that EpCAM-Claudin7 interaction negatively regulates epithelial migration by inhibiting ERK and actomyosin contractility (Barth et al., 2018).

Taken together, the literature does to my knowledge not provide many cues to understand how and why Claudin7 becomes located at the apical pole of hepatoblasts connecting with bile ducts. Therefore, studying the role of Claudin7 is of obvious interest.

3.2. Perspectives

Several approaches can be proposed to study Claudin7. *In vivo*, loxP-flanked *Claudin7* (Tanaka et al., 2015; Xu et al., 2021) can be inactivated in mice using Alfp-Cre, and bile acid flow can subsequently be visualised by CLF injection. The limitations of this approach are that mating the mice is time-consuming, and that the use of *Alfp-Cre* will inactivate *Claudin7* in the hepatoblasts forming junctions as well as in the cholangiocytes. Therefore, *in utero* injection of Claudin7-siRNA in the vitelline veins of pregnant mice is expected to more specifically target the hepatoblasts when the siRNAs are integrated into lipid nanoparticles (Belicova et al., 2021). This strategy does not require mouse matings, but is not strictly liver specific and may be associated with general toxicity. Such toxicity might be bypassed by resorting to *in vitro* strategies. In the latter context, however, we still need to obtain a culture system that faithfully recapitulates the formation of the canaliculi-duct junctions. Would such system be developed, *Claudin7* gain- and loss-of-function studies would become relevant (Lioni et al., 2007).

Finally, I only investigated Claudin7 expression in embryonic livers (E18.5), not in adult mice. Others detected Claudin7 at low levels in parenchymal hepatocytes (Holczbauer et al., 2014), but to our knowledge Claudin7 was not studied in adult duct-canaliculi junctions or canals of Hering. Neither has it been investigated at those sites where ductular reactions connect biliary lumina with canaliculi. Since developmental processes are often recapitulated in adult regenerating livers, it is

tempting to speculate that Claudin7 might display interesting properties both in developing and regenerating liver.

4. Biliary morphogenesis

In the present study, we investigated different aspects of biliary morphogenesis: the formation of the bile duct lumen, its connection with the hepatocyte canaliculi, and the involvement of hepatic mesenchyme in bile duct morphogenesis (or the involvement of cholangiocytes in mesenchyme growth).

Although the study was split into three parts, we anticipate that these parts can be linked in a near future. First, both biliary lumen formation and development of bile duct-canaliculi junctions are connected, not only morphologically, but likely also mechanistically via the secretion of bile by hepatocytes. To strengthen this link, reconstituting the duct-canaliculi junction *in vitro* would represent a significant adavance. In that context, our computer model of bile duct lumen formation should integrate the junction with canaliculi.

We did not find clues that the mesenchyme controls formation of the biliary lumen or duct-canaliculi junctions. However, the presence of mesenchymal cells near cholangiocytes during lumen and junction formation, which is well illustrated by the expression of eYFP in *Sm22-Cre;Rosa26R*^{eYFP} mice (data from C. De Schrevel), together with the expression profile of axon guidance genes showing potential interactions between mesenchyme and cholangiocytes via pathways that have not been explored (e.g. ephrin), still convince us that mesenchyme can control biliary morphogenesis.

Bibliography

Adams, M.T., Gilbert, J.M., Hinojosa Paiz, J., Bowman, F.M., Blum, B., 2018. Endocrine cell type sorting and mature architecture in the islets of Langerhans require expression of Roundabout receptors in beta cells. Sci Rep 8, 10876.

Andrew, D.J., Ewald, A.J., 2010. Morphogenesis of epithelial tubes: Insights into tube formation, elongation, and elaboration. Dev Biol 341, 34-55.

Andrews, W.D., Barber, M., Parnavelas, J.G., 2007. Slit-Robo interactions during cortical development. J Anat 211, 188-198.

Andrews, T.S., Atif, J., Liu, J.C., Perciani, C.T., Ma, X.-Z., Thoeni, C., Slyper, M., Eraslan, G., Segerstolpe, A., Manuel, J., Chung, S., Winter, E., Cirlan, I., Khuu, N., Fischer, S., Rozenblatt-Rosen, O., Regev, A., McGilvray, I.D., Bader, G.D., MacParland, S.A., 2021. Single Cell, Single Nucleus and Spatial RNA Sequencing of the Human Liver Identifies Hepatic Stellate Cell and Cholangiocyte Heterogeneity. BioRxiv doi: https://doi.org/10.1101/2021.03.27.436882

Anselmo, M.A., Dalvin, S., Prodhan, P., Komatsuzaki, K., Aidlen, J.T., Schnitzer, J.J., Wu, J.Y., Kinane, T.B., 2003. Slit and robo: expression patterns in lung development. Gene Expr Patterns 3, 13-19.

Antoniou, A., Raynaud, P., Cordi, S., Zong, Y., Tronche, F., Stanger, B.Z., Jacquemin, P., Pierreux, C.E., Clotman, F., Lemaigre, F.P., 2009. Intrahepatic bile ducts develop according to a new mode of tubulogenesis regulated by the transcription factor SOX9. Gastroenterology 136, 2325-2333.

Ao, J.Y., Chai, Z.T., Zhang, Y.Y., Zhu, X.D., Kong, L.Q., Zhang, N., Ye, B.G., Cai, H., Gao, D.M., Sun, H.C., 2015. Robo1 promotes angiogenesis in hepatocellular carcinoma through the Rho family of guanosine triphosphatases' signaling pathway. Tumour Biol 36, 8413-8424.

Asahina, K., Sato, H., Yamasaki, C., Kataoka, M., Shiokawa, M., Katayama, S., Tateno, C., Yoshizato, K., 2002. Pleiotrophin/heparin-binding growth-associated molecule as a mitogen of rat hepatocytes and its role in regeneration and development of liver. Am J Pathol 160, 2191-2205.

Asahina, K., Zhou, B., Pu, W.T., Tsukamoto, H., 2011. Septum transversum-derived mesothelium gives rise to hepatic stellate cells and perivascular mesenchymal cells in developing mouse liver. Hepatology 53, 983-995.

Asahina, K., 2012. Hepatic stellate cell progenitor cells. J Gastroenterol Hepatol 27 Suppl 2, 80-84.

Avci, M.E., Konu, O., Yagci, T., 2008. Quantification of SLIT-ROBO transcripts in hepatocellular carcinoma reveals two groups of genes with coordinate expression. BMC Cancer 8, 392.

Bacakova, L., Travnickova, M., Filona, E., Matějka, R., Stepanovska, J., Musilkova, J., Zarubova, J., Molitor, M., 2018. The Role of Vascular Smooth Muscle Cells in the Physiology and Pathophysiology of Blood Vessels, in: Sakuma, K. (Ed.), Muscle Cell and Tissue - Current Status of Research Field. IntechOpen, pp. 229-257.

Baeten, J.T., Lilly, B., 2015. Differential Regulation of NOTCH2 and NOTCH3 Contribute to Their Unique Functions in Vascular Smooth Muscle Cells. J Biol Chem 290, 16226-16237.

Baeten, J.T., Lilly, B., 2017. Notch Signaling in Vascular Smooth Muscle Cells. Adv Pharmacol 78, 351-382.

Ballard, M.S., Hinck, L., 2012. A roundabout way to cancer. Adv Cancer Res 114, 187-235.

Barth, A.I.M., Kim, H., Riedel-Kruse, I.H., 2018. Regulation of epithelial migration by epithelial cell adhesion molecule requires its Claudin-7 interaction domain. PLoS One 13, e0204957.

Bayzit Koçer, İ., Yörük, M.D., Bilge, O., 2018. Arterial sources of the liver: two different variations with a brief review. Glob Surg 4 (1): DOI: 10.15761/GOS.1000175.

Beaussier, M., Wendum, D., Schiffer, E., Dumont, S., Rey, C., Lienhart, A., Housset, C., 2007. Prominent contribution of portal mesenchymal cells to liver fibrosis in ischemic and obstructive cholestatic injuries. Lab Invest 87, 292-303.

Belicova, L., Repnik, U., Delpierre, J., Gralinska, E., Seifert, S., Valenzuela, J.I., Morales-Navarrete, H.A., Franke, C., Raagel, H., Shcherbinina, E., Prikazchikova, T., Koteliansky, V., Vingron, M., Kalaidzidis, Y.L., Zatsepin, T., Zerial, M., 2021. Anisotropic expansion of hepatocyte lumina enforced by apical bulkheads. J Cell Biol 220, in press.

Benhamouche-Trouillet, S., O'Loughlin, E., Liu, C.H., Polacheck, W., Fitamant, J., McKee, M., El-Bardeesy, N., Chen, C.S., McClatchey, A.I., 2018. Proliferation-independent role of NF2 (merlin) in limiting biliary morphogenesis. Development 145 (9):dev162123.

Berg, T., Rountree, C.B., Lee, L., Estrada, J., Sala, F.G., Choe, A., Veltmaat, J.M., De Langhe, S., Lee, R., Tsukamoto, H., Crooks, G.M., Bellusci, S., Wang, K.S., 2007. Fibroblast growth factor 10 is critical for liver growth during embryogenesis

and controls hepatoblast survival via beta-catenin activation. Hepatology 46, 1187-1197.

Betts, J.G., Desai, P., Johnson, E., Johnson, J.E., Koro, O., Kruse, D., Poe, B., Wise, J.A., Womble, M., Young, K.A., 2013. The digestive system, Anatomy and Physiology, https://openstax.org/details/books/anatomy-and-physiology, pp. 1085-1148.

Bisiak, F., McCarthy, A.A., 2019. Structure and Function of Roundabout Receptors. Subcell Biochem 93, 291-319.

Blasky, A.J., Mangan, A., Prekeris, R., 2015. Polarized protein transport and lumen formation during epithelial tissue morphogenesis. Annu Rev Cell Dev Biol 31, 575-591.

Blockus, H., Chedotal, A., 2016. Slit-Robo signaling. Development 143, 3037-3044.

Brandner, J.M., Zorn-Kruppa, M., Yoshida, T., Moll, I., Beck, L.A., De Benedetto, A., 2015. Epidermal tight junctions in health and disease. Tissue Barriers 3, e974451.

Carmeliet, P., 2000. Mechanisms of angiogenesis and arteriogenesis. Nat Med 6, 389-395.

Carneiro, C., Brito, J., Bilreiro, C., Barros, M., Bahia, C., Santiago, I., Caseiro-Alves, F., 2019. All about portal vein: a pictorial display to anatomy, variants and physiopathology. Insights Imaging 10, 38.

Carotti, S., Morini, S., Carpino, G., Gaudio, E., 2020. Liver histology, in: Florentina Radu-Ionita, N.T.P., Mariana JingaIon C. Tintoiu, Zhonghua Sun, Ecaterina Bontas (Ed.), Liver Diseases. Springer, Cham, pp. 17-28.

Carpentier, R., Suner, R.E., van Hul, N., Kopp, J.L., Beaudry, J.B., Cordi, S., Antoniou, A., Raynaud, P., Lepreux, S., Jacquemin, P., Leclercq, I.A., Sander, M., Lemaigre, F.P., 2011. Embryonic ductal plate cells give rise to cholangiocytes, periportal hepatocytes, and adult liver progenitor cells. Gastroenterology 141, 1432-1438.

Chakraborty, R., Chatterjee, P., Dave, J.M., Ostriker, A.C., Greif, D.M., Rzucidlo, E.M., Martin, K.A., 2021. Targeting smooth muscle cell phenotypic switching in vascular disease. JVS: Vascular Science 2, 79-94.

Chang, J., Lan, T., Li, C., Ji, X., Zheng, L., Gou, H., Ou, Y., Wu, T., Qi, C., Zhang, Q., Li, J., Gu, Q., Wen, D., Cao, L., Qiao, L., Ding, Y., Wang, L., 2015. Activation of Slit2-Robo1 signaling promotes liver fibrosis. J Hepatol 63, 1413-1420.

Clerbaux, L.A., Manco, R., Van Hul, N., Bouzin, C., Sciarra, A., Sempoux, C., Theise, N.D., Leclercq, I.A., 2019. Invasive Ductular Reaction Operates Hepatobiliary Junctions upon Hepatocellular Injury in Rodents and Humans. Am J Pathol 189, 1569-1581.

Clotman, F., Lannoy, V.J., Reber, M., Cereghini, S., Cassiman, D., Jacquemin, P., Roskams, T., Rousseau, G.G., Lemaigre, F.P., 2002. The onecut transcription factor HNF6 is required for normal development of the biliary tract. Development 129, 1819-1828.

Clotman, F., Jacquemin, P., Plumb-Rudewiez, N., Pierreux, C.E., Van der Smissen, P., Dietz, H.C., Courtoy, P.J., Rousseau, G.G., Lemaigre, F.P., 2005. Control of liver cell fate decision by a gradient of TGF beta signaling modulated by Onecut transcription factors. Genes Dev 19, 1849-1854.

Collardeau-Frachon, S., Scoazec, J.Y., 2008. Vascular development and differentiation during human liver organogenesis. Anat Rec (Hoboken) 291, 614-627.

Cordi, S., Godard, C., Saandi, T., Jacquemin, P., Monga, S.P., Colnot, S., Lemaigre, F.P., 2016. Role of beta-catenin in development of bile ducts. Differentiation 91, 42-49.

Coyne, C.B., Gambling, T.M., Boucher, R.C., Carson, J.L., Johnson, L.G., 2003. Role of claudin interactions in airway tight junctional permeability. Am J Physiol Lung Cell Mol Physiol 285, L1166-1178.

Crawford, L.W., Foley, J.F., Elmore, S.A., 2010. Histology atlas of the developing mouse hepatobiliary system with emphasis on embryonic days 9.5-18.5. Toxicol Pathol 38, 872-906.

Cullen, J.M., Stalker, M.J., 2016. Chapter 2 - Liver and Biliary System, in: Maxie, M.G. (Ed.), Kennedy & Palmer's Pathology of Domestic Animals: Volume 2 (Sixth Edition), pp. 258-352.

Das, A., Shergill, U., Thakur, L., Sinha, S., Urrutia, R., Mukhopadhyay, D., Shah, V.H., 2010. Ephrin B2/EphB4 pathway in hepatic stellate cells stimulates Erk-dependent VEGF production and sinusoidal endothelial cell recruitment. Am J Physiol Gastrointest Liver Physiol 298, G908-915.

Datta, A., Bryant, D.M., Mostov, K.E., 2011. Molecular regulation of lumen morphogenesis. Curr Biol 21, R126-136.

De Minicis, S., Rychlicki, C., Agostinelli, L., Saccomanno, S., Trozzi, L., Candelaresi, C., Bataller, R., Millan, C., Brenner, D.A., Vivarelli, M., Mocchegiani, F., Marzioni, M., Benedetti, A., Svegliati-Baroni, G., 2013. Semaphorin 7A contributes to TGF-beta-mediated liver fibrogenesis. Am J Pathol 183, 820-830.

Castro Dias, M., Mapunda, J.A., Vladymyrov, M., Engelhardt, B., 2019. Structure and Junctional Complexes of Endothelial, Epithelial and Glial Brain Barriers. Int J Mol Sci 20 (21):5372.

Dobie, R., Wilson-Kanamori, J.R., Henderson, B.E.P., Smith, J.R., Matchett, K.P., Portman, J.R., Wallenborg, K., Picelli, S., Zagorska, A., Pendem, S.V., Hudson, T.E., Wu, M.M., Budas, G.R., Breckenridge, D.G., Harrison, E.M., Mole, D.J., Wigmore, S.J., Ramachandran, P., Ponting, C.P., Teichmann, S.A., Marioni, J.C., Henderson, N.C., 2019. Single-Cell Transcriptomics Uncovers Zonation of Function in the Mesenchyme during Liver Fibrosis. Cell Rep 29, 1832-1847 e1838.

Domenga, V., Fardoux, P., Lacombe, P., Monet, M., Maciazek, J., Krebs, L.T., Klonjkowski, B., Berrou, E., Mericskay, M., Li, Z., Tournier-Lasserve, E., Gridley, T., Joutel, A., 2004. Notch3 is required for arterial identity and maturation of vascular smooth muscle cells. Genes Dev 18, 2730-2735.

Domyan, E.T., Branchfield, K., Gibson, D.A., Naiche, L.A., Lewandoski, M., Tessier-Lavigne, M., Ma, L., Sun, X., 2013. Roundabout receptors are critical for foregut separation from the body wall. Dev Cell 24, 52-63.

Dou, C., Wang, H., Zhou, G., Zhu, H., Wen, H., Xu, S., 2018. Slit3 regulates migration of endothelial progenitor cells by activation of the RhoA/Rho kinase pathway. Int J Clin Exp Pathol 11, 3398-3404.

Drasdo, D., Hoehme, S., Hengstler, J.G., 2014. How predictive quantitative modelling of tissue organisation can inform liver disease pathogenesis. J Hepatol 61, 951-956.

Duan, L., Woolbright, B.L., Jaeschke, H., Ramachandran, A., 2020. Late Protective Effect of Netrin-1 in the Murine Acetaminophen Hepatotoxicity Model. Toxicol Sci 175, 168-181.

Escot, S., Willnow, D., Naumann, H., Di Francescantonio, S., Spagnoli, F.M., 2018. Robo signalling controls pancreatic progenitor identity by regulating Tead transcription factors. Nat Commun 9, 5082.

Fabris, L., Cadamuro, M., Libbrecht, L., Raynaud, P., Spirli, C., Fiorotto, R., Okolicsanyi, L., Lemaigre, F., Strazzabosco, M., Roskams, T., 2008. Epithelial expression of angiogenic growth factors modulate arterial vasculogenesis in human liver development. Hepatology 47, 719-728.

Fan, X., Li, Q., Pisarek-Horowitz, A., Rasouly, H.M., Wang, X., Bonegio, R.G., Wang, H., McLaughlin, M., Mangos, S., Kalluri, R., Holzman, L.B., Drummond, I.A., Brown, D., Salant, D.J., Lu, W., 2012. Inhibitory effects of Robo2 on nephrin: a crosstalk between positive and negative signals regulating podocyte structure. Cell Rep 2, 52-61.

Fu, D., Wakabayashi, Y., Ido, Y., Lippincott-Schwartz, J., Arias, I.M., 2010. Regulation of bile canalicular network formation and maintenance by AMP-activated protein kinase and LKB1. J Cell Sci 123, 3294-3302.

Fujita, H., Chiba, H., Yokozaki, H., Sakai, N., Sugimoto, K., Wada, T., Kojima, T., Yamashita, T., Sawada, N., 2006. Differential expression and subcellular localization of claudin-7, -8, -12, -13, and -15 along the mouse intestine. J Histochem Cytochem 54, 933-944.

Giancotti, A., Monti, M., Nevi, L., Safarikia, S., D'Ambrosio, V., Brunelli, R., Pajno, C., Corno, S., Di Donato, V., Musella, A., Chiappetta, M.F., Bosco, D., Panici, P.B., Alvaro, D., Cardinale, V., 2019. Functions and the Emerging Role of the Foetal Liver into Regenerative Medicine. Cells 8(8):914.

Gilbert, J.M., Adams, M.T., Sharon, N., Jayaraaman, H., Blum, B., 2020. Morphogenesis of the islets of Langerhans is guided by extra-endocrine Slit2/3 signals. Mol Cell Biol, 41(3):e00451-20.

Gissen, P., Arias, I.M., 2015. Structural and functional hepatocyte polarity and liver disease. J Hepatol 63, 1023-1037.

Goldman, O., Han, S., Hamou, W., Jodon de Villeroche, V., Uzan, G., Lickert, H., Gouon-Evans, V., 2014. Endoderm generates endothelial cells during liver development. Stem Cell Reports 3, 556-565.

Goncalves, A.N., Correia-Pinto, J., Nogueira-Silva, C., 2020. ROBO2 signaling in lung development regulates SOX2/SOX9 balance, branching morphogenesis and is dysregulated in nitrofen-induced congenital diaphragmatic hernia. Respir Res 21, 302.

Gonda, Y., Namba, T., Hanashima, C., 2020. Beyond Axon Guidance: Roles of Slit-Robo Signaling in Neocortical Formation. Front Cell Dev Biol 8, 607415.

Gordillo, M., Evans, T., Gouon-Evans, V., 2015. Orchestrating liver development. Development 142, 2094-2108.

Grieshammer, U., Le, M., Plump, A.S., Wang, F., Tessier-Lavigne, M., Martin, G.R., 2004. SLIT2-mediated ROBO2 signaling restricts kidney induction to a single site. Dev Cell 6, 709-717.

Guijarro-Munoz, I., Cuesta, A.M., Alvarez-Cienfuegos, A., Geng, J.G., Alvarez-Vallina, L., Sanz, L., 2012. The axonal repellent Slit2 inhibits pericyte migration: potential implications in angiogenesis. Exp Cell Res 318, 371-378.

Gunzel, D., Fromm, M., 2012. Claudins and other tight junction proteins. Compr Physiol 2, 1819-1852.

Halpern, K.B., Shenhav, R., Massalha, H., Toth, B., Egozi, A., Massasa, E.E., Medgalia, C., David, E., Giladi, A., Moor, A.E., Porat, Z., Amit, I., Itzkovitz, S., 2018. Paired-cell sequencing enables spatial gene expression mapping of liver endothelial cells. Nat Biotechnol 36, 962-970.

Harburg, G., Compton, J., Liu, W., Iwai, N., Zada, S., Marlow, R., Strickland, P., Zeng, Y.A., Hinck, L., 2014. SLIT/ROBO2 signaling promotes mammary stem cell senescence by inhibiting Wnt signaling. Stem Cell Reports 3, 385-393.

Harris, K.P., Tepass, U., 2010. Cdc42 and vesicle trafficking in polarized cells. Traffic 11, 1272-1279.

Hick, A.C., van Eyll, J.M., Cordi, S., Forez, C., Passante, L., Kohara, H., Nagasawa, T., Vanderhaeghen, P., Courtoy, P.J., Rousseau, G.G., Lemaigre, F.P., Pierreux, C.E., 2009. Mechanism of primitive duct formation in the pancreas and submandibular glands: a role for SDF-1. BMC Dev Biol 9, 66.

Higashiyama, H., Uemura, M., Igarashi, H., Kurohmaru, M., Kanai-Azuma, M., Kanai, Y., 2018. Anatomy and development of the extrahepatic biliary system in mouse and rat: a perspective on the evolutionary loss of the gallbladder. J Anat 232, 134-145.

Hofmann, J.J., Zovein, A.C., Koh, H., Radtke, F., Weinmaster, G., Iruela-Arispe, M.L., 2010. Jagged1 in the portal vein mesenchyme regulates intrahepatic bile duct development: insights into Alagille syndrome. Development 137, 4061-4072.

Homolya, L., Fu, D., Sengupta, P., Jarnik, M., Gillet, J.P., Vitale-Cross, L., Gutkind, J.S., Lippincott-Schwartz, J., Arias, I.M., 2014. LKB1/AMPK and PKA control ABCB11 trafficking and polarization in hepatocytes. PLoS One 9, e91921.

Hwang, D.Y., Kohl, S., Fan, X., Vivante, A., Chan, S., Dworschak, G.C., Schulz, J., van Eerde, A.M., Hilger, A.C., Gee, H.Y., Pennimpede, T., Herrmann, B.G., van de Hoek, G., Renkema, K.Y., Schell, C., Huber, T.B., Reutter, H.M., Soliman, N.A., Stajic, N., Bogdanovic, R., Kehinde, E.O., Lifton, R.P., Tasic, V., Lu, W., Hildebrandt, F., 2015. Mutations of the SLIT2-ROBO2 pathway genes SLIT2 and SRGAP1 confer risk for congenital anomalies of the kidney and urinary tract. Hum Genet 134, 905-916.

Ijpenberg, A., Perez-Pomares, J.M., Guadix, J.A., Carmona, R., Portillo-Sanchez, V., Macias, D., Hohenstein, P., Miles, C.M., Hastie, N.D., Munoz-Chapuli, R., 2007. Wt1 and retinoic acid signaling are essential for stellate cell development and liver morphogenesis. Dev Biol 312, 157-170.

Inverso, D., Shi, J., Lee, K.H., Jakab, M., Ben-Moshe, S., Kulkarni, S.R., Schneider, M., Wang, G., Komeili, M., Velez, P.A., Riedel, M., Spegg, C., Ruppert, T., Schaeffer-Reiss, C., Helm, D., Singh, I., Boutros, M., Chintharlapalli, S., Heikenwalder, M.,

Itzkovitz, S., Augustin, H.G., 2021. A spatial vascular transcriptomic, proteomic, and phosphoproteomic atlas unveils an angiocrine Tie-Wnt signaling axis in the liver. Dev Cell 56, 1677-1693.

Ishibashi, H., Nakamura, M., Komori, A., Migita, K., Shimoda, S., 2009. Liver architecture, cell function, and disease. Semin Immunopathol 31, 399-409.

Ito, Y., Matsui, T., Kamiya, A., Kinoshita, T., Miyajima, A., 2000. Retroviral gene transfer of signaling molecules into murine fetal hepatocytes defines distinct roles for the STAT3 and ras pathways during hepatic development. Hepatology 32, 1370-1376.

Ito, H., Funahashi, S., Yamauchi, N., Shibahara, J., Midorikawa, Y., Kawai, S., Kinoshita, Y., Watanabe, A., Hippo, Y., Ohtomo, T., Iwanari, H., Nakajima, A., Makuuchi, M., Fukayama, M., Hirata, Y., Hamakubo, T., Kodama, T., Tsuchiya, M., Aburatani, H., 2006. Identification of ROBO1 as a novel hepatocellular carcinoma antigen and a potential therapeutic and diagnostic target. Clin Cancer Res 12, 3257-3264.

Jakab, C., Kiss, A., Schaff, Z., Szabo, Z., Rusvai, M., Galfi, P., Szabara, A., Sterczer, A., Kulka, J., 2010. Claudin-7 protein differentiates canine cholangiocarcinoma from hepatocellular carcinoma. Histol Histopathol 25, 857-864.

Jewett, C.E., Prekeris, R., 2018. Insane in the apical membrane: Trafficking events mediating apicobasal epithelial polarity during tube morphogenesis. Traffic, 16:10.1111/tra.12579.

Jones, C.A., Nishiya, N., London, N.R., Zhu, W., Sorensen, L.K., Chan, A.C., Lim, C.J., Chen, H., Zhang, Q., Schultz, P.G., Hayallah, A.M., Thomas, K.R., Famulok, M., Zhang, K., Ginsberg, M.H., Li, D.Y., 2009. Slit2-Robo4 signalling promotes vascular stability by blocking Arf6 activity. Nat Cell Biol 11, 1325-1331.

Kalra, A., Yetiskul, E., Wehrle, C.J., Tuma, F., 2021. Physiology, Liver, StatPearls, Treasure Island (FL).

Kamiya, A., Kinoshita, T., Ito, Y., Matsui, T., Morikawa, Y., Senba, E., Nakashima, K., Taga, T., Yoshida, K., Kishimoto, T., Miyajima, A., 1999. Fetal liver development requires a paracrine action of oncostatin M through the gp130 signal transducer. EMBO J 18, 2127-2136.

Kanno, N., LeSage, G., Glaser, S., Alvaro, D., Alpini, G., 2000. Functional heterogeneity of the intrahepatic biliary epithelium. Hepatology 31, 555-561.

Karin, D., Koyama, Y., Brenner, D., Kisseleva, T., 2016. The characteristics of activated portal fibroblasts/myofibroblasts in liver fibrosis. Differentiation 92, 84-92.

Katoh, K., Kano, Y., Noda, Y., 2011. Rho-associated kinase-dependent contraction of stress fibres and the organization of focal adhesions. J R Soc Interface 8, 305-311.

Kesavan, G., Sand, F.W., Greiner, T.U., Johansson, J.K., Kobberup, S., Wu, X., Brakebusch, C., Semb, H., 2009. Cdc42-mediated tubulogenesis controls cell specification. Cell 139, 791-801.

Khan, J.A., Mendelson, A., Kunisaki, Y., Birbrair, A., Kou, Y., Arnal-Estape, A., Pinho, S., Ciero, P., Nakahara, F., Ma'ayan, A., Bergman, A., Merad, M., Frenette, P.S., 2016. Fetal liver hematopoietic stem cell niches associate with portal vessels. Science 351, 176-180.

Koch, A.W., Mathivet, T., Larrivee, B., Tong, R.K., Kowalski, J., Pibouin-Fragner, L., Bouvree, K., Stawicki, S., Nicholes, K., Rathore, N., Scales, S.J., Luis, E., del Toro, R., Freitas, C., Breant, C., Michaud, A., Corvol, P., Thomas, J.L., Wu, Y., Peale, F., Watts, R.J., Tessier-Lavigne, M., Bagri, A., Eichmann, A., 2011. Robo4 maintains vessel integrity and inhibits angiogenesis by interacting with UNC5B. Dev Cell 20, 33-46.

Koch, P.S., Lee, K.H., Goerdt, S., Augustin, H.G., 2021. Angiodiversity and organotypic functions of sinusoidal endothelial cells. Angiogenesis 24, 289-310.

Kodama, Y., Hijikata, M., Kageyama, R., Shimotohno, K., Chiba, T., 2004. The role of notch signaling in the development of intrahepatic bile ducts. Gastroenterology 127, 1775-1786.

Krishna, M., 2013. Microscopic Anatomy of the Liver. Clinical Liver Disease 2, 4-7.

Lassau, J.P., Bastian, D., 1983. Organogenesis of the venous structures of the human liver: A hemodynamic theory. Anat. Clin 5, 97–102.

Lazaro-Dieguez, F., Cohen, D., Fernandez, D., Hodgson, L., van Ijzendoorn, S.C., Musch, A., 2013. Par1b links lumen polarity with LGN-NuMA positioning for distinct epithelial cell division phenotypes. J Cell Biol 203, 251-264.

Lee, D.H., Park, J.O., Kim, T.S., Kim, S.K., Kim, T.H., Kim, M.C., Park, G.S., Kim, J.H., Kuninaka, S., Olson, E.N., Saya, H., Kim, S.Y., Lee, H., Lim, D.S., 2016. LATS-YAP/TAZ controls lineage specification by regulating TGFbeta signaling and Hnf4alpha expression during liver development. Nat Commun 7, 11961.

Lee, J.L., Streuli, C.H., 2014. Integrins and epithelial cell polarity. J Cell Sci 127, 3217-3225.

Lejmi, E., Bouras, I., Camelo, S., Roumieux, M., Minet, N., Lere-Dean, C., Merkulova-Rainon, T., Autret, G., Vayssettes, C., Clement, O., Plouet, J., Leconte,

L., 2014. Netrin-4 promotes mural cell adhesion and recruitment to endothelial cells. Vasc Cell 6, 1.

Lemaigre, F.P., 2020. Development of the Intrahepatic and Extrahepatic Biliary Tract: A Framework for Understanding Congenital Diseases. Annu Rev Pathol 15, 1-22.

Lemoinne, S., Cadoret, A., Rautou, P.E., El Mourabit, H., Ratziu, V., Corpechot, C., Rey, C., Bosselut, N., Barbu, V., Wendum, D., Feldmann, G., Boulanger, C., Henegar, C., Housset, C., Thabut, D., 2015. Portal myofibroblasts promote vascular remodeling underlying cirrhosis formation through the release of microparticles. Hepatology 61, 1041-1055.

Li, B., Dorrell, C., Canaday, P.S., Pelz, C., Haft, A., Finegold, M., Grompe, M., 2017. Adult Mouse Liver Contains Two Distinct Populations of Cholangiocytes. Stem Cell Reports 9, 478-489.

Li, C., Yang, G., Lin, L., Xuan, Y., Yan, S., Ji, X., Song, F., Lu, M., Lan, T., 2019. Slit2 signaling contributes to cholestatic fibrosis in mice by activation of hepatic stellate cells. Exp Cell Res 385, 111626.

Li, L., Krantz, I.D., Deng, Y., Genin, A., Banta, A.B., Collins, C.C., Qi, M., Trask, B.J., Kuo, W.L., Cochran, J., Costa, T., Pierpont, M.E., Rand, E.B., Piccoli, D.A., Hood, L., Spinner, N.B., 1997. Alagille syndrome is caused by mutations in human Jagged1, which encodes a ligand for Notch1. Nat Genet 16, 243-251.

Li, W.Y., Huey, C.L., Yu, A.S., 2004. Expression of claudin-7 and -8 along the mouse nephron. Am J Physiol Renal Physiol 286, F1063-1071.

Li, Y., Wang, J., Asahina, K., 2013. Mesothelial cells give rise to hepatic stellate cells and myofibroblasts via mesothelial-mesenchymal transition in liver injury. Proc Natl Acad Sci U S A 110, 2324-2329.

Lioni, M., Brafford, P., Andl, C., Rustgi, A., El-Deiry, W., Herlyn, M., Smalley, K.S., 2007. Dysregulation of claudin-7 leads to loss of E-cadherin expression and the increased invasion of esophageal squamous cell carcinoma cells. Am J Pathol 170, 709-721.

Liu, D., Hou, J., Hu, X., Wang, X., Xiao, Y., Mou, Y., De Leon, H., 2006. Neuronal chemorepellent Slit2 inhibits vascular smooth muscle cell migration by suppressing small GTPase Rac1 activation. Circ Res 98, 480-489.

Lokmane, L., Haumaitre, C., Garcia-Villalba, P., Anselme, I., Schneider-Maunoury, S., Cereghini, S., 2008. Crucial role of vHNF1 in vertebrate hepatic specification. Development 135, 2777-2786.

Long, H., Sabatier, C., Ma, L., Plump, A., Yuan, W., Ornitz, D.M., Tamada, A., Murakami, F., Goodman, C.S., Tessier-Lavigne, M., 2004. Conserved roles for Slit and Robo proteins in midline commissural axon guidance. Neuron 42, 213-223.

Lozier, J., McCright, B., Gridley, T., 2008. Notch signaling regulates bile duct morphogenesis in mice. PLoS One 3, e1851.

Lu, W., van Eerde, A.M., Fan, X., Quintero-Rivera, F., Kulkarni, S., Ferguson, H., Kim, H.G., Fan, Y., Xi, Q., Li, Q.G., Sanlaville, D., Andrews, W., Sundaresan, V., Bi, W., Yan, J., Giltay, J.C., Wijmenga, C., de Jong, T.P., Feather, S.A., Woolf, A.S., Rao, Y., Lupski, J.R., Eccles, M.R., Quade, B.J., Gusella, J.F., Morton, C.C., Maas, R.L., 2007. Disruption of ROBO2 is associated with urinary tract anomalies and confers risk of vesicoureteral reflux. Am J Hum Genet 80, 616-632.

Lu, Z., Kim, D.H., Fan, J., Lu, Q., Verbanac, K., Ding, L., Renegar, R., Chen, Y.H., 2015. A non-tight junction function of claudin-7-Interaction with integrin signaling in suppressing lung cancer cell proliferation and detachment. Mol Cancer 14, 120.

Lua, I., Asahina, K., 2016. The Role of Mesothelial Cells in Liver Development, Injury, and Regeneration. Gut Liver 10, 166-176.

Lubarsky, B., Krasnow, M.A., 2003. Tube morphogenesis: making and shaping biological tubes. Cell 112, 19-28.

Lucas, B., Hardin, J., 2017. Mind the (sr)GAP - roles of Slit-Robo GAPs in neurons, brains and beyond. J Cell Sci 130, 3965-3974.

Macias, H., Moran, A., Samara, Y., Moreno, M., Compton, J.E., Harburg, G., Strickland, P., Hinck, L., 2011. SLIT/ROBO1 signaling suppresses mammary branching morphogenesis by limiting basal cell number. Dev Cell 20, 827-840.

Mano, Y., Aishima, S., Fukuhara, T., Tanaka, Y., Kubo, Y., Motomura, T., Toshima, T., Iguchi, T., Shirabe, K., Maehara, Y., Oda, Y., 2013. Decreased roundabout 1 expression promotes development of intrahepatic cholangiocarcinoma. Hum Pathol 44, 2419-2426.

Margolis, B., Borg, J.P., 2005. Apicobasal polarity complexes. J Cell Sci 118, 5157-5159.

Matsumoto, K., Yoshitomi, H., Rossant, J., Zaret, K.S., 2001. Liver organogenesis promoted by endothelial cells prior to vascular function. Science 294, 559-563.

Matsumoto, K., Imasato, M., Yamazaki, Y., Tanaka, H., Watanabe, M., Eguchi, H., Nagano, H., Hikita, H., Tatsumi, T., Takehara, T., Tamura, A., Tsukita, S., 2014. Claudin 2 deficiency reduces bile flow and increases susceptibility to cholesterol gallstone disease in mice. Gastroenterology 147, 1134-1145.

McConnell, R.E., Edward van Veen, J., Vidaki, M., Kwiatkowski, A.V., Meyer, A.S., Gertler, F.B., 2016. A requirement for filopodia extension toward Slit during Robo-mediated axon repulsion. J Cell Biol 213, 261-274.

McDaniell, R., Warthen, D.M., Sanchez-Lara, P.A., Pai, A., Krantz, I.D., Piccoli, D.A., Spinner, N.B., 2006. NOTCH2 mutations cause Alagille syndrome, a heterogeneous disorder of the notch signaling pathway. Am J Hum Genet 79, 169-173.

Miki, H., Sasaki, T., Takai, Y., Takenawa, T., 1998. Induction of filopodium formation by a WASP-related actin-depolymerizing protein N-WASP. Nature 391, 93-96.

Molina, L.M., Zhu, J., Li, Q., Pradhan-Sundd, T., Krutsenko, Y., Sayed, K., Jenkins, N., Vats, R., Bhushan, B., Ko, S., Hu, S., Poddar, M., Singh, S., Tao, J., Sundd, P., Singhi, A., Watkins, S., Ma, X., Benos, P.V., Feranchak, A., Michalopoulos, G., Nejak-Bowen, K., Watson, A., Bell, A., Monga, S.P., 2021. Compensatory hepatic adaptation accompanies permanent absence of intrahepatic biliary network due to YAP1 loss in liver progenitors. Cell Rep 36, 109310.

Mommersteeg, M.T., Andrews, W.D., Ypsilanti, A.R., Zelina, P., Yeh, M.L., Norden, J., Kispert, A., Chedotal, A., Christoffels, V.M., Parnavelas, J.G., 2013. Slit-roundabout signaling regulates the development of the cardiac systemic venous return and pericardium. Circ Res 112, 465-475.

Mommersteeg, M.T., Yeh, M.L., Parnavelas, J.G., Andrews, W.D., 2015. Disrupted Slit-Robo signalling results in membranous ventricular septum defects and bicuspid aortic valves. Cardiovasc Res 106, 55-66.

Morales-Navarrete, H., Nonaka, H., Scholich, A., Segovia-Miranda, F., de Back, W., Meyer, K., Bogorad, R.L., Koteliansky, V., Brusch, L., Kalaidzidis, Y., Julicher, F., Friedrich, B.M., Zerial, M., 2019. Liquid-crystal organization of liver tissue. Elife 8:e44860.

Morini, S., Carpino, G., Carotti, S., Gaudio, E., 2020. Anatomy and Embryology of the Liver, in: Florentina Radu-Ionita, N.T.P., Mariana Jingalon C. Tintoiu, Zhonghua Sun, Ecaterina Bontas (Ed.), Liver Diseases. Springer, Cham, pp. 3-16.

Myllymaki, S.M., Teravainen, T.P., Manninen, A., 2011. Two distinct integrin-mediated mechanisms contribute to apical lumen formation in epithelial cells. PLoS One 6, e19453.

Nakayama, A., Nakayama, M., Turner, C.J., Hoing, S., Lepore, J.J., Adams, R.H., 2013. Ephrin-B2 controls PDGFRbeta internalization and signaling. Genes Dev 27, 2576-2589.

Neuman, M.G., 2020. Hepatotoxicity: Mechanisms of Liver Injury, in: Florentina Radu-Ionita, N.T.P., Mariana JingaIon C. Tintoiu, Zhonghua Sun, Ecaterina Bontas (Ed.), Liver Diseases. Springer, Cham, pp. 75-84.

Ng, L., Chow, A.K.M., Man, J.H.W., Yau, T.C.C., Wan, T.M.H., Iyer, D.N., Kwan, V.H.T., Poon, R.T.P., Pang, R.W.C., Law, W.L., 2018. Suppression of Slit3 induces tumor proliferation and chemoresistance in hepatocellular carcinoma through activation of GSK3beta/beta-catenin pathway. BMC Cancer 18, 621.

Noseda, M., Fu, Y., Niessen, K., Wong, F., Chang, L., McLean, G., Karsan, A., 2006. Smooth Muscle alpha-actin is a direct target of Notch/CSL. Circ Res 98, 1468-1470.

Ober, E.A., Lemaigre, F.P., 2018. Development of the liver: Insights into organ and tissue morphogenesis. J Hepatol 68, 1049-1062.

Oda, T., Elkahloun, A.G., Pike, B.L., Okajima, K., Krantz, I.D., Genin, A., Piccoli, D.A., Meltzer, P.S., Spinner, N.B., Collins, F.S., Chandrasekharappa, S.C., 1997. Mutations in the human Jagged1 gene are responsible for Alagille syndrome. Nat Genet 16, 235-242.

Ogita, H., Kunimoto, S., Kamioka, Y., Sawa, H., Masuda, M., Mochizuki, N., 2003. EphA4-mediated Rho activation via Vsm-RhoGEF expressed specifically in vascular smooth muscle cells. Circ Res 93, 23-31.

Park, K.W., Morrison, C.M., Sorensen, L.K., Jones, C.A., Rao, Y., Chien, C.B., Wu, J.Y., Urness, L.D., Li, D.Y., 2003. Robo4 is a vascular-specific receptor that inhibits endothelial migration. Dev Biol 261, 251-267.

Parviz, F., Matullo, C., Garrison, W.D., Savatski, L., Adamson, J.W., Ning, G., Kaestner, K.H., Rossi, J.M., Zaret, K.S., Duncan, S.A., 2003. Hepatocyte nuclear factor 4alpha controls the development of a hepatic epithelium and liver morphogenesis. Nat Genet 34, 292-296.

Payen, V.L., Lavergne, A., Sarika, N.A., Colonval, M., Karim, L., Deckers, M., Najimi, M., Coppieters, W., Charloteaux, B., Sokal, E.M., El Taghdouini, A., 2021. Single Cell, Single Nucleus and Spatial RNA Sequencing of the Human Liver Identifies Hepatic Stellate Cell and Cholangiocyte Heterogeneity. JHEP Reports 3, 1-20.

Payushina, O. V., 2012. "Hematopoietic Microenvironment in the Fetal Liver: Roles of Different Cell Populations", International Scholarly Research Notices, vol. 2012, , 7p.

Pepe-Mooney, B.J., Dill, M.T., Alemany, A., Ordovas-Montanes, J., Matsushita, Y., Rao, A., Sen, A., Miyazaki, M., Anakk, S., Dawson, P.A., Ono, N., Shalek, A.K., van Oudenaarden, A., Camargo, F.D., 2019. Single-Cell Analysis of the Liver Epithelium

Reveals Dynamic Heterogeneity and an Essential Role for YAP in Homeostasis and Regeneration. Cell Stem Cell 25, 23-38.

Poisson, J., Lemoinne, S., Boulanger, C., Durand, F., Moreau, R., Valla, D., Rautou, P.E., 2017. Liver sinusoidal endothelial cells: Physiology and role in liver diseases. J Hepatol 66, 212-227.

Poncy, A., Antoniou, A., Cordi, S., Pierreux, C.E., Jacquemin, P., Lemaigre, F.P., 2015. Transcription factors SOX4 and SOX9 cooperatively control development of bile ducts. Dev Biol 404, 136-148.

Rama, N., Dubrac, A., Mathivet, T., Ni Charthaigh, R.A., Genet, G., Cristofaro, B., Pibouin-Fragner, L., Ma, L., Eichmann, A., Chedotal, A., 2015. Slit2 signaling through Robo1 and Robo2 is required for retinal neovascularization. Nat Med 21, 483-491.

Rhee, J., Buchan, T., Zukerberg, L., Lilien, J., Balsamo, J., 2007. Cables links Robo-bound Abl kinase to N-cadherin-bound beta-catenin to mediate Slit-induced modulation of adhesion and transcription. Nat Cell Biol 9, 883-892.

Rodés J, Benhamou J-P, Blei A, Reichen J, M, R., 2007. Textbook of Hepatology: From Basic Science to Clinical Practice, 3rd Edition ed. Blackwell Publishing.

Rogers, A.B., Dintzis, R.Z., 2018. 13 - Hepatobiliary system, in: Treuting, P.M., Montine, K.S., Dintzis, S.M. (Eds.), Comparative Anatomy and Histology, 2nd ed. Academic Press, pp. 229-239.

Russell, S.A., Bashaw, G.J., 2018. Axon guidance pathways and the control of gene expression. Dev Dyn 247, 571-580.

Sakaguchi, T.F., Sadler, K.C., Crosnier, C., Stainier, D.Y., 2008. Endothelial signals modulate hepatocyte apicobasal polarization in zebrafish. Curr Biol 18, 1565-1571.

Samama, B., Boehm, N., 2005. Reelin immunoreactivity in lymphatics and liver during development and adult life. Anat Rec A Discov Mol Cell Evol Biol 285, 595-599.

Saxena, R., Theise, N., 2004. Canals of Hering: recent insights and current knowledge. Semin Liver Dis 24, 43-48.

Schluter, M.A., Margolis, B., 2009. Apical lumen formation in renal epithelia. J Am Soc Nephrol 20, 1444-1452.

Semela, D., Das, A., Langer, D., Kang, N., Leof, E., Shah, V., 2008. Platelet-derived growth factor signaling through Ephrin-B2 regulates hepatic vascular structure and function. Gastroenterology 135, 671-679.

Senga, K., Mostov, K.E., Mitaka, T., Miyajima, A., Tanimizu, N., 2012. Grainyhead-like 2 regulates epithelial morphogenesis by establishing functional tight junctions through the organization of a molecular network among claudin3, claudin4, and Rab25. Mol Biol Cell 23, 2845-2855.

Sheldon, H., Andre, M., Legg, J.A., Heal, P., Herbert, J.M., Sainson, R., Sharma, A.S., Kitajewski, J.K., Heath, V.L., Bicknell, R., 2009. Active involvement of Robo1 and Robo4 in filopodia formation and endothelial cell motility mediated via WASP and other actin nucleation-promoting factors. FASEB J 23, 513-522.

Shewan, A., Eastburn, D.J., Mostov, K., 2011. Phosphoinositides in cell architecture. Cold Spring Harb Perspect Biol 3, a004796.

Si-Tayeb, K., Lemaigre, F.P., Duncan, S.A., 2010. Organogenesis and development of the liver. Dev Cell 18, 175-189.

Sigurbjornsdottir, S., Mathew, R., Leptin, M., 2014. Molecular mechanisms of de novo lumen formation. Nat Rev Mol Cell Biol 15, 665-676.

Slim, C.L., Lazaro-Dieguez, F., Bijlard, M., Toussaint, M.J., de Bruin, A., Du, Q., Musch, A., van Ijzendoorn, S.C., 2013. Par1b induces asymmetric inheritance of plasma membrane domains via LGN-dependent mitotic spindle orientation in proliferating hepatocytes. PLoS Biol 11, e1001739.

Slim, C., 2014. The polarized architecture of hepatocytes: Regulation by intrinsic and extrinsic factors. PhD Thesis, University of Groningen.

Son, S., Kojima, T., Decaens, C., Yamaguchi, H., Ito, T., Imamura, M., Murata, M., Tanaka, S., Chiba, H., Hirata, K., Sawada, N., 2009. Knockdown of tight junction protein claudin-2 prevents bile canalicular formation in WIF-B9 cells. Histochem Cell Biol 131, 411-424.

Spence, J.R., Lange, A.W., Lin, S.C., Kaestner, K.H., Lowy, A.M., Kim, I., Whitsett, J.A., Wells, J.M., 2009. Sox17 regulates organ lineage segregation of ventral foregut progenitor cells. Dev Cell 17, 62-74.

Steffen, A., Ladwein, M., Dimchev, G.A., Hein, A., Schwenkmezger, L., Arens, S., Ladwein, K.I., Margit Holleboom, J., Schur, F., Victor Small, J., Schwarz, J., Gerhard, R., Faix, J., Stradal, T.E., Brakebusch, C., Rottner, K., 2013. Rac function is crucial for cell migration but is not required for spreading and focal adhesion formation. J Cell Sci 126, 4572-4588.

Suzuki, K., Tanaka, M., Watanabe, N., Saito, S., Nonaka, H., Miyajima, A., 2008. p75 Neurotrophin receptor is a marker for precursors of stellate cells and portal fibroblasts in mouse fetal liver. Gastroenterology 135, 270-281 e273.

Tabibian, J.H., Masyuk, A.I., Masyuk, T.V., O'Hara, S.P., LaRusso, N.F., 2013. Physiology of cholangiocytes. Compr Physiol 3, 541-565.

Takashima, Y., Terada, M., Kawabata, M., Suzuki, A., 2015. Dynamic three-dimensional morphogenesis of intrahepatic bile ducts in mouse liver development. Hepatology 61, 1003-1011.

Tanaka, H., Takechi, M., Kiyonari, H., Shioi, G., Tamura, A., Tsukita, S., 2015. Intestinal deletion of Claudin-7 enhances paracellular organic solute flux and initiates colonic inflammation in mice. Gut 64, 1529-1538.

Tanimizu, N., Kikkawa, Y., Mitaka, T., Miyajima, A., 2012. alpha1- and alpha5-containing laminins regulate the development of bile ducts via beta1 integrin signals. J Biol Chem 287, 28586-28597.

Tanimizu, N., Kaneko, K., Itoh, T., Ichinohe, N., Ishii, M., Mizuguchi, T., Hirata, K., Miyajima, A., Mitaka, T., 2016. Intrahepatic bile ducts are developed through formation of homogeneous continuous luminal network and its dynamic rearrangement in mice. Hepatology 64, 175-188.

Tanimizu, N., Ichinohe, N., Sasaki, Y., Itoh, T., Sudo, R., Yamaguchi, T., Katsuda, T., Ninomiya, T., Tokino, T., Ochiya, T., Miyajima, A., Mitaka, T., 2021. Generation of functional liver organoids on combining hepatocytes and cholangiocytes with hepatobiliary connections ex vivo. Nat Commun 12, 3390.

Tchorz, J.S., Kinter, J., Muller, M., Tornillo, L., Heim, M.H., Bettler, B., 2009. Notch2 signaling promotes biliary epithelial cell fate specification and tubulogenesis during bile duct development in mice. Hepatology 50, 871-879.

Tong, M., Jun, T., Nie, Y., Hao, J., Fan, D., 2019. The Role of the Slit/Robo Signaling Pathway. J Cancer 10, 2694-2705.

Trefts, E., Gannon, M., Wasserman, D.H., 2017. The liver. Curr Biol 27, R1147-R1151.

Tremblay, K.D., Zaret, K.S., 2005. Distinct populations of endoderm cells converge to generate the embryonic liver bud and ventral foregut tissues. Dev Biol 280, 87-99.

Treyer, A., Musch, A., 2013. Hepatocyte polarity. Compr Physiol 3, 243-287.

Tseng, R.C., Lee, S.H., Hsu, H.S., Chen, B.H., Tsai, W.C., Tzao, C., Wang, Y.C., 2010. SLIT2 attenuation during lung cancer progression deregulates beta-catenin and E-cadherin and associates with poor prognosis. Cancer Res 70, 543-551.

Van der Wouden, J.M., Van IJzendoorn, I.S.C., Hoekstra, D., 2002. Oncostatin M regulates membrane traffic and stimulates bile canalicular membrane biogenesis in HepG2 cells. EMBO J 21, 6409-6418.

Van Liedekerke, P., Palm, M.M., Jagiella, N., Drasdo, D., 2015. Simulating tissue mechanics with agent-based models: concepts, perspectives and some novel results. Comp. Part. Mech. 2, 401–444.

Van Liedekerke, P., Neitsch, J., Johann, T., Warmt, E., Gonzalez-Valverde, I., Hoehme, S., Grosser, S., Kaes, J., Drasdo, D., 2020. A quantitative high-resolution computational mechanics cell model for growing and regenerating tissues. Biomech Model Mechanobiol 19, 189-220.

Vartak, N., Drasdo, D., Geisler, F., Itoh, T., R, P.J.O.E., van de Graaf, S.F.J., Chiang, J., Keitel, V., Trauner, M., Jansen, P., Hengstler, J.G., 2021. On the Mechanisms of Biliary Flux. Hepatology 74, 3497-3512.

Verboven, E., Moya, I.M., Sansores-Garcia, L., Xie, J., Hillen, H., Kowalczyk, W., Vella, G., Verhulst, S., Castaldo, S.A., Alguero-Nadal, A., Romanelli, L., Mercader-Celma, C., Souza, N.A., Soheily, S., Van Huffel, L., Van Brussel, T., Lambrechts, D., Roskams, T., Lemaigre, F.P., Bergers, G., van Grunsven, L.A., Halder, G., 2021. Regeneration Defects in Yap and Taz Mutant Mouse Livers Are Caused by Bile Duct Disruption and Cholestasis. Gastroenterology 160, 847-862.

Wainwright, E.N., Wilhelm, D., Combes, A.N., Little, M.H., Koopman, P., 2015. ROBO2 restricts the nephrogenic field and regulates Wolffian duct-nephrogenic cord separation. Dev Biol 404, 88-102.

Waugh, A., Grant, A., 2014. Ross & Wilson Anatomy and Physiology in Health and Illness, 12th ed.

Wei, Y., Wang, Y.G., Jia, Y., Li, L., Yoon, J., Zhang, S., Wang, Z., Zhang, Y., Zhu, M., Sharma, T., Lin, Y.H., Hsieh, M.H., Albrecht, J.H., Le, P.T., Rosen, C.J., Wang, T., Zhu, H., 2021. Liver homeostasis is maintained by midlobular zone 2 hepatocytes. Science 371.

Wells, K.L., Patel, N., 2010. Lumen formation in salivary gland development. Front Oral Biol 14, 78-89.

Wells, R.G., 2014. The portal fibroblast: not just a poor man's stellate cell. Gastroenterology 147, 41-47.

Willenborg, C., Prekeris, R., 2011. Apical protein transport and lumen morphogenesis in polarized epithelial cells. Biosci Rep 31, 245-256.

Woods, A., Heslegrave, A.J., Muckett, P.J., Levene, A.P., Clements, M., Mobberley, M., Ryder, T.A., Abu-Hayyeh, S., Williamson, C., Goldin, R.D., Ashworth, A., Withers, D.J., Carling, D., 2011. LKB1 is required for hepatic bile acid transport and canalicular membrane integrity in mice. Biochem J 434, 49-60.

Wu, M.F., Liao, C.Y., Wang, L.Y., Chang, J.T., 2017a. The role of Slit-Robo signaling in the regulation of tissue barriers. Tissue Barriers 5, e1331155.

Wu, N., Nguyen, Q., Wan, Y., Zhou, T., Venter, J., Frampton, G.A., DeMorrow, S., Pan, D., Meng, F., Glaser, S., Alpini, G., Bai, H., 2017b. The Hippo signaling functions through the Notch signaling to regulate intrahepatic bile duct development in mammals. Lab Invest 97, 843-853.

Wu, J.H., Zhou, Y.F., Hong, C.D., Chen, A.Q., Luo, Y., Mao, L., Xia, Y.P., He, Q.W., Jin, H.J., Huang, M., Li, Y.N., Hu, B., 2019. Semaphorin-3A protects against neointimal hyperplasia after vascular injury. EBioMedicine 39, 95-108.

Xu, C., Ding, Y.H., Wang, K., Hao, M., Li, H., Ding, L., 2021. Claudin-7 deficiency promotes stemness properties in colorectal cancer through Sox9-mediated Wnt/beta-catenin signalling. J Transl Med 19, 311.

Xu, J., Liu, X., Koyama, Y., Wang, P., Lan, T., Kim, I.G., Kim, I.H., Ma, H.Y., Kisseleva, T., 2014. The types of hepatic myofibroblasts contributing to liver fibrosis of different etiologies. Front Pharmacol 5, 167.

Yagai, T., Miyajima, A., Tanaka, M., 2014. Semaphorin 3E secreted by damaged hepatocytes regulates the sinusoidal regeneration and liver fibrosis during liver regeneration. Am J Pathol 184, 2250-2259.

Yanai, M., Tatsumi, N., Hasunuma, N., Katsu, K., Endo, F., Yokouchi, Y., 2008. FGF signaling segregates biliary cell-lineage from chick hepatoblasts cooperatively with BMP4 and ECM components in vitro. Dev Dyn 237, 1268-1283.

Yang, Y.H., Manning Fox, J.E., Zhang, K.L., MacDonald, P.E., Johnson, J.D., 2013. Intraislet SLIT-ROBO signaling is required for beta-cell survival and potentiates insulin secretion. Proc Natl Acad Sci U S A 110, 16480-16485.

Yang, L., Wang, W.H., Qiu, W.L., Guo, Z., Bi, E., Xu, C.R., 2017. A single-cell transcriptomic analysis reveals precise pathways and regulatory mechanisms underlying hepatoblast differentiation. Hepatology 66, 1387-1401.

Ypsilanti, A.R., Zagar, Y., Chedotal, A., 2010. Moving away from the midline: new developments for Slit and Robo. Development 137, 1939-1952.

Yu, W., Datta, A., Leroy, P., O'Brien, L.E., Mak, G., Jou, T.S., Matlin, K.S., Mostov, K.E., Zegers, M.M., 2005. Beta1-integrin orients epithelial polarity via Rac1 and laminin. Mol Biol Cell 16, 433-445.

Yuan, W., Rao, Y., Babiuk, R.P., Greer, J.J., Wu, J.Y., Ornitz, D.M., 2003. A genetic model for a central (septum transversum) congenital diaphragmatic hernia in mice lacking Slit3. Proc Natl Acad Sci U S A 100, 5217-5222.

Yuan, M., Guo, H., Li, J., Sui, C., Qin, Y., Wang, J., Khan, Y.H., Ye, L., Xie, F., Wang, H., Yuan, L., Ye, J., 2016. Slit2 and Robo1 induce opposing effects on metastasis of hepatocellular carcinoma Sk-hep-1 cells. Int J Oncol 49, 305-315.

Zaret, K.S., 2001. Hepatocyte differentiation: from the endoderm and beyond. Curr Opin Genet Dev 11, 568-574.

Zeng, Z., Wu, Y., Cao, Y., Yuan, Z., Zhang, Y., Zhang, D.Y., Hasegawa, D., Friedman, S.L., Guo, J., 2018. Slit2-Robo2 signaling modulates the fibrogenic activity and migration of hepatic stellate cells. Life Sci 203, 39-47.

Zhang, B., Dietrich, U.M., Geng, J.G., Bicknell, R., Esko, J.D., Wang, L., 2009. Repulsive axon guidance molecule Slit3 is a novel angiogenic factor. Blood 114, 4300-4309.

Zhang, N., Bai, H., David, K.K., Dong, J., Zheng, Y., Cai, J., Giovannini, M., Liu, P., Anders, R.A., Pan, D., 2010. The Merlin/NF2 tumor suppressor functions through the YAP oncoprotein to regulate tissue homeostasis in mammals. Dev Cell 19, 27-38.

Zhang, H., Pu, W., Tian, X., Huang, X., He, L., Liu, Q., Li, Y., Zhang, L., He, L., Liu, K., Gillich, A., Zhou, B., 2016. Genetic lineage tracing identifies endocardial origin of liver vasculature. Nat Genet 48, 537-543.

Zhao, J., Mommersteeg, M.T.M., 2018. Slit-Robo signalling in heart development. Cardiovasc Res 114, 794-804.

Zhou, W.J., Geng, Z.H., Chi, S., Zhang, W., Niu, X.F., Lan, S.J., Ma, L., Yang, X., Wang, L.J., Ding, Y.Q., Geng, J.G., 2011. Slit-Robo signaling induces malignant transformation through Hakai-mediated E-cadherin degradation during colorectal epithelial cell carcinogenesis. Cell Res 21, 609-626.

Zong, Y., Panikkar, A., Xu, J., Antoniou, A., Raynaud, P., Lemaigre, F., Stanger, B.Z., 2009. Notch signaling controls liver development by regulating biliary differentiation. Development 136, 1727-1739.

Zong, Y., Stanger, B.Z., 2012. Molecular mechanisms of liver and bile duct development. Wiley Interdiscip Rev Dev Biol 1, 643-655.

Zorn, A.M., Liver development (2008), StemBook, ed. The Stem Cell Research Community, StemBook, doi/10.3824/stembook.1.25.1

Zovein, A.C., Luque, A., Turlo, K.A., Hofmann, J.J., Yee, K.M., Becker, M.S., Fassler, R., Mellman, I., Lane, T.F., Iruela-Arispe, M.L., 2010. Beta1 integrin establishes endothelial cell polarity and arteriolar lumen formation via a Par3-dependent mechanism. Dev Cell 18, 39-51.